Out-of-pile thermophysical properties of metallic fuel for fast reactors in India

Joydipta Banerjee[a†]**, Santu Kaity**[a]**, K. Ravi**[a]**, M.R. Nair**[a]**, M.T. Saify**[b]**, Rajeev Keswani**[c]**, Arun Kumar**[d]**, G.J. Prasad**[d]

[a] Radiometallurgy Division, Bhabha Atomic Research Centre, Mumbai, India

[b] Atomic Fuels Division, Bhabha Atomic Research Centre, Mumbai, India

[c] Metallic Fuels Division, Bhabha Atomic Research Centre, Mumbai, India

[d] Nuclear Fuels Group, Bhabha Atomic Research Centre, Mumbai, India

Abstract. Two design concepts for the metallic fuel development program for fast breeder reactors (FBRs) are being considered in India e.g. mechanically bonded pin with U-15wt.%Pu alloy as fuel and sodium bonded pin with U-15wt%Pu-6wt%Zr alloy as fuel. Mechanically bonded binary alloy fuel pin will have a 'Zr' liner inside the T91 steel clad to prevent the fuel-clad chemical interaction. Present paper highlights the characterization results obtained so far on U-15%Pu alloy fuel which includes microstructure, phase transformation, coefficient of thermal expansion, hot hardness and studies on the fuel-clad (T91) chemical compatibility by diffusion couple experiments. U-6wt%Zr is the proposed blanket material for sodium bonded ternary U-Pu-Zr fuel. The data generated on U-6wt%Zr alloy sample prepared by injection melting are also presented here which includes coefficient of thermal expansion, specific heat, thermal conductivity, hot hardness, microstructure, phase analysis and chemical compatibility of this alloy with T91 cladding by diffusion couple experiments.

1. Introduction

The knowledge of thermophysical properties such as specific heat, coefficient of thermal expansion, density, thermal conductivity etc. of the fuel as a function of temperature are extremely important and must be known in order to effectively model and predict fuel behavior under normal and off-normal irradiation conditions.

Primarily, two design concepts have been proposed for the metallic fuel development programme for FBRs in India [1]. Two fuel concepts being explored are:

- Mechanically bonded pin with U-15 wt%Pu alloy as fuel,

- Sodium bonded pin with U-15 wt%Pu-6 wt%Zr alloy as fuel.

Fig. 1(a) shows the cross section of conventional sodium bonded fuel pin where Na acts as a thermal bond between the fuel (U-Pu-Zr) and cladding material. U-6wt%Zr (hereafter, referred as U-6Zr) is a subsystem of U-15 wt%Pu-6 wt%Zr alloy, and is also proposed as a blanket material for the sodium bonded ternary U-Pu-Zr fuel. U with low Zr (6 wt%) in the fuel is preferred in the Indian nuclear power programme with the objective of achieving a higher breeding ratio [1].

Fig. 1(b) shows the cross-section of a proposed mechanically bonded fuel pin where Zr is used as a barrier layer between fuel and cladding to prevent the fuel clad chemical interaction. T91 steel (mod.

---

† Email: joydipta@barc.gov.in

9Cr1Mo steel) will be used as the cladding material. T91 cladding tube having Zr barrier layer will be swaged on the fuel slug and it is expected that there will not be any physical gap between barrier layer and fuel slug. Two semicircular grooves, placed diametrically opposite, are provided in the fuel slug for the accommodation of irradiation induced fuel swelling and to facilitate early release of fission gasses. Helium gas is filled in the groove region.
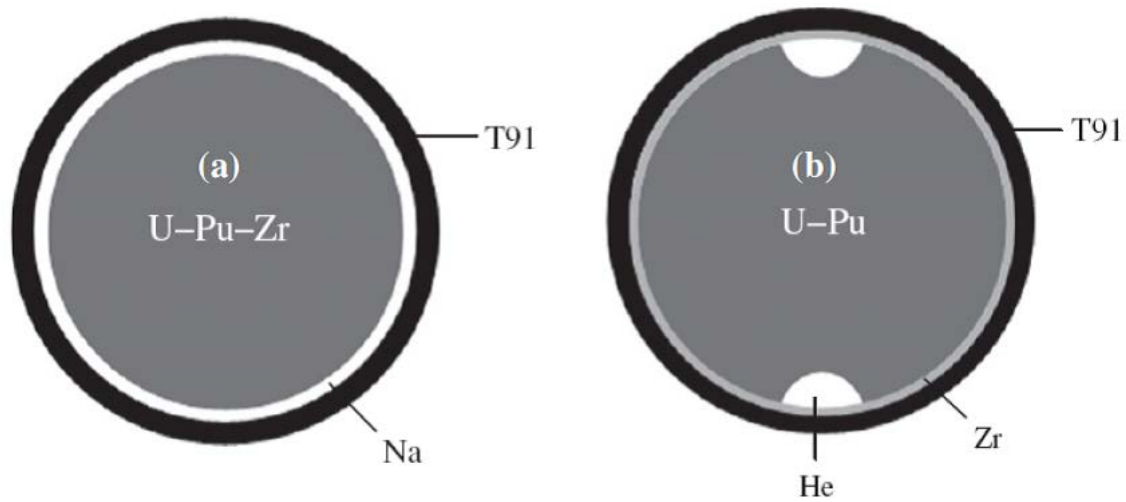

FIG. 1. Cross section of metallic fuel for (a) U-Pu-Zr ternary and (b) U-Pu binary alloy.

The present paper emphasizes on studies carried out on Zr as FCCI barrier layer for U-15wt%Pu (hereafter, referred as U-15Pu) binary fuel. Detailed report on the effectiveness of Zr as a barrier layer between U-15Pu alloy and T91 steel is limited and requires further investigation. Moreover, there are many reports available for U-Zr alloys with various Zr content; but no detailed studies have been reported on U-6Zr alloy.

The main objectives of the present study are:

i) Investigation on the microstructures of as-cast, quenched and heat treated U-6Zr alloy. Investigation on the microstructures of as-cast U-15Pu alloy by XRD and optical microscope,

ii) Determination of phase transformation temperatures and coefficient of thermal expansion for U-15Pu alloy with the help of differential thermal analysis (DTA) and dilatometer, respectively. Determination of thermophysical properties like coefficient of thermal expansion, specific heat, thermal conductivity of U-6Zr alloy sample prepared by injection melting,

iii) Evaluation of the hot-hardness data for U–6Zr alloy and U-15Pu binary fuel from room temperature to 973 K,

iv) Studies on the chemical compatibility of U-6Zr/ U-15Pu alloy with T91grade steel by diffusion couple experiments.

2. Experimental Procedure

2.1. Alloy preparation

U-15Pu alloy was prepared by melting and casting route. The U and Pu slugs were melted together using induction melting in an yttria coated graphite crucible. Graphite crucible was coated with alcohol based yttria slurry to prevent carbon pick-up from crucible. U–6Zr alloy sample was prepared by heating the casting charge to about 1700 K under vacuum. Once the melting procedure was over, open ends of quartz molds were immersed in the melt. The furnace chamber was pressurized with inert

gas to push molten alloy into the quartz molds. The fuel slugs are removed from the quartz molds using de-molding set up. Fuel slugs were subjected to dimensional and visual examinations. Typical diameter of the alloy slugs was about 5 mm.

2.2. *XRD and Microstructural analysis*

The phase analysis of the fuel alloy was carried out using XRD with Cu Kα radiation. Standard metallographic techniques were adopted for grinding and polishing. Electrolytic etching was carried out using 2V potential and SS 304 as cathode. A solution containing orthophosphoric acid, ethylene glycol and ethanol was used as electrolyte for U-15Pu alloy and 50% H_3PO_4 aqueous solution was used for U-6Zr alloy.

2.3. *Determination of phase transformation temperature by differential thermal analysis (DTA)*

The transformation temperature measurements were carried out using a differential thermal analyzer (Model No. Setsys Evolution 24, combined TG/DTA/DSC; make: M/s Setaram Instrumentation, France). Sample of about 200 mg was cut from the bulk one and then loaded into the crucible. The furnace was purged with highly purified argon gas flowing at 2 dm^3h^{-1} and the heating and cooling rates were programmed at 5 K min^{-1}. The temperature calibration was accomplished by measuring the melting points of high purity metals, such as Zn, Al, Ag and Au.

2.4. *Dilatometry*

The expansion behavior of U-6Zr was studied using a high temperature vertical dilatometer (make: SETARAM Instrumentation, France; model: Setsys Evoluation 24). The heating rate used for the present study was 5 K min^{-1}. Here, the sample is loaded inside a sample holder which is made of Al_2O_3. The change of the length of the sample was transmitted through the frictionless push rod to an LVDT transducer. A nominal load of 5 g was chosen to be applied by the push rod over the sample. A calibrated thermocouple was placed to record the sample temperature. The dilatometric experiments were carried out in high purity argon atmosphere at a dynamic gas flow rate of 2 dm^3 h^{-1}.

2.5. *Thermal conductivity*

Thermal conductivity of U-6Zr alloy was determined by Transient Plane Source (TPS) technique [2][3][4] based on a specially designed Wheatstone bridge with TPS sensor as one of the arms. The TPS unit was calibrated by the Inconel 600 standard sample from room temperature to 973 K. The mica sensor of radius 3.189 mm was sandwitched between the polished surfaces two identical cylindrical U-6Zr alloy samples of diameter 20 mm and height 10 mm. The samples were heated in high purity argon atmosphere to avoid oxidation.

2.6. *Specific heat*

Specific heat measurements were carried out using a heat flux type differential scanning calorimeter, DSC-131 supplied by SETARAM Instrumentation, France using three experiments (runs) namely, blank, standard and sample. In the first (blank) run, two empty identical aluminum crucibles of identical masses and 10^{-4} dm^3 capacity with covering lid were kept in the sample and reference cells and the heat flow versus temperature were recorded. In the second (standard) run, the heat flow versus temperature were recorded by loading NIST synthetic sapphire (SRM-720) in the powder form (~200 mg) into the aluminum crucible in the sample cell keeping the crucible in the reference cell empty. In the third sample run, heat flow versus temperature were measured by loading the actual experimental sample (~200 mg) into the aluminum crucible in the sample side and keeping the crucible in the reference side empty. In all the three sets of experiments, high purity argon as a carrier gas with the flow rate of 3 dm^3 h^{-1} and furnace heating rate of 5 K min^{-1} were maintained.

2.7. *Hot hardness*

Hot hardness measurements were carried out using a hot hardness tester (Nikon, Model QM) with the help of a diamond Vickers pyramid indenter. Sample of 5 mm length was cut from the alloy slug of diameter 5 mm and was metallographically prepared before loading into the specimen holder. A load of 1 N at a rate of 0.2 mm min^{-1} and a dwell time of 5 s were used. Calibration of the equipment was done using a standard sample (Cu: SRM; NIST, USA).

2.8. *Chemical compatibility with T91 cladding*

For the diffusion couple experiment, a thin Zr foil of thickness 100 µm was sandwiched between the alloy (3 mm thick disc) and T91 discs (0.5 mm thick disc). The components of the diffusion couple were stacked within a fixture made of Inconel 600 to ensure intimate contact during annealing. Tantalum foil was used to prevent any chemical reaction between couple and fixture. The fixture containing the samples was encapsulated in a stainless steel tube under helium atmosphere to avoid any leakage of radioactivity during heating and was further encapsulated in a quartz tube under helium atmosphere. These were heated in resistance heating furnaces for various temperatures and duration. Subsequent to annealing, these couples were sectioned using a slow speed diamond cutting wheel and metallographically polished. The interfaces were examined under optical microscope or by using SEM-EDS.
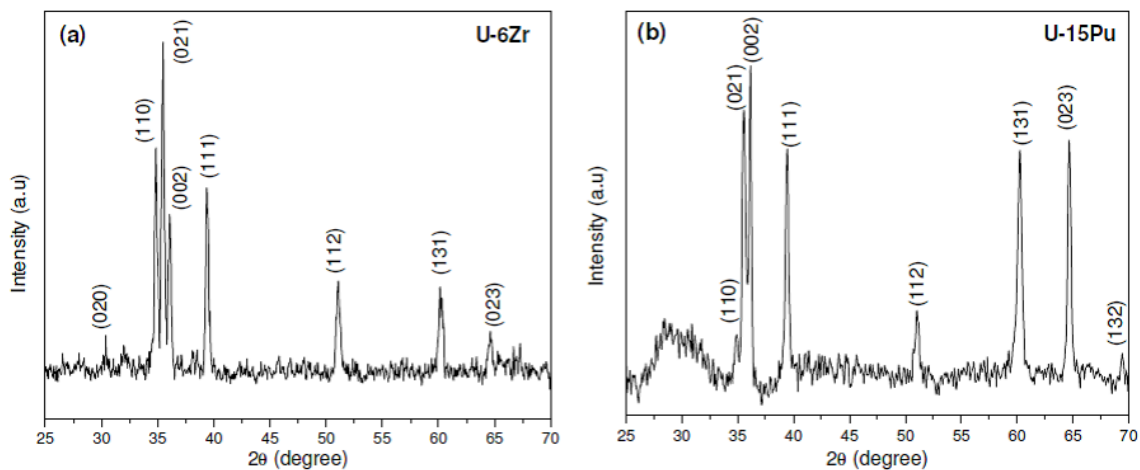
3. Results and Discussion

FIG. 2. XRD data of as-cast (a) U-6Zr alloy and (b) U-Pu alloy.

The XRD pattern obtained for U-6Zr and U-15Pu alloy are shown in Fig. 2. The peaks observed for the former in the XRD data as shown in Fig. 2(a) correspond to single phase having orthorhombic 'α' phase of uranium. No peak corresponding to δ phase was observed for the as cast alloy. This is expected as the formation of δ phase is kinetically sluggish. The microstructure contains only supersaturated α phase in Widmanstatten morphology (Fig. 3 (a)). Water quenched microstructure of U-6Zr, however, shows martensitic plates (Fig. 3(b)). For U-15Pu alloy, all the XRD peaks correspond to 'α' phase of uranium (Fig. 2 (b)). XRD data do not contain any peak corresponding to the ζ phase. Formation of this phase was not evident from the microstructure of this alloy also (Fig. 4). The reason for this could be either the amount of this phase was below detectible limit of the XRD instrument used or there was no ζ phase formation as it would be kinetically unfavoured for the high cooling rate in the cast structure.

Transition temperatures observed in DTA for U-6Zr are shown in Fig. 5(a). To investigate the peak observed at 843 K, the U–6Zr alloy samples were subjected to the various heat treatments (Fig. 5(b)). This peak was observed for both the as-cast and quenched sample. After the sample was isothermally

held at 823 K of 1 h, the DTA peak height gets diminished. After the sample was annealed at 823 K for 24 h, no peak at that temperature was observed. Even after this long isothermal holding, no peak was observed corresponding to decomposition of δ phase which occurs at temperature 890 K. Therefore, the peak observed at 843 K can be attributed to the martensitic to non-martensitic transformation. The peaks observed at 943 K and 968 K corresponds to phase changes ($\alpha + \gamma''$ to $\beta + \gamma''$) and ($\beta + \gamma''$ to $\gamma' + \gamma''$), respectively. Slope changes corresponding to these two transition temperatures were also observed in dilatometric curve (Fig. 7(a)). The peak at 1448 K (Fig. 5(a)) indicates the solidus temperature. Fig. 6(a) shows the transition temperatures as observed in DTA for U-15Pu alloy. The peak observed at 837 K corresponds to $\alpha(U) \leftrightarrow \beta(U)$ transition and that at 991 K is due to the $\beta(U) \leftrightarrow \varepsilon(Pu) + \gamma(U)$ transition. These transformation temperatures were also observed as slope changes in expansion vs. temperature plot and are shown in Fig. 7(b). The peak at 1248 K (Fig. 6(a)) corresponds to the solidus temperature. The eutectic temperature between U-15Pu alloy and T91 was found to be 948 K and the corresponding DTA curve is shown in Fig. 6(b).
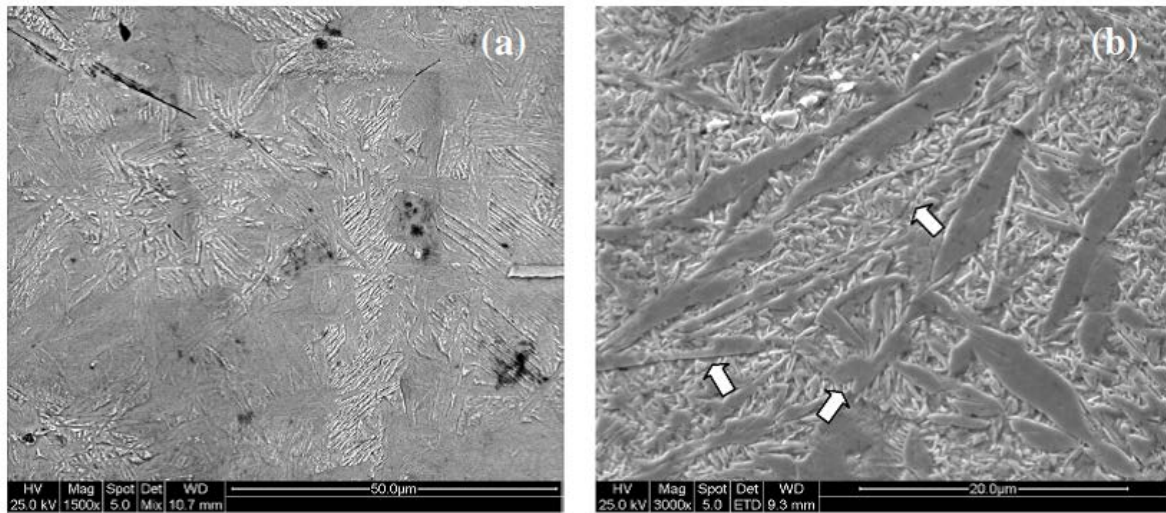

FIG. 3. Microstructure of U-6Zr alloy (a) as-cast: showing Widmanstatten morphology; (b) water quenched from 1173 K : showing martensitic plates and prior γ grain boundaries (indicated by arrows).
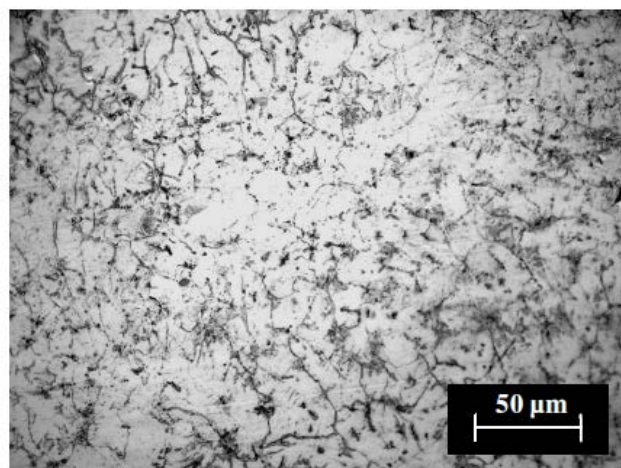

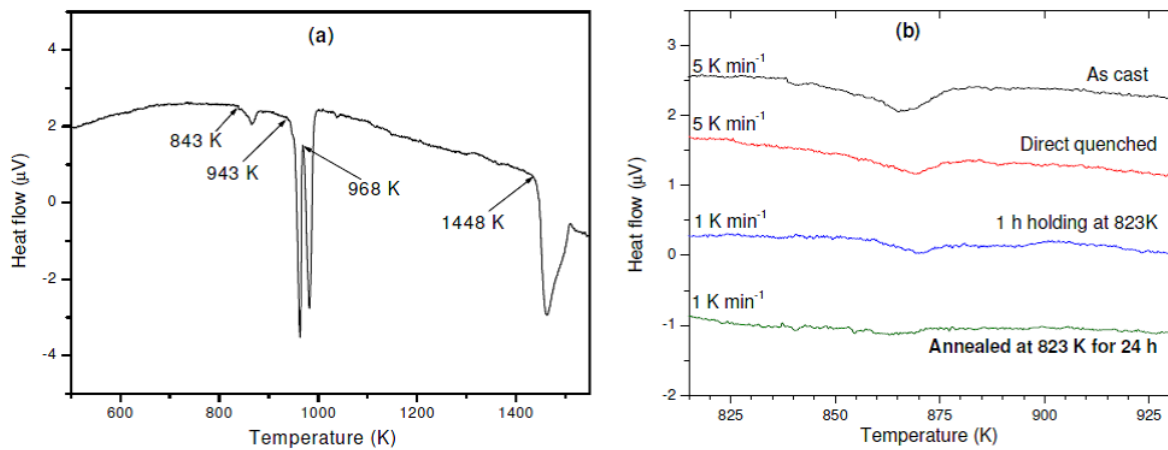FIG. 4. Microstructure of as-cast U-15Pu alloy.

FIG. 5. DTA curve showing different phase transformations of U-6Zr alloy (a) for as cast and (b) after various heat treatments.
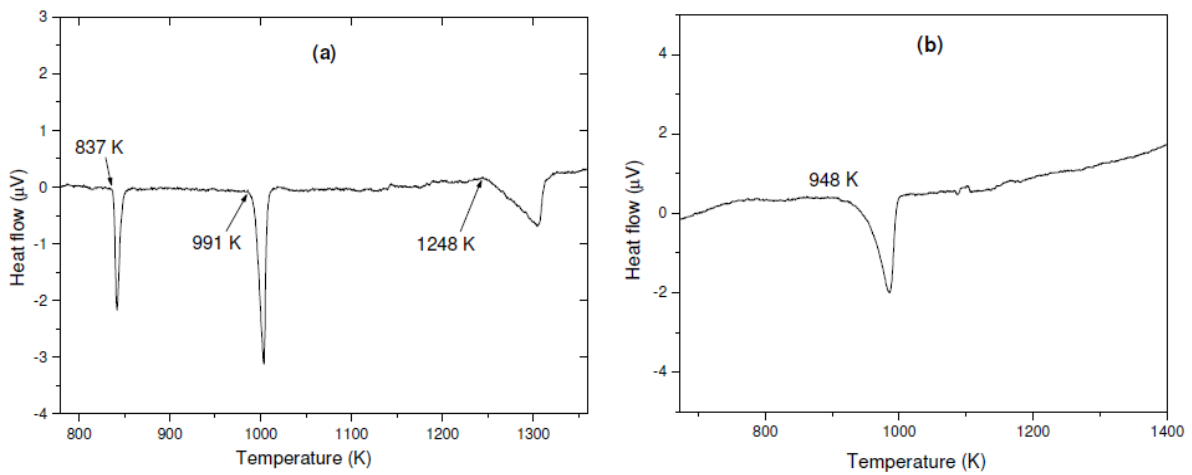

FIG. 6. DTA curve of as cast U-15Pu alloy showing (a) different phase transformations and (b) eutectic reaction temperature between the alloy and T91 grade steel.

The thermal expansion behaviour of the alloys are shown in Fig. 7(a) and Fig. 7(b). The average coefficient of thermal expansion of U-6Zr and U-15Pu alloy was found to be 18.28×10^{-6} K^{-1} and 18.58×10^{-6} K^{-1}, respectively, in the temperature range 300-823 K.

Specific heat for U-6Zr was observed to be varying from ~135 $J.Kg^{-1}.K^{-1}$ at 300 K to ~218 $J.Kg^{-1}.K^{-1}$ at 923 K. The specific heat curve shows a phase transition at 845 K and is shown in Fig. 8(a) along with literature data of U and Zr [5]. Thermal conductivity of both the uranium and U-Zr alloy increases with increas in temperature [6][7][8] and U-6Zr alloy was observed to have lower thermal conductivity than that of uranium (Fig. 8(b)).

The hardness vs. temperature curves for U-6Zr alloy consist of two straight lines with different slope intersecting at 748K (~ $0.5T_m$) and is shown in Fig. 9(a) together with literature data of U-5Zr [9]. The hardness (H) vs. temperature (T) plot for U-15Pu alloy in the temperature range of 298-988 K is shown in Fig. 9(b). The plot shows a steady decrease in hardness over the entire temperature range up to ~700 K. Beyond ~990 K, due to the formation of soft γ phase, hardness decreases very steeply and measurement was not practicable.
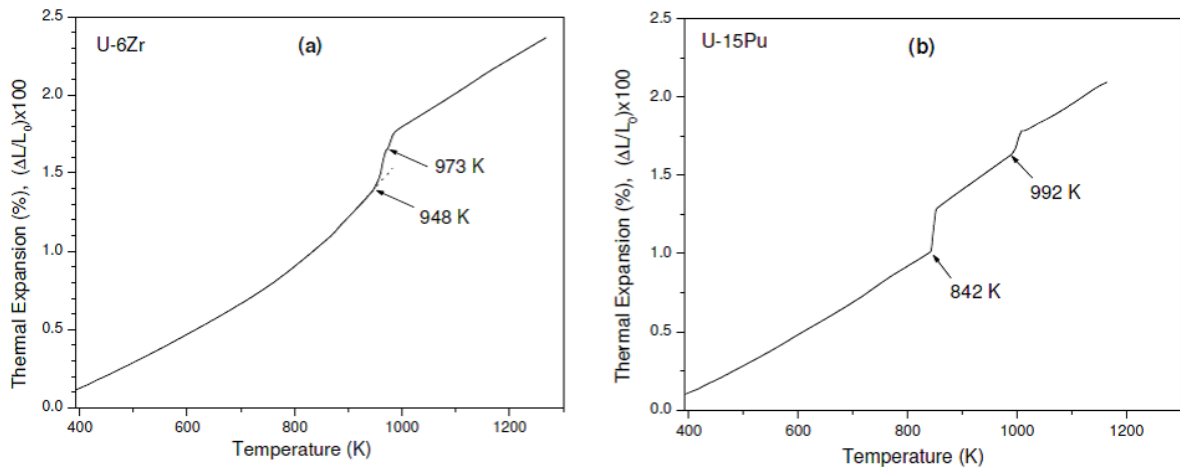
FIG. 7. Thermal expansion curve obtained from the dilatometer for (a) U-6Zr and (b) U-15Pu alloy.
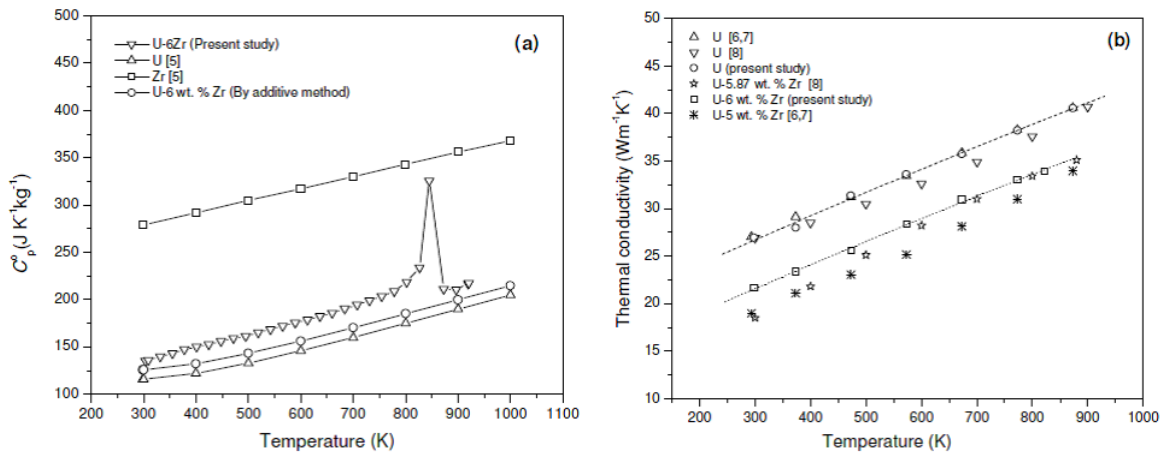

FIG. 8. (a) Specific heat data for U-6Zr alloy obtained as a function of temperature; Specific heat of U-6Zr alloy determined by additive method and literature data [5] of U, Zr are also shown. (b) Thermal conductivity data of U and U-6Zr alloy obtained as a function of temperature together with that of U and U-Zr alloys reported in the literature [6][7][8].

Fig. 10 shows the diffusion couple-fixture assembly used for this study. Fig. 11(a) shows the microstructure of the interdiffusion layer formed at the interface of the U–6Zr/T91 diffusion couple after annealing at 973 K for 500 h [10]. The magnified micrograph of the interface is shown in Fig. 11(b). The interdiffusion between the two specimens resulted in the formation of three different layers at the interface: a (U,Zr)(Fe,Cr)2 type layer of thickness around 10 µm on the T91 side, a 15-20 µm thick Zr depleted layer (having ~94 at.% U, 4 at.% Zr, 2 at.% Fe) on the U–Zr alloy side and a thin Zr rich layer (having ~9 at.% U, 87 at.% Zr, 4 at.% Fe) of thickness 2-3 µm between the above two. This Zr rich layer at the interface acts as fuel-clad diffusion barrier. However, no melting has been observed at this temperature. The measured eutectic temperature between U–6Zr alloy and T91 was found to be 995 K, which is almost equal to that of U–Fe system. At 1023 K, U–6Zr/T91 couple reacted completely with each other causing a complete melt down of the clad in 100 h, and showed eutectic-melted microstructures consisting of U_6Fe, $U(Fe,Cr)_2$ and $Zr(Fe,Cr)_2$ phases identified with the help of S. The melted microstructure of this couple is shown in the Fig. 11(c).
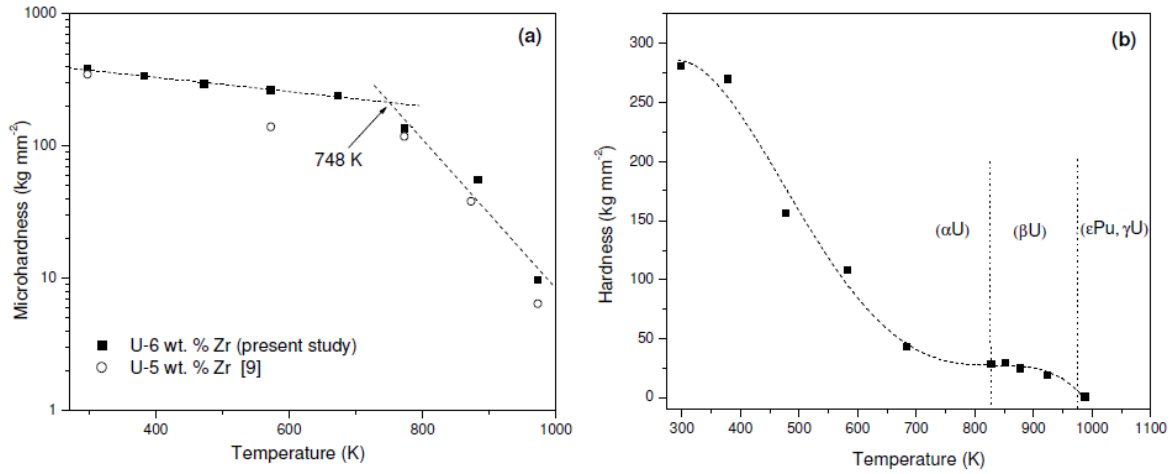
FIG. 9. Hardness versus temperature plot for (a) U-Zr alloy showing the transition point and (b) U-15Pu alloy, showing the variation of hardness in different phases.
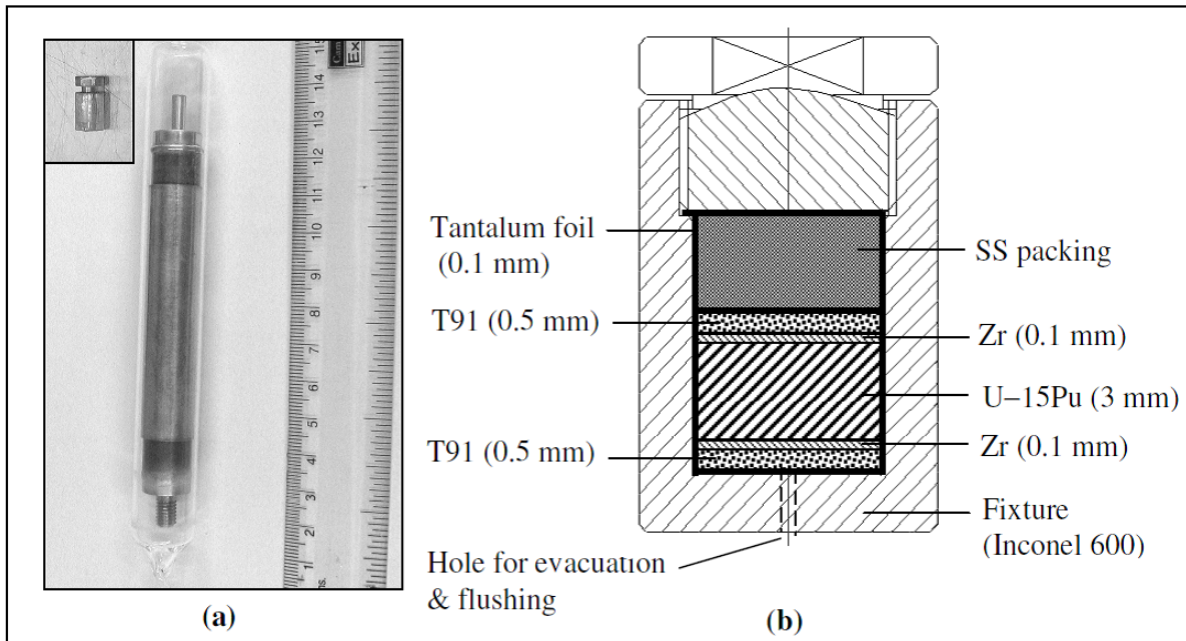
FIG. 10. (a) Photograph of quartz encapsulated stainless steel tube containing diffusion couple-fixture assembly with Inconel 600 fixture shown in the inset and (b) schematic of the diffusion couple-fixture assembly used showing the details.

The microstructure of the U-15Pu/Zr/T91 diffusion couple annealed at 973 K for 500 h is shown in Fig. 12(a). The microstructural analysis of U-15Pu/Zr/T91 diffusion couples revealed an excellent bond formation at both the U-15Pu/Zr and Zr/T91 interfaces after annealing [11]. The thickness of interdiffusion layer at the U-15Pu/Zr interface at 973 K was found to be in the range of 10-20 µm (Fig. 12(b)). The formation of interdiffusion layer was not evident from microstructure of Zr/T91interface (Fig. 12(c)).

FIG. 11. SEM images obtained for (a) the interdiffusion layer formed at the interface of U-6Zr/T91 couple after annealing at 9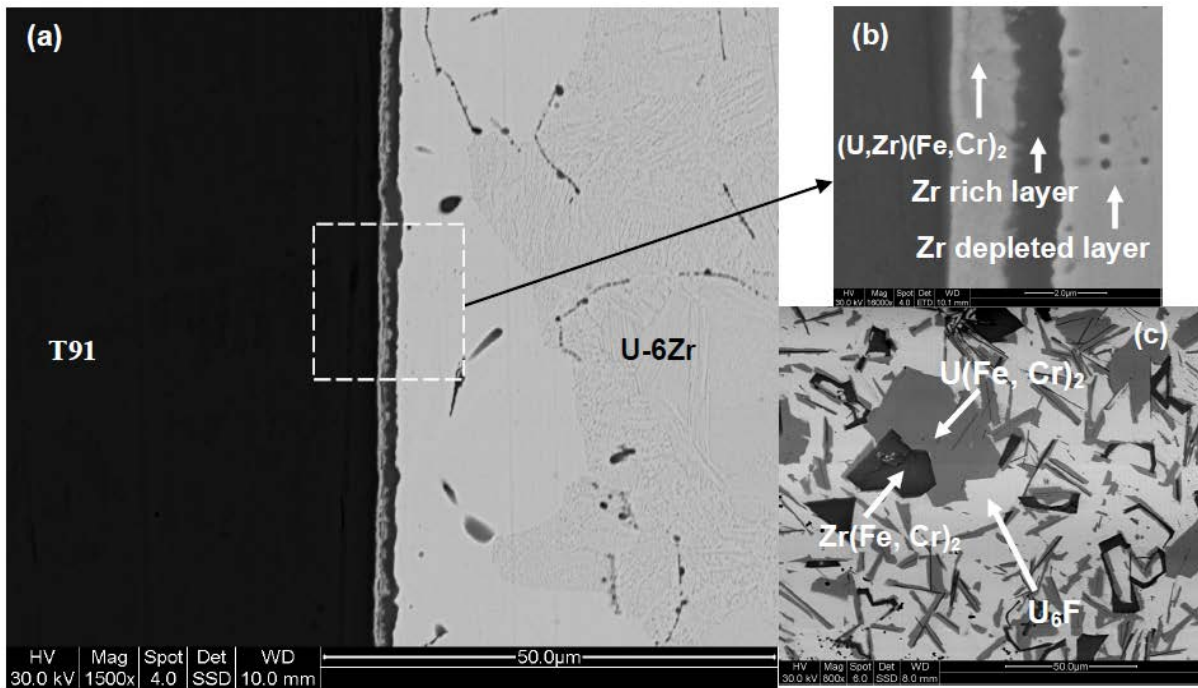73 K for 500 h, (b) Magnified micrograph of the interface, showing formation of the various layers and (c) the melted structure of U-6Zr/T91 diffusion couple after annealing at 1023 K for 100 h.
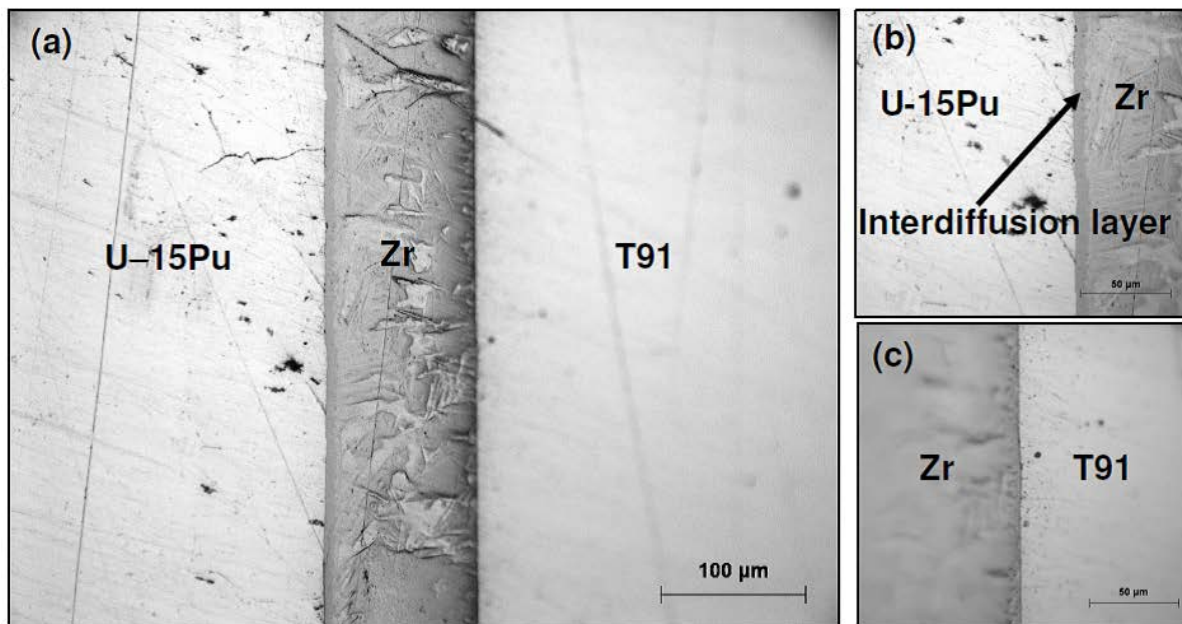
FIG. 12. Microstructure of (a) U-15Pu/Zr/T91 diffusion couple annealed at 973 K for 500 h, (b) Magnified view of the U-15Pu/Zr interface and (c) Magnified view of the Zr/T91 interface.

4.   Summary and Conclusions

U-6Zr alloy: The DTA curve of as-cast U-6Zr alloy showed a peak at 843 K, which does not correspond to the any transformation of equilibrium U-Zr phase diagram. This peak can be attributed to the martensitic α'_a to non-martensitic α transformation. The average coefficient of thermal expansion was found to be 18.28 x 10^{-6} K^{-1} in the temperature range 298-823 K. The thermal conductivity, measured by TPS method, of both the uranium and U–6Zr alloy increases with

increasing temperature and U-6Zr alloy is having a lower thermal conductivity than that of uranium. The specific heat versus temperature curve shows a phase transition at 845 K. Hardness vs. temperature plot showed two straight lines with different slopes which intersect at around 748 K. The eutectic reaction temperature between U–6Zr alloy and T91 steel system is almost equal to that of U-Fe, i.e. 995 K. The interdiffusion between U-6Zr and T91 at 973 K for 500 h results in the formation of a $(U, Zr)(Fe, Cr)_2$ type layer on the cladding side and a Zr depleted layer on the fuel side. A Zr rich layer was found between these two which acts a fuel cladding interdiffusion barrier. At 1023 K, U-6Zr/T91 couple reacted completely with each other causing a complete melt down of the cladding in 100 h, and showed eutectic-melted microstructures of U_6Fe, $U(Fe,Cr)_2$ and $Zr(Fe,Cr)_2$ phases.

U-15Pu alloy: The XRD and microstructure of as-cast U-15Pu alloy showed only the presence of α-U phase. ζ phase could not be detected in this alloy. The solidus temperature was found to be 1248 K. The average coefficient of thermal expansion was found to be 18.58×10^{-6} K^{-1} in the temperature range 300-823 K. The hardness temperature plot showed a transition around 800 K due to the appearance of the tetragonal β. In the β-phase, which extends up to 978 K, the decrease in hardness with increase in temperature is meager. The γ phase region of U-15Pu was found to be very soft. The eutectic reaction temperature between U-15Pu alloy and T91 steel system was found to be 948 K. The Zr liner was found to be effective in preventing fuel–cladding chemical interaction at 973 K for 500 h for U-15Pu/Zr/T91 diffusion couple.

REFERENCES

[1]   K. Devan, A. Bachchan, A. Riyas, T. Sathiyasheela, P. Mohanakrishnan, S.C. Chetal, Nucl. Eng. Des. 241 (2011) 3058.

[2]   S.E. Gustafsson, Rev. Sci. Instrum. 62 (3) (1991) 797.

[3]   S.E. Gustafsson, International Patent Application No. PCT/SE89/00137.

[4]   Hot Disk Thermal Constants Analyser, Instruction Manual, Software version 5.9, Hot Disk, Sweden, 2007.

[5]   I. Barin, Thermochemical Data of Pure Substance, third ed., VCH, Weinheim, 412 1995.

[6]   Y.S. Touloukian, R.K. Kirby, R.E. Taylor and P.D. Desai, Thermal Expansion, Thermophysical Properties of Matter, Vol.12, IFI/Plenum, New York-Washington (1975).

[7]   Y.S. Touloukian, R.W. Powell, C.Y. Ho, P.G. Klemens, Thermophysical Properties of Matter, Vol. 1 (IFI/Plenum, New York, 1970).

[8]   Y. Takahashi, M. Yamawaki, K. Yamamoto, J. Nucl. Mater. 154 (1988) 141.

[9]   W. Chubb, G.T. Muehlenkamp, A.D. Schwope, A hot-hardness survey of the Zirconium-Uranium system, Report No. BMI-833, Metallurgy and Ceramics, Battelle Memorial Institute, 1953 (May).

[10]   Santu Kaity, Joydipta Banerjee, M.R. Nair, K. Ravi, Smruti Dash, T.R.G. Kutty, Arun Kumar, R.P. Singh, J. Nucl. Mater. 427 (2012) 1.

[11]   Santu Kaity, Joydipta Banerjee, K. Ravi, R. Keswani, T.R.G. Kutty, Arun Kumar, G.J. Prasad, J. Nucl. Mater. 433 (2013) 206.

Fabrication of Metallic Fuel Slugs for Irradiation Experiments in Fast Breeder Test Reactor

M.T. Saify[a], S.K. Jha[a], K.K. Abdulla[a], Arun Kumar[b], G.J. Prasad[b]

[a] Atomic Fuels Division, Bhabha Atomic Research Centre, Mumbai, India

[b] Nuclear Fuels Group, Bhabha Atomic Research Centre, Mumbai, India

Abstract. First stage of Indian nuclear power programme comprises of natural uranium oxide fuelled Pressurized Heavy Water Reactors (PHWRs). Liquid metal cooled fast breeder reactors fuelled with plutonium form the second stage. In view of the limited uranium resources in India, a shorter doubling time and high breeding ratio is essential to accelerate the nuclear power growth. Metallic fuels are known to provide shorter doubling time necessitating its use as driver fuel for fast breeder reactors. A metallic fuel fabrication and inspection facility has been set-up in glove boxes at Bhabha Atomic Research Centre (BARC), Mumbai, India. This facility, which consists of injection casting process step, has successfully demonstrated production of 5.0mm and 6.0mm diameter binary U-Zr alloy slugs having varying zirconium content and length with random grain orientation which otherwise would require a number of thermo-mechanical working operations. The paper covers fuel fabrication and inspection details. Parameters have been optimized for production of binary uranium-zirconium alloy fuel slugs meeting required specifications. Natural and enriched U-6wt.%Zr alloy fuel slugs meeting the specifications with respect to chemical analysis, dimensions, mass and defect size have been produced for fabrication of test fuel pins for irradiation studies in FBTR.

1.0 Introduction

Sodium cooled fast breeder reactors fuelled with plutonium bearing fuels form the second stage of 3-stage Indian Nuclear Power Programme. The programme is designed so as to effectively utilize India's limited uranium resources and abundant thorium for meeting the growing energy demand. Thorium, though it possesses a number of superior physical and nuclear characteristics than uranium, does not have fissile isotope of its own, and therefore, it cannot be used as driver fuel [1]. Plutonium is obtained from the first stage comprising of natural uranium oxide fuelled Pressurized Heavy Water Reactors. From the reactor engineering point of view, fuel capable of performing under high power density and high specific power environment is preferable. From the Indian perspective, a well established pressurized heavy water reactor technology involving fuel fabrication, reactor operation and reprocessing of oxide fuel using PUREX process, already exists. As a part of the second stage, the FBR programme was started in India with the 40 MW(Th) Fast Breeder Test Reactor (FBTR) at IGCAR, Kalpakkam. This reactor is fuelled with indigenously developed mixed (U+Pu) carbide fuel, which has undergone burn-up of 165 GWd/t from the initially anticipated burn-up of 25 GWd/t. Successfull operation of FBTR has led to the design and construction of 500 MW(e) Prototype Fast Breeder Reactor (PFBR). Based on the expertise of manufacturing and reprocessing of oxide based fuels, PFBR is planned to be fuelled with mixed oxide fuel. However, in order to accelerate the nuclear power growth in India, there is a need for fuel systems incorporating shorter doubling time and hence higher breeding ratio. Metallic fuels provide shorter doubling times, making it preferable to be used as driver fuel for Indian fast breeder reactors. In addition to this, metallic fuels provide for higher thermal conductivity, higher fissile atom density and good compatibility with metallic coolants. Further, higher irradiation induced swelling rates of metallic fuels can be offset by designing fuels with lower smear densities [2].

Based on the experience reported [1, 4] it has been decided to study the performance of ternary U-Pu-Zr based and binary U-Pu based metallic fuels in India. U-19wt.%Pu-6wt.%Zr alloy having satisfactory compatibility with T91 cladding can be used in sodium bonded configuration. Zirconium is added as an alloying element for increasing the solidus temperature of the fuel and to avoid fuel clad

chemical interaction (FCCI). However, there will be penalty on thermal conductivity and breeding ratio. In the case of ternary alloy, gap between the fuel and clad (arising due to ~75% smear density) is filled with sodium from heat transfer considerations. U-15wt.%Pu binary alloy doesn't have good compatibility with T91 cladding due to formation of low melting point eutectics. In the case of binary alloy fuels, Zircaloy-4 lined T-91 cladding is proposed to be used to prevent fuel clad chemical interaction. Further, the solidus of binary fuel will be on lower side as compared to that of the ternary alloy.

For development of technologies involving fuel slug fabrication, sodium bonding, pin fabrication, eveluation of thermo-physical properties, reprocessing studies and subsequent irradiation trials, it has been decided to use U-6wt.%Zr binary alloy to simulate the fuel material. Accordingly, U-6wt.%Zr binary alloy fuel slugs were produced meeting required specifications. The U-6wt.%Zr binary alloy is an important sub-system of U-19wt.%Pu-6wt.%Zr ternary alloy and also proposed as a blanket material. However, attempt were made to match the linear heat rating of ternary alloy with that of U-Zr binary alloy by having suitable enrichment of U-235 in the later case. Zirconium in U-Zr alloy were kept at ~6wt.% with the objective of achieving higher breeding ratio [5].

The paper briefly describes injection casting based fuel fabrication and inspection facility covering various sub-systems.

2.0 Specification

Broad specifications establishing technical requirements with respect to chemical composition, metrology, mass, and internal defects of binary metallic fuel slugs for irradiatiom experiments in FBTR have been listed in Table 1.

Table 1. Specifications for metallic fuel slugs

	Specifications
Fuel	Enriched U-Zr alloy
Zr-content, *(wt.%)*	6.0 (+1 / -0)
Mass, *g*	51.7 (+2.4 / -3.2)
Length, *mm*	160 ± 2
Diameter, *mm*	4.90 ± 0.06
Linear Mass, *g/cm*	3.23 (+0.11 / -0.16)
Straightness	0.2/160
Surface Roughness, *Ra, (µm)*	3.2
ECT	Max. acceptable total sub-surface defect in any cross-section shall be 1% area of the slug

3.0 Fuel fabrication

One of the important advantages of metallic fuel cycle is that it lends itself to pyroprocessing involving elctro-refining. Uranium, plutonium, minor actinides and some of the fission products are deposited at the cathode. The retained fission products keep the fuel highly radioactive, which means all recycling and re-fabrication steps need to be carried out remotely in a hot cell [2]. The task of designing the facilities to meet this requirement is a formidable one. The fuel fabrication and inspection facility have been designed, fabricated and installed in glove boxes in order to make it amenable for handling plutonium-based fuel also. As a prototype facility, its primary aim was to establish and optimize various parameters for fabrication of acceptable quality of fuel slugs for evaluation of thermo-physical properety data, pyro-processing studies and irradiation trials. Flow-

sheet depicting various process steps involved in manufacturing of binary alloy fuel slugs has been highlighted in Fig.1a.
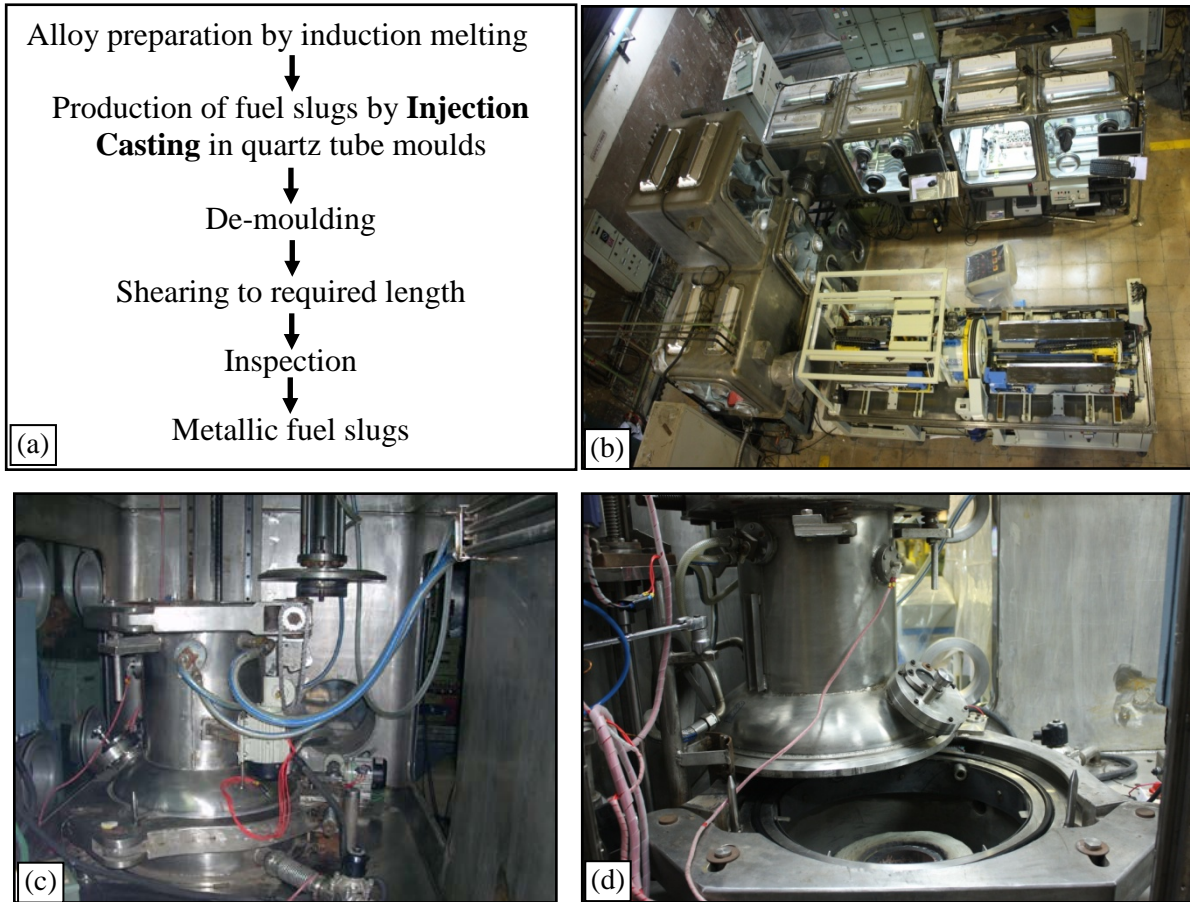

FIG. 1. Metallic Fuel Fabrication; (a) Flow-sheet, (b) Fuel fabrication and inspection facility at BARC, (c) & (d) Inside view of Injection casting glove box

3.1 Alloy preparation

Materials used for preparation of alloy were pure uranium ingots produced by magnesio-thermic reduction of fluoride and arc melted zirconium in sheet form. Potential concerns in preparation of homogenous U-Zr alloys meeting specified chemical composition by induction melting route were (i) large difference in melting points of uranium and zirconium, (ii) large difference in density, (iii) higher reactivity of zirconium with carbon (graphite crucible used for melting) and (iv) oxidation of uranium and zirconium; limiting the alloying by diffusion. These concerns were addressed by adopting careful charge preparation, appropriate charging sequencing, crucible design, etc.

3.2 Injection casting

Fabrication of slender fuel slugs (having high L/D ratio) using conventional methodology of melting, casting and mechanical working operation would induce fabrication texture in anisotropic α-phase uranium, leading to vast dimensional changes during in-reactor performance. In the light of aforementioned considerations, injection casting technology has been adopted for fabrication of metallic fuels having smaller diameters and random grain orientations. The technique finds its basis in an elementary physical concept – the possibility of supporting a liquid column within a tube, by the application of a pressure difference across the liquid interface inside and outside the tube [6] (Fig. 3).
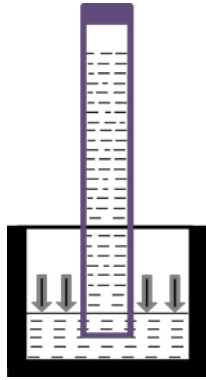
FIG. 3. Principle of injection casting technique

Apart from the ability to produce randomly oriented grain structure, the injection casting technique for fabrication of metallic fuel envisages several important advantages over conventionally adopted methodologies [6].

a. Higher degree of cast product reproducibility with respect to grain size and structure.
b. Capacity of producing precision casting requiring no subsequent machining.
c. Possibility of multi-mould casting – limited only by criticality considerations and handling facilities.
d. Adaptability to remotization of fabrication process steps because of the few and simple steps involved and its limited space requirement.
e. Applicability to wide range of alloy compositions.

At BARC, a facility has been set-up for injection casting of uranium metal/alloy slugs in quartz tube moulds, de-moulding of cast slugs, end-shearing of slugs and an automated inspection system for inspection of fuel slugs with respect to mass, length, diameter and diameter variation along the length and internal & external porosities/voids. All the above facilities have been set up in glove boxes and have successfully been used for fabrication of uranium bearing fuel slugs. The facility has been designed for fabrication and inspection of Pu-bearing metallic fuels also.

U-Zr alloy having varying composition, prepared by induction melting, were cast into higher L/D ratio metallic fuel slugs by injection casting in quartz tube moulds. Prior to injection casting, each tube was coated with graphite slurry on inner surface in order to prevent reaction between molten uranium and quartz. The as-cast surface finish obtained was well within the specification. In this process, a bunch of one-end sealed quartz tube moulds are suspended, open-end down, with the help of a suitable fixture above the graphite crucible loaded with predetermined quantity of charge. The furnace is evacuated to the required level of vacuum and the metal is melted and superheated to a predetermined temperature using induction power source. The moulds are lowered to the required depth in the molten metal and the chamber is isolated from the vacuum system. The furnace chamber is then pressurized with an inert gas to a set pressure thereby forcing the molten metal in the evacuated moulds. Induction power is now put-off and moulds are raised approximately 20 sec. after the presuurization step and allowed to cool. After attaining room temperature the furnace is opened and the moulds are removed from the fixture along with castings.

3.3 De-moulding

moulds with castings are then transferred to the second glove box housing demoulding and shearing units. Demoulding unit has been designed to handle moulds of different diameters. Injection cast slugs after demoulding are collected on tray and broken quartz pieces are collected in a waste collection tray.

FIG. 4. Injection casting; (a) View of quartz tube moulds dipped in molten alloy, (b) Mould cassette holding cast slugs along with moulds

3.4 Shearing

After demoulding, fuel slugs are automatically transferred to the "End-Shearing Unit" located adjacent to demoulding unit in the same glove box. The unit has been designed to produce a "burr-free" face suitable for use as fuel slug without any further mechanical operation.
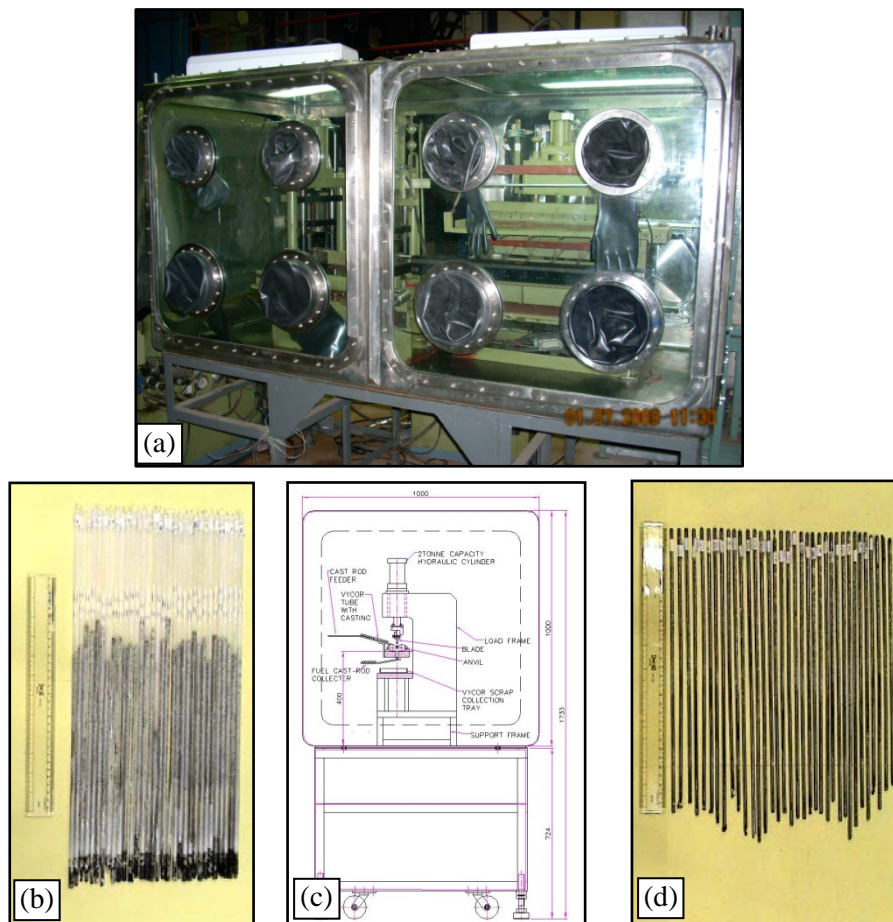

FIG. 5. Demoulding operation; (a) Demoulding machine installed in glove box, (b) Cast slugs with moulds, (c) Sketch of demoulding machin with glove box, (c) Cast slugs after demoulding

4.0 Quality control

Slugs after end-shearing are transferred to feeding-tray of an "Automated Inspection System" located in third glove box. The system is capable of measurement and recording of technical requirements with respect to length, diameter/diameter variation, mass and casting defects. Movement and handling of the slugs from one station of the inspection system to another station are completely automated. Sequence of inspection followed is; one of the slugs from feeding-tray is transferred to a static load cell with the help of an arm and mass is measured with an accuracy of ±0.1 gm and recorded. Later, the slug is transferred to second station where length is measured by LVDT probe with an accuracy of ± 1 mm. After this, the slug is moved to third station where diameter is measured using LVDT probe with an accuracy of ± 0.02 mm at preset locations along the length of the slug. At each location, diameter is measured in two mutually perpendicular directions. Later the slug is passed through a differential encircling ECT coil for detecting porosities / voids, if any. This sequence of inspection is repeated for other slugs, one at a time. The slugs are automatically segregated into "Accepted" adnd "Rejected" categories on the basis of mass, length, diameter and porosities / voids and transferred to the respective trays. Fuel slugs manufactured using this metallic fuel fabrication facility were found to be meeting all the specifications. Eddy current test (ECT) result for one slug is shown in Fig. 6. Additionally, gamma radiography was done on a batch of fuel slugs, and the findings were matching with the ECT results.
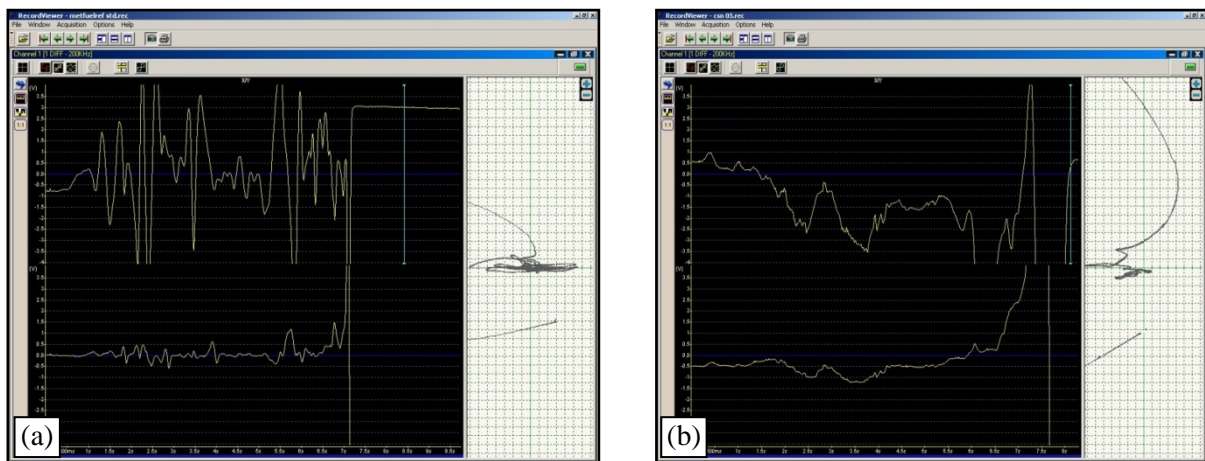

FIG. 6. ECT chart of metallic fuel slugs; (a) Reference standard having 5 nos. of flat bottom holes showing 5 ECT signals in the bottom part of the chart, (b) No ECT signal having amplitude more than the reference signal as shown in the bottom part of ECT chart of metallic fuel slug

5.0 Results and discussion

(a) First melt for preparation of homogeneous U-Zr alloy is carried with zirconium content being ~0.75 wt.% higher than the targeted composition. This is to compensate for the loss of zirconium to the slag phase in the form of carbide and oxidation losses.

(b) Acceptable surface finish of the as-cast slug was not obtanied using water and alchohol based alumina and yttria slurries as coating on quartz inner surface in order to avoid reaction between uranium and silica. This can be attributed to coarser particle size of the ceramic powders and non-uniform coating. Alchohol based graphite slurry yielded desired results.

(c) It was established for the present slug diameter (as-cast), quartz mould inner diameter has to be ~180 µ higher.

(d) For longer slug length (~300 mm), pre-heating of mould is required.

6.0 Conclusions

(a) Metallic fuel slug fabrication and inspection facility has successfully been set-up at BARC, Mumbai, India.

(b) Parameters have been optimized for producing binary U-Zr alloy fuel slugs meeting required specifications.

(c) Required number of natural U-6wt%Zr alloy and enriched U-6%Zr alloy metallic fuel slugs meeting the specifications with respect to chemical homogeneity, casting defects, linear mass and dimensional have been produced using the above described facilities and supplied to IGCAR, Kalpakkam for fabrication of wire wrapped sodium bonded test fuel pins for irradiation studies in FBTR.

ACKNOWLEDGEMENTS

REFERENCES

[1]   BARC Document No.: 03/July, 2001, Shaping the Third Stage of Indian Nuclear Power Programme.

[2]   G.L. Hofman, L.C. Walters, and T.H. Bauer, Metallic Fast Reactor Fuels, Progress in Nuclear Energy, 31, 1/2, 83-110, 1997.

[3]   INTERNATIONAL ATOMIC ENERGT AGENCY, Status and Trends of Nuclear Fuels Technology for Sodium Cooled Fast Reactors, IAEA Nuclear Energy Series No. NF-T-4.1, Vienna (2011).

[4]   J.H. Kittel, B.R.T. Frost, J.P. Mustelier, K.Q. Bagley, G.C. Crittenden, J. Van Dievoet, J. Nucl. Mater. 204 (1993) 1.

[5]   K. Devan, A. Bachchan, A. Riyas, T. Sathiyasheela, P. Mohanakrishnan, S.C. Chetal, Nucl. Eng. Des. 241 (2011) 3058.

[6]   F.L. Yaggee, J.E. Ayer, H.F. Jelinek, Nuclear Met., Am. Inst. Mining Met. Engr., Inst. Metals Div., Spec. Rept. Ser.4 (1957), 51.

[7]   Baldev Raj, H.S. Kamath, P.R. Vasudeva Rao, A Perspective on Fast Reactor Fuel Cycle in India, Progress in Nuclear Energy, 47, 1-4, 369-379, 2005.

Studies on stability of U-UO$_2$/PuO$_2$ Cermet fuel for fast reactor and its interaction with T91 cladding

Sudhir Mishra[a], Santu Kaity[a], P.S. Kutty[a], G.K. Dey[b], Arun Kumar[c], G.J. Prasad[c]

[a] Radiometallurgy Division, Bhabha Atomic Research Centre, Trombay, Mumbai

[b] Materials Science Division, Bhabha Atomic Research Centre, Trombay, Mumbai

[c] Nuclear Fuels Group, Bhabha Atomic Research Centre, Trombay, Mumbai

Abstract.

Cermet is an advanced fuel concept for fast reactor systems. The fuel consists of ceramic fissile material dispersed in a metallic matrix. The advantages of this fuel include high thermal conductivity, ability to retain fission products etc. The cermet fuel can be either (U, PuO$_2$) or (enriched U, UO$_2$). In the present study chemical compatibility of (U, Nat UO$_2$) cermet fuel with T91 cladding has been carried out by diffusion couple experiment. U-UO$_2$ cermet fuel has been fabricated by a powder metallurgy route. The thermal stability of U-UO$_2$ cermet fuel was studied by heating the fuel at 1223 K for 1000 h. SEM results reveal no change in the microstructure indicating good stability of the fuel at 1223 K. The results of the diffusion couple experiments indicate that Zr liner was effective in preventing fuel-clad chemical interaction.

1. Introduction

A cermet fuel is ideally designed to have the optimal properties of both a ceramic, such as high temperature resistance and hardness, and those of a metal, which improves the composite's thermal conductivity and mechanical properties. Cermet nuclear fuels have significant potential to enhance fuel performance because of low internal fuel temperatures and low stored energy. As a cermet fuel UO$_2$ has been used primarily in stainless steel matrices and to a lesser extent in refractory metals. The higher oxides U$_3$O$_8$ has been tested exclusively in aluminum and has been used in various research reactors. Zirconium and Zircaloy based UO$_2$ cermet fuel is being used in naval reactors [1]. Cermet fuel utilization allows reducing the centre line temperature and consequently reduced fuel temperature under normal reactor operation. Savchenko et al. [2] in their recent publication discuss about a new concept of Pu and minor actinides (MA) containing fuel for fast reactor. The U-PuO$_2$ fuel proposed is based on dispersion of PuO$_2$ particles in U or U alloy matrix. In the new fuel element design, a frame work fuel element with porous uranium alloy metal is filled with PuO$_2$ powder of < 50 µm size. The high uranium content fuel metal is metallurgically bonded to cladding and forms a heat conducting frame work. U-UO$_2$ cermet fuel used in the present investigation was fabricated by a powder pellet route. The fuel will be cladded in T91 steel. In order to achieve its full potential it is important to understand the fuel clad chemical interaction (FCCI) and introduce necessary steps to avoid it.

FCCI is considered as a potential problem area in the application of the fuel in liquid-metal cooled fast reactors. The problem can be eliminated in two ways i.e. either by alloying of uranium or by using a barrier layer between fuel and clad. Zr is known to increase the solidus temperature and to improve the chemical compatibility between fuel and steel cladding material by suppressing the interdiffusion between the fuel and cladding components [1]. Hence, Zr was chosen as an alloying element as well as a barrier layer.

T91 grade steel is a 9Cr–1MoVNb type steel, having a ferritic-martensitic structure. This steel being ferritic has the advantage of a higher resistance to void swelling. However, a rise of the ductile-brittle transition temperature (DBTT) due to fast neutron irradiation is a matter of concern. The above mentioned steel exhibits a high mechanical strength and combines low thermal expansion with high heat conductivity [3].

The clad provides a barrier to the release of radionuclides hence its integrity is a very important issue. For reliable operation of a fast breeder reactor, the fuel elements must be resistant to breaching even in case of overpower transients [4]. From the standpoint of accident transients, the most important factor is the accelerated rate of cladding attack, once eutectic liquefaction forms at the interface. The chemical compatibility between the fuel and clad material is of prime importance because of the formation of low melting eutectics which may often limit the life of the fuel pin in a reactor. The temperature of the eutectic reaction between the fuel and the cladding is considered as a critical parameter for the design of the metallic fuel pin [5].

HT9 [6] and T91 grade steels are suitable for high burn-up operation because of low-swelling behavior. Therefore, FCCI is more important in these types of steels. The interdiffusion between U–10Zr alloy and HT9 at 973 K was studied by Lee et al [6]. The diffusion behavior between U–10Zr with T91 was investigated by Ryu et al [7]. The fuel-clad chemical compatibility between U–Zr alloys and ferritic/martensitic steels have been reported in the literature, with emphasis on the U–10Zr alloy fuel and HT9 cladding steel. However, the work on fuel–clad chemical interaction between U-UO$_2$ cermet and T91 steel is not available in the open literature and requires investigation.

The main objectives of the present study are

- To investigate thermal stability of U-UO$_2$ cermet fuel

- To evaluate performance of Zr as FCCI barrier layer between U-UO$_2$ cermet and T91 by diffusion couple experiments

- Chemical compatibility behaviour between U-UO$_2$ and T91 by diffusion couple experiments.

2.   Experimental Procedure

Cermet compacts of two different composition namely U-15 wt% UO$_2$ (hereafter referred as U-15%UO$_2$) and U-30wt% UO$_2$ (hereafter referred as U-30%UO$_2$) were fabricated by a powder pellet route. The chemical composition of U and UO$_2$ powders used for the fabrication of cermet compacts are shown in Table 1 and Table 2, respectively. The typical diameter of the sintered cermet compact was about 6.80 mm. To investigate the thermal stability of the sintered fuel comapcts of U-15%UO$_2$ and U-30%UO$_2$, the samples wrapped in a tantalum foil were encapsulated in a quartz tube under helium atmosphere and heated at 1223 K for 1000 h.

T91 grade steel was used in the standard normalized and tempered condition with a hardness of 220 kg mm^{-2} (Vickers diamond indenter, H$_{(VHN)}$ (kg mm^{-2}) = 1.854$\times$ P/d^2, where P is the applied load in kg and d is the average diagonal in mm). The heat treatment of T91 consists of austenization at 1323 K and air quenching, followed by tempering at 1023 K for 1 h. The chemical composition of T91 steel is given in Table 3. The compacts of two different compositions U-UO$_2$ were cut into 5 mm thick discs and T91 steel rod of the same diameter was cut into discs of about 0.5 mm thickness. The surfaces of all these discs were metallographically polished to 1 μm surface finish. Two types of diffusion couples were prepared as described below:

a) Couples between U-UO$_2$ and T91 discs with a Zr foil of thickness ~100 μm in between them, referred to as U-UO$_2$/Zr/T91 couples, and

b) Couples between U-UO$_2$ and T91 discs without a Zr foil in between, referred to as U-UO$_2$/T91 couples.

The components of the diffusion couples were kept in fixtures made of Inconel 600, to ensure intimate contact during annealing. A Ta foil was used to prevent any chemical reaction between couples and fixture. The diffusion couple-fixture assembly is shown schematically in Fig. 1. The fixtures containing these couples were encapsulated in a quartz tube (Fig. 2) in helium atmosphere and annealed in a resistance heating furnace maintained at 1023 K for durations up to 1000 h.

Subsequent to annealing, the couples were sectioned using a slow speed diamond cutting wheel in presence of kerosene as coolant. The exposed cross sections were metallographically polished to 1 μm surface finish. The extent of reaction and phases formed at the interface were characterised using a scanning electron microscope (SEM) with energy dispersive spectrometer (EDS). The X-ray line scans of U, Fe, Cr and Zr were acquired across the interfaces of the diffusion couples to determine the distribution of each element.

Table 1. Chemical composition of U metal powder (ppm)

Al	B	Ca	Cd	Co	Cr	Cu	Fe	Mg	Mn	Mo	Si	V	W	Zn	Pb	Ni
<20	0.2	20	0.30	<10	25	30	40	35	6	20	<120	10	300	20	10	30

Table 2. Chemical composition of UO$_2$ ceramic powder (ppm)

Al	B	Ca	Cd	Co	Cr	Cu	Fe	Mg	Mn	Mo	Si	V	W	Zn	Pb	Ni
14	5	23	0.16	<10	<10	2	14	24	<2	5	67	<10	<10	10	5	5

Table 3. Chemical composition of T91 (wt.%)

Cr	Mo	V	Nb	Al	Ti	Ni	Cu	Mn	Si	C	N
9.16	0.882	0.207	0.079	0.008	0.003	0.197	0.068	0.368	0.209	0.099	0.0457

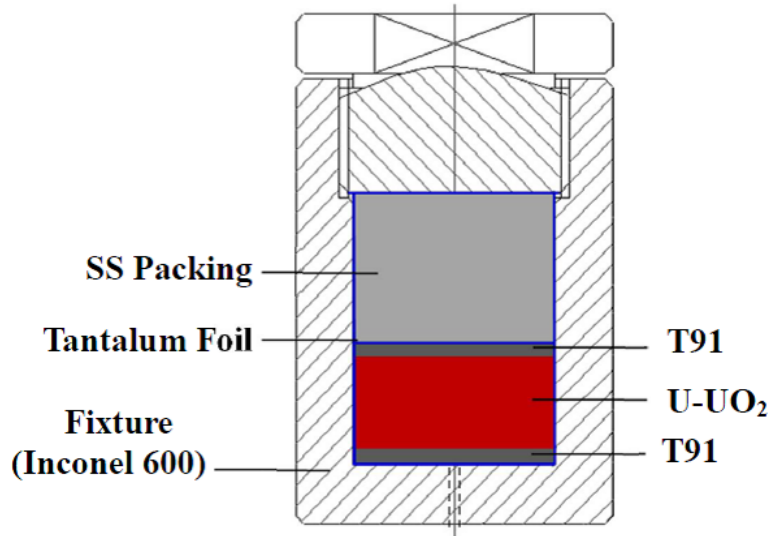| P	S	Fe
0.015	0.0013	Balance

FIG. 1. The schematic diagram of the fixture and arrangement of samples inside the fixture. Stainless Steel (SS) was used as packing material.

FIG. 2. Quartz encapsulated diffusion couple fixture.

3. Results

The microstructures of the as-sintered and annealed U-30%UO$_2$ fuel pellets are shown in Fig. 3. The microstructures of as-sintered and annealed U-30%UO$_2$ fuel pellets are found to be similar with UO$_2$ particles homogeneously distributed throughout the U metal matrix. The magnified micrographs and elmental mapping of uranium for both the sintered and annealed samples are shown in Fig. 4 (a-d). The elemental distrubution of U is found to be similar in both the cases . The dark portion observed in the elemtal mapping (Fig. 4 (b & d)) is because of the presence of the poriosity. O/M ratio of the sintered UO$_2$ particle in the fuel compact was found to be near 2.0 and anealing was carried out in helium atmosphere. Hence, the formation of higher oxides of UO$_2$ and the oxidation of uranium metal matrix may not take place. O/M ratio changing below 2.0 and release of oxygen may happen at higher temperature like 1900 K in vacuum but that condition does not exist in the present investigation [8]. Hence, it can be concluded that the thermal stability of the fuel compact is fairly good.

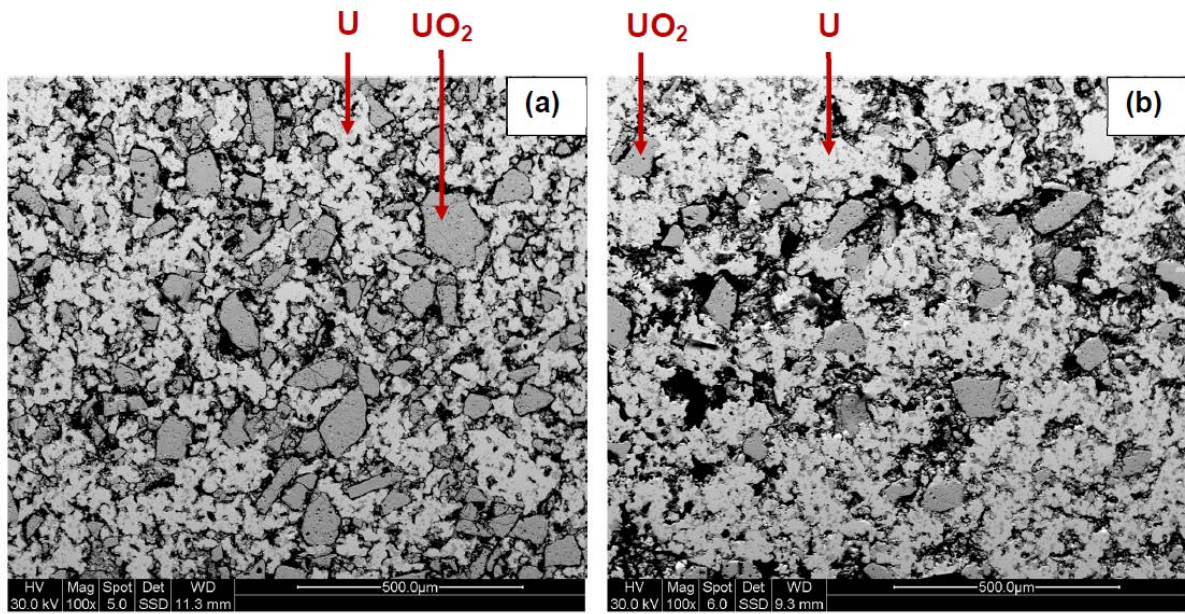FIG. 3. Microstructures(back scattered electron image) of U-30%UO$_2$ fuel pellets (a) as-sintered and (b) after annealing at 1223 K for 1000 h.
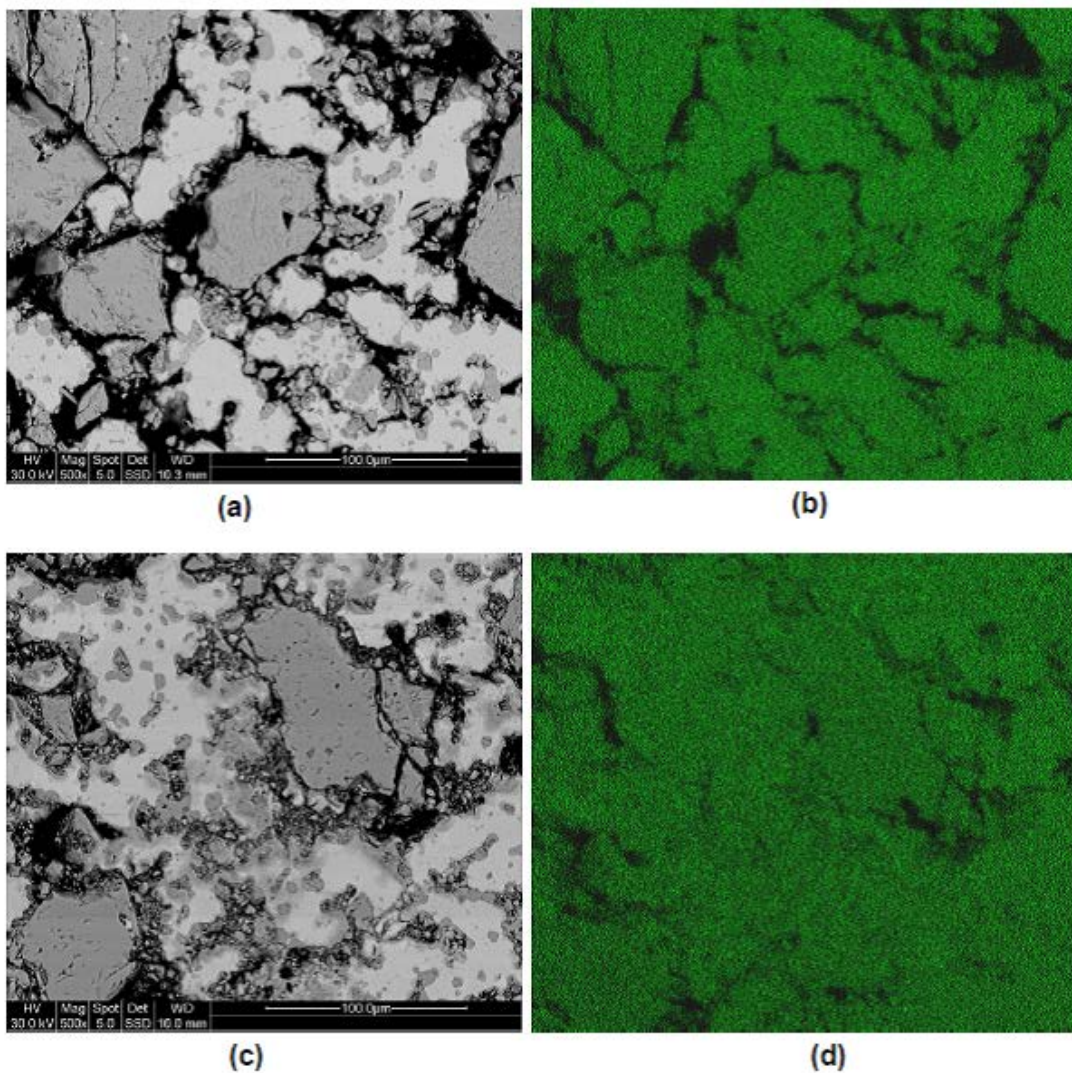

FIG. 4. (a) and (b) Microstructure (back scattered electron image) and elemental mapping of uranium for sinetred U-30%UO$_2$ fuel pellet. (c) and (d) Microstructure and elemental mapping of uranium for annealed U-30%UO$_2$ fuel pellets after annealing at 1223 K for 1000 h.

3.1. Interfacial reactions in U-UO$_2$/Zr/T91 couples

The microstructure of the U-15%UO$_2$/Zr/T91 diffusion couple annealed at 1023 K for 1000 h is shown in Fig. 5. The microstructure and the elemental mapping across the interface of U-15%UO$_2$/Zr/T91 couple annealed at 1023 K for 1000 h are shown in Fig. 6(a-e). The microstructural analysis of U-15%UO$_2$/Zr/T91diffusion couples revealed an excellent bond formation at both the U-15%UO$_2$/Zr and Zr/T91 interfaces after annealing. The microstructure of U-15%UO$_2$/Zr/T91 diffusion couple shows that there is no diffusion of U into 100 μm thick Zr barrier layer. Further, no eutectic melting between U-15%UO$_2$/Zr and Zr/T91 interface was observed. The formation of any intermetallic compound was not observed at the Zr/T91 interface, even at 1023 K. It is also evident from U, Zr, Fe and Cr X-ray mapping that, there is no penetration of U in Zr metal as well as that of Zr in T91.
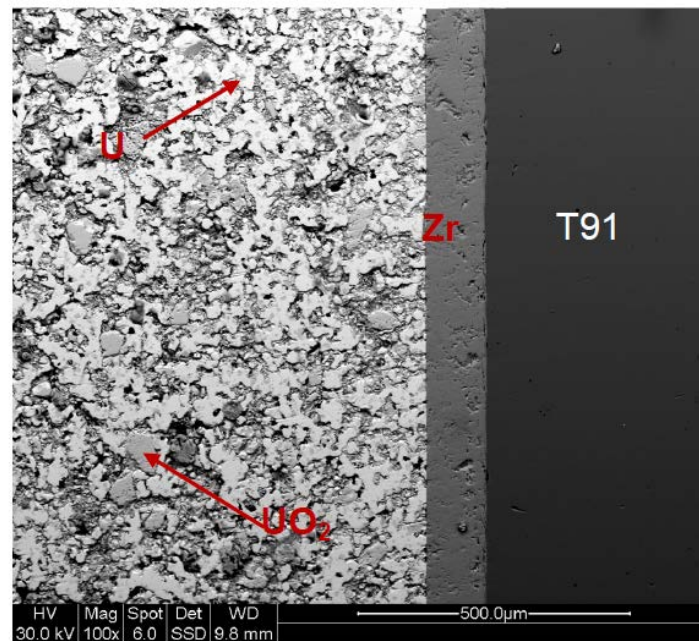
FIG. 5. SEM micrograph of diffusion couple U-15%UO$_2$/Zr/T91 annealed at 1023 K for 1000 h.

The microstructure of the U-30%UO$_2$/Zr/T91 diffusion couple annealed at 1023 K for 1000 h is shown in Fig. 7. The diffusion couples revealed an excellent bond formation at both the U-30%UO$_2$/Zr and Zr/T91 interfaces after annealing. The results of the U-30%UO$_2$/Zr/T91 diffusion couple was found to be similar to that of U-15%UO$_2$/Zr/T91 diffusion couple. The results of the U-UO$_2$/Zr/T91 diffusion couples indicate that the Zr liner was effective in preventing fuel-clad chemical interaction.
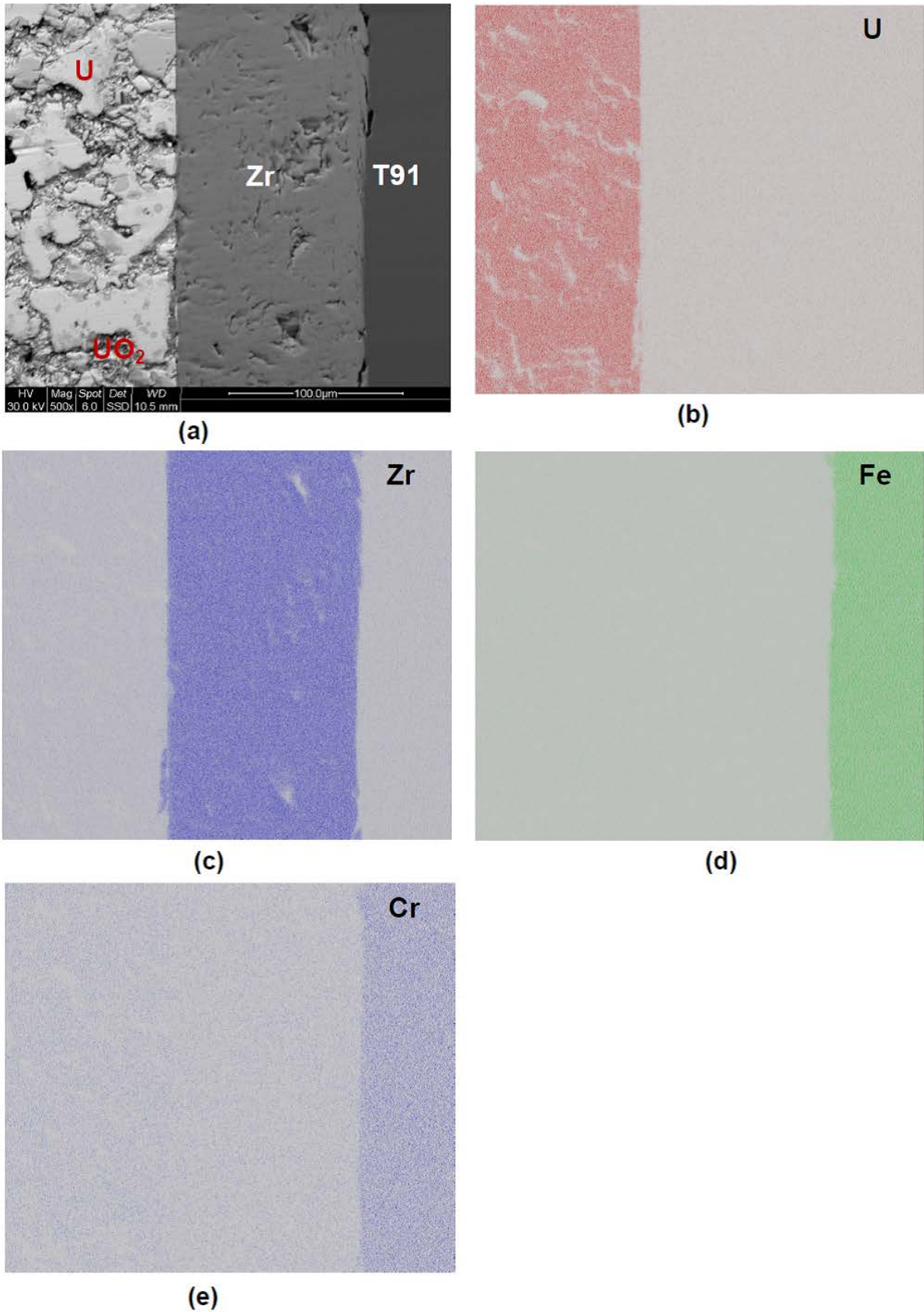
FIG. 6. SEM image and EDS results showing the distribution of different elements at the interfaces of U–15%UO₂/Zr/T91diffusion couple after heat treatment at 1023 K for 1000 h: (a) SEM image and mapping results of (b) U, (c) Zr, (d) Fe, and (e) Cr.
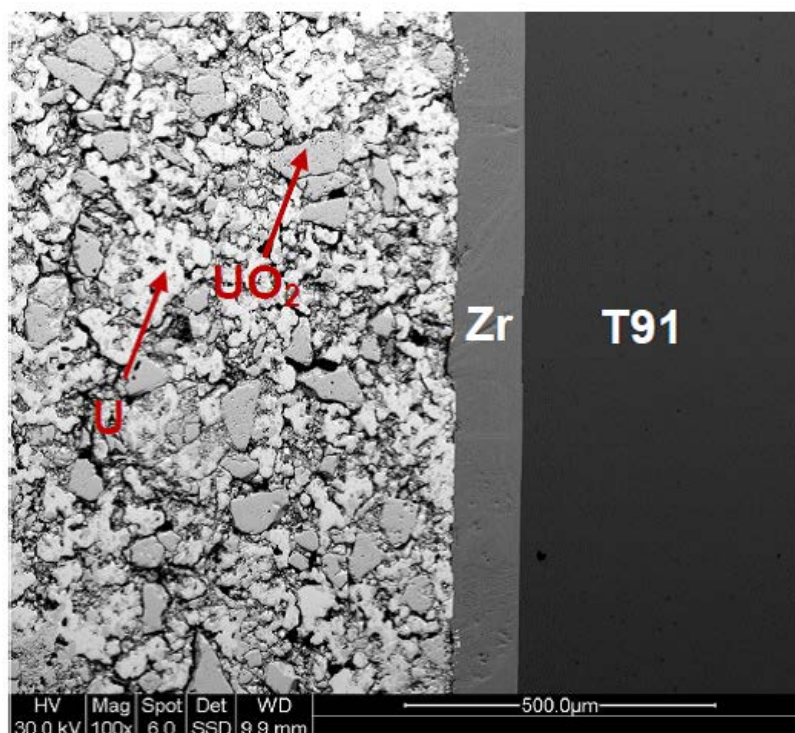
FIG. 7. Microstructure of U-30%UO$_2$/Zr/T91 diffusion couple annealed at 1023 K for 1000 h.

3.2. Interfacial reactions in U-UO$_2$/T91 couples

Fig. 8 shows SEM micrograph of U-15%UO$_2$/T91 diffusion couple. The microstructural analysis of U-15%UO$_2$/T91diffusion couple revealed an excellent bond formation at U-15%UO$_2$/T91interface after annealing. The magnified SEM micrograph and elemental mapping along the interaface of U-15%UO$_2$/T91 couple annealed at 1023 K for 1000 h are shown in Fig. 9(a-d). The microstructure (Fig. 8) reveals that uranium metal reacts with T91 and forms a interdiffusion layer of arround 25-30 μm at the inetrface and the composition of the interdiffusion layer was found to be ~ 46 at%U, 48 at% Fe and 6 at% Cr. The interdiffusion layer is having rounded shape which indicates the formation of liquid phase at the inetraface due to the eutectic reaction between U nad T91.

The liquid phase formation was observed only at the interface as evident from the microstructure and it causes removal of U from the adjacent region. This results in the formation UO$_2$ rich layer on the fuel side. In fact, U may form eutectic reaction with Fe at 998 K as evident from the U-Fe phase diagram. The present investigation was carried out at temperature which is well above the eutectic temperature between U and Fe. However, it is observed from the micrograph that U metal away from the interaface has not taken part in the diffusion reaction . This may be due to the reduced area of contact between U and T91 in the U-UO$_2$/T91 diffusion couple and sluggish diffusion reaction between U and T91 in presence of UO$_2$. This fuel is expected to reach such high temperatures under accidental condition, for very short duration. The present observations indicate that even holding at temperatures higher than the eutectic temperature for more than 40 days does not cause melting of the whole capsule. Hence, it can be concluded that the fuel-clad chemical compatibility between U-UO$_2$ and T91 seems fairly good.

A similar result has been observed when the diffusion couple of U-30%UO$_2$/T91 was heated at 1023 K for 1000 h.
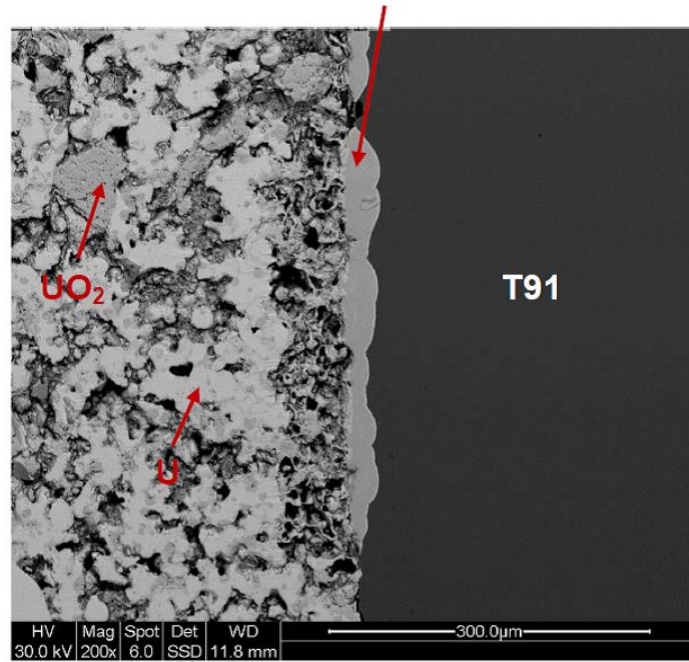
FIG. 8. SEM micrograph of diffusion couple U-15%UO$_2$/T91 annealed at 1023 K for 1000 h.
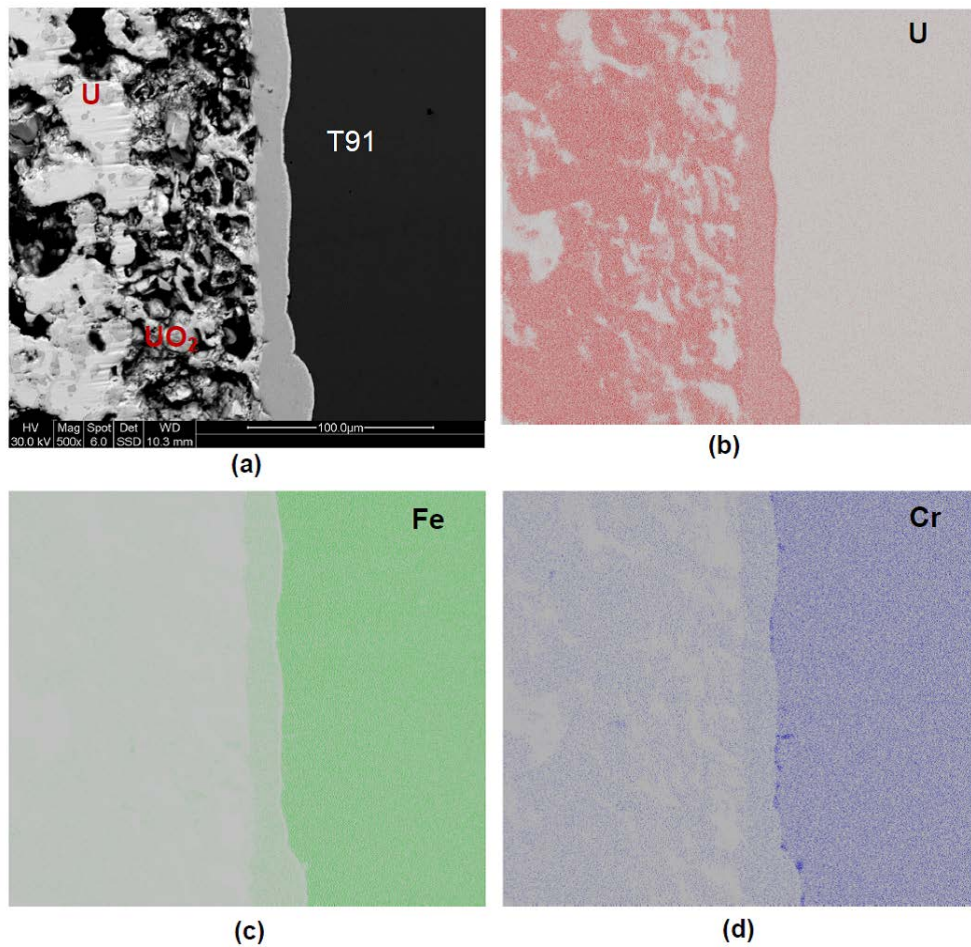
FIG. 9. SEM image and EDS results showing the distribution of different elements at the interfaces of U–15%UO$_2$/T91 after a heat treatment at 1023 K for 1000 h: (a) SEM image and mapping results of (b) U, (c) Fe, and (d) Cr.

4.   Summary and conclusions

a. The fuel compacts (U-UO$_2$) do not reveal any singificant microstrual changes even after annealing at 1223 K for 1000 h.

b. The results of the U-UO$_2$/Zr/T91 diffusion couples indicate that the Zr liner was effective in preventing fuel-clad chemical interaction.

c. Eutectic melting was observed at the interface of U-UO$_2$/T91 diffusion couple annealed at 1023 K for 1000 h.

REFERENCES

[1]   G.L. Hofman, L.C. Walters, Mater. Sci. Technol. 10A (1994) 3–43.

[2]   A.M. Savchenko, I.I. Konovalov, A.V. Vatulin, E.M. Glagovsky, J. Nucl. Mater. 385 (2009) 148–152.

[3]   R.L. Klueh, A.T. Nelson, J. Nucl. Mater., 371 (2007) 37–52.

[4]   D.D. Keiser Jr., M.A. Dayananda, Metall. Mater. Trans. A, 25A (1994) 1649–1653.

[5]   S. Kaity, T.R.G. Kutty, R. Agarwal, A. Laik, A. Kumar, Nucl. Eng. Des. 250 (2012) 267−276

[6]   C.T. Lee, H. Kim, T.K. Kim, C.B. Lee , J. Nucl. Mater., 395 (2009) 140–144.

[7]   H.J. Ryu, B.O. Lee, S.J. Oh, J.H. Kim, C.B. Lee , J. Nucl. Mater., 392 (2009) 206–212.

[8]   A. T. Chapman and R. E. Meadows, Contract No. W-7405-eng-26, ORNL-3587, 1964

Oxidation and Reduction Behaviors of Plutonium and Uranium Mixed Oxide Powders

S. Hirooka[a], M. Kato[a], T. Tamura[b], A.T. Nelson[c], K.J. McClellan[c], K. Suzuki[a]

[a] Advanced Nuclear System Research and Development Directorate, Japan Atomic Energy Agency, Tokai-mura, Naka-gun, Ibaraki, Japan

[b] Inspection Development Company, Tokai-mura, Naka-gun, Ibaraki, Japan

[c] Materials Science and Technology Division, Los Alamos National Laboratory, Los Alamos, New Mexico, USA

Abstract. As research and development activities for MOX fuel pellet production, oxidation and reduction behaviors of MOX powders were investigated by thermogravimetry and X-ray diffraction measurements. It was observed that the oxidation limit decreased with oxidizing temperature and Pu content. The MOX powders showed a two-step oxidation and kinetic stability under non-stoichiometry. The oxidation rates were evaluated from the isothermal oxidation tests. It was found that the reduction temperature of $M_4O_9 + M_3O_8$ was higher than that of M_4O_9. This indicated that the reduction of M_4O_9 was prevented by the existence of M_3O_8. Activation energy of the reduction was derived from the non-isothermal reduction tests. The data are expected to contribute to establishing a control technique for O/M ratio during MOX powder storage and pellet production.

1. INTRODUCTION

Oxidation and reduction reactions of uranium and plutonium mixed oxide (MOX) fuel under hyper-stoichiometry can be generally deduced from those reactions of UO_2 fuel that have been extensively studied [1][2]. However, some significant differences have been reported. For example, additional oxygen atoms are incorporated at interstitial sites during the oxidation of UO_2. When the oxidation proceeds, the interstitial oxygen atoms redistribute to form U_3O_7. On the other hand, when $(U_{0.75}Pu_{0.25})O_2$ is oxidized, M_4O_9 is stably formed instead of M_3O_7 [3]-[5]. Also, in the air oxidation, UO_2 becomes U_3O_8 and the corresponding oxygen-to-metal (O/M) ratio is 2.667. However, MOX cannot exist as a single phase of M_3O_8 but exists as $M_4O_9 + M_3O_8$ [6]. Thus, the oxidation limit of MOX is lower than O/M ratio 2.667.

As in the case with UO_2, MOX raw powder and recycled powder are oxidized during storage because of powder self-heating by alpha decay. The MOX powder has been directly pelletized and sintered in a simplified method developed in Japan Atomic Energy Agency for efficient MOX pellet fabrication, in which the MOX powder is obtained by the microwave heating denitration method [7]. In the sintering process, the MOX is reduced and the O/M ratio is adjusted to 1.97. It has been reported that the O/M ratio is strongly related with sintering properties, so understanding the fundamental properties of oxidation and reduction reactions of the MOX powder is important. However, reports are still limited, especially concerning Pu content ratio.

In this study, different MOX powders were oxidized by isothermal and non-isothermal heat treatments, and the effects of Pu content ratio and temperature were investigated. In the reduction, the

MOX powders were reduced from two different oxidation states at constant heating rates, and the reduction rates were analyzed.

2. EXPERIMENT

2.1. Specimen preparation

The $(U_{0.7}Pu_{0.3})O_2$ and $(U_{0.5}Pu_{0.5})O_2$ powders were prepared by the microwave heating denitration method [8]. The Pu content was adjusted during the nitrate solution stage before the solution was converted to the powders. Table 1 shows the measured specific surface area and the average particle diameter, which can affect the oxidation and the reduction rates [9][10]. The specimens were heate-treated at 1123K in H_2/Ar mixed gas to control the O/M ratio to 2.00 with thermogravimeter.

Table 1. Specific surface area and average diameter

	30%Pu-MOX	50%Pu-MOX
specific surface area (m^2/g)	6.15	5.59
average particle diameter (µm)	0.391	0.349

2.2. Measurement

2.2.1. Oxidation tests

Isothermal and non-isothermal tests were carried out. During the oxidation, weight change was measured with a thermogravimeter. In the isothermal tests, specimens were heat-treated in the temperature range of 373K - 1073K for 4h. First, the specimens were heated to the test temperatures in 5%H_2/95%Ar mixed gas, then, the gas was switched to 20%O_2/80%Ar to start the oxidation reaction. The oxidized specimens were investigated by X-ray diffraction measurements. In the non-isothermal tests, the specimens were heated from room temperature to 1073K at the constant heating rate of 3K/min in 20%O_2/80%Ar mixed gas with the flow rate of 300cm^3/min.

2.2.2. Reduction tests

30%Pu-MOX was reduced in 5%H_2/95%Ar mixed gas with 200 ppm H_2O.The starting O/M ratio of each specimen was adjusted to 2.43 or 2.28 by heat treatments at 873K and 473K for 3h each in 20%O_2/80%Ar gas. Then, the specimens were heated from room temperature to 973K at the constant heating rates of 3K/min in 5%H_2/95%Ar mixed gas with 200 ppm H_2O.

3. RESULTS AND DISCUSSION

3.1. Oxidation

In the isothermal oxidation, measurements were conducted for longer than 4h, as shown in Fig.1 (a) and (b). The oxidation would have continued very slowly if the heat treatment had not been stopped. The O/M ratios of oxidized specimens were higher at higher test temperatures. However, for 50%Pu-

MOX, the O/M ratio reached 2.294 at 773K and decreased to 2.285 at 873K and 973K. For 30%Pu-MOX, the O/M ratio reached 2.428 at 873K and decreased to 2.422 at 1073K. Oxidation limit observed in the experiment had a tendency to decrease with temperature and Pu content.
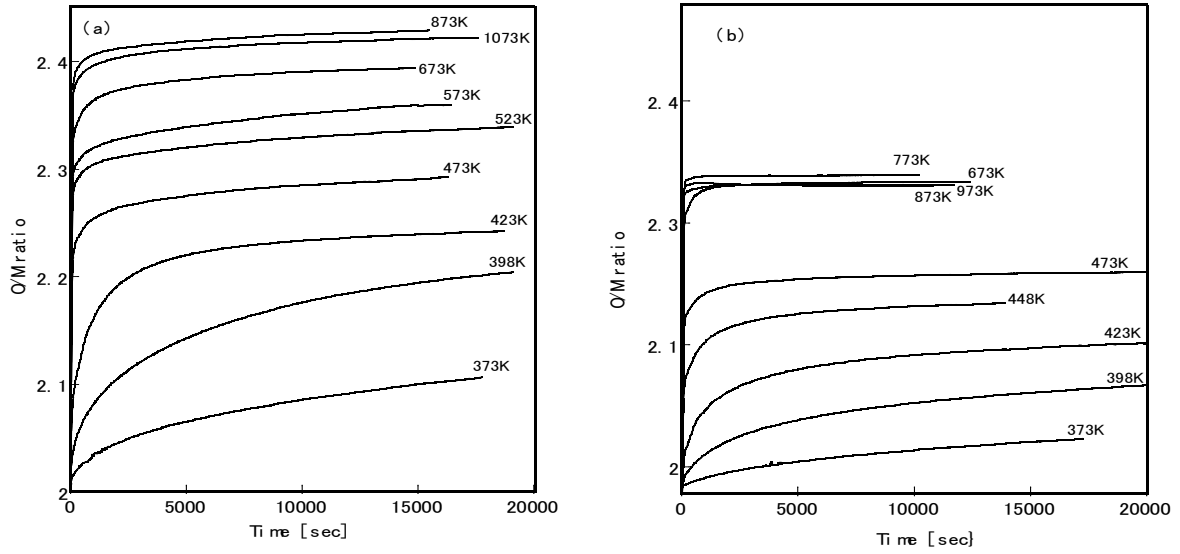
FIG. 1. The O/M ratio changes of (a) 30%Pu-MOX and (b) 50%Pu-MOX in the isothermal oxidation.

Fig. 2 (a) and (b) show X-ray diffraction results. For the specimens of O/M ratio of 2.000, (111) peaks of MO_2 were observed at 28.34 and 28.52, and the peaks shifted to higher angle with increase of x in MO_{2+x}. M_4O_9 phase was reported to form when the O/M ratio was around 2.25 [4]. It was reported that plutonium doped uranium oxide forms M_4O_9 before eventually proceeding to M_3O_8 when heated [11]. The same can be said of irradiated UO_2 including fission products. Large amount of impurities could enhance the kinetic stability of the cubic $M_4O_{9\pm y}$ structure. The structure of $M_4O_{9\pm y}$ is closely related to MO_{2+x}, which makes it difficult to distinguish the ordered $M_4O_{9\pm y}$ structure [12]. The boundary between MO_{2+x} phase and $MO_{2+x} + M_4O_{9-y}$ phase is dependent on temperature and O/M ratio [13]. The peaks of M_3O_8 were observed in 50%Pu-MOX of O/M ratios 2.283 – 2.288 and in 30%Pu-MOX of O/M ratios 2.36 - 2.43. Thus, the specimens was concluded to consist of M_4O_{9+y} and M_3O_8.
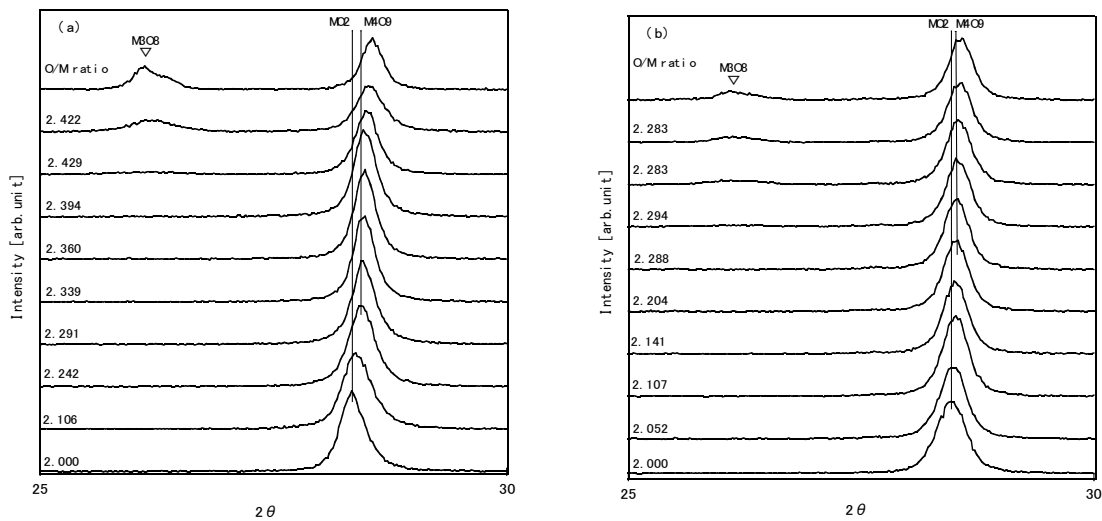
FIG. 2. X-ray diffraction results of (a) 30%Pu-MOX and (b) 50%Pu-MOX after the isothermal oxidation

Figs. 3 and 4 show the comparison of UO_2 and MOX oxidation data [14]. After oxidation of the UO_2, phase state was considered to be a single U_3O_8 phase because O/M ratios of uranium oxide reached nearly 2.667. The UO_2 achieves complete oxidation to the oxidation limit of U_3O_8 phase at low temperature; the UO_2 completed the oxidation at 573K for 1800s while 30%Pu-MOX remains M_4O_9 and M_3O_8 binary phase. At 423K, the oxidations 30% and 50%Pu-MOX were so slow that it would require much more time for the appearance of the M_3O_8 phase. In the oxidation of UO_2 at 573K, oxidation proceeded with 2 steps. The O/M ratio at the end of the first step (the beginning of the second step) was 2.34. Thus, it was considered that the first step was the change from UO_2 to U_3O_7 and the second step was the change from U_3O_7 to U_3O_8.
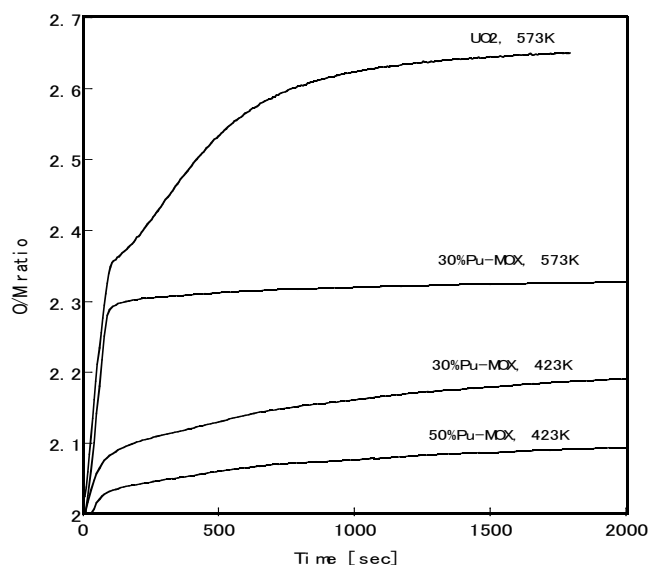
FIG. 3. The O/M ratio changes of UO_2, 30% Pu-MOX and 50%Pu-MOX in the isothermal oxidation at 423K and 573K
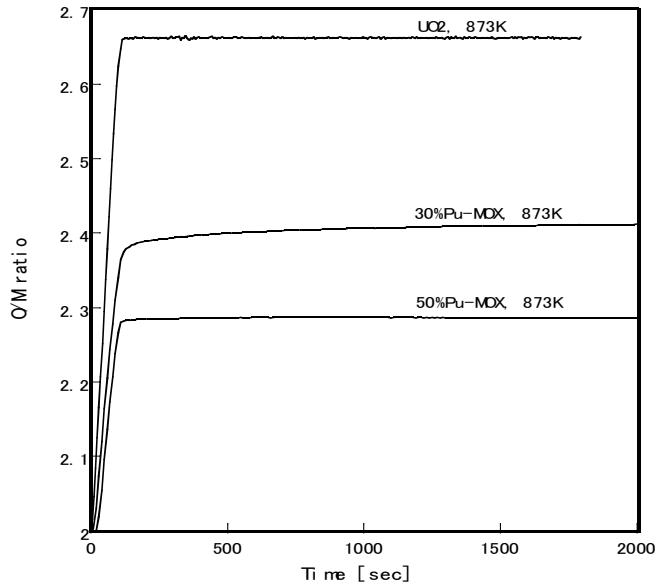
FIG. 4. The O/M ratio changes of UO$_2$, 30% Pu-MOX and 50%Pu-MOX in the isothermal oxidation at 873K

In the non-isothermal oxidation, as shown in Fig. 5, two oxidation steps were also observed. It was considered that the O/M ratio increased from 2.00 to 2.25 in the first step during which MO$_2$ phase changed to M$_4$O$_9$ phase via the MO$_{2+x}$ + M$_4$O$_{9-y}$ phase. In the second step, O/M ratio increased from 2.25 during which M$_4$O$_9$ phase changed to M$_4$O$_{9+y}$ + M$_3$O$_8$.
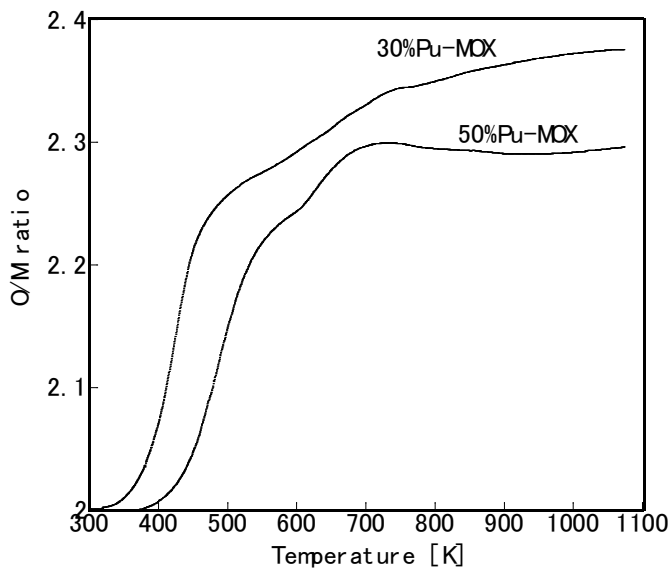
FIG. 5. The O/M ratio changes of 30% Pu-MOX and 50%Pu-MOX heated at the constant heating ratio of 3K/min

The mechanism of the first oxidation has been explained as diffusion of oxygen through a discrete layer of M_4O_9 on the surface of MO_2 particles which thickens with time [1][4][15][16]. Assuming that the powder is spherical, the oxidation rate is described as:

$$\left[1-(1-\alpha)^{1/3}\right]^2 = kt \qquad (1)$$

where α is fraction of reaction and t is time [17][18]. k is the rate constant and a function of temperature:

$$k(T) = A\exp\left(-\frac{E}{RT}\right) \qquad (2)$$

where A is a pre-exponential factor, E is activation energy, R is the gas constant, and T is temperature. The rate constants of the first oxidation were obtained as a function of T:

$$k = 2.4\times10^7 \exp\left(\frac{-94\times10^3}{RT}\right) \qquad (3) \qquad \text{(for 30\%Pu-MOX)}$$

$$k = 5.6\times10^5 \exp\left(\frac{-86\times10^3}{RT}\right) \qquad (4) \qquad \text{(for 50\%Pu-MOX)}$$

The activation energies for the formation of M_4O_9 on the MO_2 surface were estimated to be 94kJ/mol and 86kJ/mol, respectively, for 30%Pu-MOX and 50%Pu-MOX. Fig. 6 (a) and (b) show fitting curves of the oxidation obtained with equation (1). Good agreement between experimental results and calculation results was confirmed at the temperatures of 373K and 398K. However, the model does not reproduce the experimental results well at the temperature higher than 423K. This result may attribute to variety of particle diameter. The model simulates the oxidation of a spherical powder with a certain diameter. It is considered that the variety of the diameter broadened the rapid oxidation stage.
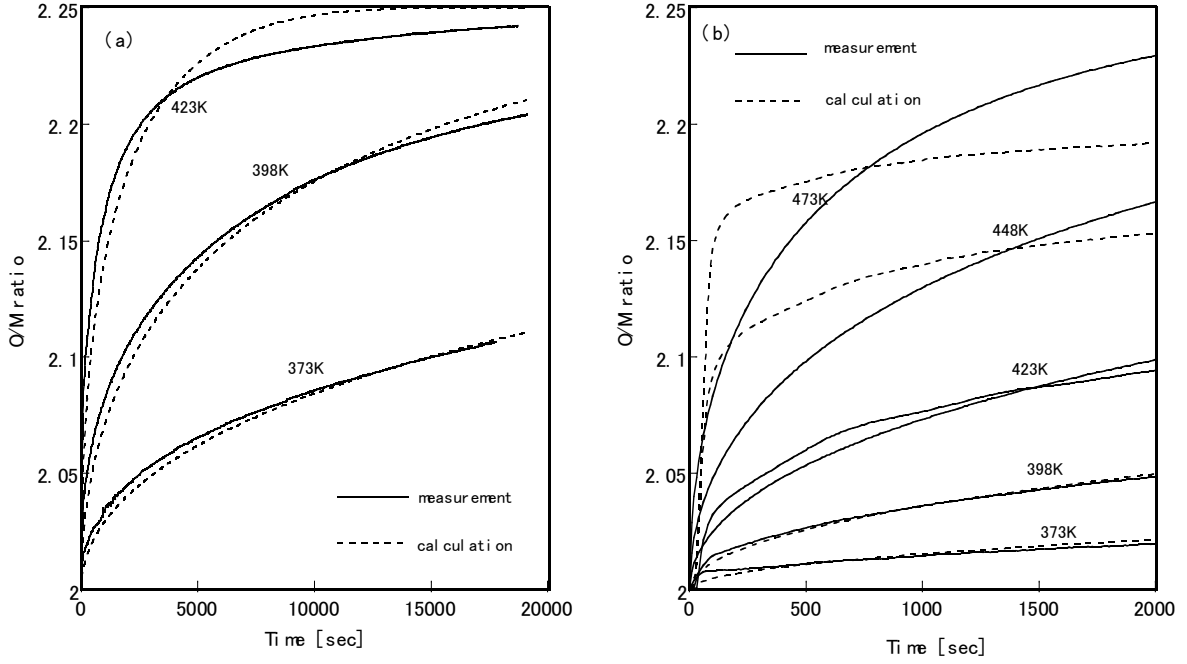
FIG. 6. Fitting results of the O/M ratio changes of (a) 30%Pu-MOX and (b) 50%Pu-MOX in the isothermal oxidation

3.2. Reduction

Fig. 7 shows the results of non-isothermal reduction of 30%Pu-MOX. Phase states were considered to be $M_4O_{9+y} + M_3O_8$ and M_4O_{9+y} for O/M ratios of 2.43 and 2.29, respectively. The specimen of O/M ratio 2.29 started to undergo reduction at 450K where M_4O_{9+y} phase changed to MO_2 via $MO_{2+x} + M_4O_{9-y}$ phase. The specimen of O/M ratio 2.43 started to undergo reduction at 750K. Unlike the oxidation, the reductions proceeded to O/M ratio of 2.00 in one step. It was noted that M_4O_{9+y} in $M_4O_{9+y} + M_3O_8$ did not reduce at 450K. This result was supported by the phase diagram that shows MO_2 and M_3O_8 do not coexist [6].

In the reductions at four different heating rates, the reductions of $M_4O_{9+y} + M_3O_8$ to MO_2 started at the same temperature, but the reductions proceeded during a lower temperature with slower heating rate. From this result, the reduction rate was evaluated. Generally, the kinetic equation is expressed as the following equation:

$$\frac{d\alpha}{dt} = k(T)f(\alpha) \qquad (4)$$

where $f(\alpha)$ is a function determined by the rate-limiting mechanism. For example, as the rate-limiting mechanism, growth at the surface of a particle according to the sphere-contracting model was proposed in the reduction of U_3O_8 by hydrogen [19]. This time, activation energy was obtained as 125kJ/mol by the Ozawa method from the results obtained for different constant heating rates [20]:

$$\log\beta_1 + 0.4567\frac{E}{RT_1} = \log\beta_2 + 0.4567\frac{E}{RT_2} \qquad (5)$$

7

where β is the constant heating rate. This method can derive the activation energy without $f(\alpha)$, i.e. knowledge of the rate-limiting mechanism is not necessary. After deriving the activation energy from the measurement data, shape of $f(\alpha)$ is obtained.
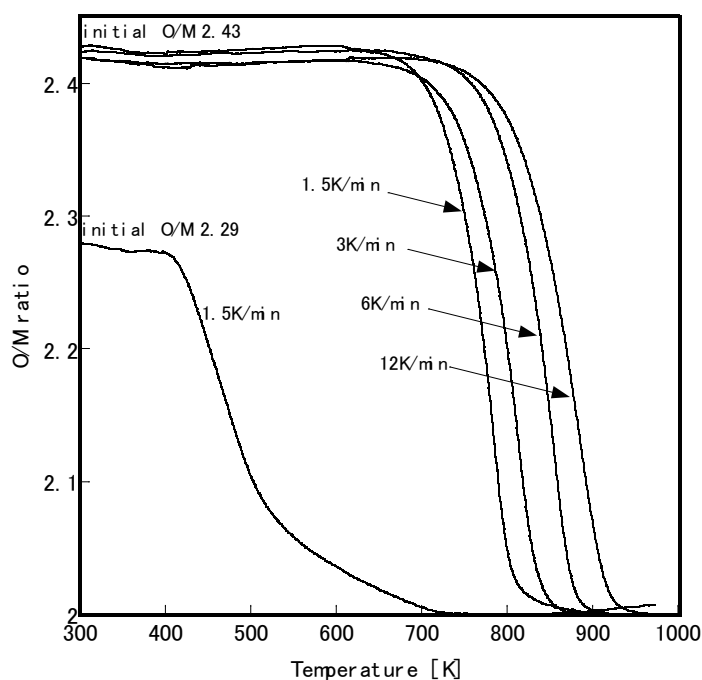
FIG. 7. The O/M ratio changes of 30%Pu-MOX in the reduction heated at the different heating ratios

4. CONCLUSIONS

Oxidation and reduction behaviors of MOX powder were investigated to provide data for realization of a better control technique of O/M ratio. In the study, the following points were seen.

(1) In the isothermal oxidation, O/M ratio of 30%Pu-MOX heate-treated at 873K reached 2.428. O/M ratio of 50%Pu-MOX heat-treated at 773K reached 2.294. Phase states of the oxidized specimens were M_4O_{9+y} and M_3O_8. In the oxidation of UO_2, on the other hand, O/M ratio reached nearly 2.667, which indicated that the phase state of the oxidized specimens was M_3O_8.

(2) Oxidation limit of the MOX powders had a tendency to decrease with temperature and Pu content.

(3) X-ray diffraction peaks of MO_{2+x} and $M_4O_{9\pm y}$ shifted to higher angle with O/M ratio. Thus, these phases had enhanced kinetic stability. The peaks of M_3O_8 phase were observed in 30%Pu-MOX with O/M ratio over 2.360 and 50%Pu-MOX with O/M ratio over 2.288.

(4) In the non-isothermal oxidation, two steps were observed. The first step was the change of MO_2 to M_4O_9 via $MO_{2+x} + M_4O_{9-y}$, and the second step was the range of M_4O_9 to $M_4O_{9+y} + M_3O_8$. Oxidation rate of the first step was evaluated with the oxygen diffusion model.

(5) In the non-isothermal reduction of 30%Pu-MOX, the specimen of M_4O_{9+y} started to undergo reduction at 450K while the specimen of $M_4O_{9+y} + M_3O_8$ started to undergo reduction at 750K. This result indicated that the reduction of M_4O_{9+y} was prevented by the M_3O_8 phase, and that conclusion was supported by the phase diagram.

(6) Non-isothermal reductions of 30%Pu-MOX were conducted at different constant heating rates. Activation energy of the reduction of $M_4O_{9+y} + M_3O_8$ to MO_2 was obtained as 125kJ/mol by the Ozawa method.

REFERENCES

[1] R.J. McEachern, P. Taylor, J. Nucl. Mater. 254 (1998) 87.
[2] M. Pijolat, C. Brun, F. Valdivieso, M. Soustelle, Solid State Ionics, 101 (1997) 931.
[3] C. Berthinier, C. Rado, C. Chatillon, F. Hodaj, J. Nucl. Mater. 433 (2013) 265.
[4] R.J. McEachern, J. Nucl. Mater. 245 (1997) 238.
[5] V.J. Tennery, T.G. Godfrey, J. Am. Ceram. Soc. 56 (1973) 129.
[6] T.L. Markin, R.S. Street, J. Inorg. Nucl. Chem. 29 (1967) 2265.
[7] M. Kato, T. Segawa, K. Takeuchi, M. Kashimura, Y. Kihara, Proceedings of Global 2009, Paris, France
[8] H. Oshima, J. Nucl. Sci. and Technol. 26 (1989) 161.
[9] J.S. Anderson, E.A. Harper, S. Moorbath, L.E.J. Roberts, UK Atomic Energy Authority Report, AERE C/R 887, (1953).
[10] J.S. Anderson, L.E.J. Roberts, E.A. Harper, J. Chem. Soc. (1955) 3946.
[11] L.E. Thomas, R.E. Einziger, H.C. Buchanan, J. Nucl. Mater. 201 (1993) 310.
[12] B. Belbeoch, C. Piekarski, P. Perio, Acra Cryst. 14 (1961) 837.
[13] W. Van Lierde, J. Pelsmaekers, A. Lecocq-Robert, J. Nucl. Mater. 37 (1970) 276.
[14] A.T. Nelson, K. Suzuki, S.A. Voit, K.J. McClellan, M. Kato, NuMat 2012, Osaka, Jaoan, October 24, 2012
[15] D.A. Dominey, J. Inorg. Nucl. Chem. 30 (1968) 1757.
[16] J.S. Anderson, L.E. Roberts, E.A. Harper, J. Chem. Soc. 6330 (1955) 3946.
[17] J. Burke, The Kinetics of Phase Transformations in Metals, Pergamon Press Ltd., New York, (1965)
[18] J. Sestak, V. Satava, W.W.Wendlandt, Thermochim. Acta, 7 (1973) 333.
[19] M. Pijolat, C. Brun, F. Valdivieso, M. Soustelle, Solid State Ionics, 101 (1997) 931.
[20] T. Ozawa, J. Thermal Anal., 2 (1970) 301.

Characterization of U-10Zr-5In, U-10Zr-5In-2Ce and U-10Zr-5Sb-2Ce Alloys

Yeon Soo Kim, T. Wiencek, E. O'Hare, J. Fortner, G.L. Hofman

Argonne National Laboratory
9700 South Cass Avenue
Argonne, IL 60439
U. S. A.

Abstract

Advanced fast reactor concepts to achieve ultra-high burnup (~50%) without requiring refueling by way of using metallic alloy fuel have gained interest for multiple reasons. The accumulation of fission product lanthanides at high burnup for available fuel types is substantial and its migration to cladding and reaction with cladding is a potential life-limiting phenomenon. As a means to prevent this problem, adding an element that forms stable compounds with lanthanides and, as a result, to immobilize them has been proposed. Theoretical assessment shows that indium and antimony are good candidates. Because indium is a low-melting element, liquid metal embrittlement of cladding is of concern. U-10Zr-5In, U-10Zr-2Ce-5In and U-10Zr-2Ce-5Sb have been fabricated and characterized by optical microscopy and scanning electron microscopy to examine their effectiveness.

1. Introduction

It has been proposed that reactor design concepts can achieve ultra-high burnup without requiring refueling by way of using metallic alloy U-10Zr fuel, with a burnup goal as high as ~50 at%. In order to fulfill this goal, fuel pin integrity should be maintained by minimizing fuel-cladding-chemical interaction (FCCI) and fuel-swelling-driven fuel cladding mechanical interaction (FCMI). The latter issue was addressed in Ref. [1]. The FCCI issue is important particularly because the fuel is aimed to achieve high burnup where fission product accumulation and migration in the fuel are high.

Fission product lanthanides (LA) such as La, Pr, Ce, and Nd accumulate at a rate approximately 0.4 at% or 0.25 wt% per at% burnup in U-10wt%Zr. Migration of LA to the fuel surface during irradiation [2] is of concern because LA are more reactive with Fe-base cladding than withfuel constituents. Additionally, the reaction products lower the cladding melting point.

As a remedy to prevent LA migration and reaction with cladding, a chemical doping method of fuel has been proposed at ANL [2]. One or more of elements are added to the fuel to form thermodynamically stable compounds with LA in order to immobilize them. The candidate elements should preferably form compounds with LA. The candidate elements include indium, thalium, gallium, palladium and antimony. Since some of these candidates are low-melting elements, elemental precipitation of the additives from the alloy matrix provides a potential problem to the cladding by a phenomenon known as liquid metal embrittlement.

In this paper, theoretical assessments of the candidate elements' thermodynamic affinity in compound formation with LA are compared. Alloys of U-10Zr-5In, U-10Zr-2Ce-5In and U-10Zr-2Ce-5Sb (where

the numbers in front of elements denote concentrations in weight %) were fabricated, cast, and metallographically examined,. Optical microscopy and scanning electron microscopy were also performed to characterize these alloys in further detail.

2. Theoretical Assessment

The Gibbs free energy of formation of a compound ($\Delta G = \Delta H - T\Delta S$) is the measure of the spontaneity of the reaction and also the stability of the compound: The lower the Gibbs free energy, the larger the reaction potential exists between the reactants. Since enthalpy is the dominant part of Gibbs free energy, particularly at low temperatures, comparing the compound formation enthalpies of two compounds provides an approximate indicator of which compound is more preferred to form.

The Miedema model analytically assesses the enthalpy change during mixing of two elements by using an empirical correlation [3]. The correlation for the formation enthalpy of a compound between two elements A and B is given by

$$\Delta \mathrm{H}^{\mathrm{f}} = c_A \, f_B^A \, \frac{2 V_A^{2/3}}{\left(n_{ws\,A}^{-1/3} + n_{ws\,B}^{-1/3} \right)} \left\{ - P(\Delta\varphi)^2 + Q\left(\Delta n_{ws}^{1/3}\right)^2 - R \right\} \tag{1}$$

where ΔH^{f} is given in kJ/mol of atoms of A and B with concentrations in the compound, and c_A the concentration of A. f_B^A is the degree to which A atoms are in contact with B atoms. V is the atomic volume, n_{ws} is the electron density, φ is the electronic charge. P, Q and R are constants fitted to experimental data (see Ref. [3] for more in details).

2.1 Indium

The enthalpies of formation of X-In binary alloys where X denotes cladding and fuel constituents and LA elements were calculated using Eq. (1). The results are shown as a function of In concentration in **Fig. 1**. The lower (i.e., larger negative value) enthalpies of formation of binary alloys between In and all LA than those between In and fuel constituents imply that In will preferentially form compounds with the LA. LA may therefore be immobilized in the fuel matrix. The positive enthalpies of formation of the cases for Fe and Cr predict that In will not react with cladding.

Indium's low melting point (157 $^{\mathrm{o}}$C) is a concern because the liquid metal can embrittle the cladding if it exists as pure elemental precipitates during the early irradiation stage when not enough LA are available. However, this is unlikely to occur because these elements will form compounds with Zr when LA are unavailable; the Zr-additive compounds have higher melting points than the elemental melting points - higher than ~1000 $^{\mathrm{o}}$C. When more reactive LA are produced as burnup increases, the additives form compounds with LA to immobilize them.

2.2 Antimony

In **Fig. 2**, similar calculation results for Sb are obtained, but Sb appears to be slightly less favorable than In. Unlike In, the enthalpies of formation of binary alloys between Zr and Sb are lower than those between LA and Sb, meaning that Sb tends to form compounds more favorably with Zr than with LA. This suggests that more Sb will be needed to compensate for the amount that is lost by forming compounds with Zr. Sb is advantageous, however, because its elemental melting point is much higher (630 $^{\mathrm{o}}$C) than In, giving more margin for melting if it is present in the fuel as a pure element or as additive-rich precipitates.

2
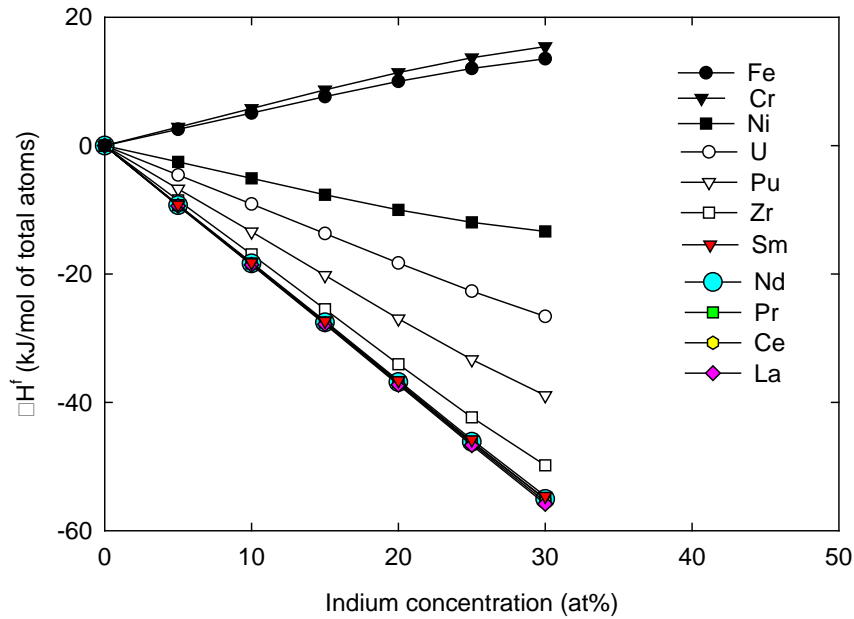
Fig. 1 Enthalpies of formation of binary alloys with In.
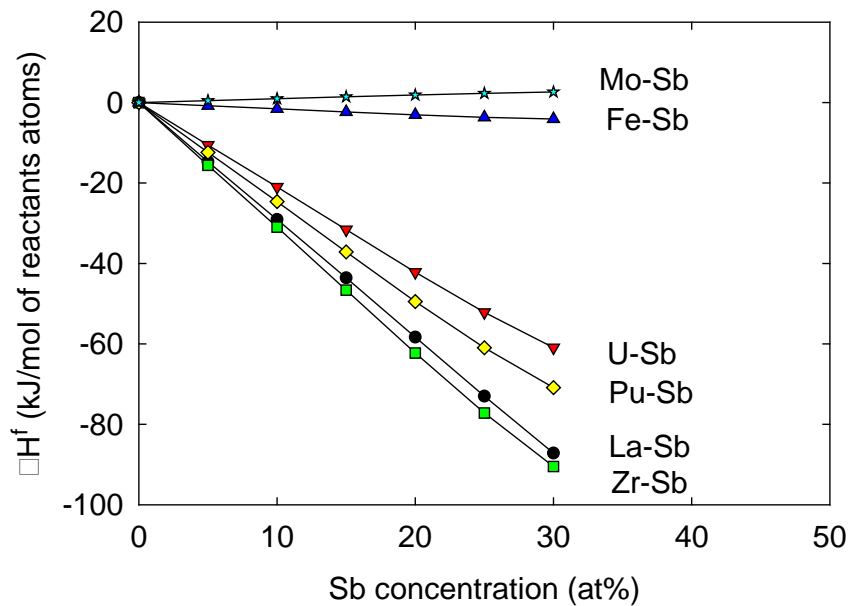
Fig. 2 Enthalpies of formation of binary alloys with Sb.

2.3. Choice of the alloy compositions to be studied

Indium
The combined yield of all LA fission products is approximately 0.5 per fission, which gives 3.6 at%
LA concentration at 20 at% burnup in U–10Zr fuel. For all LA, indium forms LAIn3, LAIn2, LAIn,
LA2In, and LA3In type compounds. Using the average of the atom ratios of all phases, 7.2 at% (or 4.4
wt%) In is needed to immobilize all LA at this burnup. Ce was chosen to represent the LA for the
present study, which is reasonable because LA behave similarly chemically. The Ce composition
tested was 2 wt% (or 2.8 at%) and In was added to provide 5 wt% (or 8.4at%), which gives the alloy

composition as U-10Zr-5In-2Ce. In order to simulate the BOL condition when there is negligible LA concentration, U-10Zr-5In was also tested.

Antimony
The intermetallic phases between Sb and LA are LA_2Sb, LA_4Sb_3, $LASb$, $LASb_2$. Based on the average of the atom ratios of the phases, Sb also needs 7.2 at% (or 4.4 wt%) to immobilize all LA, from which the Sb concentration was set 5wt%.

3. Alloy characterization

3.1 Alloy fabrication

U-10Zr-5In, U-10Zr-5In-2Ce, and U-10Zr-5Sb-2Ce were fabricated and characterized. U-10Zr-5In was examined because it is the composition at beginning of life. Indium's low melting point was a concern because of the liquid metal can embrittle the cladding if it exists as pure elemental precipitates at early irradiation stage when not enough LA are available. The other two alloys were to simulate fuel alloys at ~10at% burnup with additions of In and Sb as dopants.

The alloy sample preparation steps are as follows:
1. Weigh out chosen weight of sample elements.
2. Place material mixture in arc-melting furnace.
3. Arc-melt the material and flip the alloyed button over.
4. Repeat step 3 three more times to improve homogeneity in the alloy.
5. Change arc melting hearth to rod casting mold and cast alloyed button into 9-mm diameter rod.
6. Using diamond-wafering-cut-off machine, cut one end of rod flat and perpendicular, and polish the cut surface of the sample for optical microscopy (OM) and scanning electron microscopy (SEM).

3.2 Optical microscopy (OM)

U-10Zr-5In
Characterizations by OM of the U-10Zr-5In alloy were performed by optical microscopy. **Fig. 3** shows an image of OM after polishing and oxidizing the sample cross section. Indium appears to form precipitate phases in the continuous U-Zr phase.
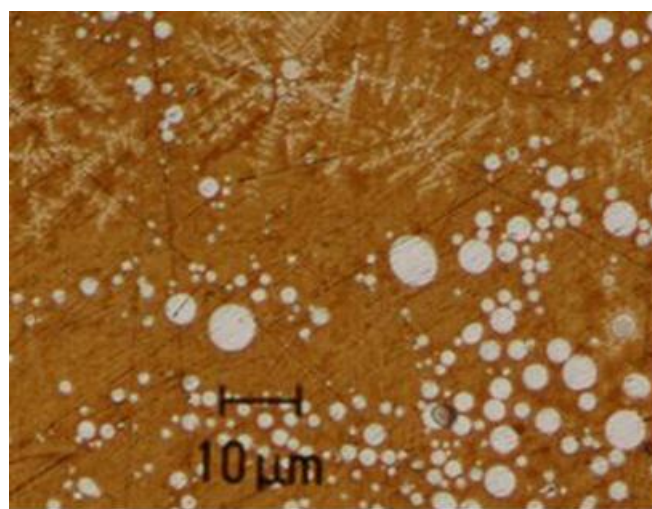
Fig. 3 Optical micrograph of the cross section of U-10Zr-5In alloy sample after oxidized.

U-10Zr-5In-2Ce

Characterizations by optical microscopy of the U-10Zr-2Ce-5In alloy were performed. **Fig. 4** shows an optical micrograph of a sample cross section. In this image, it appears that the alloy has three phases: the continuous phase, the precipitate phase, and a darker phase enclosed in the precipitate phase.
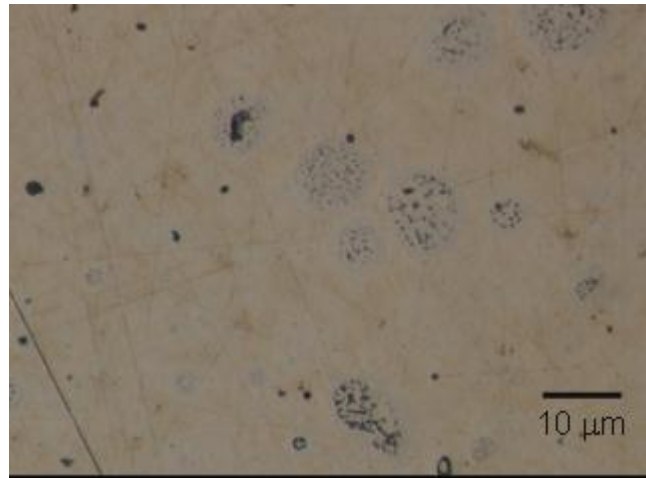
Fig. 4 Optical micrograph of the cross section of U-10Zr-2Ce-5In alloy sample.

U-10Zr-5Sb-2Ce

Optical micrography of a cross section of the U-10Zr-2CE-5Sb alloy was performed. **Fig. 5** shows a micrograph on the cross section surface taken after it was polished and etched. A precipitate phase is observable in the continuous phase.
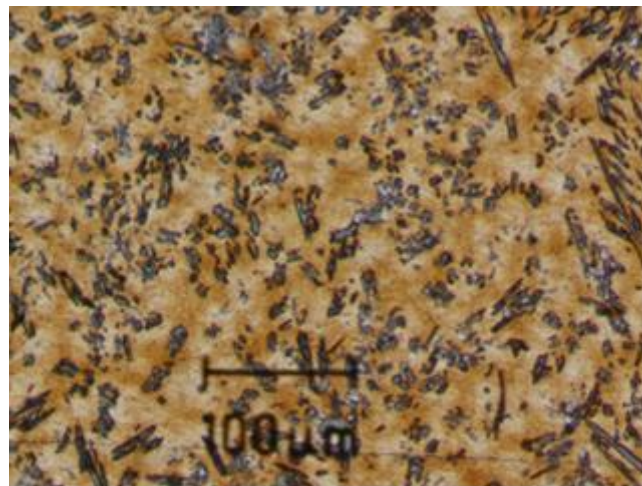
Fig. 5 Optical micrograph of sample cross section after polishing and etching.

3.3 Scanning electron microscopy (SEM)

U-10Zr-5In

Characterizations by scanning electron microscopy (SEM) of U-10Zr-5In were performed. In the SEM image, shown in **Fig. 6**, it is clearly noticeable that there are just two phases: A uranium-rich (> 80at%, often > 95at% U measured) and a Zr-rich (~ 60at% Zr, 20at% In, and 20at% U), according to EDS measurements. The Zr-rich phase precipitated in a lot of different patterns and size ranges, making precise analysis of the U-rich phase difficult: there were almost always little bubbles of Zr-rich material about. Sometimes it appeared dendritic, other times more typical of eutectic solidification.
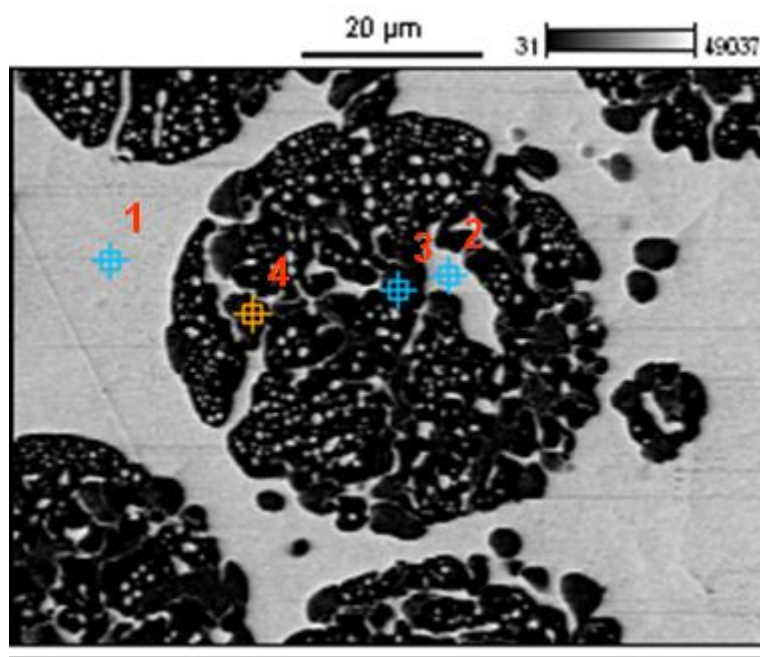
Fig. 6 SEM BSE image of cross section of U-10Zr-5In sample and EDS locations superimposed.

Composition analysis (EDS) was performed with the sample. Four points were picked to analyze: one in the continuous phase (point 1), two in the precipitate phase (point 4 and point 3), and one in the brighter phase in the agglomerated darker particles (point 2). At point 1, the general continuous phase, U is the dominant element. Indium is almost excluded from this phase. At point 2, the compositions are similar to those in point 1, suggesting this phase is virtually similar to point 1. At point 3 and point 4, the darker precipitate phase, all three elements are found. However, at this darker precipitate phase, Zr is the richest element and considerable indium compositions are observed, which suggests that In is closely attached with Zr. In **Table 1**, the measured compositions at these four points are given.

No phases containing pure indium or In-rich phase were observed, which indicates that In forms compounds with other elements, Zr and U. Because In forms compounds with fuel constituents, their melting points are much higher than pure In. Therefore, low melting characteristic of indium and liquid metal embrittlement of cladding does not appear to occur.

Table 1 Composition analysis for phases observed in U-10Zr-5In sample (at%)

	Zr	In	U
Point 1	5.6	0.3	94.1
Point 2	14.8	0.9	84.3
Point 3	59.0	22.5	18.5
Point 4	56.9	21.8	21.3

U-10Zr-5In-2Ce

Characterizations by scanning electron microscopy (SEM) were also performed. In the SEM image, shown in **Fig. 7**, it is clearly noticeable that there are indeed three phases that were vaguely observable in the optical image shown in **Fig. 4**. It is unknown why the phase represented by Point 3 formed small-diameter spheroids in a collection separated from the continuous phase by a thick layer of the precipitate phase, as indicated by Point 2. The Ce was fully melted during sample preparation. The geometry might be associated with surface tension and/or the order in which the phases solidified from the melt.

Composition analysis (EDS) was performed with the sample. Three points were picked to analyze: one in the continuous phase, one in the precipitate phase, and one in the darker phase in the precipitate phase. At Point 1, the general continuous phase, U is the dominant element. At Point 2, the precipitate phase, U, Zr and In are observable. Ce is not found withinthis point. At Point 3, the darker phase enclosed in the precipitate phase, all four elements are found. Ce is included in this phase. In **Table 2**, the measured compositions at these three points are given, as determined from a complete fitting of the spectrum.

Because Ce is found in the phase with In, it appears that Ce forms a compounds involved with In. The In-to-Ce ratio is about 2. Some indium found in the compounds with Zr is due to its affinity to Zr (even though indium tends to be preferentially attracted to Ce than to Zr). However, in pratical irradiation, this excessive amount of In will also likely be used to form compounds with Ce. This result confirms the effectiveness of its addition as an immobilizer for lanthanides.

In addition, In does not appear to form high-In phases. The formation of high In-content compounds – or, even worse – pockets of In residing as a pure unalloyed element was of concern because of low melting of these that can cause liquid metal embrittlement of the cladding. When In forms a compound with fuel constituents, their melting points are much higher than the pure element.

Fig. 7 SEM BSE image of cross section of U-10Zr-2Ce-5In sample and EDS locations superimposed.

Table 2 Composition analysis for phases observed in U-10Zr-5In-2Ce sample (at%)

	In	Ce	Zr	U
Point 1	3.6	0.1	7.0	89.3
Point 2	18.9	1.1	51.2	28.2
Point 3	27.2	15.7	39.2	17.9

U-10Zr-5Sb-2Ce

SEM analysis was also performed. A SEM image is shown **Fig. 8** with composition analysis points superimposed on the SEM image. A total of 8 locations were selected for composition (EDS) analysis.

Composition analysis results at the points indicated in **Fig. 8** are summarized in **Table 3**. In general, it appears that there are three kinds of phases formed. The darkest phase (Point 1, Point 6 and Point 7) is a Zr-rich Zr-Sb phase, in which a small portion U is also included and the content of Ce in this phase is negligibly small. The brightest phase is the U-rich U-Zr phase analyzed at Point 3 and Point 8, which is the continuous phase. This phase contains only U and Zr. The intermediate phase between the above two phases, analyzed at Point 2, Point 4 and Point 5, is a different kind of U-rich U-Zr phase that also contains a small content of Ce and a considerable amount of Sb.

From this composition analysis, it can be concluded that Ce is always found with Sb, indicating that Sb and Ce form compounds. It is also confirmed that Zr forms compounds with Sb, which reduces Sb content in the alloy that could otherwise form compounds with Ce.
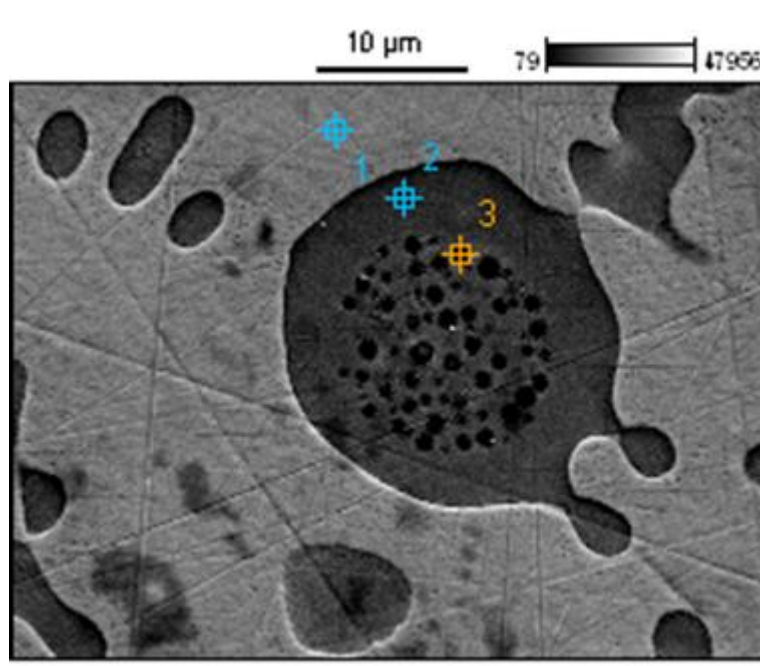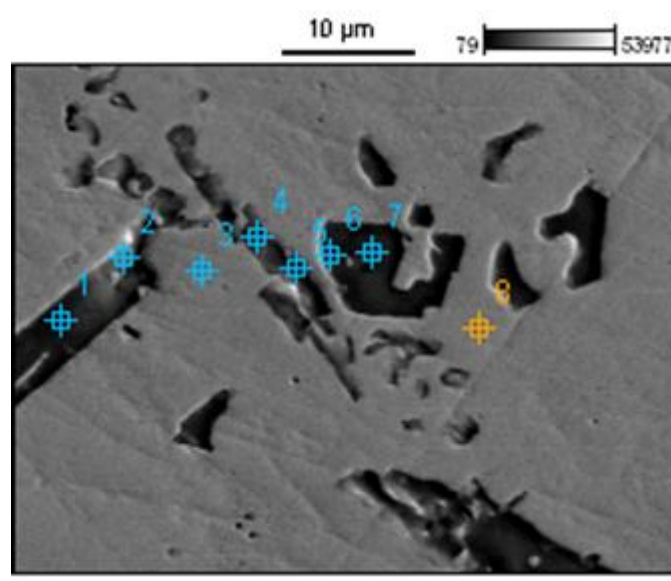

Fig. 8 SEM BSE image of cross section of U-10Zr-5Sb-2Ce sample and EDS locations superimposed.

Table 3 Composition analysis for phases observed in U-10Zr-5Sb-2Ce sample (at%)

	Zr	Sb	Ce	U
Point 1	52.2	30.5	0.7	16.6

Point 2	26.8	6.3	4.2	62.7
Point 3	12.8	0.0	0.00	87.2
Point 4	41.3	13.8	1.5	43.4
Point 5	27.8	6.3	0.4	65.5
Point 6	50.6	38.8	4.5	6.1
Point 7	52.9	37.0	1.1	9.0
Point 8	10.8	0.00	0.00	89.2

4. Summary

Predictions using a semi-empirical thermodynamics model showed that indium does not react with Fe-based alloy cladding and preferentially form compounds with fission product lanthanides.

Alloying tests also showed that indium does not appear to form high-indium phases or reside as a pure element when it was added to U-10Zr, which confirmed that indium will not enhance liquid metal embrittlement in cladding. The alloying tests also showed consistent results with the theoretical predictions, i.e., that indium formed compounds with cerium when added to U-10Zr-2Ce alloy, suggesting its effectiveness as an immobilizer for lanthanide fission products.

Antimony also showed similar theoretical and experimental results, indicating its effectiveness similar to indium although slightly less powerful than indium.

The results of this study conclusively showed that the addition of metals such as indium and antimony to U-10Zr fast reactor fuels can significantly reduce LA migration, which otherwise is a major cause of cladding and provides an obstacle to achieving high burnup.

Out-of-pile tests of U-10Zr-5In-2Ce and U-10Zr-5Sb-2Ce under a thermal gradient for about 4 months are planned. The migration of Ce will be examined with and without an In or Sb addition.

XRD measurements on the 3 alloys to try to determine more precisely the phases in presence are planned for future work.

ACKNOWLEDGMENTS

REFERENCES

[1] Yeon Soo Kim, Y.S. Choo, H.J. Ryu, A.M. Yacout, G.L. Hofman, Trans. Am. Nucl. Soc., 103, 289, 2010.
[2] Yeon Soo Kim, G.L. Hofman, A.M. Yacout, J. Nucl. Mater., 392 (2009) 164.
[3] F.R. de Boer, R. Boom, W.C.M. Mattens, A.R. Miedema, A.K. Niessen, Cohesion in

metals, North-Holland, Amsterdam, 1988.

$U_{1-x}Am_xO_2$ bearing blanket fabrications for the DIAMINO irradiation experiment

T. Delahaye[†], F. Lebreton, D. Horlait, N. Herlet

CEA, Nuclear Energy Division, Fuel Cycle Technology Department, F-30207 Bagnols-sur Cèze Cedex, France

Abstract. French DIAMINO (Dispositif d'Irradiation d'Actinides MIneurs dans Osiris) irradiation experiment in OSIRIS reactor (CEA, Saclay) aims to assess the influence of microstructure and Am content on He release and fuel swelling for different irradiation temperatures during heterogeneous transmutation. In this context, Am-bearing blanket fuels with two compositions ($U_{1-x}Am_xO_{2\pm\delta}$ (x = 0.075, 0.15)) and two microstructures (dense: no open porosity and porous: presenting a majority of open porosity) were fabricated in the ATALANTE facility through powder metallurgy processes. Prior to the irradiation, several characterizations were performed to ensure the compliance of the fuel characteristics with the program specifications.

1. Introduction

Fissions occurring during fuel irradiation in nuclear reactor lead to the formation of fission products, but also, by neutron captures, of Minor Actinides (MA). The latter, which mainly include neptunium (237) and americium (241, 243), are major contributors to spent fuel radiotoxicity. Radioactive waste management research on these long-lived heavy elements is notably directed towards Partitioning and Transmutation (P&T) in Fast Neutron Reactors (FNR) or Accelerator Driven Systems (ADS) [1]. For FNR, two recycling modes are generally considered: homogeneous and heterogeneous transmutation. In the first case, MA are added in small quantities (less than 5 wt%) in the fuel [2] whereas in the second case, dedicated fuels, known as blanket fuels, include larger amounts of MA (from 7 to 30 wt%) and are destined for the core periphery [3]. Such a configuration presents a limited impact on the core neutronic behaviour. In this context, $U_{1-x}Am_xO_{2\pm\delta}$ oxide solid solutions are increasingly studied as promising blanket fuels for Am recycling in FNR. The French DIAMINO[1] analytical irradiation program in the OSIRIS reactor (CEA, Saclay) takes part in this research. Indeed, in complement to the MARIOS analytical experiment [3], DIAMINO aims to assess the influence of microstructure and Am content on He release and fuel swelling for different irradiation temperatures during heterogeneous transmutation. In this context, Am-bearing blanket fuels with two compositions ($U_{1-x}Am_xO_{2\pm\delta}$ (x = 0.075, 0.15)) and two microstructures (dense: no open porosity and porous: presenting a majority of open porosity) were defined, corresponding to four sample sets. Forty-three disc fuels were fabricated in the ATALANTE facility through powder metallurgy processes. More particularly, a dedicated fabrication process, called UMACS (Uranium Minor Actinide Conventional Sintering), was developed to produce the dense ones. Porous samples were fabricated using a process previously developed and patented for similar fabrications. Prior to the irradiation, several characterizations were performed to ensure the compliance of the fuel characteristics with the program specifications.

[†] thibaud.delahaye@cea.fr
[1] DIAMINO: Dispositif d'Irradiation d'Actinides MINeurs dans Osiris

2. DIAMINO disc fabrications

Both dense and tailored porosity (porous) discs (Fig. 1) were fabricated in the ATALANTE facility. Due to high α and γ activities of ^{241}Am, these works were conducted in hot cells or glove boxes specially equipped for these kinds of operations.
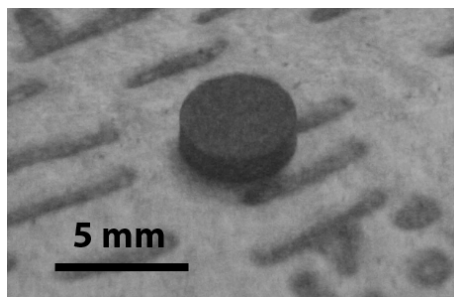
FIG. 1. Rectified disc before cladding.

2.1.1. Dense discs

The dense discs were fabricated using the UMACS process [4] presented Fig. 2. This process is based on the dissociation of the solid solution formation (i.e.: $U_{1-x}Am_xO_{2\pm\delta}$) and its sintering through the use of two dedicated thermal treatments. In this way, it is possible to avoid the competition between these two phenomena which is commonly encountered when using a reactive sintering. Obtained samples present higher densities (around 95% of the theoretical density) with homogeneous microstructures.
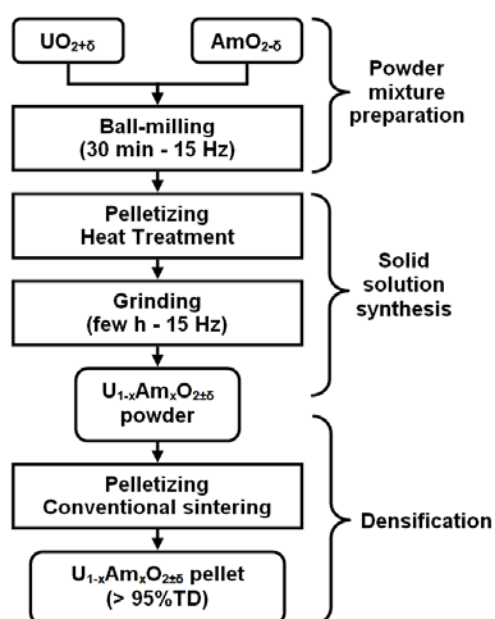
FIG. 2. Flow chart of the UMACS process.

Considering DIAMINO dense disc fabrications with the UMACS process, the solid solutions were synthesized during a thermal treatment of 4h at 1873 K in 25% of Ar/H$_2$ (4%) and 75% of Ar/O$_2$ (100 ppm). Obtained compounds were then sintered for 4h at 2023 K in Ar/H$_2$ (4%).

2.1.2. Porous discs

Fabrication of $U_{1-x}Am_xO_{2\pm\delta}$ porous discs was performed following a protocol, reported in Fig. 3, similar to that used in the frame of the MARIOS program. In this patented [5] process, the formation of an open porosity network is ensured by the addition of large and stable (i.e., not crushed during the pelletizing) U_3O_8/AmO_2 agglomerates in a powder mixture of UO_2 and AmO_2. During the reactive sintering under a reductive atmosphere, two synergistic phenomena occur. The agglomerates undergo a homothetic sintering and the reduction of the U_3O_8 of these agglomerates to UO_2 generating an additional shrinkage of the structure (around 36 % vol.)
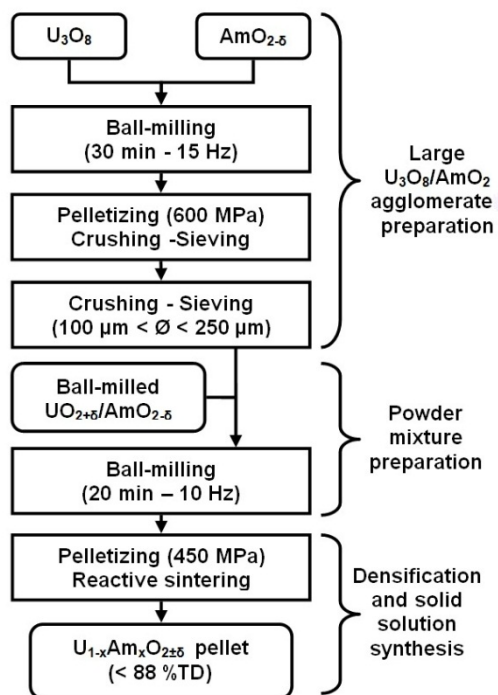
FIG. 3. Flow chart of the process employed for porous sample fabrications.

The sintering conditions employed for porous sample preparation were similar to those used for dense discs (4h at 2023 K in Ar/H_2 (4%)).

3. Disc characterization

3.1. Thermal stability

Before all characterizations, produced pellets and discs were visually inspected to check the absence of macroscopic defects. Their relative densities were then determined from geometric measurements. Obtained values, reported in Table 1, all comply with DIAMINO requirements.

To prevent microstructural evolution during irradiation, a stability test was performed on one pellet from each batch. This stability test consists in an additional thermal treatment similar to that used for the sintering. For all samples, neither de-densification nor shrinkage phenomena greater than 1% of the initial volume were measured (DIAMINO specifications is less than 2%).

Table 1. Average DIAMINO disc dimensions and relative densities.

Batch	Diameter (mm)	Thickness (mm)	Relative density (% TD)	Open porosity (volume %)
Dense $U_{0.85}Am_{0.15}O_{2\pm\delta}$	4.44	1.56	95.7	< detection limit
Dense $U_{0.925}Am_{0.075}O_{2\pm\delta}$	4.44	1.53	96.6	< detection limit
Porous $U_{0.85}Am_{0.15}O_{2\pm\delta}$	4.57	1.55	81.8	13(2)
Porous $U_{0.925}Am_{0.075}O_{2\pm\delta}$	4.56	1.52	84.6	11(2)
DIAMINO specifications	4.5 ± 0.2	1.5 ± 0.1	Dense: > 93 Porous: $\leq$ 89.5	Dense: < 3 Porous: > 8

3.2. XRD Analyses

XRD analyses were carried out on powdered samples using a Bruker D8 operating in Bragg-Brentano reflection geometry with Cu ($K_{\alpha1/\alpha2}$) radiation. Gold powder was added to the samples as a reference for 2θ calibration of XRD peak positions. A polymer grease was also added to avoid the contamination of the sample cell. XRD patterns of the four sets of sintered pellets are presented in Fig. 4. For the dense and porous samples, only the $U_{1-x}Am_xO_{2\pm\delta}$ solid solution is observed. No traces of precursors or additional phases were identified. Lattice parameters of these fluorite phases were refined by the Rietveld method using the FULLPROF software [6]. Dense and porous $U_{0.85}Am_{0.15}O_{2\pm\delta}$ lattice parameters are, respectively, 5.468(1) and 5.473(1) Å, while those of $U_{0.925}Am_{0.075}O_{2\pm\delta}$ dense and porous samples were found to be, respectively, 5.469(1) and 5.472(1) Å. These values are consistent with those previously reported in the literature for these oxides [7].

FIG. 4. XRD patterns obtained on powdered $U_{1-x}Am_xO_{2\pm\delta}$ samples. The asterisks point out the gold powder used as a 2θ reference.

3.3. Microstructures

The sample microstructures were studied using a FEG-SEM (Field Emission-Gun Scanning Electron Microscope) Zeiss SUPRA 55/55VP. S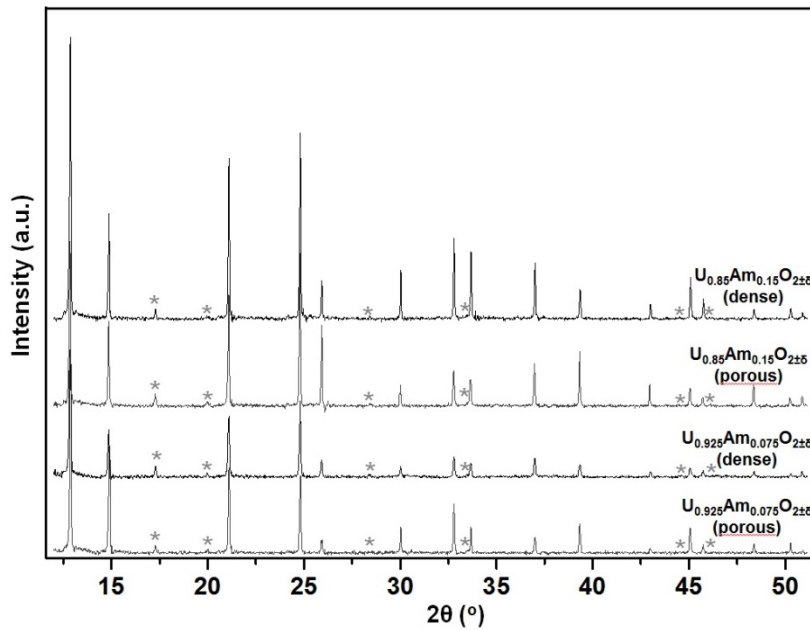EM observations were performed on fracture surfaces in order to reveal grain boundaries, grain size and morphology (Fig. 5). In addition, observations with an optical microscope (OLYMPUS BX30M) were carried out on a porous $U_{0.925}Am_{0.075}O_{2\pm\delta}$ polished surface to clearly evidence porosity repartition and morphology (Fig. 6). Through these characterizations, no real differences were evidenced when comparing 7.5% and 15% Am compounds fabricated with the same process. Conversely, dense and porous samples are as expected quite different.

Concerning dense samples, observations (Fig. 5 a and b) reveal coarse and well faceted grains with exhibiting only a residual porosity. SEM micrographs and density measurements confirm that the last stage of sintering was reached for both dense samples.

For porous samples, from SEM observations in Fig. 5 c and d, the positions of some initial U_3O_8/AmO_2 agglomerates can also be discerned, as they appear surrounded by curved and elongated pores. As evidenced by optical microscopy (Fig. 6 a and b), a large porosity network appears constituted of very wide and elongated-shape pores from 5 to 60 µm width. This porosity repartition is directly associated with the employed process. Indeed, during heating under reducing atmosphere, U_3O_8 is reduced as follows:

$$U_3O_8 + 2H_2 \longrightarrow 3UO_2 + 2H_2O$$
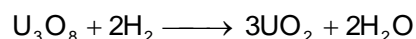
Since UO_2 theoretical density is 10.97 and U_3O_8 one is 8.38, a volume contraction of around 24% of the initial U_3O_8 grains happens and provokes the formation of a large porosity network inside the agglomerates. Besides, since the U_3O_8/AmO_2 agglomerates are initially pressed under a higher pressure than the green pellet will be, released gases are preferentially evacuated along lower constrained zones, such as the periphery of the agglomerates. At the end of U_3O_8 reduction, an important porous volume is thus present around the initial U_3O_8/AmO_2 agglomerates.

From hydrostatic weight measurements, less than one third of the porosity volume appears to be closed. Thus, more than 11vol% of each disc is an open porosity network, satisfying the DIAMINO requirements (more than 8%). From SEM observations on fractured pellets (Fig. 5 c and d), such porosity is not fairly evidenced since the pellets are expected to be fractured along these porosity networks. SEM observations notwithstanding indicate that this kind of porosity is exclusively located along grain boundaries of what initially were U_3O_8/AmO_2 agglomerates. As for dense samples, since after heat treatment, the grains are well-faceted and a grain growth has taken place (grain size mainly from 5 to 20 µm (Fig. 5 c and d)), the ultimate stage of sintering has been reached. Despite the large porosity networks, the pellets are thus well-consolidated.
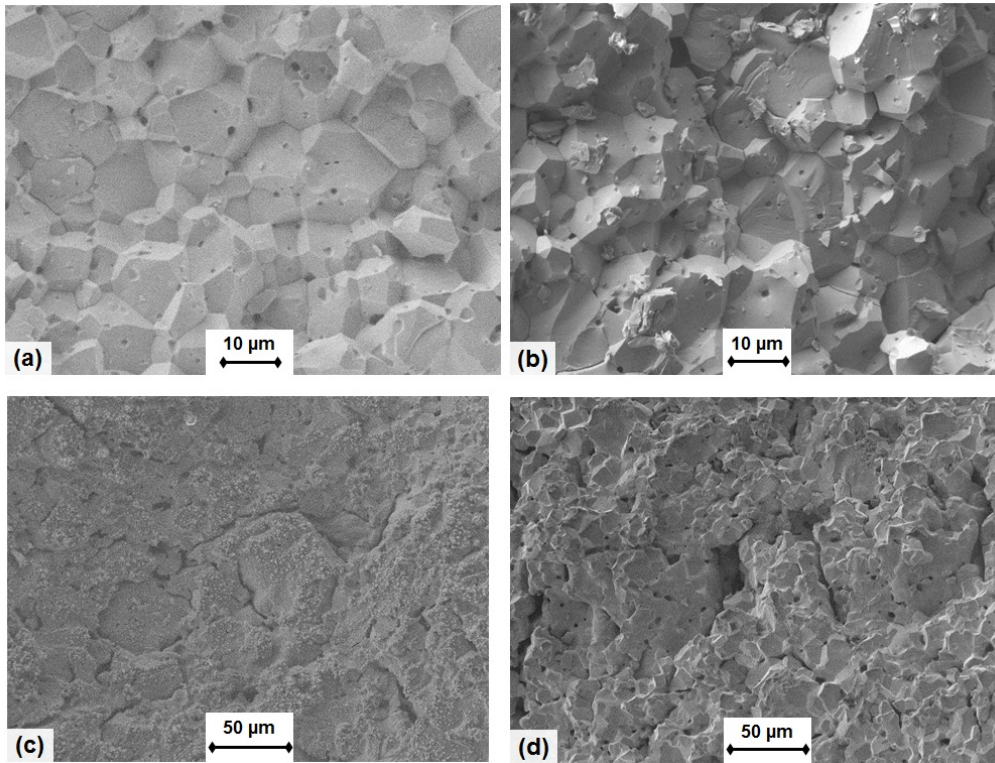
FIG. 5. SEM micrographs of dense $U_{0.925}Am_{0.075}O_{2\pm\delta}$ (a) and $U_{0.85}Am_{0.15}O_{2\pm\delta}$ (b) and porous $U_{0.925}Am_{0.075}O_{2\pm\delta}$ (c) and $U_{0.85}Am_{0.15}O_{2\pm\delta}$ (d) discs.
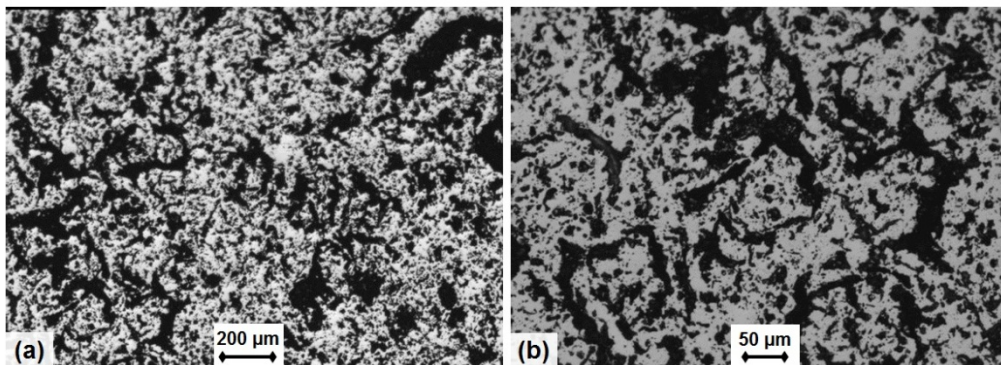
FIG. 6. Optical micrographs of a porous $U_{0.925}Am_{0.075}O_{2\pm\delta}$ sample.

4. Conclusion

In the framework of the French DIAMINO analytical irradiation program, four sets of highly dense and tailored-open porosity $U_{1-x}Am_xO_{2\pm\delta}$ discs (with x = 0.075 or 0.15) were fabricated.

Dense sample fabrications were based on the UMACS process and the dissociation of the solid solution synthesis and the sintering. Highly dense discs were obtained with density higher than 95%TD implying only close porosity.

Concerning porous samples, they were fabricated using a previously patented process. The latter uses two synergistic phenomena: the homothetic sintering of large and stable agglomerates dispersed into the pellets and the reduction of the U_3O_8 contents into these compacts in UO_2. Generated open porosity is adapted for He release and is large enough to be stable during irradiation.

As the conformity of all four sets of discs with regards to DIAMINO requirements has been confirmed, the discs will be cladded into analytical pins and will soon be irradiated in Osiris reactor (Saclay, France).

REFERENCES

[1]   D. Warin, J. Nucl. Sci. Technol., 44 (2007) 410-414.

[2]   F. Lebreton, D. Prieur, A. Jankowiak, T. Delahaye, M. Tribet, L. Donnet, P. Dehaudt, J. Nucl. Mater., 420 (2011) 213-217.

[3]   D. Prieur, A. Jankowiak, T. Delahaye, N. Herlet, P. Dehaudt, P. Blanchart, J. Nucl. Mater., 414 (2011) 503-507.

[4]   T. Delahaye, F. Lebreton, D. Prieur, P. Coste, M. Bataille, Procédé de préparation d'un combustible nucléaire dense à base d'au moins un actinide mineur, French patent N° 11-60597 (2011).

[5]   A. Jankowiak, N. Herlet, C. Leorier, N. Astier, P. Coste, B. Deschamps, D. Prieur, P. Blanchart, Procédé de préparation d'un combustible nucléaire poreux à base d'au moins un actinide mineur, French patent N° 09-55985 (2009).

[6]   J. Rodriguez-Carvajal, Phys. B, 192 (1993) 55-69.

[7]   D. Prieur, A. Jankowiak, D. Roudil, S. Dubois, C. Leorier, N. Herlet, P. Dehaudt, J.-P. Laval, P. Blanchart, J. Nucl. Mater., 411 (2011) 15-19.

α self-irradiation effects in $U_{1-x}Am_xO_{2\pm\delta}$ solid solutions monitored by XRD: Preliminary results

D. Horlait[a], F. Lebreton[a], T. Delahaye[a], P. Roussel[b]

[a] CEA, DEN, DTEC/SDTC/LEMA, F-30207 Bagnols-sur-Cèze Cedex, France

[b] UCCS - UMR CNRS 8181, Université de Lille, USTL-ENSCL, BAT C7, BP 90108, 59652 Villeneuve d'Ascq, France

Abstract. Five $U_{1-x}Am_xO_{2\pm\delta}$ homogeneous solid solutions (with $0.075 \leq x \leq 0.49$) were succesfully produced using solid state reactions. The evolution of the lattice parameter of these solid solutions under self-irradiation was monitored by regular XRD analysis and this paper presents the first conclusive results obtained for the $U_{0.925}Am_{0.075}O_{2\pm\delta}$ and $U_{051}Am_{0.49}O_{2\pm\delta}$ samples.

1. Introduction

In order to reduce the radiotoxicity of nuclear waste, the transmutation of minor actinides (MA) into short-lived elements is currently evaluated in the framework of fast neutron reactors (FNR) development [1,2]. At the current state of the art, uranium-based mixed-oxide $U_{1-x}MA_xO_{2\pm\delta}$ are considered as promising fuels to perform the transmutation of MA. In details, the heterogeneous mode (which has nowadays become the reference mode) consists of integrating MA in specific fuels exclusively destined to the core periphery, therefore called minor actinide bearing blanket (MABB) fuels. To that end, MA are integrated in $U_{1-x}MA_xO_{2\pm\delta}$ fuels in relatively high concentrations (7 to 30 at.% of the heavy metals). Since americium's long-term activity is predominant compared to the other MA, the current research is mainly focused on $U_{1-x}Am_xO_{2\pm\delta}$ MABB fuels [3–5].

Nuclear fuels [6–8] and more generally α- emitter-bearing ceramics [9–18] or alloys [19] are known to present swelling during storage at ambient temperature at both microscopic (crystalline structure) and macroscopic scales, but for the $U_{1-x}Am_xO_{2\pm\delta}$ compounds, experimental data is very limited [20]. To initiate extensive research on this problematic, we monitored XRD diffraction patterns of some $U_{1-x}Am_xO_{2\pm\delta}$ samples (with x = 0.075, 0.15, 0.32, 0.39 and 0.49) over several months to appraise the effect of self-irradiation at the crystal lattice scale. The aim of this paper is to report the experimental procedure employed for this study and to present the conclusive results already obtained on the $U_{0.925}Am_{0.075}O_{2\pm\delta}$ and the $U_{0.51}Am_{0.49}O_{2\pm\delta}$ samples.

2. Experimental

2.1. Sample plates preparation

Each of the five samples of $U_{1-x}Am_xO_{2\pm\delta}$ was prepared from the same $UO_{2\pm\delta}$ and $^{241}AmO_{2\pm\delta}$ starting powders. The employed batch of $^{241}AmO_{2\pm\delta}$ was purified 3 years ago, and contains some lanthanide impurities around 2 wt.%, mostly Ce and Nd) as well as ^{237}Np generated by α-decay of ^{241}Am, which should represent about 0.4 at.% of the Am amount.

The formation of homogenous solid solutions was achieved using a recently developed process, UMACS [4] which consists of two successive heat treatments on pelletized powders, separated by a long grinding step. The first heat treatment aims to form the solid solution, the second is a conventional sintering. Details of the sample fabrications can be found in [4]. The Am/(U+Am) ratio of each sintered sample (x) was determined using Thermal Ionization Mass Spectrometry, with an accuracy of ±0.01. The results are given in Table 1.

After the fabrication, a fragment (few tens milligrams) of each obtained pellet is deposited on a tungsten wedge in a furnace (graphite chamber). Each sample undergoes the same thermal cycle: one hour of plateau at 1100°C reached with a heating rate of 10°C·min^{-1}, then a cooling to room temperature at 25°C·min^{-1}, all the cycle under an Ar/H$_2$(4%) flow. The aim of this cycle is "to heal" all the self-irradiation effects integrated between the date of fabrication and that of the XRD experiment start. The moment when the sample is cooled down to room temperature is thus considered to be the initial time, noted t_0. The sample is then manually ground in an agate mortar, embedded in a grease and finally layer-deposited on a silicon mirror disc used as support.

2.2. XRD Measurements

XRD patterns were recorded using a D8 Bruker Advance diffractometer adapted for radioactive material measurements (Cu K$\alpha_{1,2}$ radiation, $\lambda_1 = 1.5406$ Å). This device is equipped with a linear Lynx-Eye detector. The diffractograms were collected between 25 and 120° ($\theta-2\theta$ mode). A step of 0.0105° (2θ) and a counting time of 0.83 s·step^{-1} were routinely employed, corresponding to 3 h recordings. As the overall experiment here presented proceeds over several months, the stability of the XRD device had to be checked. The absence of instrumental deviation was thus verified by adding a gold powder as an internal standard on each sample plate (gold was indeed initially mix with the grease). For each sample, no modification of gold patterns (peak position, width and intensity) was noted, thus ensuring that the evolution of the U$_{1-x}$Am$_x$O$_{2\pm\delta}$ patterns were only due to sample ageing.

2.3. Data processing

2.3.1. Unit cell parameter determination

To determine the unit cell parameters, the modified Thompson-Cox-Hastings Pseudo-Voigt profile function (TCH-Z) was selected in order to take into account a potential change in microstructure (strain and/or size effects). Unit cell parameters were determined using the FullProf suite software. National Institute of Standard Technology (NIST) LaB$_6$ SRM660b was used as a standard to subtract the contribution of instrumental resolution to diffraction line broadening.

2.3.2. Use of dpa as a time scale

To fairly compare the self-irradiation effects of the samples from 7.5 to 49 at.% of the heavy metals, a scale time which corresponds to the integrated dose was selected. The dpa values (number of displacements per atoms) are calculated for a given time t (in seconds) following Equation 1:

$$\text{dpa} = \frac{((N_{Am})_0 - (N_{Am})_t e^{-\lambda t}) \times n_{d,\alpha}}{N}$$

(1)

with N the number of atoms per gram, $n_{d,\alpha}$ the number of atoms displaced by one α-decay (considered by analogy with UO$_2$ and (U,Pu)O$_2$ oxides to be 1600) and λ the decay constant of ^{241}Am (4.4.10^{-6} d^{-1}).

The XRD monitoring of U$_{0.925}$Am$_{0.075}$O$_{2\pm\delta}$ and U$_{0.51}$Am$_{0.49}$O$_{2\pm\delta}$ structural evolutions were, at the moment of this paper writing, performed over 245 and 71 days respectively, which correspond to calculated dpa values of 0.042 and 0.116.

3. Results

3.1. Crystalline structure

A few weeks after the sample preparation, an X-ray diffractogram was recorded for each studied compound (Figure 1). For every one of them, only fluorite patterns were observed. Moreover, as all the diffraction peaks have a symmetrical shape (Figure 1 insert), a sole $U_{1-x}Am_xO_{2\pm\delta}$ fluorite solid solution is presumably obtained for each sample, in agreement with other works on uranium-americium mixed-oxides [21,22].
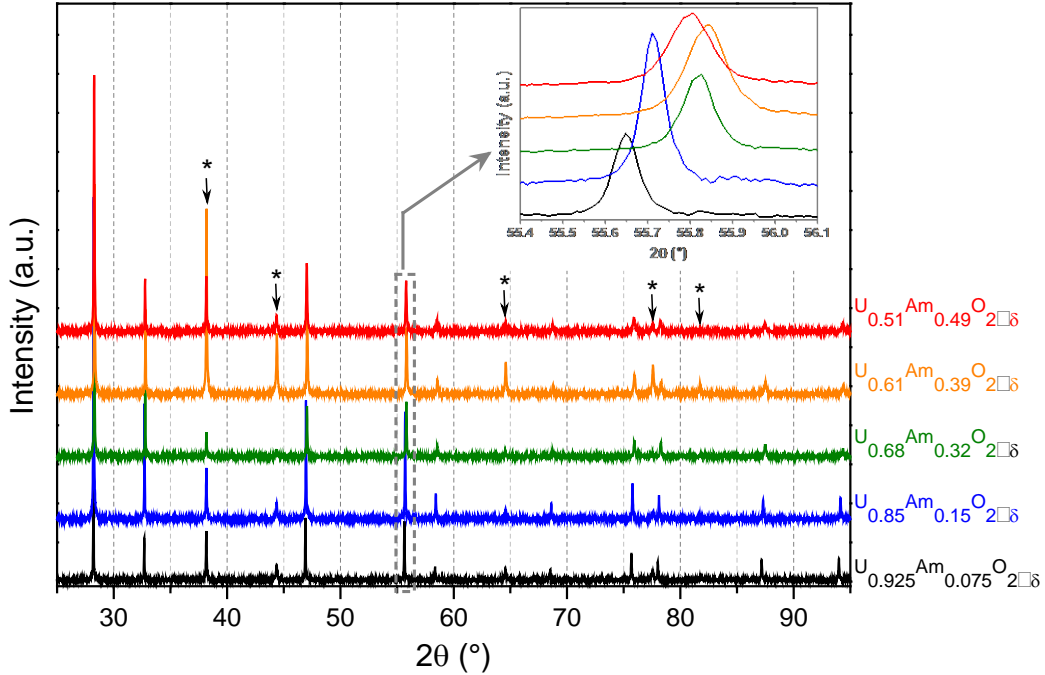
FIG. 1. X-ray diffractograms of the $U_{1-x}Am_xO_{2\pm\delta}$ samples (x =0.075, 0.15, 0.32, 0.39 and 0.49). Only the fluorite pattern is observed, indicating solid solution formation. Asterisks point the diffraction peaks of the internal standard (gold).

3.2. Self-irradiation effects on the $U_{1-x}Am_xO_{2\pm\delta}$ fluorite lattice

To date, two samples, $U_{0.925}Am_{0.075}O_{2\pm\delta}$ and $U_{0.51}Am_{0.49}O_{2\pm\delta}$, have been regularly analyzed by XRD over several month and the corresponding unit cells parameters were determined. Up to the writing of this paper, the fluorite structure was kept and no important evolutions of the width or relative intensity of the diffraction peaks were evidenced, thus indicating that the integrated doses ($1.8.10^{17}$ and $4.8.10^{17}$ $\alpha.g^{-1}$ for $U_{0.925}Am_{0.075}O_{2\pm\delta}$ and $U_{0.51}Am_{0.49}O_{2\pm\delta}$, respectively) are not sufficient to quantitatively alter the phase or render amorphous content. However, the unit cell parameters, reported in Figure 2 were, as expected [16,17,20] found to increase with the sample ageing following the exponential function:

$$a = a_0 + K*(1-e^{-K't})\tag{2}$$

which is nowadays often reported to describe the evolution of a cell parameter during self-irradiation [12,15,16]. The regression of the unit cell parameter evolutions as a function of time was performed and allowed the determination of the K and K' constants, as well as the a_0 values, which are given in Table 1. a_0 values being now calculated, they were used to plot the evolution of $\triangle a/a_0$ as the function of the sample ageing expressed in time (Figure 2A) and in dpa (Figure 2B).

A
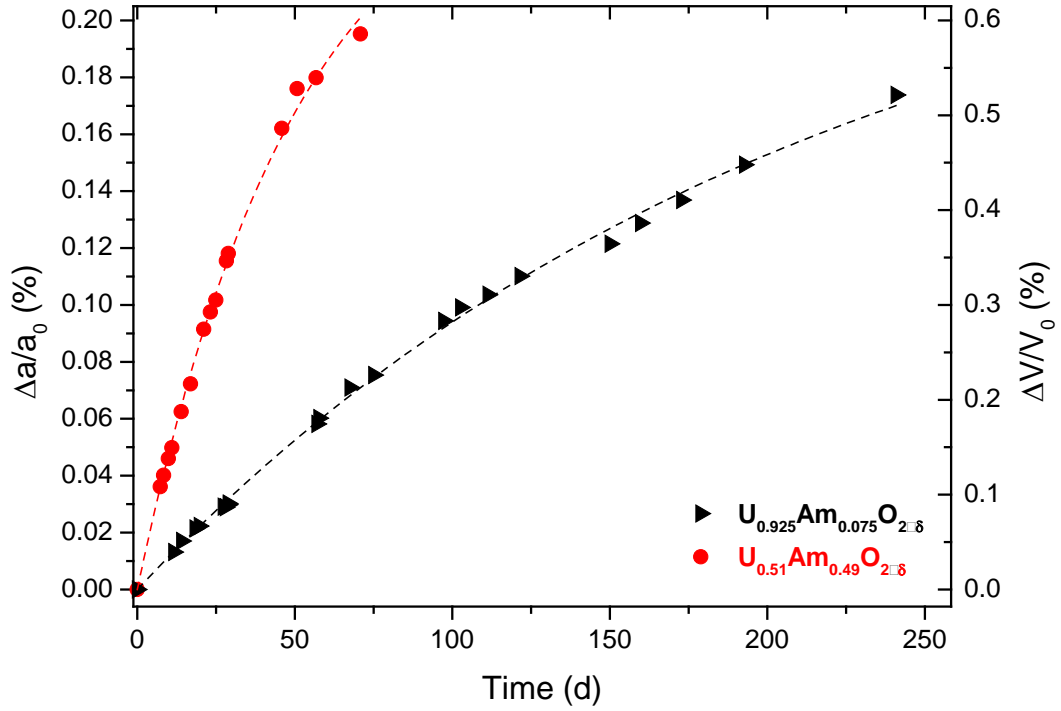
B
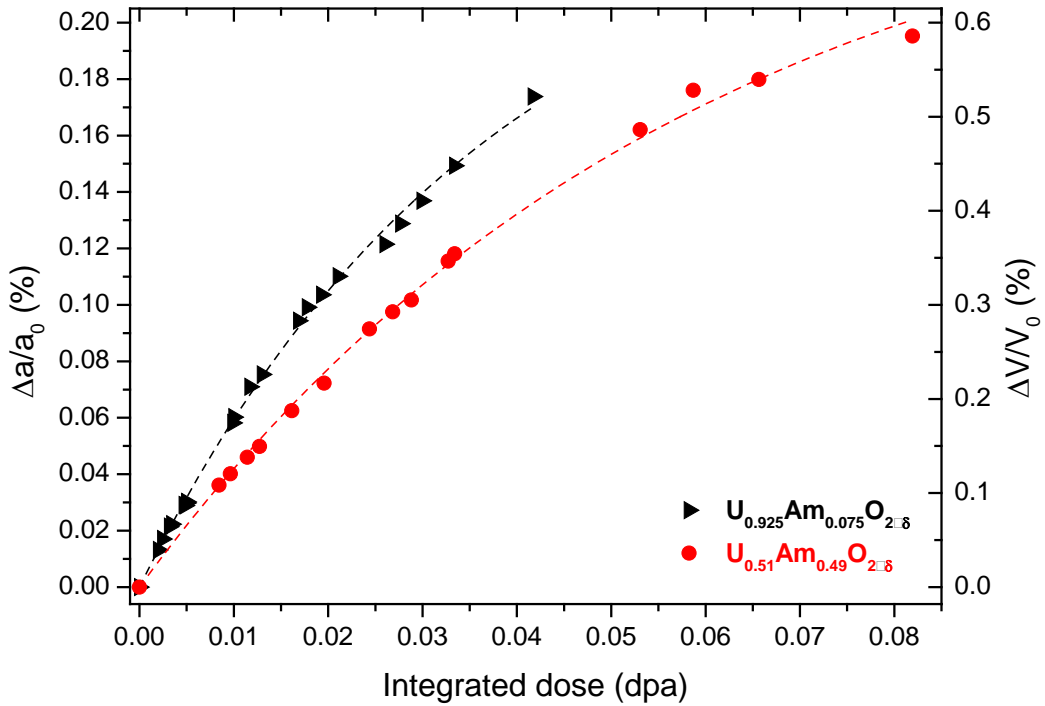
FIG. 2. Relative evolution of the fluorite unit cell parameter ($\Delta a/a_0$, left scale) or volume ($\Delta V/V_0$, right scale) of the $U_{1-x}Am_xO_{2\pm\delta}$ solid solutions for x = 0.075 and 0.49 as a function of sample ageing expressed in time (A) or dpa (B).

From these new results, the Equation 2 was modified to describe the evolution of $\triangle a/a_0$ as a function of time:

$$\triangle a/a_0 = A(1-e^{-Bt}) \tag{3}$$

or if a time equivalent scale in dpa is selected:

$$\triangle a/a_0 = A(1-e^{-B'dpa}) \tag{4}$$

The calculated values of A, B and B' are given in Table 1. In Equations 3 and 4, A corresponds to the maximum expansion that could be reached by the lattice parameter due to self-irradiation. For the two samples monitored to date, values of A close to 0.26% were determined, even if such values was not yet experimentaly attained. It corresponds to a cell volume maximum swelling due to α self-irradiation of ~0.8vol.%. This result is consistent with the values reported for $AmO_{2-\delta}$, which vary from 0.224% to 0.325%[14, 16–18]. Moreover the proximity between the A values tends to indicate that the maximum expansion of the $U_{1-x}Am_xO_{2\pm\delta}$ fluorite unit cell is not modified by the americium content.

The value of B, as given in Equation 3 is related to the rate of cell volume expansion, which, as expected, was found to increase with americium concentration in the samples (Table 1).

Likewise, the values of B' obtained from Equation 4 are also related to the rate of cell volume expansion, but as the sample ageing is here normalized in dpa (Equation 1), B' should be similar for all $U_{1-x}Am_xO_{2\pm\delta}$ samples. However the B' value obtained for $U_{0.51}Am_{0.49}O_{2\pm\delta}$ (17.1) was found to be abnormally lower than that obtained for $U_{0.925}Am_{0.075}O_{2\pm\delta}$ (27.0) and that reported for $AmO_{2-\delta}$ (24.4 to 35.3) [14, 16–18]. This observation is also graphically evidenced in Figure 2B as $U_{0.51}Am_{0.49}O_{2\pm\delta}$ unit cell parameter increase is slower than that of $U_{0.925}Am_{0.075}O_{2\pm\delta}$. Although this observation still need to be confirmed with the upcoming results of $U_{0.85}Am_{0.15}O_{2\pm\delta}$, $U_{0.68}Am_{0.32}O_{2\pm\delta}$ and $U_{0.61}Am_{0.39}O_{2\pm\delta}$ self-irradiation monitoring, it tends to indicate that the $U_{0.51}Am_{0.49}O_{2\pm\delta}$ solid solution is comparatively less affected by the α self-irradiation. In other terms, the rate of cell volume expansion seems to partially depend on americium content.

Table 1. Summary of self-irradiation experiment results.

x (molar fraction in $U_{1-x}Am_xO_{2\pm\square}$	Initial unit cell parameter (a_0) (Å)	Maximum integrated dose		Fitted parameters		
		α.g^{-1}	dpa	A (%)	B	B'
0.075	5.4660	$1.75.10^{17}$	0.042	0.252	$1.95.10^{-4}$	27.0
0.49	5.4544	$3.40.10^{17}$	0.082	0.266	$8.26.10^{-4}$	17.1
1*	-	-	-	0.224 to 0.325	1.70 to $2.46.10^{-3}$	24.4 to 35.3

* $AmO_{2-\delta}$ results come from refs. [14,16–18]

4. Conclusion

Several $U_{1-x}Am_xO_{2\pm\delta}$ solid solutions were obtained by solid state reaction. For $U_{0.925}Am_{0.075}O_{2\pm\delta}$ and $U_{051}Am_{0.49}O_{2\pm\delta}$ samples, regular analyses by XRD allowed the evolution of the crystalline structure to be followed as a function of the integrated dose. Up to now, no considerable evolutions of diffraction peak shape were denoted, indicating that the α irradiation do not alter the phase and does not render amorphous to a measureable extent the solid solutions for the considered integrated dose. From the evolution of unit cell parameters, fitting of the experimental data allowed determining predictive laws of the form $\triangle a/a_0 = A(1-e^{-B'dpa})$, with A corresponding to the maximum unit cell parameter expansion. Values of A close to 0.26% were obtained for both samples, in agreement with the data reported for $AmO_{2-\delta}$ [14,16–18].Monitoring by XRD of the $U_{1-x}Am_xO_{2\pm\delta}$ solid solutions is currently still in progress and extensive results including experiments on $U_{0.85}Am_{0.15}O_{2\pm\delta}$, $U_{0.68}Am_{0.32}O_{2\pm\delta}$ and $U_{0.61}Am_{0.39}O_{2\pm\delta}$ will soon be available.

REFERENCES

[1]   WARIN, D., Status of the French research program on partitioning and transmutation, J. Nucl. Sci. Technol. 44 (2007) 410.

[2]   LEBRETON F., et al., Fabrication and characterization of americium, neptunium and curium bearing MOX fuels obtained by powder metallurgy process, J. Nucl. Mater. 420 (2012) 213.

[3]   PRIEUR D., et al., Fabrication and characterisation of $U_{0.85}Am_{0.15}O_{2-x}$ for MARIOS irradiation program, J. Nucl. Mater. 414 (2011) 503.

[4]   DELAHAYE T., et al., $U_{1-x}Am_xO_{2\pm\delta}$ (x=0.075, 0.15) Blanket Fuel Fabrication and Characterization in the Framework of the DIAMINO Transmutation Experiment: First Application of the UMACS Process, J. Nucl. Mater. 432 (2012) 305.

[5]   LEBRETON F., et al., Recent progress on actinide-bearing oxide fuel synthesis at CEA Marcoule, J. Nucl. Mater. 438 (2013) 99.

[6]   WISS T., et al., Radiation damage in UO_2 by swift heavy ions, Nucl. Instr. and Meth. in Phys. Res. B 122 (I997) 583.

[7]   STAICU D., Impact of auto-irradiation on the thermophysical properties of oxide nuclear reactor fuels, J. Nucl. Mater., 397 (2010) 8.

[8]   KATO M., Self-radiation damage in plutonium and uranium mixed dioxide, J. Nucl. Mater. 393 (2009) 134.

[9]   WEBER W.J., et al., Radiation effects in crystalline ceramics for the immobilization of high-level nuclear waste and plutonium, J. Mater. Res. 13 (1998) 1434.

[10]   CLINARD JR F.W., et al., Self-irradiation effects in [238]Pu-substituted zirconolite, J. Nucl. Mater. 126 (1984) 245.

[11]   STRACHAN D.M., et al., Effects of self irradiation from [238]Pu candidate ceramics for Pu immobilization, Pacific Northwest National Laboratory report PNNL-14232 (2003).

[12]   GOUBARD F., et al., Alpha self-irradiation effects in ternary oxides of actinides elements The zircon-like phases $Am^{III}VO_4$ and $A^{II}Np^{IV}(VO_4)_2$ (A=Sr,Pb), J. Solid State Chem. 178 (2005) 1898.

[13]   BELIN R.C., et al., Experimental insight into the radiation resistance of zirconia-Based americium ceramics, Inorg. Chem. 48 (2009) 5376.

[14]   HURTGEN C., FUGER, J., Self-irradiation effects in americium oxides, Inorg. Nucl. Chem. Lett. 13 (1977) 179.

[15]   WEBER W.J., et al., The radiation-induced crystalline-to-amorphous transition in zircon, J. Mater. Res. 9 (1994) 688.

[16]   LEBRETON F., et al., In-situ X-ray diffraction study of phase transformations in the Am–O system J. Solid State Chem. 196 (2012) 217

[17]   PRIEUR D., et al., Fabrication and characterization of minor actinides bearing fuels obtained by conventional powder metallurgy process, Powder Tech. 208 (2011) 553.

[18]   CHIKALLA T.D., EYRING L., Phase relationships in the americium-oxygen system, J. Inorg Nucl. Chem. 30 (1968) 133

[19]   BACLET N., et al., Self-irradiation effects in plutonium alloys, J. Alloys Compd. 444 (2007) 305.

[20]   PRIEUR D., et al., Self-irradiation effects in dense and tailored porosity $U_{1-y}Am_yO_{2-x}$ (y = 0.10; 0.15) compounds, J. Nucl. Mater. 411 (2011) 15.

[21]   PRIEUR D., et al., Local Structure and Charge Distribution in Mixed Uranium−Americium Oxides: Effects of Oxygen Potential and Am Content Inorg. Chem. 50 (2011) 12437.

[22]   MAYER K., et al., On the valency state of americium in $(U_{0.5}Am_{0.5})O_{2-x}$, J. Alloys Compd. 231 (1994) 456.

Dilatometric Study of $U_{1-x}Am_xO_{2\pm\delta}$ Transmutation Fuels

F. Lebreton[a,b]**, D. Horlait**[a]**, T. Delahaye**[a]**, P. Blanchart**[b]

[a] CEA, DEN, DTEC/SDTC/LEMA, Bagnols-sur-Cèze, France

[b] ENSCI/GEMH, Limoges, France

Abstract. $U_{1-x}Am_xO_{2\pm\delta}$ blanket fuels for heterogeneous transmutation in fast reactors, and more precisely their fabrication via sintering, were for the first time studied by dilatometry. Several experiments, performed at up to 2023 K and under a controlled atmosphere, are analyzed to understand and characterize the densification behaviour of such materials. Two types of sintering, namely reactive and conventional, were considered in this study. For reactive sintering, mixtures of simple oxides ($UO_{2+\delta}$ and $AmO_{2-\delta}$) powders were used to prepare the green pellets, and solid solution formation and its densification are thus performed during a single thermal treatment. For conventional sintering, the precursors are $U_{1-x}Am_xO_{2\pm\delta}$ solid solution powders previously fabricated by solid-state reaction at high temperature. Obtained results allow the description of sintering processes and their temperatures of interest (temperatures of sintering onset, or of maximum shrinkage rates). The influences of the type of sintering (reactive or conventional) and of the composition (i.e., americium content in the sample) are also discussed based on the obtained data.

1. Introduction

Minor actinides (isotopes of neptunium, americium and curium) produced in nuclear fuels are the second-highest contributors (after plutonium isotopes) to the radiotoxicity and decay heat of nuclear waste after 100 years [1]. Among the minor actinides, americium, and more particularly its 241 isotope, is primarily responsible for this radiotoxicity due to its high activity (10^4 times that of ^{237}Np) and relative abundance (10 times that of all curium isotopes). In this context, transmutation of these isotopes into less radiotoxic and shorter-lived (or even stable) elements appears to be an alternative to direct final disposal in deep geological repositories, and could notably be used to reduce both the storage duration and ecological footprint of these repositories. In France, research has been focused on transmutation in fast reactors in homogeneous and heterogeneous modes [2]. The former consists of adding a few percent (up to 5 wt.%) of minor actinides to the MOX (mixed-oxide) driver fuels of the reactor [3]. For the latter, which is nowadays the reference in France, a higher amount of minor actinides would be added to depleted UO_2 fuels, known as MABB (minor actinide-bearing blanket, i.e., only destined for the periphery of the core). Considering minor actinide differences and specificities, transmutation scenarios may vary for each of them [4]. Recently, research has been focused on heterogeneous transmutation of only americium. Notably, two experimental irradiations were scheduled. The first one, MARIOS, was performed in the HFR (High Flux Reactor, Petten, Netherlands) between March 2011 and April 2012 [5,6] whereas the second, DIAMINO, should begin soon in the OSIRIS reactor (CEA Saclay, France) [5]. For both these experiments, all the disc fuels were fabricated in the Atalante facility (CEA Marcoule, France), after a phase of dedicated R&D.

Two types of fuels were used for these experiments, differing in terms of microstructure, with on one hand standard dense fuels, with a density higher than 93%TD (of the theoretical density), and on the other, tailored open-porosity fuels, with a density lower than 89%TD, and at least 8 vol.% of open porosity. The purpose of the latter fuel concept is to have a way to decrease the effects (such as formation of cracks or fuel swelling) of the considerable gas release (decay He and fission products) caused by ^{241}Am [6]. For these porous fuels, a dedicated process was developed in the framework of

the MARIOS and DIAMINO irradiations. It is based on powder mixtures and a reactive sintering and allows fuels complying with the specifications to be fabricated at laboratory scale [6,9] (which are presented in FIG. 1). In the case of dense fuels, however, compliance with the specifications (density superior to 93%TD, and less than 3 vol.% of open porosity) remains tricky. The porosity was not quantified with hydrostatic weighing-basedmethod. Notably, processes based on a reactive sintering, i.e., the direct sintering of a UO_2-AmO_2 powder mixture (and thus solid solution synthesis and sintering during the same thermal treatment) proved to be limited in terms of density [7]. For instance, the average density of these fuels was below 92%TD for this process, and thus generated an undesired amount of open porosity (> 3 vol.%). A new process called UMACS (for uranium-minor actinide conventional sintering) was thus developed in the framework of the R&D on dense fuel fabrication for DIAMINO. In the latter, the solid solution formation and the densification are dissociated by the use of two different thermal treatments [8]. By this means, pellets with densities up to 95%TD could be fabricated for the DIAMINO program, using the same UO_2 and AmO_2 precursor powders as for MARIOS, as well as the same sintering thermal cycle.

This difference in results between these two processes highlights the need for data and understanding of the progression of sintering of uranium-americium mixed oxides. Dilatometric analyses were performed at the CEA Marcoule Atalante facility to acquire such data and identify the mechanisms and the associated temperatures of interest. Several parameters, such as the type of sintering (conventional or reactive) or the composition (i.e., the americium amount) were studied.
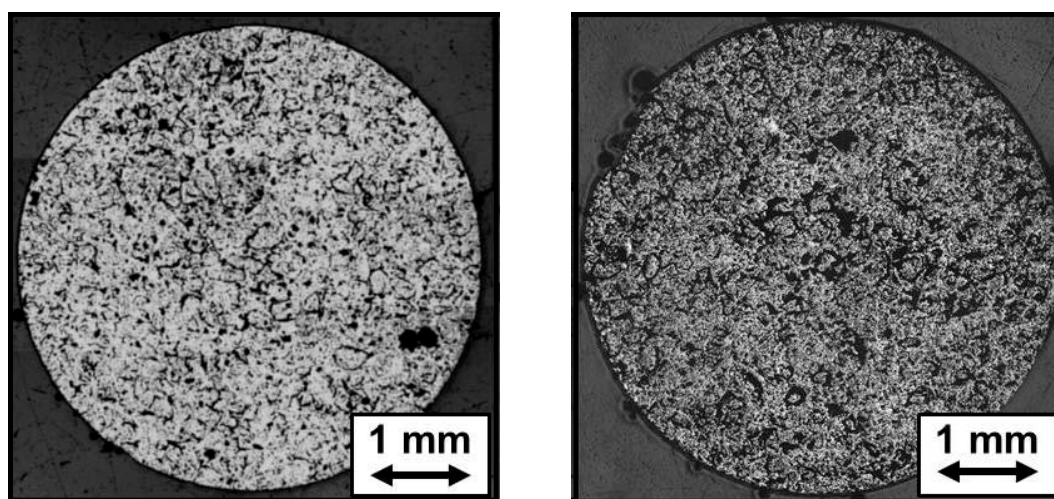
FIG. 1. Optical microscope observations of polished surfaces of porous $U_{0.85}Am_{0.15}O_{2\pm\delta}$ MABB fuels fabricated at the CEA Marcoule Atalante facility for the (left) MARIOS [7] and (right) DIAMINO [8] experimental irradiations. The dark spots in the left upper corner of picture 8 (right) are gas bubbles formed during the coating of the disc before grinding. The missing interface is the consequence of the cutting step: this disc was damaged during the cutting and thus not selected for irradiation but kept for characterization

2. Experimental

2.1. Precursor powders

Two initial powders were used in this study: depleted UO_2 (0.4 wt.% of [235]U) and [241]AmO_2 (including less than 2 wt.% of [243]Am). Their respective properties are given in TABLE 1. These powders present similar morphologies, i.e., agglomerates of submicronic particles. Their main difference is the particle size: for UO_2, 50 vol.% of the particles are under 1 μm and 95 vol.% under 10 μm, whereas for AmO_2, only 50 vol.% of the particles are under 10 μm, and even 10 vol.% of the particles are larger than 50 μm. Thus, though the UO_2 powder can be used as-is for pelletizing, the addition of AmO_2 requires the use of a milling step[1]. The other

---

[1] These are the characteristics of the starting powders before any grinding steps. These thus mainly depend on the supplier and were not chosen

difference between these powders is the impurity level. The UO_2 powder is quite pure and only presents a small thorium impurity, whereas the AmO2 powder include larger and significant amount of impurities due to the synthesis process (Ce, Nd, Fe…) and α-decay of ^{241}Am (^{237}Np). These two powders were used for the preparation of several precursor powders for the fabrication of pellets and their study by dilatometry. The imputity measurements were performed after dissolution of powders, which precludes any information on the localization of the porosity to be obtained.

TABLE 1. Properties of the starting single uranium and americium oxide powders.

		$UO_{2+\delta}$		$AmO_{2-\delta}$
Isotopic composition and impurities	^{234}U	0.0011 (6) wt.%	^{241}Am	98.34 (1) wt.%[*]
	^{235}U	0.258 (1) wt.%	^{243}Am	1.25 (1) wt.%[*]
	^{238}U	99.742 (2) wt.%	^{237}Np	0.40 (1) wt.%[†]
			Ce	1.7 (5) wt.%[‡]
			Na	0.6 (2) wt.%[‡]
			Nd	0.5 (1) wt.%[‡]
			Fe	0.4 (1) wt.%[‡]
O/M ratio		2.06 (1)		< 2.00
Granulometric factors	d_{10}	9.8 (5) µm		1.8 (1) µm
	d_{50}	27 (1) µm		9.7 (5) µm
	d_{90}	46 (2) µm		51 (3) µm

[*] Obtained by TIMS (thermal ionization mass spectrometry).

[†] Calculated based on ^{241}Am half-life.

[‡] Obtained by ICP/AES (inductively coupled plasma-atomic emission spectroscopy).

The first precursor powder is a $UO_{2+\delta}/AmO_{2-\delta}$ powder mixture that will be used for reactive sintering. It contains 15 wt.% of $AmO_{2-\delta}$, hence an expected Am/(U+Am) ratio close to 0.15. The mixture was prepared by a two-milling-step process. First a 30 wt.% AmO_2 mixture was prepared and milled. The milling steps were performed in stainless steel jars using a Retsch oscillatory ball-miller, in which stainless steel 12-mm diameter balls were used.

The other powders are single $U_{1-x}Am_xO_{2\pm\delta}$ oxide powders prepared according to the UMACS (uranium-minor actinide conventional sintering) process. This study concerns three compositions, x = 0.15, 0.30 and 0.40. These powders were prepared by heat treatment of UO_2/AmO_2 pellets for 4 h at 2023 K under an Ar-H_2(2 %)-O_2(50 ppm) atmosphere, followed by a milling step ensuring that a powder suitable for pelletizing is obtained. For each powder, XRD analyses confirm the presence of a solid solution after the heat treatment. The final Am/(U+Am) ratios were measured by TIMS and found to be 14.8(5), 32(1) and 39(1) wt.%, respectively.

2.2. Dilatometric measurements

The green pellets for the dilatometric measurements were prepared in hot cells by telemanipulation. The pelletizing was performed in uniaxial mode using a three-part die allowing homogeneous distribution of stresses in the samples. A standard pressure of around 450 MPa was applied. The dimensions and weights of the pellets (before and after dilatometric measurements) are given in Section 3. Before and after measurements, the samples were weighed and measured to calculate their geometrical density. Heights were measured using a vertical comparator, whereas diameter

measurements were performed every 16 µm along the pellets using a laser profilometer. After these measurements, the samples were transferred to the glovebox where the dilatometer is located. This procedure avoids manipulation of americium-bearing powders in gloveboxes because of their lower radiation protection compared to hot cells.

For this study, a horizontal *Netschz DIL 402 C* dilatometer fully integrated in a glovebox dedicated to work with americium was used (FIG. 2). The sample chamber is graphite, except for all parts in contact with the samples, which are made of tungsten in order to avoid interactions with the oxide materials tested. The temperature is controlled using two C-type thermocouples (W-5%Re/W-26%Re) which allow both a precise sample temperature measurement (sample thermocouple) and accurate and constant heating and cooling rates (furnace thermocouple). All measurements were performed during a constant heating rate mode at 3 K.min^{-1} under an atmosphere of flowing Ar-H$_2$ (4%). For each pellet, its relative linear shrinkage dL/L_0 (L_0 being the initial sample length, and dL: L_T–L_0), relative density, and shrinkage rate $d(dL/L_0)/dT$ are presented as functions of temperature in Section 3. After sintering, the sample densities are measured following the same procedure as for green pellets.

FIG. 2. Horizontal dilatometer integrated in glovebox at the CEA Marcoule Atalante facility.

3. Results

3.1. *Reactive sintering of U$_{0.85}$Am$_{0.15}$O$_{2\pm\delta}$*

The dilatometric curves corresponding to the reactive sintering are presented in FIG. 3. During this experiment, the pellet density increases from 57(1)%TD to 85(5)%TD. The shrinkage begins around 1000 K and reaches a first maximum around 1200 K. Then, the shrinkage rate decreases up to 1350 K, temperature at which it reaccelerates to reach another maximum around 1700 K. After a new shrinkage rate decrease, a last acceleration is noted for temperatures superior to 1850 K. In this experiment, the end of the sintering was not reached, as the temperature was limited to 1940 K. This is partially responsible for the low density measured after sintering.
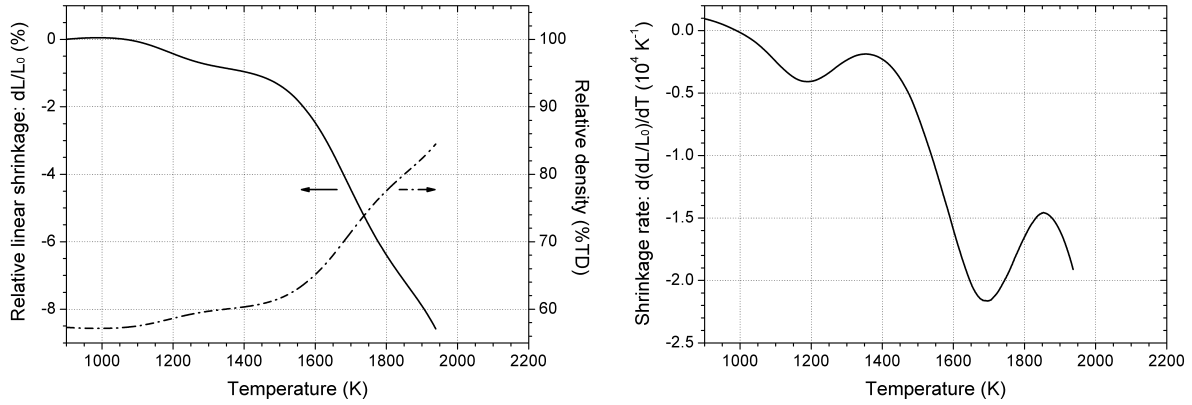
FIG. 3. Evolution of (left) linear shrinkage and relative density and (right) shrinkage rate of $U_{0.85}Am_{0.15}O_{2\pm\delta}$ reactive sintering as functions of temperature.

3.2. Conventional sintering of $U_{0.85}Am_{0.15}O_{2\pm\delta}$

Results concerning the study of conventional sintering of the 15% Am compound are presented in FIG. 4. In this case, the starting density was equal to 70(1)%TD, and rose to 95(1)%TD after sintering. In this case, a simpler curve is obtained. Shrinkage begins around 1200 K and then progressively increases. The maximum is found between 2000 and 2100 K. Above 2100 K, the shrinkage rate quickly decreases, indicating the end of the sintering, which is consistent with the high final density obtained.
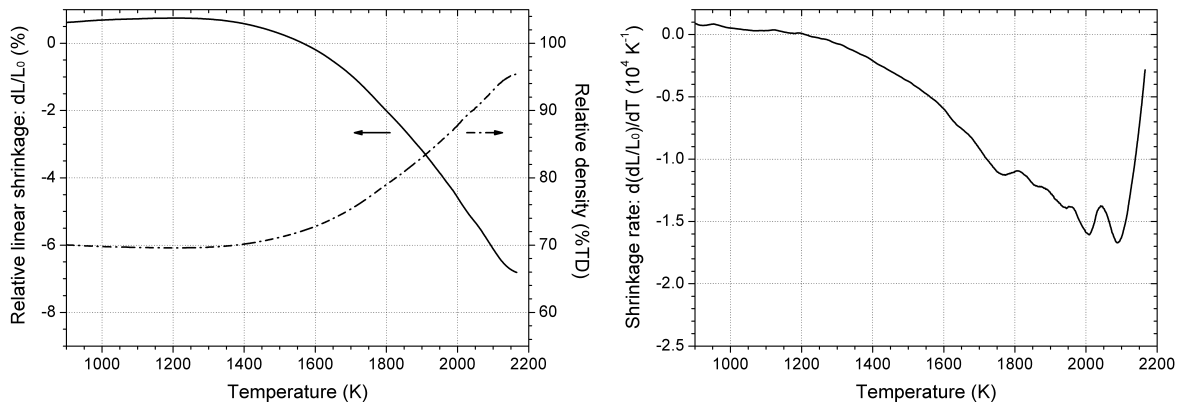
FIG. 4. Evolution of (left) linear shrinkage and relative density and (right) shrinkage rate of $U_{0.85}Am_{0.15}O_{2\pm\delta}$ conventional sintering as functions of temperature.

3.3. Conventional sintering of $U_{0.70}Am_{0.30}O_{2\pm\delta}$

The results corresponding to the conventional sintering of $U_{0.70}Am_{0.30}O_{2\pm\delta}$ are presented in FIG.5 (measurements were not of good quality above 2070 K, hence the dotted line for the shrinkage and no derivative values). Green and sintered densities of the pellets were of 69(1)%TD and 92(1)%TD, respectively. In this case, the sintering begins around 1000 K, with an optimal temperature around 1750 K. The shrinkage rate then decreases but remains significant, as the densification is not over.

Since the final density is close to that obtained after 4 h at 2023 K (around 93(1)%TD), the densification can be considered complete after the cycle.
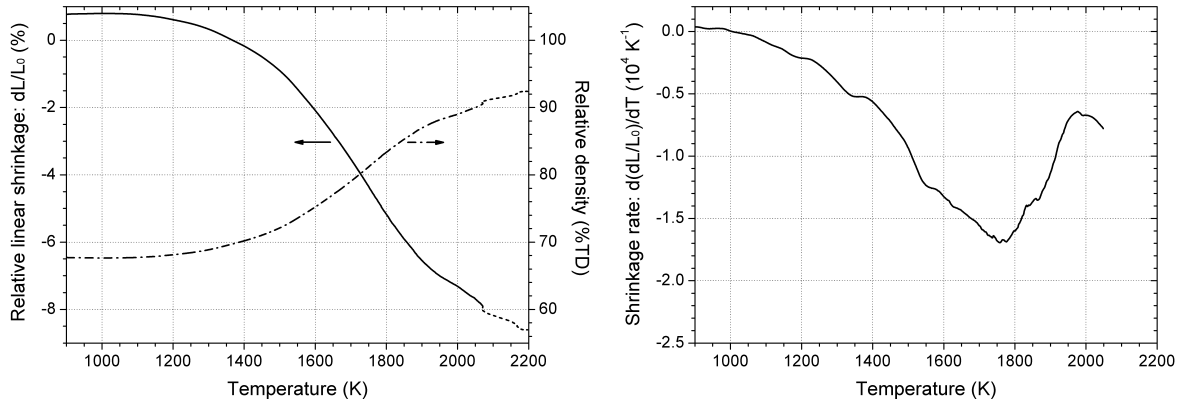
FIG. 5. Evolution of (left) linear shrinkage and relative density and (right) shrinkage rate of $U_{0.70}Am_{0.30}O_{2\pm\delta}$ conventional sintering as functions of temperature.

3.4. *Conventional sintering of $U_{0.60}Am_{0.40}O_{2\pm\delta}$*

The results corresponding to the conventional sintering of $U_{0.60}Am_{0.40}O_{2\pm\delta}$ are presented in FIG. 6. Like for the previous sample, the measurements cannot be fully trusted above 1900 K due to ageing of the thermocouple. Green and sintered densities of the pellets were respectively 70(1)%TD and 89(1)%TD. The sintering begins around 1250 K, and the shrinkage rate progressively increases up to 1650 K, where it seems to stabilize. Then, it decreases until 1850 K. The relatively high uncertainty on measurement data at such a temperature (considering the ageing of the sample thermocouple) has to be taken into account, however, for these preliminary results. Considering the latter point, an optimal temperature of sintering is likely to be found between 1650 and 1800 K.
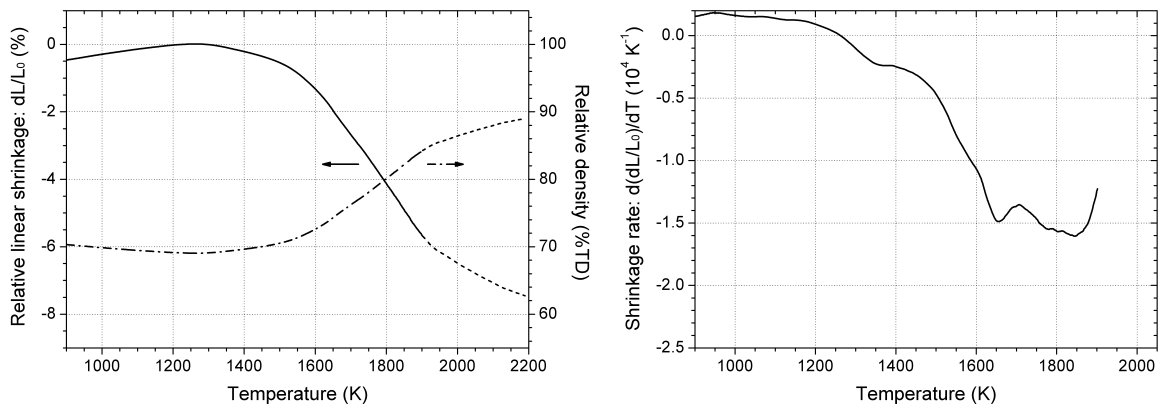
FIG. 6. Evolution of (left) linear shrinkage and relative density and (right) shrinkage rate of $U_{0.60}Am_{0.40}O_{2\pm\delta}$ conventional sintering as functions of temperature.

4. Discussion

4.1. *Description of the conventional sintering*

In FIG. 4, showing the conventional sintering of a $U_{0.85}Am_{0.15}O_2$ solid solution, the shrinkage rate progressively increases between the beginning of shrinkage and the temperature of maximum

shrinkage rate. At this point, the pellet is already quite dense (around 94%TD), which causes the shrinkage rate to quickly drop off. In comparison with a UO_2 sample prepared from the same UO_2 batch as that used for the mixed-oxide samples, the densification begins around 1000 K, i.e., 200 K lower than the mixed-oxide sample. This is presumably caused by the charge distribution in uranium-americium mixed oxides: as described by Prieur *et al*. for this system [9,10], americium has a (+III) valence, while that of uranium is a mixed (+IV/+V). This increases the iono-covalent nature of bonds, which consequently decreases the cation mobility causing the shrinkage delay [11]. Moreover, during the solid solution powder synthesis, the latter underwent a high temperature heat-treatment causing sintering to occur, even if this is not the purpose of this heat treatment. Thus, the powder obtained is supposed to be less reactive than a typical powder obtained by a wet chemical route, which may partially explain the high sintering-onset temperature for UMACS. The progressive increase of the shrinkage rate that follows is typical of a conventional sintering and coherent for a monophasic powder.

4.2. *Description of the reactive sintering*

In the case of the reactive sintering, a more peculiar behaviour is observed, presenting three steps of shrinkage rate increase. The first one, between 1000 K and 1200 K, can be associated with the sintering of UO_2 particles together, as it is similar to that observed in UO_2 and other uranium-based mixed-oxide reactive sintering, such as that of UO_2-CeO_2 [12] or UO_2-Gd_2O_3 [13,14]. During this phase, only the UO_2 grains can sinter together, as the uranium-americium interdiffusion has not yet started. The AmO_2 particles might also sinter to themselves, but their low amount and homogeneous distribution in the powder mixture render this sintering inefficient at pellet scale. Their presence even have a blocking effect on the pellet shrinkage, as it lowers the interaction surface between UO_2 grains and thus prevents their sintering, which explains why the shrinkage slows down between 1200 and 1350 K. Starting at 1350 K, the uranium-americium interdiffusion is activated, which allows the densification to re-accelerate, and the solid solution to start forming. At this stage, the chemical heterogeneity (presence of UO_2 and AmO_2 grains) generates large chemical potentials which might become one of the driving forces for the sintering, causing a large increase of the shrinkage rate until 1650 K. As uranium and americium interdiffuse, the pellet composition homogenizes, and thus the chemical potentials progressively decrease. This may explain the decrease of shrinkage rate observed between 1700 and 1850 K. Above 1850 K, the solid solution formation is supposed to be well-advanced, and the shrinkage now resembles that of a standard sintering. The shrinkage rate thus begins to increase again above 1850 K.

Due to the use of a reducing $Ar/H_2(4\%)$ atmosphere, higher order oxides cannot form during the sintering.

4.3. *Influence of the sintering type*

Before comparing the results presented in Sections 3.1 and 3.2, it is worth noting that the samples have different green densities, which is caused by a particularity of UMACS, which produces highly dense green pellets, typically close to 70%TD, whereas the pellets pressed using the reactive-sintering rocess barely reach 60%TD. This difference generates a lower linear shrinkage for the UMACS pellet, but is not supposed to affect the evolution of the shrinkage rate. A qualitative comparison between the shrinkage rates of the UMACS and the reactive-sintering pellets can thus be performed. The main discrepancy between the two processes is the density obtained after the heat treatment, which is 10%TD lower for the reactive-sintering pellet. As previously stated, this is partially due to the lower temperature reached for the experiment, but results obtained after 4 h at 2023 K in both cases show a difference of around 5%TD (between pellets obtained using the same precursors powders) [7,8]. The obtained microstructures are also different, as presented in FIG. 7, and notably show that the porosity is reduced for the UMACS process, and presents a more homogeneous distribution both in size and within the pellet. This difference can be explained using the dilatometric measurements.
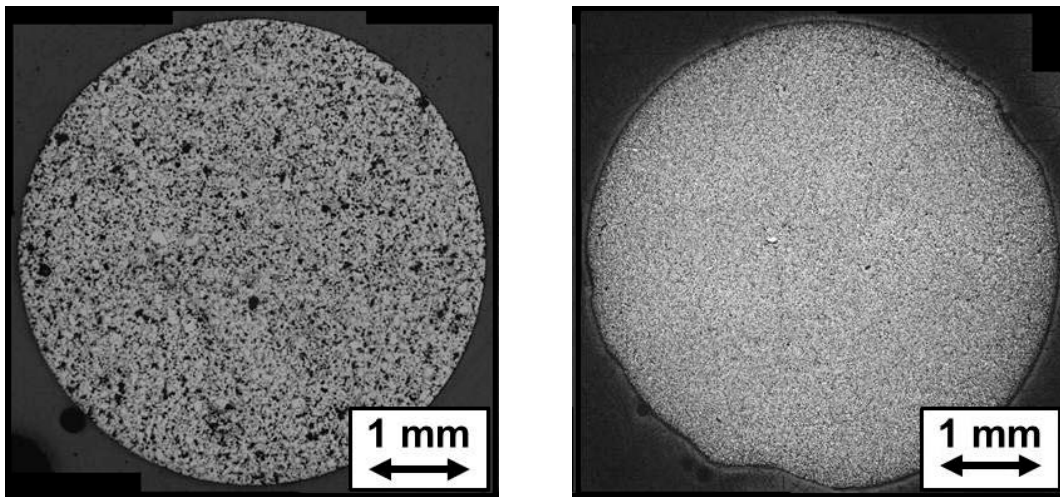
FIG. 7. Optical microscope observations of polished surfaces of $U_{0.85}Am_{0.15}O_{2\pm\delta}$ MABB fuels fabricated in the CEA Marcoule Atalante facility by (left) reactive sintering [7] and (right) the UMACS process [8].

As described before, in a reactive sintering, the solid solution formation modifies the progression of sintering and notably causes some shrinkage rate decreases. These phenomena can be detrimental to sintering, as during these steps the microstructure can be stabilized while a high density is not yet reached. This means that large porosity initially present in the samples can be stabilized during the earliest stage of sintering, decreasing the final density. Moreover, the occurrence of the Kirkendall effect [15], caused by the difference in self-diffusion coefficients between U and Am , is responsible for the generation of additional porosity during solid solution formation. This porosity, which is formed at interfaces between $UO_{2+\delta}$ and $AmO_{2-\delta}$ grains, is not easily resorbable, and will also slow down the sintering. The effect of the impurities contained in the $AmO_{2-\delta}$ powder (as shown in TABLE 1) on the sintering can also vary depending on the sintering type. Some of them, such as Na, are easily removed from the pellet during a thermal treatment. Therefore, such impurities can have an influence on a reactive sintering, as the powder is used "as-is", but not on a UMACS sintering, because the powder mixture underwent a thermal treatment before the heat treatment for sintering. Another distinction is the long milling step in contact with stainless steel used for UMACS, which can slightly increase the Fe impurity content, as was observed during the fabrication of the DIAMINO samples [8]. It can thus be concluded that the effect of impurities on the sintering differs depending on the process.

Above 1850 K for the reactive sintering, an increase of the shrinkage rate is noted, but the measurements stopped before a maximum rate was reached. As the solid solution formation is well advanced at this stage, it would thus not be surprising that similar behaviours would occur for the reactive and the conventional sintering. As a first approach, an optimal temperature close to that obtained for the conventional sintering, i.e. between 2000 and 2100 K, can be considered.

4.4. Influence of americium content

Based on the comparison between UO_2 and $U_{0.85}Am_{0.15}O_{2\pm\delta}$ conventional sinterings that shows that the presence of americium in the solid solution delays the sintering, a similar behaviour would be expected for the 30 and 40% Am compounds: a high temperature for the onset of shrinkage followed by a constant increase of the shrinkage rate up to a maximum temperature above 2000 K. The results presented in Section 3.3 for the $U_{0.70}Am_{0.30}O_{2\pm\delta}$ sintering, however, show that the latter begins around 1000 K and that the shrinkage rate reaches a maximum at around 1750 K. For the 40% Am sample presented in Section 3.4, the sintering is closer to that of the 15% Am sample. The shrinkage begins at a higher temperature, around 1250 K, and, due to ageing of the thermocouple, the measurements at higher temperatures present a large uncertainty. By considering only the evolution of the temperature at which the sintering begins with americium content, a behaviour change in $U_{1-x}Am_xO_{2\pm\delta}$ sintering between x = 0.15 and x > 0.3 appears. Based on a single dilatometric curve for each composition, only

assumptions can explain this behaviour change. More particularly, the influence of the charge distribution in these mixed oxides (i.e., the reduction of americium and the partial oxidation of uranium), which was only studied up to x = 0.2 [9], could provoke such a behaviour. Further studies on this subject might help interpret the results obtained.

The final densities obtained suggest a decrease of sintering efficiency with the americium content, as this was already observed for lower americium content in both conventional (x = 0.075 and 0.15) [8] and reactive sinterings (x = 0.10, 0.15 and 0.20) [16]. Other pellets were also fabricated in a high temperature furnace to confirm this evolution. For these fabrications, the standard conditions were used, i.e., sintering for 4 h at 2023 K, with heating and cooling rates of 3 K.min^{-1}, under a flowing Ar-H$_2$ (4%) atmosphere. The results obtained are summarized in FIG. 8, with other results obtained in the same conditions with the UMACS process. Based on this data, the decrease of density with americium content is clearly visible, but its cause remains unclear. It can be supposed that the increase of americiun content in the structure renders it more complex in terms of charge distribution, which might result in a decrease of cation mobility. Impurities initially contained in the AmO$_{2-\delta}$ powder presumably participate in this density decrease, as their final amount increases with that of americium.
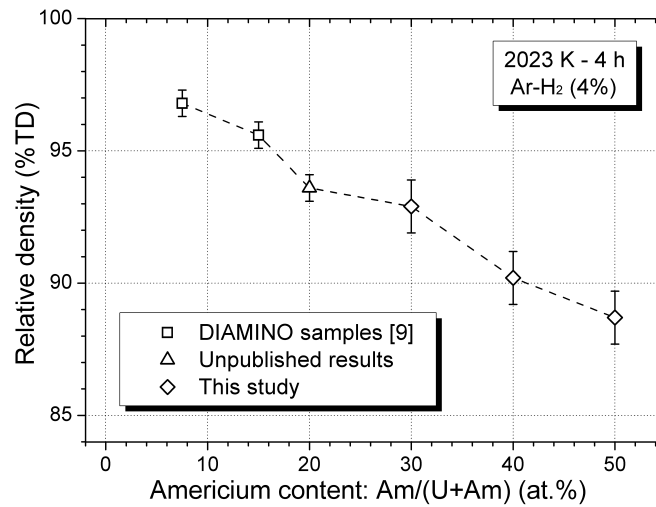
FIG. 8. Relative densities obtained for U$_{1-x}$Am$_x$O$_{2\pm\delta}$ fuels as a function of americium content (all fuels were fabricated with the UMACS process under similar conditions).

5. Conclusion

This work was dedicated to the study of sintering behaviour of U$_{1-x}$Am$_x$O$_{2\pm\delta}$ MABB fuels transmutation using dilatometry. Several compounds prepared from different precursors were studied by dilatometry to identify and understand the processes occurring during sintering. First, a comparison was made between reactive and conventional sintering in the case of U$_{0.85}$Am$_{0.15}$O$_{2\pm\delta}$. The results show that the shrinkage is, in the case of a reactive sintering, prevented and delayed by the solid solution formation occurring at the same time. This explains why a conventional sintering should be preferred for the fabrication of uranium-americium mixed oxides. The second parameter of interest was the americium content, the variable in the study of U$_{0.70}$Am$_{0.30}$O$_{2\pm\delta}$ and U$_{0.60}$Am$_{0.40}$O$_{2\pm\delta}$ conventional sintering. The results obtained suggest a change of behaviour between x = 0.15 and x > 0.30, but additional data on these compositions are required to explore this assumption.

REFERENCES

[1] SALVATORES, M., Nuclear fuel cycle strategies including Partitioning and Transmutation, Nuc. Eng. Des. **235** 7 (2005) 805-816.

[2] WARIN, D., Status of the French Research Program on Partitioning and Transmutation, J. Nucl. Sci. Techol. **44** 3 (200) 410-414.

[3] JORION, F., DELAHAYE, T., HUSSON, A., PICART, S., LEBRETON, F., REMY, E., HORLAIT, D., Research and Development for the Fabrication of Minor Actinide-Bearing Fuel Materials and Technologies, FR-13 Proceedings, IAEA, Paris, France (2012)

[4] GROUILLER, J-P., PILLON, S, DE SAINT JEAN, C., VARAINE, F., LEYVAL, L., VAMBENEPE, G., CARLIER, B., Minor actinides transmutation scenario studies with PWRs, FRs and moderated targets, J. Nucl. Mater. **320** 1-2 (2003) 163-169.

[5] D'AGATA, E, HANIA, P.R., BEJAOUI, S., SCIOLLA, C., WYATT, T., HANNINK, M.H.C., HERLET, N., JANKOWIAK, A., KLAASSEN, F.C., BONNEROT, J-M., MARIOS: Irradiation of UO_2 containing 15% americium at well defined temperature, Nucl. Eng. Des. **242** (2012) 413-419

[6] WALKER, C.T., NICOLAOU, G., Transmutation of neptunium and americium in a fast neutron flux: EPMA results and KORIGEN predictions for the superfact fuels, J. Nucl. Mater. **218** 2 (1995) 129-138.

[7] PRIEUR, D, JANKOWIAK, A., DELAHAYE, T., HERLET, N., DEHAUDT, P. BLANCHART, P., Fabrication and characterisation of $U_{0.85}Am_{0.15}O_{2-x}$ discs for MARIOS irradiation program, J. Nucl. Mater. **414** 3 (2011) 503-507.

[8] DELAHAYE, T., LEBRETON, F., HORLAIT, D., HERLET, N., DEHAUDT, P., Application of the UMACS process to highly dense $U_{1-x}Am_xO_2$ MABB fuel fabrication for the DIAMINO irradiation, J. Nucl. Mater. **432** 1-3 (2013) 305-312.

[9] PRIEUR, D. MARTIN, P.M., JANKOWIAK, GAVILAN, E., SCHEINOST, A.C., HERLET, N., DEHAUDT, P., BLANCHART, P., Local structure and charge distribution in mixed uranium-americium oxides: effects of oxygen potential and Am content, Inorg. Chem. **50** 24 (2011) 12437-12445.

[10] PRIEUR, D., MARTIN, P., LEBRETON, F., DELAHAYE, T., BANERJEE, D., SCHEINOST, A.C., JANKOWIAK, A., Accomodation of multivalent cations in fluorite-type solid solutions: case of Am-bearing UO_2, J. Nucl. Mater. **434** 1-3 (2013) 7-16.

[11] BAKUNOV, V.S., LUKIN, E.S., Particularities of the technology for producing high-density technical ceramics. Activity of oxide powders during sintering, Glass. Ceram. **65** 11-12 (2008) 402-406.

[12] HORLAIT, D., FELEDZIAK, A., LEBRETON, F., CLAVIER, N., PRIEUR, D., DACHEUX, N., DELAHAYE, T., Dilatometric study of $U_{1-x}Am_xO_{2\pm\delta}$ and $U_{1-x}Ce_xO_{2\pm\delta}$ reactive sintering, J. Nucl. Mater. **441** 1-3 (2013) 40-46

[13] DURAZZO, M., OLIVEIRA, F.B.V., URANO DE CARVALHO, E.F., RIELLA, H.G., Phase studies in the UO_2-Gd_2O_3 system, J. Ncul. Mater. **400** 3 (2010) 183-185.

[14] DURAZZO, M., SALIBA-SILVA, A.M., URANO DE CARVALHO, E.F., RIELLA, H.G., Remarks on the sintering behavior of UO_2-Gd_2O_3 fuel, J. Ncul. Mater. **405** 2 (2010) 203-205.

[15] SMIGELKAS, A.D., KIRKENDALL, E.O., Zinc diffusion in alpha brass, Trans AIME 171 (1947) 130-142.

[16] PRIEUR, D., JANKOWIAK, A., ROUDIL, D., DUBOIS, S., LEORIER, C., HERLET, N., DEHAUDT, P., LAVAL, J-P., BLANCHART, P., Self-irradiation effects in dense and tailored porosity $U_{1-y}Am_yO_{2-x}$ (y = 0.10; 0.15) compounds, J. Nucl. Mater. **411** 1-3 (2011) 15-19.

[17] LEBRETON, F., PRIEUR, D., JANKOWIAK, A., TRIBET, M., LEORIER, C.,

DELAHAYE, T., DONNET, L., DEHAUDT, P., Fabrication and characterization of americium, neptunium and curium bearing MOX fuels obtained by powder metallurgy process, J. Nucl. Mater. **420** 1-3 (2012) 213-217.

Minor Actinides Burn up Enhancement in the European Sodium Fast Reactor through Moderator Material Addition

R. Ramos[a], L. Buiron[b]

[a] National Atomic Energy Commission (CNEA), Buenos Aires, Argentina

[b] CEA, DEN, DER, Cadarache, F-13108 Saint Paul lez Durance, France

Abstract. The minor actinides (MA) burn up optimization in the European Sodium Fast Reactor (ESFR) core was studied by adding different moderating materials in the Minor Actinides Bearing Blanket subassemblies (MABB SA) using the ERANOS neutron code package. These SA are of hexagonal shape and are composed of pellets inside of pins. These pellets contain a mixture of uranium dioxide (UO_2) and americium dioxide (AmO_2). If some of these pins are replaced by other identical ones containing moderating material instead of minor actinides, a shift in the spectrum towards lower energies is expected, which might enhance the burn up performance. The results of this work demonstrated that the use of compounds of hydrogen and magnesium as moderators produces a shift in the neutron spectrum, improving the percentage of minor actinide consumption. ZrH_2 moderator material was found to exhibit the best performances for this propose, followed by MgO and $MgAl_2O_4$, in that order. The use of SiC, BeO, TiC, LiO_2 and ZrC material produced no effect on the shift of the neutron spectrum in the present configuration. For safety reasons, it seems hardly realistic to use hydrogeneous compounds in sodium fast reactors. So, compounds with magnesium are selected to be placed into the pins to improve the percentage of minor actinide consumption. Also, the decay heat generated by ^{242}Cm, ^{244}Cm and ^{238}Pu and the total neutron flux in the reactor core were estimated.

(1) INTRODUCTION

Fast reactors have received considerable attention during the last years. The fact that these reactors operate with a fast neutron spectrum leads to the possibility of breeding fissile from fertile material. Furthermore, in a fast neutron field it is also possible to perform minor actinide transmutation. Certain transmutation reactions which are not favored in thermal spectrum reactors because they have a threshold cross section, are enhanced in fast reactors.

In the context of the Generation IV International Forum (GIF), Sustainability has been put forth as a primary goal. The Sodium Fast Reactor (SFR) is therefore one of the reactor concepts to which considerable interest has been devoted in regards to minor actinide transmutation. Furthermore, the vast experience achieved in this sort of reactor over the past five decades, makes the SFR one of the preferred choices in order to perform the task.

The work described here was performed in the framework of the Scientific and Technical Cooperation Agreement signed by the Comisión Nacional de Energía Atómica (CNEA) and the Commissariat à l'Énergie Atomique et aux Énergies Alternatives (CEA) on 23 July 2010.

The goal of this work is to study a particular SFR core with Minor Actinides Bearing Blankets (MABB). The performance of the core will be evaluated in regard to the initial mass of minor actinides loaded and the amount of mass consumed after a fixed period of time. In a simplified manner, the amount of mass of a given species of minor actinide can be described by the equation:

$$C(\Delta t) = m_{(t=0)}(1 - e^{-\phi\sigma\Delta t})$$

where C(Δt) is the amount of the minor actinide consumed at a time Δt after beginning of irradiation, m(t=0) is the initial mass loaded, Φ is the mean neutron flux and σ the mean effective absorption cross section. Since the effective absorption cross section is very sensitive to the neutron spectrum and the neutron flux is more or less determined by the fuel, within certain limits, one idea to enhance transmutation is to add small amounts of moderator materials that will increase the effective absorption cross section locally while leaving the neutron flux quite invariable. Zirconium hydride (ZrH$_2$) is used in this work as a reference moderator material. For safety reasons, the use of hydrogeneous material has to be avoided in sodium reactors. So, alternative moderating materials were studied: SiC, BeO, LiO$_2$, MgO, MgAl$_2$O$_4$, TiC and ZrC.

(2) MODEL DESCRIPTION

The core to be analyzed consists of five different kinds of subassemblies: fuel subassembly, minor actinides subassembly (MA), control and shutdown device subassembly (CSD), diverse shutdown device subassembly (DSD) and reflector subassembly.

The cell calculation was performed using the module ECCO of ERANOS 2.2 and the library JEFF 3.1. The core calculation was performed using the code ERANOS 2.2 [1][2].

In Figure 1, a schematic view of the core is given. Only one third part of the core is shown since the rest of it is symmetric [3].
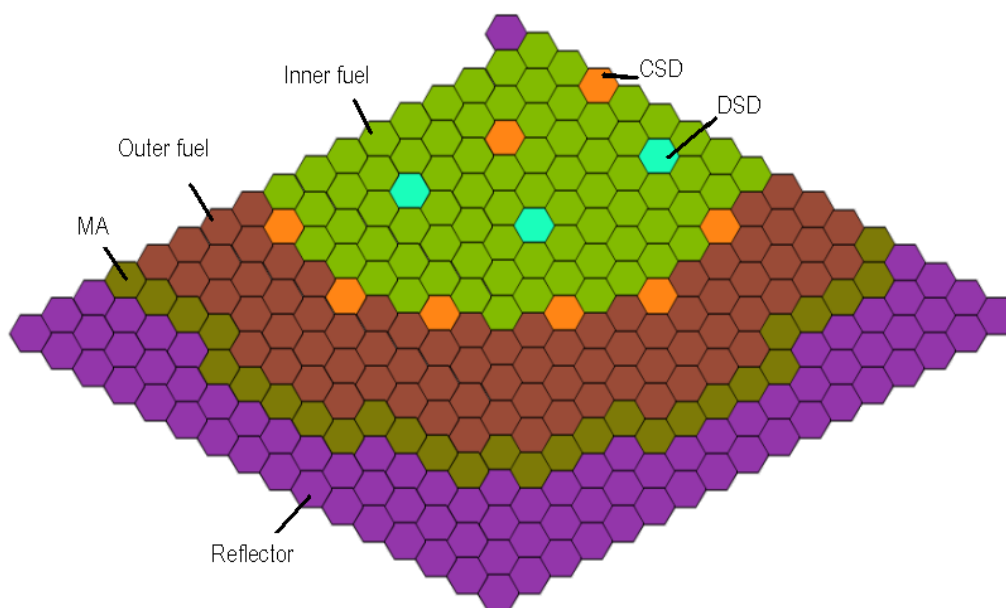
FIG. 1. Schematic view of the core.

The fuel subassembly consists of an hexagonal wrapper tube that contains a triangular arrangement of fuel pins with helical wire wrap spacers. The fuel pin consists of (U,Pu)O$_2$ pellets using Oxygen Strenghtened Steel (ODS) cladding.

There are two types of fuels, the inner and outer fuel. For both of them the specifications are those given in Table 1. They differ in the volume percent of plutonium dioxide in the mixture (U,Pu)O$_2$: INNER FUEL, 14.05 % of PuO$_2$ and OUTER FUEL, 16.35 % of PuO$_2$.

The MA subassembly consists of an hexagonal wrapper tube that contains a triangular arrangement of fuel pins with helical wire wrap spacer. In the MA subassembly, 61 pins contain pellets of moderating material (gray) and the other 210 pins contain pellets of MA (red), as shown in Figure 2.
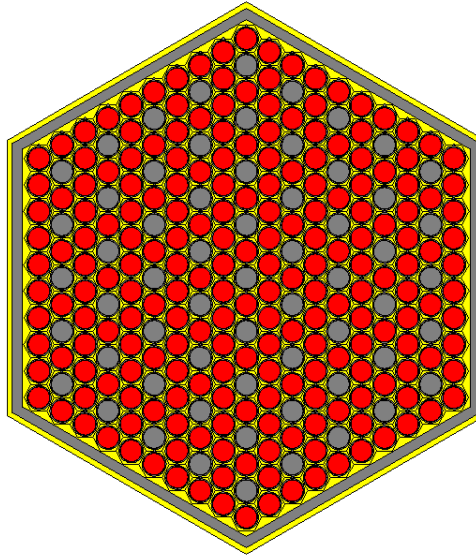
FIG. 2 Minor actinides subassembly.

The composition of minor actinides is 80% mass fraction of ^{241}Am and 20 % mass fraction of ^{243}Am. The AmO$_2$ content in the (U,Am)O$_2$ mixture is 10% volume fraction.

The CSD subassemblies contains B$_4$C like absorber, and the DSD subassemblies contain enriched boron; its isotopic composition is ^{10}B 90 % and ^{11}B 10%.

The core calculations were performed on the ground of a full three-dimensional geometrical description and the diffusion theory. The evolution with burn up was achieved in 6 calculation steps, with 5 time periods in between, of 410 effective full power (EFP) days each, and a power level of the whole core of 3600 MWth.

The mass balance was calculated in order to know the amount of minor actinides consumed after 2050 EFP days (total fuel residence time).

(3) RESULTS

With the pin configuration shown in Figure 2 (61 moderating pins in each minor actinide subassembly), the mass balance calculation was performed to find out how many kilograms of minor actinides (^{241}Am and ^{243}Am) were consumed during the period of the reactor operation. This calculation was performed using all the moderating materials. For this case, the initial masses were 909.97 kg of ^{241}Am and 227.49 kg of ^{243}Am. Table 1 shows the mass consumption of ^{241}Am, ^{243}Am, and the total mass of minor actinides consumed in percentage, calculated with the following formula:

$$Consumption\ of\ MA\ [\%] = 100\,x\,\frac{consumed\ mass(^{241}Am + ^{243}Am)}{initial\ mass(^{241}Am + ^{243}Am)}$$

Table 1.Consumption of minor actinides for each moderating material

Moderating materials	Consumption of ^{241}Am [Kg]	Consumption of ^{243}Am [Kg]	Consumption of MA [%]
SiC	220.57	46.97	23.52
BeO	220.95	47.18	23.57
LiO$_2$	219.94	46.83	23.45
MgO	230.07	49.25	24.56
MgAl$_2$O$_4$	228.27	48.83	24.36
ZrH$_2$	310.38	68.55	33.31
TiC	220.81	47.03	23.55
ZrC	220.77	47.02	23.54

Figure 3 shows the results of Table 1 in a bar graph.
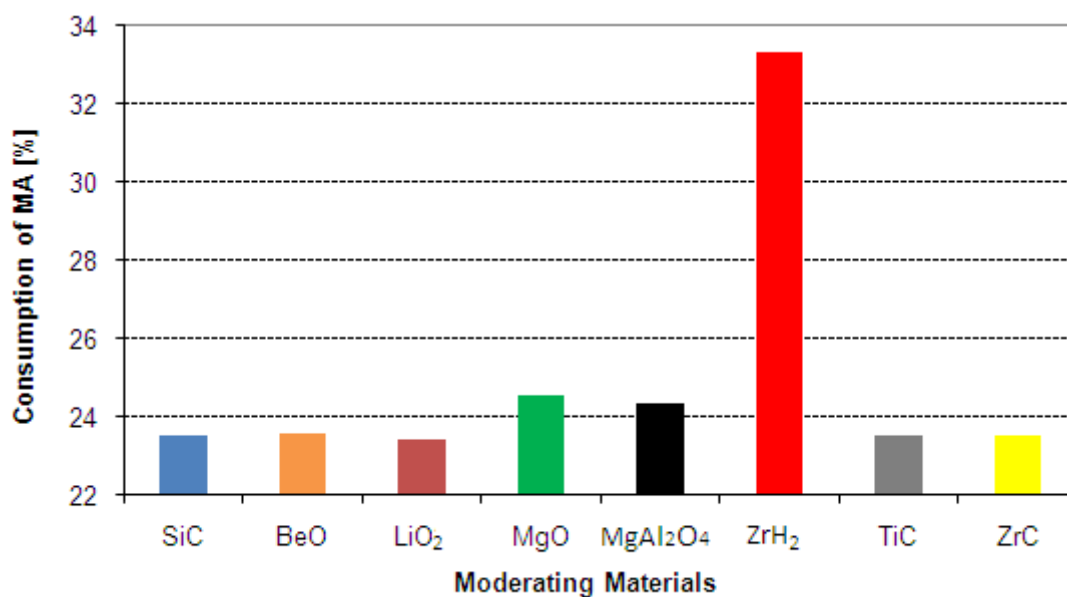
FIG. 3. Mass consumption of minor actinides in percentage for each moderating material.

This figure shows that the mass consumption of minor actinides reaches its maximum when ZrH$_2$ is used as moderating material. With other moderating materials the mass consumption is several percentage points lower than with ZrH$_2$. However, there is a difference between the compounds having magnesium (MgO and MgAl$_2$O$_4$) and the other ones (SiC, BeO, LiO$_2$, TiC and ZrC).

This led to the conclusion that ZrH$_2$ resulted the best moderator for this case, followed by MgO and MgAl$_2$O$_4$, in that order.

Not only is it necessary to study the consumption of actinides [241]Am and [243]Am, it would be also necessary to take into account the occurrence of [242]Cm, [244]Cm and [238]Pu. These isotopes will generate decay heat according to the following formula: $H(t) = h\ m(t) = h\ m_0 e^{-t\frac{\ln 2}{T_{1/2}}}$, where t is the time, $H(t)$ is the decay heat generated, $m(t)$ is the mass at time t, m_0 is the initial mass of the isotope after irradiation in the reactor, $T_{1/2}$ is the half life and h is the heat generate per mass unit. Taking into account the masses of [238]Pu, [242]Cm and [244]Cm, it is possible to calculate the decay heat contribution for the cases where MgO, $MgAl_2O_4$, SiC and ZrH_2 were used (see Figure 4).
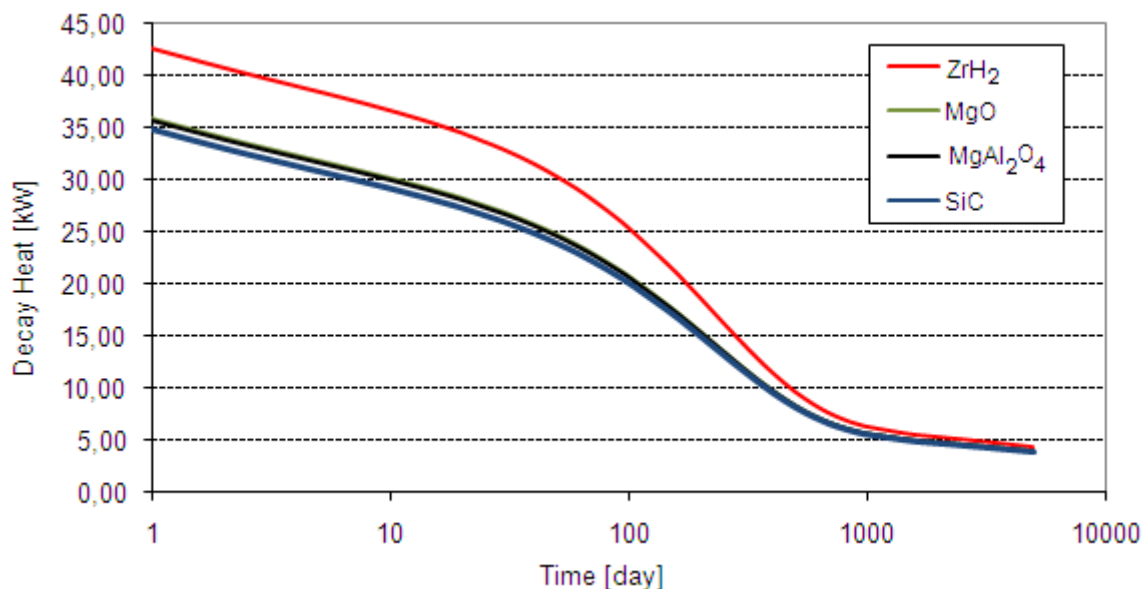
FIG. 4. Decay heat generated vs. time

It is observed that ZrH_2 presents a bigger decay heat due to the increased occurrence of Cm and Pu. However, the other compounds show a similar behavior.

Finally, to find out the impact of the moderating materials in all the reactor, the total neutron flux radial distribution at end of equilibrium cycle is shown as a function of the radial position at a height of 150 cm, at end of life (see Figure 5).
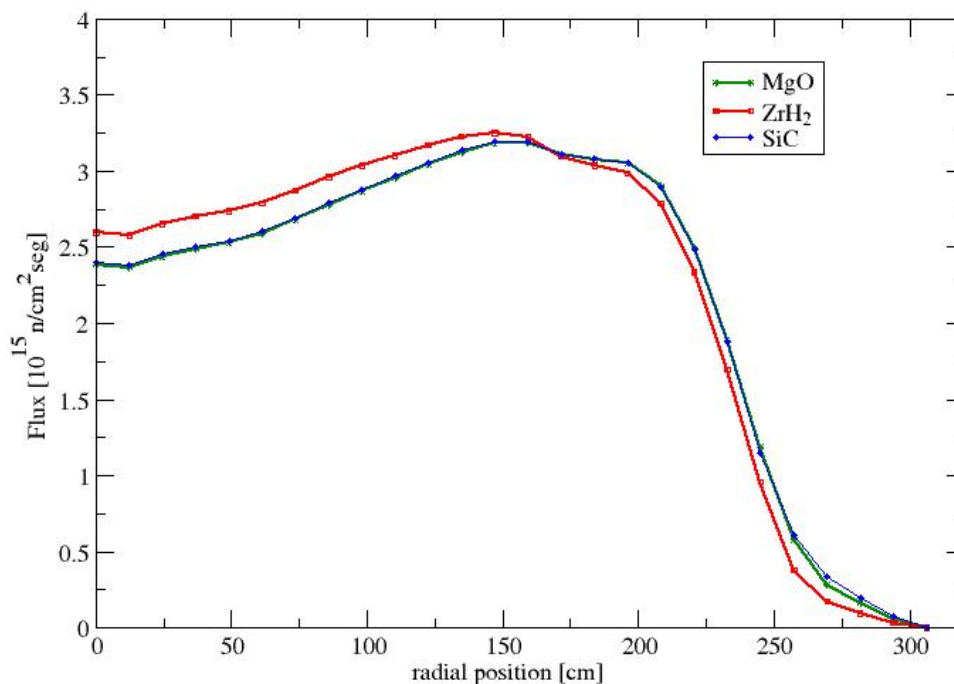
FIG. 5. Neutron flux in the reactor vs. radial position.

It is observed that the neutron flux in the inner part of the core with ZrH_2 is bigger than the neutron flux with SiC and MgO. In the outer part of the core occurs the opposite effect. The neutron flux distribution with MgO and SiC are practically the same. The maximum value of the neutron flux occurs in the inner fuel and is 3.25×10^{15} n/cm^{2}sec for ZrH_2, 3.19×10^{15} n/cm^{2}sec for MgO and 3.19×10^{15} n/cm^{2}sec for SiC.

The neutron flux in the case of $MgAl_2O_4$ (not shown in the figure) overlaps with the neutron flux of MgO.

The variation of the percentage of minor actinide consumption versus the number of moderator pins was studied. For this purpose, two configurations with 91 and 135 moderator pins were selected.

The mass balance calculation was performed for the cases with ZrH_2, SiC, MgO and $MgAl_2O_4$ as moderating materials.

Figure 6 shows the percentage of minor actinides consumed versus the number of moderator pins for ZrH_2, SiC, MgO and $MgAl_2O_4$.
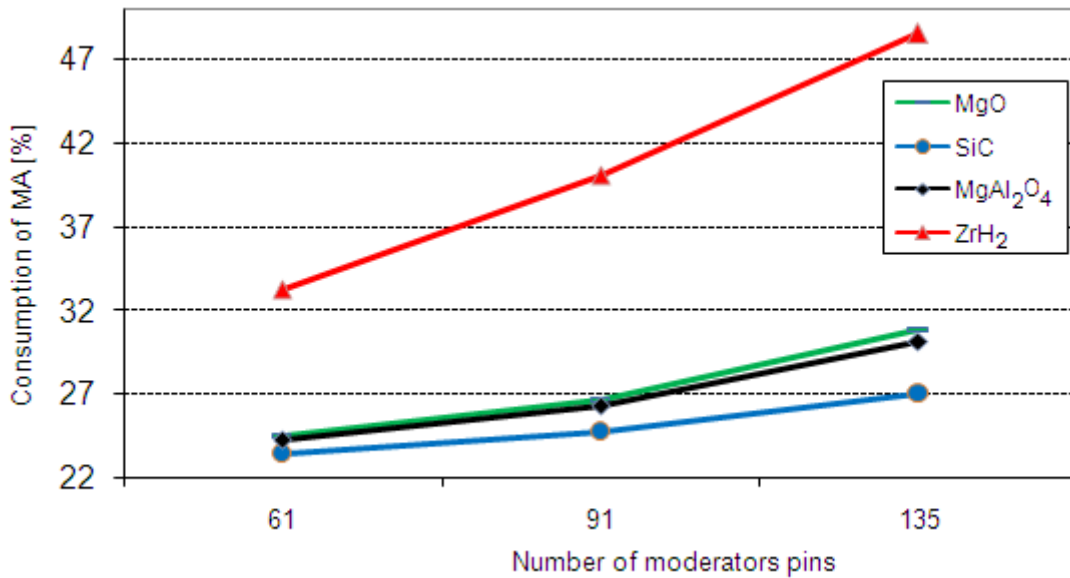
FIG. 6. Percentage of minor actinides consumed versus the number of moderator pins for ZrH_2, SiC, MgO and $MgAl_2O_4$.

This figure shows that when the number of moderator pins is increased, the percentage of minor actinides consumed increases. When the total mass of minor actinides is considered, it is observed that when the number of moderator pins is increased, the total mass of minor actinides consumed decreases. For example, in the case of MgO, with 61 pins of moderator, the consumed mass of minor actinides was 279.36 kg (of a total of 1137.46 kg), and with 135 pins, the consumed mass was 227.22 kg (of a total of 736.65 kg). In this case, the total mass consumed of MA decreased because the initial mass of MA decreased.

The decay heat generated with MgO as moderator was studied for the cases with 61, 91 and 135 moderator pins (see Figure 7)
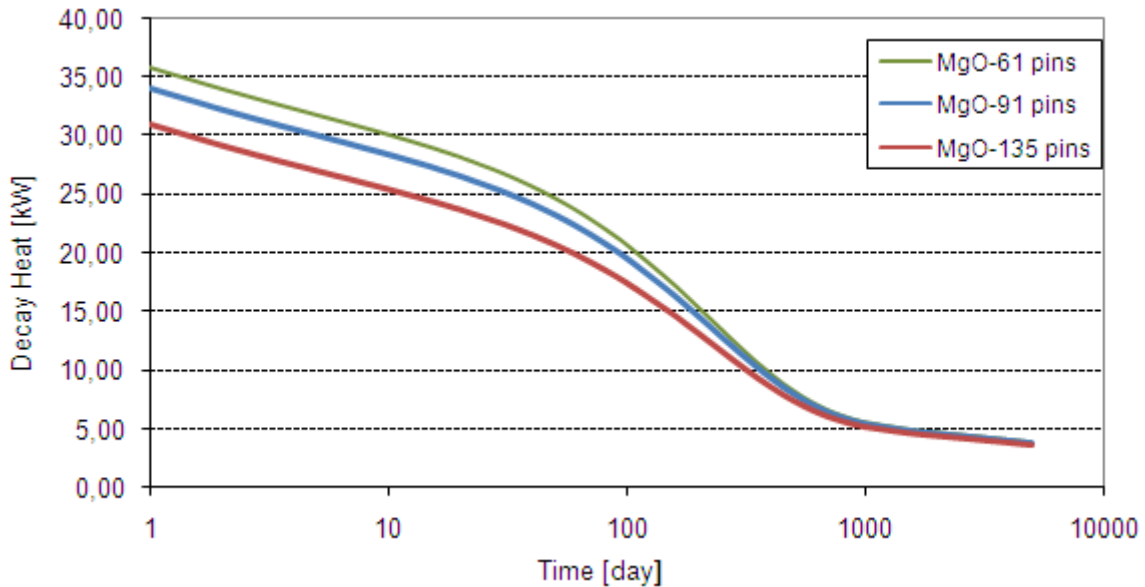
FIG. 7. Heat decay vs. number of pins for MgO.

In this figure, it is observed that when the number of moderator pins is increased, the decay heat decreases because the occurrence of Cm and Pu decreases (the initial mass of MA and UO_2 decreases).

Figure 8 shows the changes in the neutron flux as a function of the radial position at a height of 150 cm for the case of MgO with 61, 91 and 135 moderator pins.
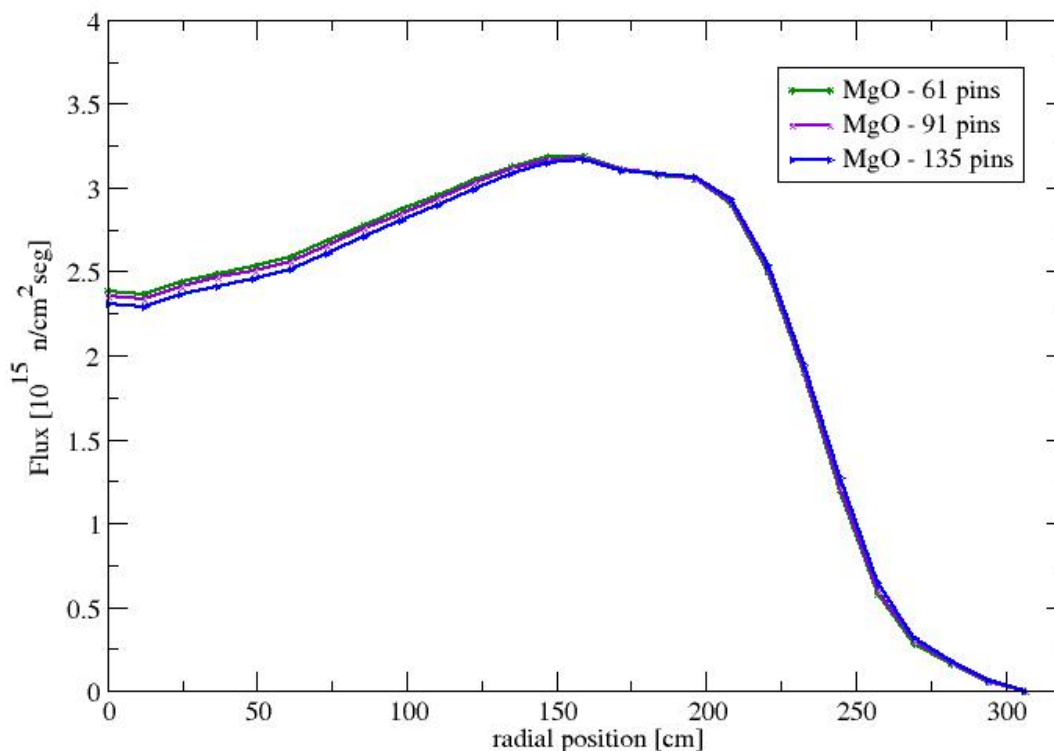
FIG. 8. Neutron flux vs. Radial position for MgO

It is observed that when the number of pins increased, the neutron flux decreased in the inner part of the reactor (r<150 cm). In the outer part of the reactor the neutron flux was the same for the three cases.

It was concluded that when the number of moderator pins is increased, the percentage of minor actinides consumed increases, the total mass consumed of minor actinides decreases, the decay heat generated decreases and the neutron flux in the reactor varies very little.

Finally, Table 2 shows the mass consumption of minor actinides for the following cases: without moderator pins (271 pins with MA), 61 moderator pins with MgO (210 pins with MA), 91 moderator pins with MgO (180 pins with MA) and 135 moderator pins with MgO (136 pins with MA).

Table 2. MA consumption as a function of moderator pins with MgO

Moderating Material	Initial mass of MA [Kg]	Consumed mass of MA [Kg]	Consumption of MA [%]
Without moderator pins	1467.87	312.13	21.26
61 pins with MgO	1137.46	279.32	24.56
91 pins with MgO	974.94	260.40	26.71
135 pins	736.65	227.22	30.85

(4) CONCLUSIONS

The results of this work demonstrated that the use of moderating compounds with hydrogen and magnesium produce a shift in the neutron spectrum, improving the percentage of minor actinide consumption.

ZrH_2 was found to be the best moderator, followed by MgO and $MgAl_2O_4$, in that order. SiC, BeO, TiC, LiO_2 and ZrC produced no significant effect on the shift of the neutron spectrum.

For safety reasons, it seems hardly realsitic to use hydrogeneous material in sodium fast reactors. So, compounds with magnesium should be selected to be placed into the pins to improve the percentage of minor actinide consumption.

It was demonstrated that when some pins with pellets of minor actinides were replaced by pins with MgO as moderating material, the percentage of minor actinides consumed increased, but the total mass of minor actinides consumed decreased. In the case where all pins contain minor actinides, the minor actinide percentage consumption was 21.26%, i.e., 312.13 kg of minor actinides were consumed from a total of 1467.87 kg in the initial configuration. In the case with 135 pins of MgO the minor actinide percentage consumption was 30.85%, i.e., 227.22 kg of minor actinides were consumed from a total of 736.65 kg in the initial configuration.

Also, the decay heat generated by the occurrence of the other minor actinides like ^{242}Cm, ^{244}Cm and ^{238}Pu was studied. It was observed that when the number of the moderator pins increased, the decay heat generated decreased due to the decrease in the occurrence of Cm and Pu.

To find out the impact of the moderating materials in all the reactor, the total neutron flux was calculated as a function of the radial position at a height of 150 cm. It was observed that when the number of moderator pins was increased, the neutron flux in the reactor varied very little.

It was concluded that when the number of moderator pins with MgO or $MgAl_2O_4$ is increased, the percentage of minor actinides consumed increases, the total mass consumed of minor actinides decreases, the decay heat generated decreases also and the neutron flux in the reactor varies very little.

For future studies it would be possible to evaluate the use of other materials with resonances in the scattering cross section in the fast range that would improve results with Mg. Moreover, it would be necessary to consider how to add moderator material without changing the initial mass of minor actinides. That is, adding the moderator at the periphery of the minor actinide elements.

REFERENCES

[1] J.-Y. DORIATH, C. W. McCALLIEN, E. KIEFHABER, U. WEHMANN and J.-M. RIEUNIER, "ERANOS - The Advanced European System of Codes for Reactor Physics Calculations", Joint Conference on Mathematical Methods and Supercomputing in Nuclear Applications, Karlsruhe, Germany, April 19-23, 1993.

[2] G. RIMPAULT, D. HONDE, J. TOMMASI, J.-M. RIEUNIER, R. JACQMIN, D. VERRIER, D. BIRON, "The ERANOS Data and Code System for Fast Reactor Neutronic Analyses", International Conference on the New Frontiers of Nuclear Technology: Reactor Physics, Safety and High-Performance Computing, PHYSOR 2002, Seoul, Korea, October 7-10, 2002.

[3] D. BLANCHET, "ESFR Core Concept", Note Teachnique DEN, CEA, CADARACHE, 10/06/09.

Metal alloy and Sphere-Pac MOX test fuel fabrication for irradiation in FBTR

G.Ravisankar, T.V.Prabhu,R.Padmanaban,R.Venkatakrishnan,P.Muralidaran,V.Ganesan,K.Nagarajan and P.R.Vasudeva Rao

Indira Gandhi Centre for Atomic Research, Kalpakkam, INDIA

Abstract. IGCAR is pursuing the development of metal alloy fuel for use in Fast Breeder Reactors (FBRs). A programme has been initiated for the irradiation testing of sodium bonded U-Zr alloys with natural as well as enriched uranium. A laboratory scale facility for the fabrication of sodium bonded test fuel pins with U-Pu-Zr alloy has been commissioned. This facility has a train of inert atmosphere glove boxes housing the equipment for fuel/blanket loading, pin welding and sodium bonding. Six U-(6%)Zr test fuel pins, sodium bonded, were fabricated in this facility and are currently under irradiation in the Fast Breeder Test Reactor (FBTR). Towards establishing the sol-gel route for the fabrication of U-Pu mixed oxide fuel (MOX) for FBRs, a laboratory scale facility consisting of a train of glove boxes fitted with master-slave manipulators has been set up and commissionned. In this facility the fuel shaped as microspheres is prepared by the internal gelation technique. After washing, drying and calcination, the sintered microspheres are filled in a clad tube and vibro-compacted to form a fuel column. This facility has been designed to demonstrate the remote handling capability of fuel pin fabrication including microsphere production, sintering at high temperature, fuel and hardware loading, vibro-compaction and pin welding. Helium bond gas pressure of 6.0-6.5 bar(g) is maintained in the fuel pin plenum to improve the thermal conductivity of the sphere-pac fuel column at start of burn-up. Two sphere-pac test fuel pins containing large fraction of MOX microspheres and fine fraction of UO_2 microspheres fabricated in this facility, are planned to be irradiated in FBTR. This paper provides the details of the test irradiation programmes as well as description of the fabrication facilities for test fuel pins that have been established at IGCAR.

1. Introduction

The future fast reactors in India are planned to be fuelled with metallic fuel to leverage a high breeding potential and meet the energy demand. Since, experience in fabrication and irradiation of metallic alloy fuel for FBRs does not exist in the country, it is imperative to generate it before launching commercial FBRs with metallic alloy fuel. In order to generate this experience, a facility consisting of a train of inert atmosphere glove boxes for fabrication of test fuel pins has been built at IGCAR. The equipments for fuel/blanket and sodium loading, pin welding and sodium bonding have been set up in the facility. Sodium bonded fuel pins with U-Zr slugs in mod. 9Cr-1Mo (T91) clad tubes have been fabricated and are currently in pile in Fast Breeder Test Reactor (FBTR). The design features of the facility and fabrication equipments and the process and quality control aspects are described in this paper.

Sol–gel based fuel fabrication processes offer several advantages over the conventional powder pellet-route [2]. Hence the development of sol-gel based fuel fabrication methods for FBRs has been taken up at IGCAR. Towards meeting this goal, as the first step, a laboratory scale facility for fabrication of sphere-pac test fuel pins through the sol-gel route in which fuel materials are made in the form of microspheres and vibrocompacted in steel clad tubes was set up and commissioned. The facility was designed with the objective of demonstrating remote fuel fabrication with contact maintenance of equipment. The facility is constructed as a train of glove boxes fitted with master slave manipulators and the process equipments are designed to meet remote operational requirements. Two sphere-pac

fuel pins containing MOX microspheres were fabricated and qualified for loading in the reactor for a test irradiation. The design features of the facility,the test fuel pin and the process are described in this paper.

2.   Fabrication of Sodium Bonded Metallic Test Fuel Pin

2.1.Design features of the pin

The sketch of the fuel pin is shown in figure 1. The clad tube and the end caps are made out of modified 9Cr -1Mo (ASTM A 387 Grade 91) material. The fuel column is made of a 160 mm U-(6%)Zr length.. A U-(6%)Zr blanket of 49 mm length is placed at the bottom. A plenum gap of 228 mm is provided at the top. The annular gap between the slug and the clad tube is filled a bond sodium and the level of sodium above the slug is 20±0.5mm.
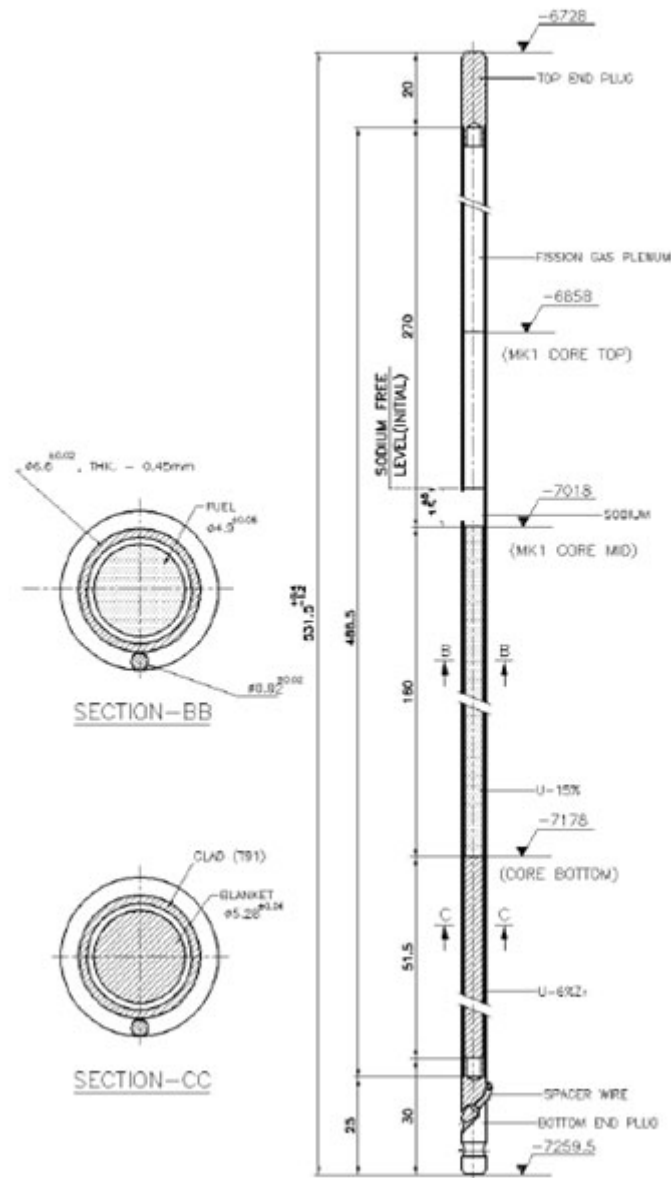
FIG. 1. Metallic fuel pin – Sodium bonded

2

2.2. *The glove box facility for metallic fuel pin fabrication*

For fabrication of the metallic fuel pins, a negative pressure argon atmosphere glove box train consisting of double and single module glove boxes with automatic pressure control, independent gas recirculation and gas purification has been set up. This facility also contains usual header lines with gas manifolds for argon, helium and argon-hydrogen gases and emergency evacuation system as shown in figure 2. The concentrations of oxygen and moisture are maintained at less than 10 ppm. In addition, a stand-alone positive pressure argon atmosphere glove box with automatic pressure control, gas recirculation and gas purification systems for sodium handling, has been set up for sodium wire extrusion and transfer into clad tube [1] . The concentrations of oxygen and moisture in the sodium handling glove box is maintained at less than 1 ppm.

FIG. 2. Argon atmosphere negative pressure glove box train with various facilities

2.3. *Test fuel pin fabrication*

The fabrication process is shown in the process flow sheet in figure 3.
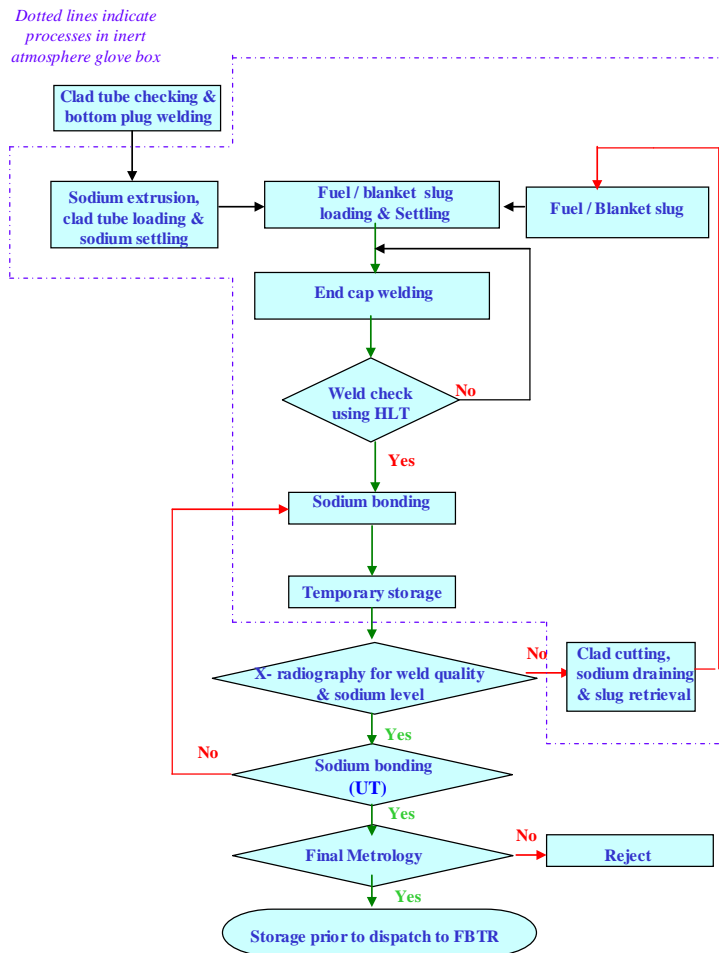
FIG. 3.Process flow sheet of Metallic fuel pin – Sodium bonded

2.4.Preparation of hardware

The bottom end cap is welded to the clad tube by pulsed TIG welding process autogenously in a qualified welding fixture on a bench top facility outside the glove box train. The end cap weld joints are subjected to a post weld heat treatment in a furnace housed in a glove box under inert atmosphere. The one end welded and qualified clad tube is taken into the sodium handling glove box.

2.5. Welding procedure development

The metallic fuel pin design involves ferritic steel cladding joined to end cap of ferritic steel. A qualified welding procedure was developped. Extensive trial welds were made to optimise welding parameters and achieve consistent quality welds [6]. Data on current weld parameters were stored in real time during the welding process. The weld joint is qualified by visual examination, helium leak testing (10^{-15} MPa m^3/s max) and X-radiography. The welds are characterised by metallography during the qualification of welding fixture and before and after the production welds.

2.6.Sodium handling facility

The sodium is handled in an argon atmosphere glove box, in which oxygen and moisture concentrations are maintained less than 1 ppm to maintain the sodium purity. Liquid sodium is maintained in a sodium bath at 473 K. Sodium metal is loaded into a specially developed extruder (fig. 4) in which an electrically driven piston mechanism pushes the sodium through a die, in the form of wire section of 3 mm in diameter, into a polyethylene tube. The sodium wire is then pneumatically injected into the clad tube by inserting the polyethylene tube containing sodium through

a guide sleeve made out of PTFE material [5]. The polyethylene tube and the PTFE sleeve avoid mouth contamination of clad tube during sodium addition which may cause defective welds during closure welding. The sodium wire is then cut to the required size by means of a cutter. The clad tube with sodium wire is placed in a tubular furnace and heated to 423 K for melting and settling of sodium.
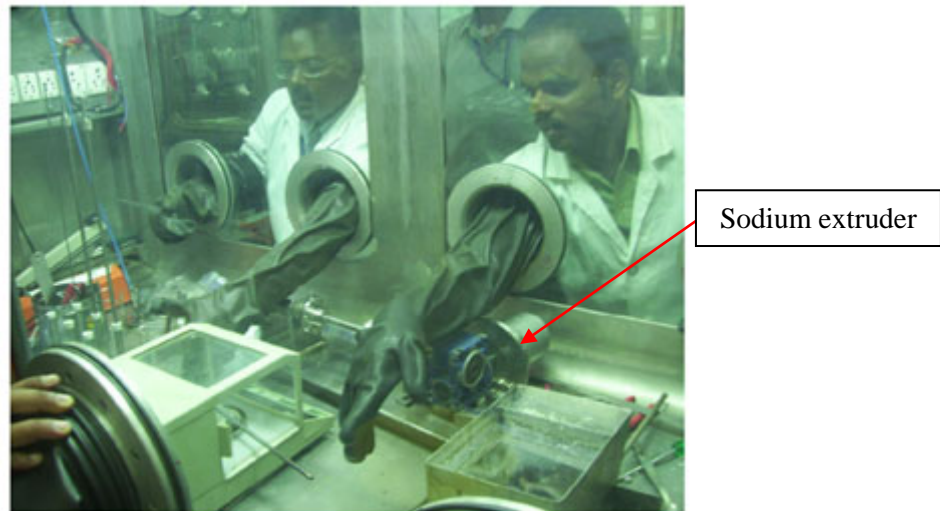
FIG. 4. Sodium handling glove box with sodium extruder

2.7. Hardware loading facility.

The sodium filled clad tube is bagged into the hardware loading glove box and placed on a hardware loading device for loading the fuel slug. The U-Zr fuel slug is qualified by eddy current testing and subjected to metrology for inspection on length, diameter, straightness and weight. The qualified fuel slug is inserted into the clad tube by a levitation method to prevent mouth contamination. The clad tube is then transferred into a furnace for settling the sodium by heating to 423 K and vibrated by a power oscillator with amplifier (Power oscillator with amplifier 50VA, Model: SI-26 Syscon make & Vibration exciter 25 Newton, Model: SI-200) in order to ensure proper settling. The settling process ensures the slug is seated at the bottom of the tube, the bond sodium raises along the annulus between the fuel slug and the clad displacing voids.

2.8. End cap welding

The clad tube with slug settled in sodium is closed with temporary teflon plug and transferred into the welding glove box through an interconnecting transfer port. The end cap closure welding is done in a specially developed leak tight welding chamber by automated pulsed TIG process. The chamber is pressurized with helium at 1.2 bar (g). In the welding chamber, the clad tube rotates in horizontal position at constant speed against a stationary tungsten electrode. A microprocessor based, inverter DC power source is used for welding and weld monitoring software for data storage. The centre alignment of the clad tube and the end plug is ensured with a help of a CCTV attachment with a video grabber and image analysis software for measuring and ensuring the arc gap and the root gap consistency during welding. After the welding, post weld heat treatment (PWHT) is carried out at 760 ±10 deg.C with holding time of 30 minutes in a furnace kept under argon atmosphere in the glove box (fig. 5). The qualification of the weld is carried out by visual examination, helium leak testing and X-radiography. The weld is radiographed at 3 orientations and weld shall be free of porosity, inclusions and cracks and weld penetration shall be > 110% of clad wall thickness. In order to ensure leak tightness before sodium bonding, the fuel pin is subjected to helium leak test by keeping it in a vacuum chamber inside the glove box connected to a helium detector.
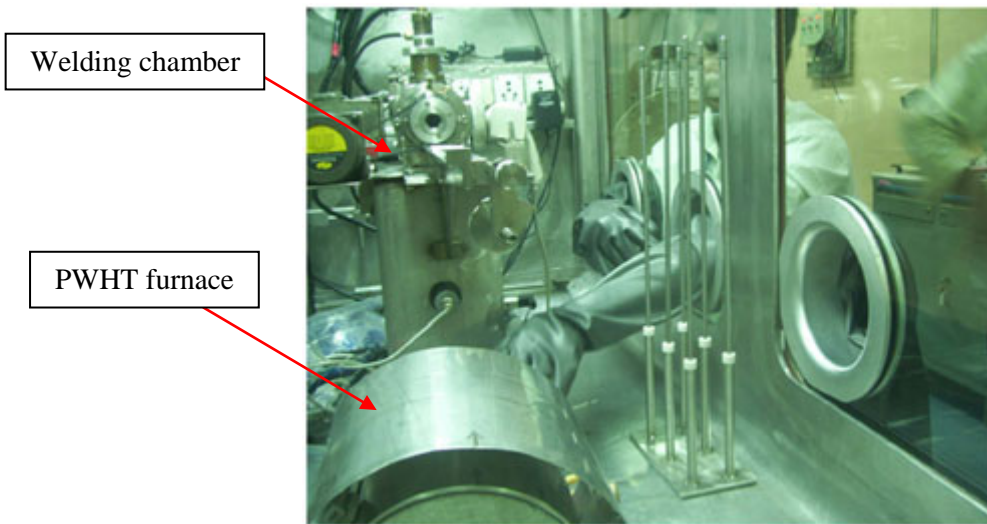
FIG. 5.Welding glove box with welding chamber and PWHT furnace

2.9.Sodium bonding

Once the fuel pin is welded and inspected, for establishing sodium bonding, it is transferred into bonding station glove box and loaded into a furnace with an arrangement for vibration of the fuel tube by a plunger (fig. 6). The temperature is maintained at 823 K and fuel tube is vibrated during 60 minutes. X-Radiography is carried out to estimate sodium level and total porosity in the sodium bonded region.

FIG. 6. Sodium bonding furnace housed below the glove box

2.10. Irradiation campaign.

Six sodium bonded metallic fuel pins were fabricated in the facility and qualified. Figure 7 shows the internals of the fuel pins by X-radiography. Two irradiation capsules each containing three fuel pins were fabricated and incorporated in the form of special subassemblies and loaded in the fourth ring of FBTR for irradiation studies.

FIG. 7. X-radiography of the sodium bonded metallic test fuel pins

3.   Sol -Gel based sphere-pac MOX fuel pin for test irradiation

3.1. Design features of the pin

The sketch of the fuel pin is shown in figure 8. The clad tube of the pin is made of 20 % CW D9 material and the bottom and top end plugs are made of AISI 316L. The pin contains fuel microspheres of two different size fractions to achieve smear density of $80 \pm 2\%$ TD. In view of the fact that the clad inner diameter is 5.7 mm, the sizes of the microspheres were chosen as 780 ± 70 µm and 115 ± 10 µm
. The coarser fraction is (U,Pu) mixed oxide (MOX) with 53% PuO_2 and the finer fraction is UO_2 mixed in the ratio of   3:1 which results in an average PuO_2 content of 40%. On either side of the fuel column, a UO_2 pellet is kept for insulation purpose. Two filters, in the form of mesh, each of 5 mm thickness are kept on either side of the fuel column to prevent the microsphere from falling but at the same time to maintain the communication between the fission gas and the top plenum. The entire fuel column stack is supported by a middle plug which is crimped to the clad. The fission gas plenum length is 95 mm at the top. A metal rod made of AISI 316 L is placed at the bottom plenum. The pin is filled with helium gas of 99.8 % purity at 6.0-6.5 Kg/cm^2 pressure (g) to serve as the bond gas.
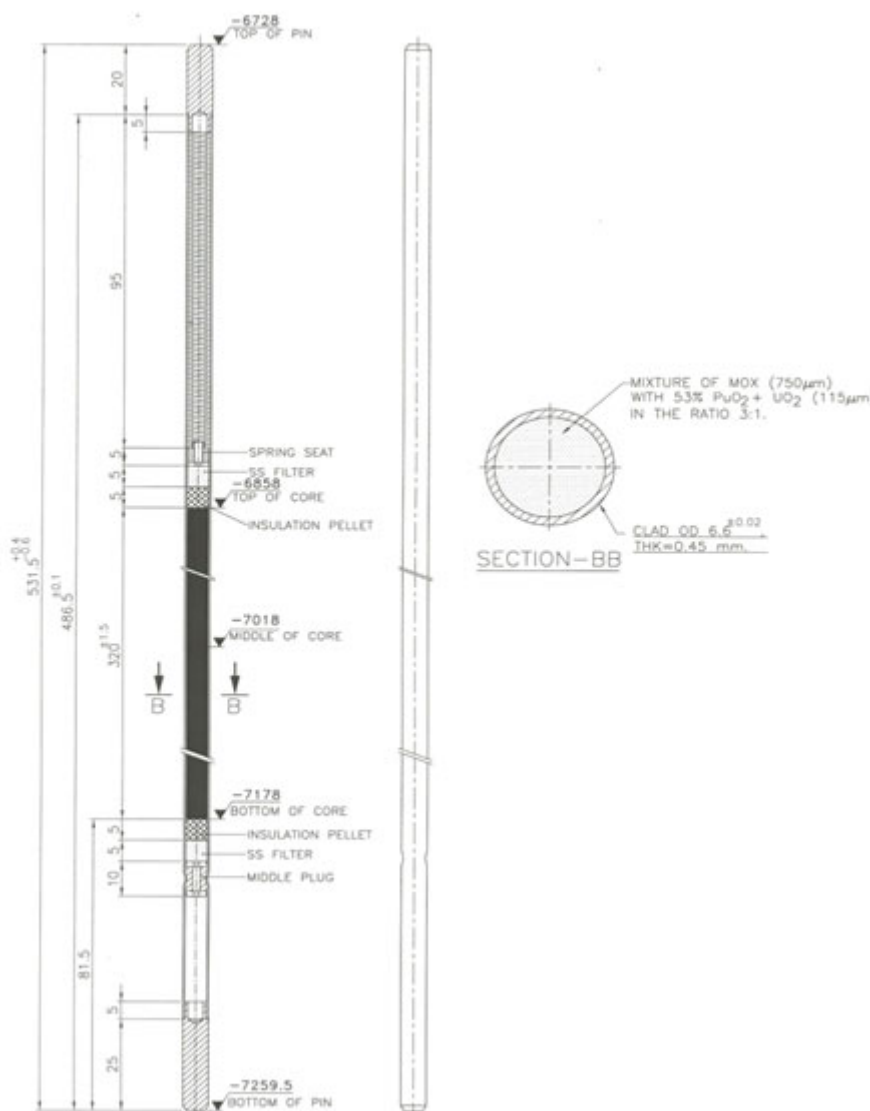
FIG. 8. Sphere-pac fuel pin for irradiation test in FBTR

3.2. Test fuel pin fabrication facility

The sol-gel based test fuel pin fabrication facility at IGCAR is shown in figure 9. It is a train of interconnected glove boxes, which are larger in size than the standard glove boxes in order to accommodate articulated type manipulators. A set of glove ports are also provided in the glove boxes to enable maintenance of equipment using gloves. The facility has been designed with remote handling features to demonstrate the remote fuel pin fabrication. The equipment for production of coarse fraction MOX microspheres, calcination and sintering of the same ??, compaction of the microspheres into pellets, degassing and aliquoting of the micropsheres, filling into clad tube and end plug welding are incorporated in these glove boxes. The fine fraction, UO_2 microspheres are produced using internal gelation method. However, the equipment used is a different one which is positioned outside the above facility. It is known as jet entrainment set up which has also been house fabricated and used for preparing several batches of fine fraction microspheres. The details of the set up are discussed elsewhere [4] .

3.3 Sphere-pac fuel pin fabrication

The sintered microspheres are transferred into a glove box where degassing is done and aliquots of microspheres having predetermined weights are prepared. The glove box has two compartments, one

for operations such as degassing, microsphere weighing and transferring and the other for fuel pin handling operations such as vibrocompaction, hardware loading and end plug welding. The partition panel separating the two compartments has a ventilation duct connecting the two compartments through a HEPA filter chamber and a suction transfer tube for transferring microspheres. This partition arrangement facilitates control of contamination on fuel pin handling compartment. The fuel pin is held vertically on a pneumatically operated three jaw chuck which is mounted on a vibrator platform. Suction transfer is employed for loading aliquots of microspheres into the fuel pin.The microspheres are added and vibrocompacted in the pin in batches by infiltration mode in which the coarse fraction is added first and then the fine fraction is added. By vibration, it is allowed to infiltrate in to the coarse fraction. This process is done in batches by dividing the fuel materials into several aliquots and added one by one. A maximum packing density of 79% was obtained using optimized vibration frequency of 1000 Hz and amplitude of 42 µm. The packing density was determined by measuring the height of the packed column.
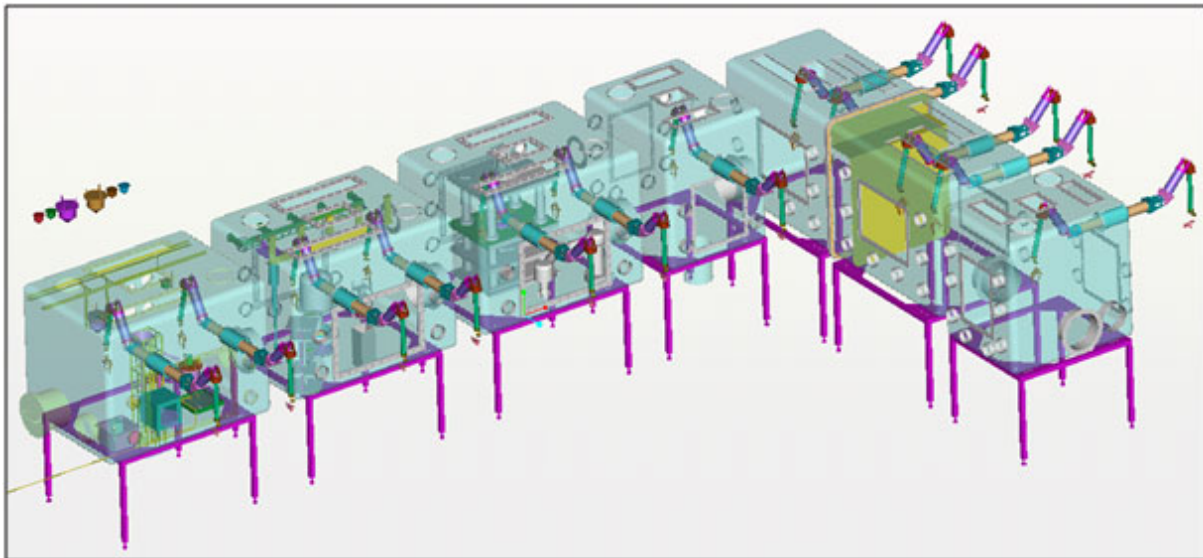
FIG. 9. Sol-gel based fuel fabrication facility

The vibrocompacted fuel pin is transferred by an automated XYZ positioning device to the adjoining hardware loading station where other hardware such as wire mesh, insulation pellet and spring are loaded and then further moved to a remotely operated welding facility [7]. The welding procedure adapted for the end plug welding of sol–gel based fuel pin is different from the one used for metal fuel fabrication. The fuel pin is held in vertical position and rotated in the welding chamber against the end plug held from the top by a three jaw chuck. The welding chamber is evacuated and filled with helium a few times to remove the air. The chamber is then filled with helium at a pressure 6-6.5 kg/cm^2 and then end plug is welded with the fuel pin by a similar pulsed TIG welding process used in metal fuel welding. The welded pin is transferred to next glove box through a transfer port, decontaminated and then bagged out for helium leak test and X- Radiography.
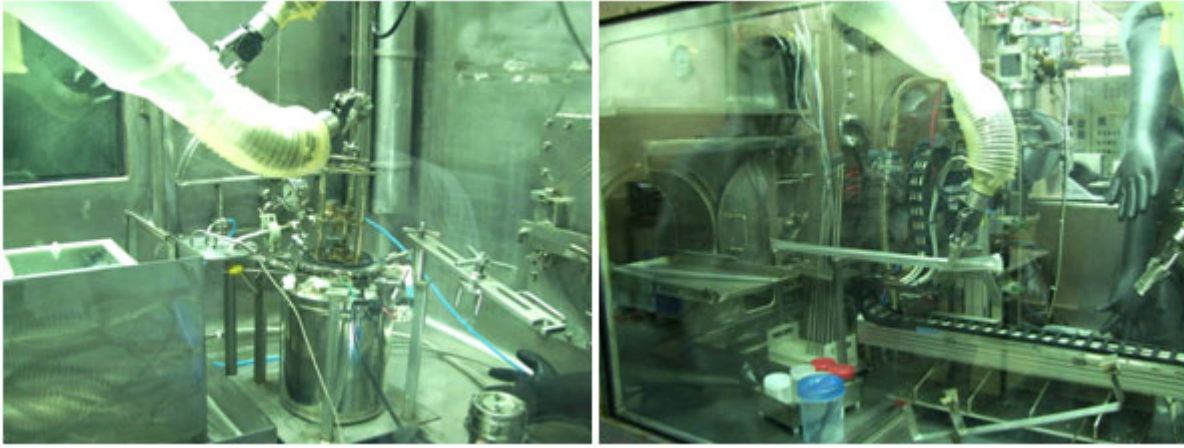
FIG. 10. Glove box for microsphere handling and fuel pin welding operations.

3.3. Remote handling and automation features

All the glove boxes in this facility are fitted with articulated arm type master slave manipulators (fig.10) to facilitate remote operation of the equipment. Some of the delicate operations in the fabrication process are automated [3]. The equipments are optimized for remote operation and maintenance and are modularized to enable remote replacement and repair. In the internal gelation system, for each batch operation, it is necessary to replace the nozzle which is mounted on a vibrator and positioned above the oil column. A counter weight actuated positioning device enables the movement of the vibrator to manipulator reach and the nozzle is replaced by a quick release mechanism. The calcination furnace is provided with a gantry mounted three stage telescopic hoist for loading and unloading of the samples.The sintering furnace has a lifting and positioning device for the top dome to facilitate loading of the charge carrier into the furnace. The charge carrier is handled by pneumatically actuated gripers held by a positioning device mounted on a gantry. Loading and unloading of the microspheres from the charge carrier is carried out by suction transfer device. A camera assisted viewing system enables the operator to view the interior of the furnace while handling the charge carrier [7] .

3.4. Qualification and test results

In order to qualify the process prior to the end plug welding of sphere-pac fuel pins, set up welds and process test pins were welded and subjected to weld qualification by X radigraphy (fig.11), helium leak test and metallography. The process test pins were subjected to plenum gas pressure and purity examination by puncturing the pins in an evacuation chamber. The helium pressure was found to be 6.1 kg/cm^2 and the purity 98% which are as per the specifications. After qualifying the process, two numbers of of sphere-pac fuel pins have been fabricated and qualified for irradiation in the fast Breeder Test Reactor, (FBTR) at Kalpakkam. The coarse fraction MOX microspheres used in the fabrication of sphere-pac test fuel pins were produced, qualified and supplied by Bhabha Atomic Research Centre (BARC) whereas the fine fraction UO$_2$ microspheres were produced and qualified at IGCAR.
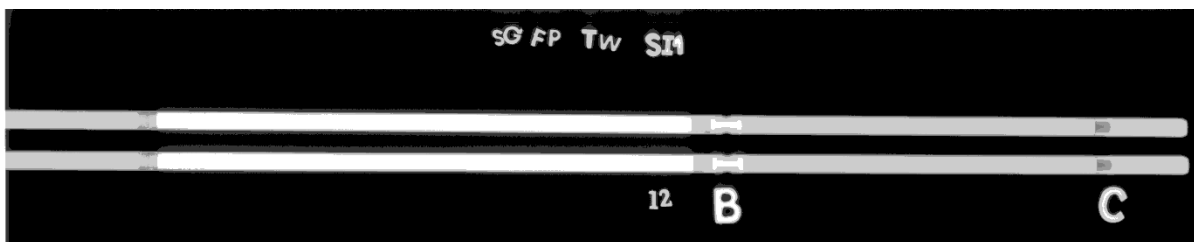
FIG. 11. X radioagrphy of the sphere-pac fuel pins

3.5.Irradiation programme

In the first test fuel campaign, it is planned to irradiate a capsule containing three test fuel pins of which two will be sphere- pac fuel pins and other will be stacked with annular pellets of (U,Pu) mixed oxide containing 45 % PuO_2.

4. Summary

Laboratory scale facilities for fabrication of metallic as well as sol-gel based test fuel pins have been established. Test fuel pins with natural U-6%Zr alloy are undergoing irradiaiton in FBTR. Sphere-pac fuel pins have been fabricated which are planned to be irradiated in FBTR. Post irradiation examination will be carried out on the performance these pins.

ACKNOWLEDGEMENTS

REFERENCES

[1] MURALIDARAN, P., PRABHU, T.V., et al., "Fabrication experience of sodium bonded metallic test fuel pin with 6%Zr in T 91 clad tube for irradiation in FBTR", (Proc. Int. Conf. CQCNF 2012), Hyderabad, India (2012).

[2] NAGARAJAN, K., VAIDYA, V.N., Sol-Gel processes for nuclear fuel fabrication (in Sol-Gel Processing for Conventional and Alternative Energy), ISGS, Springer (2012) 341.

[3] PRABHU, T.V., VENKATA KRISHNAN, R., "A Remotely Operable Facility for Fabrication of Fuel Pins for test Irradiation", (Proc. Asian Nuclear Prospects 2010), Energy Procedia 7 (2011) 222–226.

[4] VENKATAKRISHNAN, R., Nagarajan, K., et al., Sol-Gel development activities at IGCAR, Kalpakkam, J Sol-Gel Sci Technol (2011)59:394-403.

[5] PRABHU, T.V., PADMANABAN, R., et al., "Experimental study on welding of modified 9Cr -1Mo (T 91) clad tube to end plug fabricaiton odf test fuel pins" (Proc. Int.Conf. NWS 2011), Vizag, India (2011).

[6] PRABHU, T.V., RAVISANKAR,G., et al., "Development of automation systems for remote fabrication of test fuel pins" (Proc. Int. Conf. Industrial Automation 2009), Hyderabad, India (2009).

The strategy for fuelling ELECTRA

Merja Pukari[a], Jesper Ejenstam[b], Janne Wallenius[a], Peter Szakálos[b]

[a] Reactor Physics, KTH Royal Institute of Technology, Roslagstullsbacken 21, SE-10691 Stockholm, Sweden

[b] Surface and Corrosion Science, KTH Royal Institute of Technology, Drottning Kristinas väg 51, SE-10044 Stockholm, Sweden

Abstract. The general strategy for establishing a licensed fuel-cladding system for the lead-cooled ELECTRA reactor in Sweden is presented. The reference fuel and cladding materials for ELECTRA - $(Zr_{0.6}Pu_{0.4})N$ fuel with 15-15 Ti/FeCrAl-RE coated cladding - are discussed, thereby identifying the arising difficulties in the future licensing process. The focus point of the strategy is ongoing and near future research required to bring the fuel qualification to the next technical readiness level (TRL). Currently, the greatest challenge is the limited knowledge base of the cladding material under irradiation, as the stability of the corrosion-resistant FeCrAl-RE coating is not confirmed under in-pile conditions. Research on the effects of C and O impurities in the fuel, especially on internal cladding corrosion, are of paramount importance, as these effects will define the fuel fabrication parameters.

INTRODUCTION

The European Lead Cooled Training Reactor (ELECTRA) is a low power fast reactor using inert matrix nitride fuel. The reactor concept, in development at KTH since 2009, aims to leverage on research performed over the last 15 years on nitride fuels, liquid lead cooling and advanced cladding materials. The feasibility of lead-cooled, nitride fuelled reactors is largely supported by other reactor designs, such as BREST and SUPER-STAR [1, 2] out of which BREST-300 is slated for construction and operation in Tomsk by 2020. However, if ELECTRA is to be realized in the foreseeable future, it is necessary to systematically analyze the research performed on the reference materials and those closely related; to highlight the topics poorly understood; and to organize future research for providing clarifying information on those areas.

For this purpose, the current paper outlines the general road map for qualifying the fuel system specific for ELECTRA. The proposed plan divides the licensing process into four distinct phases, in line with the general fuel development route defined by Craword et al [3]. Of these, the paper focuses in detail on the currently active phase, the purpose of which is to bring the results on fundamental out-of-pile properties of the materials to a satisfactory level for licensing purposes. In addition, the required in-pile experiments of the cladding material are discussed. The potential bottlenecks in the process and alternatives to solve them are discussed, where possible.

Currently, the reference fuel material $(Zr_{0.6},Pu_{0.4})N$ and the reference cladding material 15-15 Ti surface alloyed with FeCrAl-RE are at a different stage of development. The inert matrix nitride fuel planned to be used in ELECTRA has been studied in a range of relative Zr/Pu ratios in cold and irradiation testing [4, 5] in addition to closely related research on other actinide nitrides. The beneficial qualities of this fuel, such as high thermal conductivity and heavy metal density, has motivated an extensive list of in-pile and out-of-pile experiments over the years. Similarly, 15-15 Ti is a material licensed as a reactor grade material, and presents desirable thermo-physical qualities under irradiation. Due to the corrosive nature of lead, however, it is suggested to apply FeCrAl-RE coating, which due to

1

its poorer mechanical properties would not qualify as a bulk material. Moreover, the behaviour of FeCrAl-RE alloys under irradiation is not yet clearly understood.

While the described qualification route is specific to the boundary conditions defined by ELECTRA's design and the materials chosen, the discussed ongoing and planned research will be of generic value to the Generation IV and materials science communities. The roadmap will hopefully spark discussion on the topic of qualifying such a fuel system, as well as encourage research communities to investigate the highlighted topics in parallel, as it is vital to use statistically accurate data for fuel qualification. Dedicated work on the identified shortcomings is especially important, as the major objectives of ELECTRA are to function as a test bed for lead cooled fast reactor (LFR) technology, and as a facility for training and education of LFR operators. It would also constitute a unique facility for fast reactor dynamics research.

ELECTRA

The detailed description of ELECTRA is provided elsewhere [6, 7] and therefore only a brief summary follows. The 0.5 MW_{th} ELECTRA core consists of a single assembly of 397 fuel pins and, owing to the inert matrix nitride fuel facilitated neutron economy, is reduced to 30 times 30 cm of core size. The reactor is cooled with lead, as opposed to lead-bismuth, and requires no pumps, as natural convection is employed. A single core load will be sufficient for 14 full power years of operation. The reactivity control is achieved by employing 12 rotating drums with absorbing sections, following the design of the Advanced Test Reactor in Idaho and the TOPAZ space reactors built in the Soviet Union [8].
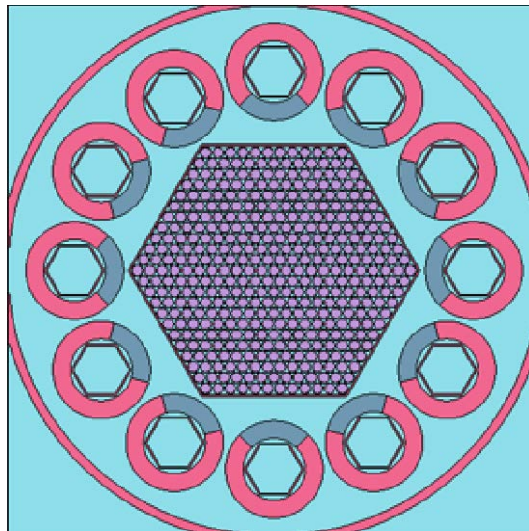
FIG. 1. Core map of the updated design of ELECTRA [7]

The choice of fuel for ELECTRA may be rationalized through the following arguments:

1) The introduction of lead coolant will increase the likelihood to achieve adequate passive safety performance in Generation-IV reactors
2) At present, materials suitable for use in pump impellers of lead cooled reactors remain to be qualified
3) In the near term (next ten years), full heat removal by natural convection will offer a short-cut to testing operation of lead cooled fast reactors
4) A very compact core with low pressure drop may be designed by application of inert matrix (uranium free) fuels

5) Among inert matrix fuels tested under irradiation, (Pu,Zr)N offers a unique combination of low swelling, low gas release, insignificant pellet-clad chemical interaction, high margin to melting or dissociation and high plutonium density.

Item (5) is based on the outcome of successful irradiations carried out in BOR-60 [5] JMTR [4] and HFR [9]. Additional out of pile data supporting our conclusions have been obtained in Switzerland, France, Russia and Japan[10–16]. The beneficial combination of high fission gas retention with low swelling is most likely due to inhibition of bubble growth facilitated by the ZrN matrix [17]. Hence, we argue that (Pu,Zr)N is the most adequate fuel option for a low power reactor functioning as a test bed for near term application of lead fast reactor technology.

The environment of the ELECTRA cladding tubes can be divided into internal and external environments, which must withstand, under irradiation, fuel-induced corrosion and mechanical stress on one hand, while resisting liquid metal corrosion and embrittlement on the other. Apart from these environmental factors, the cladding tube itself has to have high enough resistance to thermal creep and fatigue. As of today, there is no single material that can meet all demands imposed by the environment in ELECTRA. Thus, a clad system made of bulk steel, 15-15 Ti, coated with a FeCrAl-RE has been proposed [6]. 15-15 Ti was used in the French sodium cooled Phénix reactor during several years [18] and while it meets the requirements of a sodium-cooled reactor, the corrosive nature of lead limits its use with lead-based coolants. Studies have shown the rapid oxidation corrosion process of 15-15 Ti in LBE at temperatures above 500°C [19]. In search for a corrosion resistant material FeCrAl alloys, a family of ferritic alumina formers with high corrosion resistance in harsh environments at high temperatures, are currently studied [20–28]. At Karlsruhe Institute of Technology (KIT), a method has been developed where a bulk steel can be coated with a second steel, by means of low pressure plasma spray (LPPS). This is followed by the surface re-melting using a high intensity electron beam. This method, applicable for the fabrication of cladding for ELECTRA, has been named Gepulste Elektronen Strahl Anlage (GESA)[29, 30].

FRAMEWORK

In order to license a reactor, the applicant is required to show that the radiological impact is strictly kept to a minimum under all circumstances. In Sweden, the Swedish Radiation Safety Authority (SSM) is the regulatory body monitoring all activities related to radiation protection and nuclear safety. All prescriptions authored by SSM are strictly based on the Swedish radiation protection act (1988:220), which is intended to "protect people, animals, and the environment against harmful effects of radiation" [31]. For ELECTRA, prescription SSMFS 2008:17, the Swedish radiation safety authority's regulation concerning the design and construction of nuclear power reactors [32] is of particular importance. No significant radiotoxic releases (> 1 mSv/year for the general public [33]) are tolerated, hence a list of anticipated and improbable events has to be dictated, and measures to handle them must be identified. Events of particular importance are those that could threaten the integrity of the fuel and cladding, such as:

- Change of core geometry during normal operation leading to changed coolability
- Loss of coolant accident (LOCA) or degraded coolability
- Transient Over Power (TOP) leading to degradation of the cladding tubes
- Loss of active residual heat removal

SSM limits is requirements to general guidelines, rather than a definitife list. It is therefore up to the applicant to identify and analyze events relevant for the particular reactor design. The identification of such events and the countermeasures to minimize all damage is the foundation for submitting the PSAR to SSM. The IAEA and the European Utility Requirements (EUR) provide additional guidelines. For example, in the Safety guide NS-G-2.5: Core Management and Fuel Handling for nuclear Power Plants [34] guidelines for licensing a new nuclear fuel are communicated. Apart from submitting a PSAR to SSM, an environmental impact statement (EIS) has to be submitted and approved by the Swedish enviromental court.

Examples of events that are specific for ELECTRA are:

- Inadvertent control drum rotation, leading to transient over power accident and thus increased thermal stress of the cladding
- Failure of oxygen control system, leading to degradation of the cladding due to the corrosive nature of the lead coolant

The TRL (Technical Readiness Level) concept was initially developed by NASA in order to classify the readiness of space applications [35]. The concept is also used by other American organizations, such as the department of defense (DOD) [36]. Recently, Crawford et al. [3] published a study where the concept was introduced into the process of nuclear fuel development. By structuring the fuel development and qualification programme according to the TRL concept, time required for the licensing process is expected to be reduced. The TRL scale is divided into 9 levels and 4 development phases, resulting in a successful deployment of the fuel. A detailed description of the TRL level definitions is discussed by Crawford et al [3].

FUEL QUALIFICATION PROGRAMME

The fuel qualification programme for ELECTRA is divided into four phases: (1) conceptual work, (2) out-of-pile experiments on fundamental properties, (3) in-pile experiments and (4) demonstration of full-scale systems, illustrated in Figure 2. The qualification route depicted is seemingly straighforward, as it does not illustrate the iterative behaviour of the process in reality. It is compiled, to a certain extent, based on the best-case scenario, although the authors foresee several crucial challenges interfering with or significantly postponing the procedure. As future tasks heavily depend on phase (2) in the programme, only the most imminent research required is elaborated on.

1.1. Phase one.

Phase one described the work already performed on developing ELECTRA and serves as a motivation for the fuel qualification programme. The design of the primary system of ELECTRA is justified by the generally established out-of-pile research performed on nitride fuels and cladding materials. Data sets of variable level of certainty exist for lattice parameters, densities, thermal expansion, heat capacity, thermal conductivity, melting temperatures, dissociation temperatures, enthalpies of formation, melting and evaporation, elastic modulii and creep rates for the fuel components, to list the more important of them. Similarly, experiments on out-of-pile cladding material provide data on creep, tensile strength, ductile to brittle transition temperature, fatigue, fracture toughness, corrosion properties and wear. Although the majority of research on nitride fuels is not performed specifically on the $(Zr_{0.6}Pu_{0.4})N$ composition, many values can be extrapolated, as $(Zr,Pu)N$ generally behaves as a function of the relative quantities of ZrN and PuN.

The major design parameters of the ELECTRA core, reactivity control system and primary vessel have been determined [7]. Simulations of neutronic and thermal-hydraulic performance under nominal and transient conditions have been employed to optimize the design. An analytical model used to study the stability of the natural convection flow show that the design is safe, supporting its intended use for training and educational purposes [6]. The results of these studies are deemed sufficient to proceed by bringing the concept from paper to reality.

1.2. Phase two.

In the second phase of the qualification programme, three general topics are distinguishable, standing for a) determining with statistical accuracy the out-of-pile properties of fuel, b) of the cladding material, and c) of their compatibility with each other. Under each category, properties and behaviour not yet understood is listed, to be resolved before proceeding with irradiation testing. While a range of these are currently being researched, or are being prepared for (ongoing or planned experimental research), others have been identified as problematic and are not on the agenda yet (foreseen near future research). The foundation for defining these research areas lies on the ongoing compilation of a

4

database relevant for ELECTRA fuel system as well as by the necessary input for fuel performance and behaviour prediction codes, into which the results of the experiments will be eventually integrated. Obtaining a comprehensive database on out-of-pile properties is one of the core objectives of this phase.

1.2.1. Fuel.

For nitride fuel fabrication, the inclusion of O and C impurites is unavoidable, and therefore their impact on the fuel performance must be systematically studied. As ELECTRA must fit within certain cost boundaries, the authors do not foresee a minimal, but an optimal O and C impurity content to ensure reasonable fabrication routes and material choices, high safety features and predictability. For that purpose, it is relevant to, on the one hand, establish the reasonably achievable, minimal O and C levels in the materials, while on the other hand conducting a parametric study on the influence of these impurities on sintering properties, cladding internal corrosion, and solubility in nitric acid. While there are certainly studies which have dealt with these questions, they are not in excellent agreement with each other. Furthermore, it is vital that these questions are addressed by employing precisely the fabrication methods envisaged for ELECTRA fuel. The specific composition of the fuel furthermore defines the solubility of these elements, the possible phase segragation during irradiation, and thereby the altered impact. It has been witnessed that in the presence of O impurities, a secondary PuO_2 phase will form [5].

In addition to the variation in stoichiometry, O and C impurity levels also impact the diffusion in nitrides and thereby the determined thermal conductivities. As the topic of diffusion is a complex one, it is suggested to investigate the diffusion of fission gases and volatile species in non-irradiated materials in addition to radiation tests.

It is accepted that the thermal conductivities of nitrides are an order of magnitude higher than that of actinide oxides and for PuN are well established. However, experiments on measuring the thermal conductivity of ZrN do not agree with each other[11, 12, 37]. For a reliable fuel performance code, as well as thermohydraulic calculations, the cause for variations in these experiments must be identified in addition to determining the appropriate thermal conductivity for the particular composition for ELECTRA. Lastly, the high thermal conductivity is expected to be beneficial for maintaining integrity of the fuel during a power ramp. However, the effect of extreme thermal shocks on fuel must be studied.

Excellent research on mutual actinide nitride solubility and solubility into ZrN has been done by Akabori et al, confirming that a full solubility can be expected for the $(Zr_{0.6}Pu_{0.4})N$ composition [14]. However, the matter of fission product solubility into this fuel requires further research. The authors see it best to conduct additional research in out-of-pile conditions to best isolate the otherwise simultaneously occurring phenomena. It is of interest to support this topic with first-principles calculations, despite it being considerably more straightforward for ZrN or DyN than for PuN or (Zr,Pu)N.

Spark plasma sintering is considered as an option for fuel fabrication due to the sintering time being limited to minutes, thus reducing the loss of volatile AmN inevitably present as a decay product[38, 39]. Although not currently a primary choice due to the very limited experience and data on using this equipment, SPS effect on sinterability, impurity levels, actinide dissociation and grain growth will be studied. Of these, the increase of C impurity level is perhaps the limiting factor, as it may lead to the carburization of cladding during irradiation.

Optimal core design with reference materials [6][7]

REFERENCE FUEL SYSTEM
Fuel: $(Zr_{0.6}Pu_{0.4})N$
Cladding: 15-15 Ti, with FeCrAl-RE coating

Thermohydraulic calculations on the functionality of a lead cooled system with specified dimensions and materials [7]

conceptual ELECTRA design

CLADDING

Ongoing or planned research

- Compatibility with lead under operational and DBA conditions
- Hydrogen and water vapour corrosion
- Adhesion of FeCrAl-RE coating to 15-15 Ti under load: mechanical properties study

Foreseen near future research

- Irradiation of FeCrAl-RE coated 15-15 Ti sample, followed by PIE to determine the irradiation damage
- Burst-test of an ELECTRA-specific, welded cladding tube at operational and DBA conditions
- Heat ramp influence on the stability of the coating and on the thermal conductivity
- Mechanical properties at operational and DBA conditions - creep, strength, hardness, DBTT
- Weldability and welding effects on material properties

FUEL AND CLADDING

Ongoing or planned experimental research

- The effect of fission gas and volatile species on internal clad corrosion and thermo-mechanical properties
- The effect of fuel impurity levels on internal clad corrosion and thermo-mechanical properties

Foreseen near future research

- Mechanical compatibility of fuel and cladding, considering the swelling and possible fragmentation of the fuel pellets
- Fuel system compatibility with lead after the rupture of one or more fuel pins

FUEL

Ongoing or planned experimental research

- Oxygen influence on nitride fuel sinterability (ongoing)
- Conventional and spark-plasma sintering effects on nitride fuel properties and densities (ongoing)
- Dissociation behaviour of $Zr_{0.6}Pu_{0.4}N$
- O and C solubility limits in $Zr_{0.6}Pu_{0.4}N$
- UN and $Zr_{0.6}U_{0.4}N$ compatibility with lead coolant (ongoing)
- $Zr_{0.6}Pu_{0.4}N$ compatibility with lead coolant (ongoing)
- Fission gas and volatile species diffusion in ZrN, $Zr_{0.6}Pu_{0.4}N$
- FP solubility into $Zr_{0.6}Pu_{0.4}N$
- FP solubility into ZrN and DyN - an ab-initio study
- Grain growth of spark-plasma sintered ZrN, UN and $Zr_{0.6}Pu_{0.4}N$ pellets at operation conditions
- Fuel stress test for power ramps

Foreseen near future research

- Required input for a predictive fuel performance code
- Thermal conductivity of ZrN
- Self-diffusion in $Zr_{0.6}Pu_{0.4}N$ - experimental and first-principles research
- Ternary phase diagram of Zr-Pu-N
- Reasonably achievable O and C impurity levels

Compilation and continuous updating of ELECTRA fuel design database

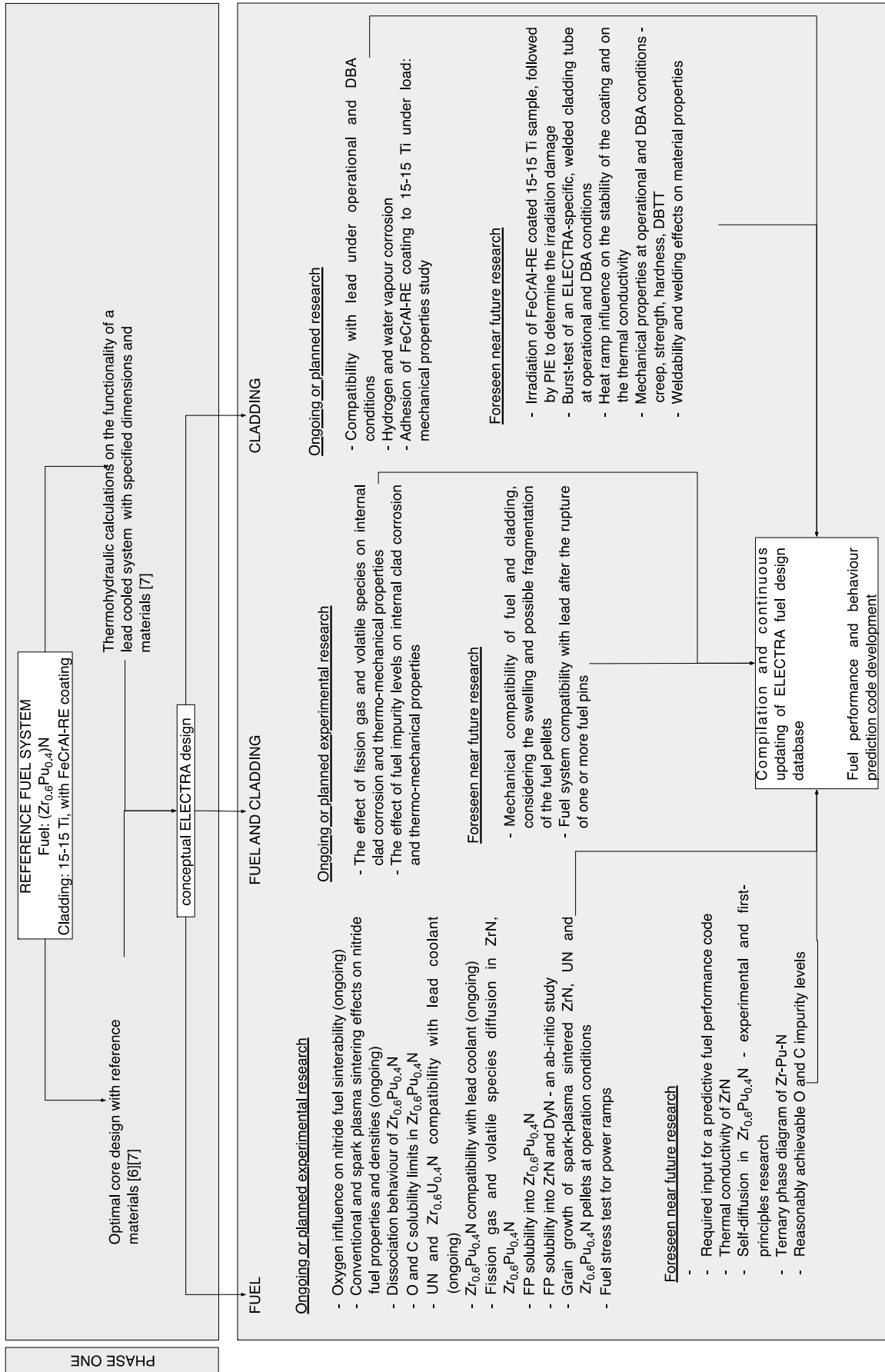Fuel performance and behaviour prediction code development

FIG. 2. ELECTRA qualification programme – outline of phases one and two.

In the event of the cladding rupture, nitride fuel will be exposed to the coolant. The experimental work conducted so far indicates good fuel-coolant compatibility at nominal oxygen conditions, albeit surface reactions are observed in oxygen saturated lead at T = 1090°C [40]. The compatibility of UN and lead is currently being studied in more detail, and that of $(Zr_{0.6}Pu_{0.4})N$ is planned to be studied to investigate the difference in corrosion resistance.

Research performed indicates that the dissociation temperature of UN is considerably increased if in solution with ZrN [41] thereby increasing the safety margins of this fuel. High temperature tests of $(Zr_{0.6}Pu_{0.4})N$ stability under vacuum, Ar and N_2 were carried out at 2300°C and 2200°C, showing that the presence of a cover gas substantially reduces the loss of material at these temperatures [13].

At which temperature the dissociation would become a significant issue for $(Zr_{0.6}Pu_{0.4})N$ may be estimated using thermo-chemical modelling tools, but the authors feel it is necessary to conduct additional experiments in order to determine the precise behaviour of this fuel at high temperatures. These experiments would further serve to finalize the Pu-Zr-N ternary diagram, which must be determined. While not very likely that fuel in the pin would experience N loss to a level where a metallic phase would segregate, it is important to prepare for these unlikely events, and therefore to have a good understanding of the behaviour of the ternary system.

It is of key importance to improve the prediction capacity of existing fuel performance codes. There is a variety of fuel performance codes developed, not all of them available for scientific research. It is currently foreseen that the code TRANSURANUS [42] is suitable for this work, after significant updating on properties and parameters.

1.2.2. Cladding.

Up to today, almost all experiments on FeCrAl-RE alloys, bulk or as coating, have been carried out out-of-pile, the only exception being low dose irradiations of Fe14Cr-ODS steel in JMTR. For use in ELECTRA, the alloys are subjected to a fast neutron flux peak value of $1,3x10^{14}$ n/cm^2/s. It is of highest priority to study the reference system under these conditions in lead. The highest estimated temperature of the clad in ELECTRA is 542°C, which will be the focus temperature of the irradiation tests [6]. Irradiation at transient temperatures must also be carried out as soon as possible. If any issues with the coating material would surface during these tests, such as cracking due to embrittlement, which was observed in low temperature proton irradiation of FeCrAl-RE coated T91 [43] an alternative reference coating has to be selected. One explanation to the cracking behavior could be the inherent thermodynamical weakness at these temperatures, as the ferritic structure will decompose into one iron rich phase (α) and one Cr-rich phase (α'). Known as spinodal decomposition, this phenomenon rapidly degrades the mechanical properties of the steel and has been shown to accelerate during irradiation [44]. By lowering the Cr content of the FeCrAl-RE alloy to about 10-12 wt.%, the phenomenon could theoretically be avoided, however the corrosion resistance would also be affected.

The corrosion test program has to be accelerated, meaning that the FeCrAl-RE coating has to be tested in a wide range of temperatures and oxygen potentials. As the tests cannot be carried out any faster, they have to be parallelized. Gaseous corrosion due to hydrogen and water vapor has to be additionally evaluated. Hydrogen and water vapor are used in the lab to set the oxygen concentration in lead. This method, combined with use of lead oxide pellets, may be used in ELECTRA to control the oxygen.

Mechanical properties of the fuel-clad system, with regards to the FeCrAl-RE coating's adhesion to the 15-15 Ti substrate under loads have to be further investigated. Some tests have been carried out at KIT already with positive outcome [45]. Bending, creep and fatigue are examples of tests that should be carried out to fully understand the behavior of the cladding.

1.2.3. Fuel and cladding combined experiments.

In order to evaluate internal clad corrosion rates in a cold state, a laboratory experiment can be designed. The formation of complexes containing clad surface species (Fe, Ni, Cr, Al, O) and fission products (FP) (Cs, Te, I) could possibly be studied by using commercially available, non-radioactive isotopes of the FP.

1.3.Phase three and four

In phase three, irradiation testing of fuel and cladding manufactured, according to the quality assured process resulting from phase two, is conducted. These irradiation tests should be carried out under prototypical conditions, which for ELECTRA means a fast flux with a magnitude of 10^{14} n/cm^2/s, a cladding temperature of 400-500°C and a lead flow of 0.2 m/s.

For TRL 5, irradiation of a few fuel pins under nominal conditions are foreseen, whereas for TRL 6 irradiation of a fuel assembly under nominal as well as off-normal conditions is suggested. Potential irradiation facilities include the High Flux Reactor (HFR) in Petten, the Halden reactor in Norway, the Jules Horowitz Reactor (JHR) in Cadarache, BOR-60 in Dimitrovgrad and the upcoming replacement for BOR-60, MBIR.

In HFR, the maximum available fast flux is 2 x 10^{14} n/cm^2/s, which means that using an irradiation rig with a hafnium shield, such as implemented for the CONFIRM irradiation, a prototypical fast flux of the relevant magnitude could be achieved. The corresponding dose rate to the cladding in the shielded assembly could reach 3-4 dpa per year, which is in the right range for ELECTRA. Moreover, a ramp facility is available on the pool side of the reactor, which would make it possible to conduct transient testing of irradiated fuel, reaching up to ten times the nominal power density of the ELECTRA fuel. Similar conditions could be achieved in JHR, once it is taken into operation. The schedule for commissioning of JHR is presently uncertain, but in 2016 the reactor should in principle be available for fuel tests of the kind here described.

The drawback of using water cooled reactors for these kind of experiments is that even though up to 90% of the thermal flux can be removed by adequate shielding, a significant fraction of the power would still derive from thermal neutrons, leading to a radial power peaking within the fuel pellet. Also, even though the damage dose rate to the cladding is similar to that found in ELECTRA, the total end-of-life dose of 40 dpa would be difficult to achieve. Therefore, fast reactor irradiations are an inevitable part of the fuel qualification programme for ELECTRA. In BOR-60, irradiation of cladding materials in lead-bismuth and lead capsules have been carried out, e.g. the LEXUR-II irradiation of 15-15 Ti to 16 dpa [46].

A dilemma in this context is that the Russian regulations currently do not allow irradiation of foreign fuel in Russian research reactors. Therefore, fuel fabrication for such tests would have to be carried out in a Russian laboratory. This means that a BOR-60 irradiation might not be fully adequate for licensing fuel from the facility that will manufacture the actual ELECTRA core. Nevertheless, a lead-capsule fast flux irradiation in BOR-60 is foreseen as part of the qualification programme for the cladding of ELECTRA. The cladding tubes for these experiments can be manufactured in Sweden and surface alloyed with the GESA technique. For the final qualification of the clad, the option of irradiating GESA treated cladding tubes in the lead-loop planned to be constructed in MBIR would have to be investigated.

Phase four is suggested to consist of irradiation of prototypic fuel derived from "production supply sources" to design conditions (TRL 7) and full scale demonstration (TRL 8). Since ELECTRA is a research reactor, and the design condition is 14 years of full power operation, we consider that production and irradiation of the first (and only) core of ELECTRA is equivalent to phase four of the indented fuel qualification programme.

CONCLUDING REMARKS

This paper outlines the general road map for qualifying the fuel-cladding system specific for ELECTRA in line with the framework suggested for development and qualification of technical programmes. It is recognized that the qualification of out-of-pile fuel properties is near completion due to the long experience with nitride fuels. The irradiation performance of these fuels is less known. Currently, the greatest threat to the licensing programme is the qualification of the reference cladding material, in addition to it being the most resource consuming work amongst the near-future research foreseen. Through the mapping of the qualification programme, the authors were able to underline the crucial areas where further research is to be done. The requirements posed by the domestic and international regulatory bodies are discussed. This work is the foundation for developing the detailed programme for subsequent irradiation testing and fuel-cladding fabrication design.

REFERENCES

[1]   E. Adamov et al, Nucl. Eng. Des. 173 (1997) 143
[2]   S. Bortot et al, Nucl. Eng. Des. 241 (2011) 3021
[3]   D.C. Crawford et al, J. Nucl. Mater. 371 (2007) 232-242
[4]   Y. Arai, M. Akabori, K. Minato "JAEA's Activities on Nitride Fuel Research for MA Transmutation", Proc. 9th IEM on Actinide and Fission Product Partitioning and Transmutation, Nimes, France, Sept 26-28, 2006, OECE/NEA 2007
[5]   B. D. Rogozkin et al, Atomic Energy 108 (2011) 369
[6]   J. Wallenius, E Suvdantsetseg, A. Fokau, Nucl Technol 177 (2012) 303-3013
[7]   E. Suvdantsetseg, J. Wallenius, S. Bortot, Nucl. Eng. Des. 252 (2012) 209
[8]   V. P. Nikitin et al, Atomic Energy 2000 (88) 2
[9]   J. Wallenius, CONFIRM final report, KTH 2009
[10] M. Streir et al, J. Nucl. Mater. 319 (2003) 51
[11] V. Basini et al, J. Nucl. Mater. 344 (2005) 186
[12] I. A. Shkabura et al, Material Science and New Materials 67 (2006) 2
[13] M. V. Skupov et al, Material Science and New Materials, 67 (2006) 2
[14] M. Akabori et al, Proceedings of GLOBAL 2005, Oct 9-13, No. 320
[15] M. Takano et al, J. Nucl. Mater. 389 (2009) 89
[16] K. Minato et al, J. Nucl. Mater. 389 (2009) 23
[17] M. Pukari, J. Nucl. Mater, *in press* (2012)
[18] J. L. Seran et al, 15th International Symposium ASTM STP 1125 (1992) 1209-33
[19] G. Muller et al, J. Nucl. Mater. 335 (2004) 163-168
[20] J. Lim, I. S. Hwang, J. H. Kim, J. Nucl. Mater. (2012)
[21] M. Del Giacco et al, J. Nucl. Mater. 421 (2012) 39-46
[22] A. Weisenburger et al, J. Nucl. Mater. 375 (2008) 274-281
[23] S. Takaya et al, J. Nucl. Mater. 386 (2009) 507-510
[24] R. Fetzer et al, Corros Sci, 55 (2012) 213-218
[25] A. Heinzel, M. Kondo, M. Takahashi, J. Nucl. Mater. 350 (2006) 264-270
[26] S. Takaya et al, J. Nucl. Mater. 398 (2010) 132-138
[27] J. Isselin et al, Mater Trans, 51 (2010) 1011-1015.
[28] P. Hosemann et al, J. Nucl. Mater. 373 (2008) 246-253.
[29] V. Engelko et al, Vacuum, 62 (2001) 211-216.
[30] G. Muller, G. Schumacher, F. Zimmerman J. Nucl. Mater. 278 (2000) 85-95
[31] Sveriges Riksdag, 1988, Strålskyddslag (1988:220)
[32] Swedish Radiation Safety Authority, "Regulations Concerning the Design and Construction of Nuclear Power Reactors" 2008, SSMFS (2008:17)
[33] IAEA Safety Standards Series No. SSG-12, "Licensing Process for Nuclear Reactors" 2010
[34] IAEA Safety Standards Series No. NS-G-2.5, "Core Management and Fuel Handling for Nuclear Power Plants" 2002
[35] J. C. Mankins, NASA, "Technology Readiness Levels", White Paper, Apr. 6, 1995

[36]   DOE, ASD R&E, "Technology Readiness Assessment Guidance", May 13, 2011

[37]   T. Nishi et al, J. Nucl. Mater. 377 (2008) 467

[38]   H. Muta et al, J. Nucl. Mater. 389 (2009) 186-190

[39]   M. Takano et al, Proc. Global 2003, Nov.16-20, 2003, New Orleans, 2285-2291

[40]   D. Grischenko, private communication, KTH 2012

[41]   R. Thetford, M. Mignanelli, J. Nucl. Mater. 320 (2003) 44-53

[42]   K. Lassmann, J. Nucl. Mater. 188 (1992) 295-302

[43]   Y. Dai et al, J. Nucl. Mater. 431 (2012) 66-76

[44]   M.K. Miller, R.E. Stoller, K.F. Russell, J. Nucl. Mater. 230 (1996) 219-225

[45]   B. Jonsson et al, High Temperature Corrosion and Protection of Materials 6, Part 1 and 2, Proceedings, 461-464 (2004) 455-462

[46]   A. Gessi, Specifica Tecnika Prove LEXUR II, Report RdS/2010/105, ENEA, September 2010

[47]   J. Lim et al, J. Nucl. Mater. 407 (2010) 205-210

Sinterability of ZrN and $(Zr_{0.6}Dy_{0.4})N$ pellets - surrogate fuel fabrication for ELECTRA

Merja Pukari[a]**, Masahide Takano**[b]

[a] KTH Royal Institute of Technolog, Roslagstulssbacken 21, SE-10691, Sweden

[b] Nuclear Sicence and Engineering Directorate, Japan Atomic Energy Agency, Tokai-mura, Ibaraki-ken, 319-1195, Japan

Abstract. Pellets of inert matrix material ZrN and surrogate nitride fuel material $(Zr_{0.6}Dy_{0.4})N$ are fabricated for the purpose of investigating the origin and the effect of C and O impurity concentrations. Oxygen concentrations of up to 1.5 wt% were deliberately introduced to the materials with two separate methods. The achievable green and sintered pellet densities of these materials as a function of O content, dimensional properties of the powder and sintering temperature are shown. The effect of O dissolved into the matrix vs oxide-rich phase segregation is discussed. Oxygen pickup during the fabrication of the product as well as its exposure to air is demonstrated. The quality of the materials is monitored by the systematic analysis of O, N and C contents throughout the fabrication and sintering processes, supported by XRD and SEM analyses.

INTRODUCTION

Nitride fuel is valued for its exceptional thermo-physical properties, such as high thermal conductivity [1] and melting temperature [2]. A recently published report on Pu-bearing nitride fuel furthermore illustrates the symbiotic swelling behaviour and fission gas retention under irradiation [3]. The compatibility with liquid lead coolant [4] in addition to nitride fuel being reprocessable with industrially established technology [5][6][7] makes nitride fuel a desirable option for the 0.5 MW ELECTRA [8]. In the low power fast reactor, cooled with natural convection of lead, $(Zr_{0.6}Pu_{0.4})N$ is the chosen fuel composition.

Over the decades, the properties of actinide nitrides and the according inert matrix materials have been generally well established. However, in order to realize the fuelling of ELECTRA, the impact of O and C impurities in the fuel must be thoroughly studied. On the one hand, high concentrations of O and C impurities might lead to internal cladding corrosion or carburization. Moreover, it has been shown that a significant O concentration in (Zr,Pu)N leads to PuO_2 phase separation [9][10]. The latter, in turn, complicates the reprocessing of fuels. On the other hand, minimising the impurity content comes at a significant cost, as it sets stringent requirements on the fabrication facilities and source materials. The impurity levels are especially difficult to keep low, due to the remnant C from carbothermic reduction of actinide oxides on the one hand, and due to the nitrides readily reacting with moisture and oxygen [11][12].

Previous experimental work suggests that an increased O content in actinide nitrides might lead to a higher sintered pellet density. The current study systematically investigates sinterability of ZrN and $(Zr_{0.6}Dy_{0.4})N$ pellets as a function of varying O content, the particle size of powders and temperature. $(Zr_{0.6}Dy_{0.4})N$ pellets are employed as a surrogate fuel material, similarly to previous studies [13], due to the chemical and lattice parameter similarities between Dy and Pu. Finally, the influence of the materials of the milling equipment used, as well as O solubility in ZrN and $(Zr_{0.6}Dy_{0.4})N$ is discussed.

The goal of studying the origin of these impurities and their impact on the fuel properties and behaviour is to optimise the fabrication route of $(Zr_{0.6}Pu_{0.4})N$ fuel for ELECTRA. The current study is

1

a part of a series of experiments focusing on C and O impurities, in course of which the fuel-cladding chemical interaction, the fission product solubility and phase segregation in a fuel corresponding to ELECTRA's specifications will be studied. Ultimately, this work will aid in the licensing of the fuel fabrication and the core for ELECTRA [14].

EXPERIMENTAL SETUP

The materials fabricated for this study follow largely the envisaged fabrication route for ELECTRA, which will be carried out in a laboratory scale facility. Metallic Zr is nitrided into ZrN through an intermediate hydrogenation step. Despite the PuN fabrication for ELECTRA being carried out by the carbothermic reduction of PuO_2, hydrogenation-nitridation of Dy metal is employed here for fabricating the actinide nitride surrogate DyN. All fabrication phases are conducted in an inert atmosphere, where O_2 and H_2O concentrations are kept at <4 ppm.

Sample preparation

High purity Zr metal chips (0.096 wt% O; <0.001 wt% N; <0.001 wt% C by measurement) are heated at 15K/min to 733 K and hydrogenated during 24 h in a 20%H_2-Ar mixed gas flow. The formation of a hydride, with a H/Zr ratio of 1.92, is confirmed with an X-ray diffraction (XRD) analysis. The coarsely pulverized $ZrH_{1.92}$ is subsequently nitrided at 1573 K (at 15K/min) for 5 h in a purified N_2 gas flow. A 30-min isotherm at 1073 K is incorporated into the heating curve, to accommodate for the exothermic reactions during nitridation. The obtained true nitride composition is determined, with the aid of a quantitative analysis of light elements, to be $Zr(N_{0.99}O_{0.01})_{0.97}$, corresponding to 0.11 wt% O and <0.01 wt% C. The same fabrication procedure is applied for a Zr metal ingot as a source material, in which case a nitride with significantly lower O content is obtained (<0.03 wt% O, <0.01 wt%C). Both materials, ZrN fabricated from metal chips and bulk material, are used in the experiments. The formation of ZrN was confirmed and the corresponding lattice parameter of 4.5753 Å determined with an XRD analysis.

A Dy metal ingot (99.9% Dy, NewMet Koch) was used to fabricate DyN in the same fashion as described above, with the exception of a 29 h hydrogenation step. After the nitridation of the coarsely pulverized $DyH_{2.15}$, a nitride with a significant O content (0.28 wt%) was obtained. The determined lattice parameter 4.9010 Å is in good agreement with the previously reported value, valid for the given O content in the material [15].

Oxygen content of up to 1.5 wt% is achieved by introducing an appropriate amount of ZrO_2 to the materials. The mixtures were homogenized by milling and heat treatment. Two batches of solid-solutionized $(Zr_{0.6}Dy_{0.4})N$ are fabricated by blending ZrN and DyN in a 60-40 molar ratio, considering their true compositions, in order to obtain a varying O content. A high-speed planetary ball mill with a 45 ml tungsten carbide (WC) pot and balls was employed in ensuring a homogeneous mixture prior to pelletizing the blends. The pellets were subsequently heat-treated at 1873 K for 20 h in a purified N_2 gas flow. The formation of a solid solution was confirmed with an XRD analysis; the representative lattice parameter 4.6881Å is discussed in a following section.

The sintered ZrN and $(Zr_{0.6}Dy_{0.4})N$ pellet densities as a function of powder particle size are studied by milling the powders for a short (60 min), a medium (100 min) and a long (120 min) period at a rotation speed of 800 rpm/revolution speed of 400 rpm prior to pelletizing. O and C pickup during milling is investigated by using a WC and an Y_2O_3-stabilized ZrO_2 (YSZ) milling equipment. Milled powders are pelletized at a pressure of 300 MPa without any binding agent, using a 6.3 mm diameter die. The pellets are subsequently sintered at 1923 or 1973 K for 6 h in a N_2 gas atmosphere. The dimensions of green and sintered pellets are measured using a micrometre screw gauge.

Sample analysis

Powder XRD measurements with Cu-Kα radiation are performed to identify the materials fabricated and to monitor the occurrence of secondary phases. A diffraction angle range from 25 to 150 degrees

in 2θ is chosen to adequately determine the lattice parameters, for which a profile fitting software with Pawley function is employed. XRD measurements are carried out in air atmosphere. The structure of the sintered pellets is additionally analysed with an optical and scanning-electron microscope (SEM). The composition of nitrides was assessed with the aid of energy-dispersive X-ray spectroscopy (EDX).

The N, O and C contents are evaluated throughout the fabrication with the quantitative analysis of light elements [15]. Surface area measurements of milled powders are carried out, complimented with particle size distribution measurements by laser diffraction.

RESULTS AND DISCUSSION

The fabricated ZrN and $(Zr_{0.6}Dy_{0.4})N$ pellets before and after sintering are shown in Figure 1. A 6-hour sintering period increases the density of the pellets from roughly 62-65 %TD to 88-94 %TD, depending on the material and the fabrication parameters in question. During sintering, the weight of ZrN pellets increases marginally, presumably due to the increasing N/Zr ratio and the residual O from the gas flow. The $(Zr_{0.6}Dy_{0.4})N$ pellets, on the other hand, show a slight decrease in weight as a consequence of sintering. Despite the absorption of light atoms, it is likely that the dissociation of Dy dominates the weight balance.

FIG. 1. From left, images of green ZrN pellets, sintered ZrN pellets and green $(Zr_{0.6}Dy_{0.4})N$ pellets. A sintered $(Zr_{0.6}Dy_{0.4})N$ pellet is nearly identical in its appearance to a sintered ZrN pellet

The lattice parameters of the sintered ZrN pellets over the tailored O concentration range are indistinguishable from that of the fabricated ZrN (4.5753 Å) with the lowest O concentration. A different trend governs sintered $(Zr_{0.6}Dy_{0.4})N$, as the lattice parameter for the sintered material decreases with an increasing sintering temperature and milling. The obtained lattice parameters, corresponding to the specific fabrication details, are provided in Table 1. The relevance of the decrease in lattice parameters is discussed below.

Table 1. Variations in the lattice parameters of sintered $(Zr_{0.6}Dy_{0.4})N$ pellets as a function of the preparation parameters, including milling time, sintering temperature and O content.

Milling time, min	60	60	100	60	60
Sintering T, K	1923	1973	1973	1923	1973
O content	Low	Low	Low	High	High
a	4.6869	4.6867	4.6862	4.684	4.6839

Milling time and equipment effect on impurity concentrations

ZrN powders were milled for 60 or 120 minutes with either YSZ or WC milling pot and balls in order to determine the suitable fabrication path. As indicated in Figure 2, both the milling time and the equipment used have a measureable effect, as O levels are increased between 40 and 250% during milling. YSZ is inherently more likely to contaminate the powder, whereas a longer milling time will accommodate O pickup regardless of the milling equipment used. Despite the purified N_2 gas flow

used for sintering, O contamination increases significantly during sintering, as ZrN is particularly susceptible to oxidation at elevated temperatures [12]. The rise in O levels corresponds to the smaller powder particle size. Note that the sintering of YSZ-milled and WC milled pellets was carried out on two separate occasions, and therefore the non-consistent O content in the furnace atmosphere is the likely cause for the elevated values of YSZ-milled samples.
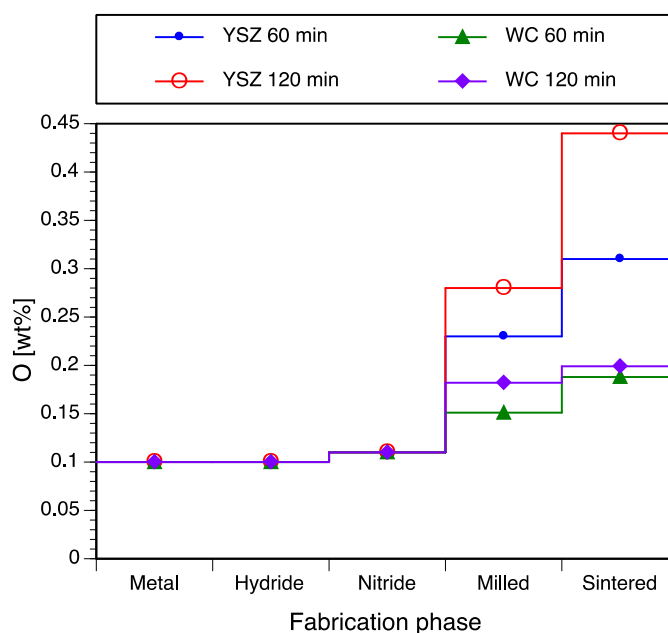

FIG. 2. Oxygen pick-up during the fabrication of ZrN pellets

The length of milling times with YSZ and WC equipment is not strictly comparable, as powders with different particle size are obtained due to the differences in the densities of the milling equipment materials. The conducted surface area measurements reveal that a 60 and 120-min milled ZrN with WC equipment yields powders with specific surface areas of 5.86 $m^2 \cdot g^{-1}$ and 7.68 $m^2 \cdot g^{-1}$. The same milling times with YSZ equipment result in 4.13 $m^2 \cdot g^{-1}$ and 6.49 $m^2 \cdot g^{-1}$, respectively. In light of these values, the effect of the milling equipment material, illustrated in Figure 2, is even more pronounced.

The drawback of using WC equipment is the elevated C concentration. The C content at <0.01 wt% in the fabricated ZrN does effectively not increase during milling with the YSZ equipment. Conversely, the levels are increased to 0.03 wt% if WC equipment is used. Carbon limits in fuel have not been singularly defined and therefore the importance of the C quantity is hard to estimate. Based on the impurity concentration introduced by the fabrication route, the YSZ milling equipment was not used for fabricating $(Zr_{0.6}Dy_{0.4})N$.

Exposure to air

The O concentration and its effect on the sintered pellets is investigated by contaminating samples of the 60 and 120-minute milled ZrN powders, exposing them to air for a maximum of 130 and 60 minutes, respectively. The relative weight gain of these powders, as a function of time, is illustrated in Figure 3. Additionally, a separate set of powders was exposed for a 10-minute period, in order to obtain a lower O contamination.

A substantial weight is absorbed by the sample briefly after the material is exposed. However, the weight gain can arise due to oxidation as well as moisture absorption in the sample, as the humidity in the air (84%) was substantially higher than that in the glove box. These powders were subsequently pressed into pellets and sintered, in order to detect whether the O would result in an oxynitride, an oxide, or be dissolved into the lattice. As the NOC analysis reveals, O content is significantly increased in these samples, it being higher in the finer powder. The results indicate that the O content

4

increases rapidly during the first minutes of exposure. We must therefore also conclude that the handling of ZrN powder for even a short amount of time outside the inert atmosphere will render other measures to protect the samples from oxidation useless.
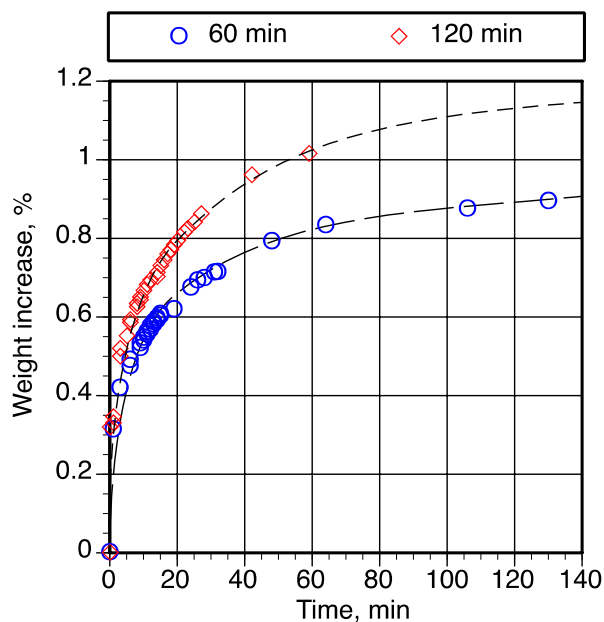

FIG. 3. Weight increase of a 60-min and 120-min milled ZrN powders when exposed to air for 130 min and 60 min, respectively.

Sinterability

The achieved densities of sintered ZrN pellets with the O content varying between 0.2 and 1.23 wt% is provided in Table 2. The obtained densities of 87.5 – 92.1 %TD depend on the fabrication methods applied. Higher O content ZrN pellets, fabricated by introducing a small fraction of ZrO_2 into the material, reveal no conclusive trend on the achievable densities, although a small proportional increase is seen in the 120-min, YSZ milled material. To the contrary, WC milled material, exposed to air for a short or a long interval, reaches consistently higher densities in comparison with the low O concentration material. The values for pellets, fabricated from air-exposed material, must be considered with some reservation, as a single pellet per fabrication parameters was sintered, in contrast to the 3 pellets sintered otherwise. As expected, a longer milling time, and therefore a smaller particle size, leads to a higher sintered density. Nevertheless, the increase in density between materials milled with WC equipment for 60 (5.86 m^2/g) and 120 minutes (7.68 m^2/g) is negligible, corresponding to 89.6 %TD and 90.1 %TD.

Similar values for $(Zr_{0.6}Dy_{0.4})N$ are reported in Table 3, where the effect of temperature is additionally demonstrated. The sintered pellet densities, in the range of 92.4 – 94.5 %TD, are somewhat higher than those for ZrN pellets, in spite of the same fabrication methods. In addition, the ZrO_2-induced higher O content has a measureable effect on the sintered pellet density, increasing it by more than 1%TD at the standard sintering temperature of 1973 K. The effect is less pronounced at 1973 K, measuring to about 0.5 %TD. As expected, a lower sintering temperature yields a lower pellet density.

The density of pellets fabricated from 100-min milled powder is in fact lower than that from 60-min milled powder, contrary to expectations. A thorough investigation has revealed that a longer milling time seems to have, in fact, adverse impact on the sinterability, as a finer powder results in 56% higher weight loss during sintering, which may originate from Dy dissociation. Loss of material during the sintering of actinide nitrides, especially that of Am, is well established [12]. Therefore, the dissociation of the chemically similar Dy is expected, and is furthermore supported by an XRD analysis. The determined lattice parameter of the single-phase $(Zr_{0.6}Dy_{0.4})N$, after forming a solid

solution (a=4.6881 Å), is notably lower than that expected from Vegard's law, indicating that Zr/Dy > 1.5 as a consequence of the heat treatment. The subsequent sintering of the nitride decreases the lattice parameter further. The latter is supported by EDX analysis, though is not conclusively determinable by relative weight changes during the heat treatment. The effect of an inaccurate determination of hypostoichiometry does not significantly alter the required ZrN to DyN ratio to be initially blended, so that the divergence from the designed 60-40 ratio must derive from a post-blending step. A similar change in the composition is observed on three separate occasions of fabricating $(Zr_{0.6}Dy_{0.4})N$. The Zr/Dy ratio determined by EDX analysis is the foundation for determining the theoretical density of the materials, used in further calculations. In summary, the best estimate of the true compositions of the materials has been used to determine the theoretical density.

Table 2. Properties of sintered ZrN pellets as a function of their preparation parameters, including milling time, equipment used and O content.

Milling time, min	60	60	60	120	120	120	60	60	60	120	120	120
added ZrO_2	-	low	high	-	low	high	-	-	-	-	-	-
Milingl equipment	YSZ	YSZ	YSZ	YSZ	YSZ	YSZ	WC	WC	WC	WC	WC	WC
exposure to air	-	-	-	-	-	-	-	short	long	-	short	long
O wt%	0.31	0.71	1.23	0.44	0.86	1.22	0.2	0.88	0.8	0.2	0.9	1.04
C wt%	0.01	0.01	0.01	0.01	0.01	0.01	0.03	0.02	0.03	0.03	0.02	0.02
non-metal/metal	1.01	1.03	1.05	1.02	1.03	1.05	0.99	1.01	1	1	1.02	1.03
N/(N+O+C)	0.98	0.95	0.92	0.97	0.94	0.92	0.98	0.94	0.94	0.98	0.94	0.93
O/(N+O+C)	0.02	0.05	0.08	0.03	0.05	0.08	0.01	0.06	0.05	0.01	0.06	0.07
C/(N+O+C)	0	0	0	0	0	0	0	0	0	0	0	0
%TD	87.5	87.9	87.7	91.3	91.5	91.8	89.6	91.6	91.3	90.1	91.7	92.1
Error %TD	0.3	0.3	0.2	0.2	0.4	0.1	0.4	single d.p.	single d.p.	0	single d.p.	single d.p.

Table 3. Properties of sintered $(Zr_{0.6}Dy_{0.4})N$ pellets as a function of their preparation parameters, including milling time, sintering temperature and O content.

ZrO_2 added	-	-	-	low	low
Milling time, min	60	60	100	60	60
Sintering T, K	1923	1973	1973	1923	1973
O wt%	0.239	0.24	0.258	0.585	0.586
C wt%	0.015	0.018	0.039	0.013	0.014
non-metal/metal	0.971	0.971	0.971	0.991	0.991
N/(N+O+C)	0.979	0.978	0.974	0.951	0.95
O/(N+O+C)	0.02	0.02	0.021	0.048	0.048
C/(N+O+C)	0.002	0.002	0.004	0.001	0.002
%TD	92.4	93.2	93.1	92.9	94.5
error %TD	0.1	0.1	0.3	0.4	0.4

Oxygen solubility

It is frequently shown that a fabricated ZrN tends to be hypostoichiometric [16]. Therefore, the non-metal to metal atom ratios provided in Table 2 lead to the conclusion that an O-rich secondary phase must be present in the fabricated materials, presumably ZrO_2. Whether this occurs due to a poor homogenization during the fabrication of the materials, or the inherently low O solubility in ZrN is not

clear. The presence of a secondary, O-rich phase is observable by analysis with XRD, SEM and an optical microscope. An indicator for a very low amount of O dissolved into the ZrN is the invariance of lattice parameters, regardless of the O content introduced. However, this cannot be seen as conclusive evidence, as previous work has shown that the crystal structure of ZrN is not prone to alterations in the event of, for example, a high number of vacancies [16][17].

The segregation of an O-rich phase was not confirmed in ZrN pellets fabricated from material exposed to air. We must therefore conclude that the differences in obtainable densities of sintered ZrN are caused by the different mechanism of O inclusion in the material. This is supported by the fact that in the air-exposed materials, at an O content of about 0.8 wt%, no oxide phase is detected. To the contrary, at O concentrations as low as 0.3 wt% an oxide phase is present, if the O contamination is obtained by an addition of ZrO_2. A measurement on 60-min and 120-min milled materials, exposed to air for over a week, revealed no oxide phase present.

The non-metal to metal atom ratios in Table 3 illustrate that no O-rich phase is present at the given O concentrations. Previous research has shown that O in DyN is highly soluble at high temperatures [15] and therefore it is credible that at 0.6 wt% O, the solubility limit is not reached.

CONCLUSIONS

Our findings indicate that O, if dissolved into the rock-salt nitride phase, aids to some extent in reaching a higher density of $(Zr_{0.6}Dy_{0.4})N$ pellets. Furthermore, O might aid the sinterability of ZrN pellets, if dissolved into the material. It is possible that the obtained densities of the ZrO_2-enriched ZrN pellets do not reveal such a trend due to the oxide phase segregation in the material. The materials of milling equipment influence significantly the impurity levels in the product. After reaching the surface area of about 6 $m^2 \cdot g^{-1}$, the gain in sintered pellet density is negligible. Furthermore, a smaller particle size enhances the dissociation of Dy, and by extension, actinides. A decrease in sintering temperature reduces the achievable density. Sintering of $(Zr_{0.6}Dy_{0.4})N$ pellets yields higher densities than those of ZrN, all fabrication parameters kept same. Therefore, the matrix material ZrN serves only as a first approximation for ELECTRA specific fuel fabrication. Similar research on $(Zr_{0.6}Pu_{0.4})N$ must be carried out in order to adequately determine the influence of C and O impurities on ELECTRA fuel.

ACKNOWLEDGEMENTS

REFERENCES

[1] S. Hayes, J. Thomas, K. Peddicord, JNM 171 (23) (1990) 289-299
[2] S. Sunder, N. H. Miller, J. Alloys Compd, 271-273 (1998) 568-572
[3] J. Wallenius, CONFIRM: Final Technical Report on Collaboration on Nitride Fuel Irradiation and Modelling, Royal Institute of Technology 2009
[4] H. Bailly, D. Menessier, C. Prunier, The Nuclear Fuel of Pressurized Water Reactors and Fast Reactors: Design and Behaviour, Intercept Ltd, 1999H.
[5] Kleykamp, JNM 275 (1) (1999) 1-11
[6] L. M. Ferris, Journal of Inorganic and Nuclear Chemistry 30 (10) (1968) 2661-2669
[7] N. Hadibi-Olschewski et al, JNM 188 (1992) 244-248
[8] J. Wallenius, E. Suvdantseg, A. Fokau, Nuclear Technology 177 (2012) 303-313
[9] L. Zabudko et al, "Fuels for Advanced Sodium Cooled Fast Reactors in Russia: State-of-Art and Prospects", presented at Proc. Int. Conf. Fast Reactors and Related Fuel Cycles FR09, Kyoto, Japan, December 7-11, 2009
[10] M. Streit, F. Ingold, Journal of the European Ceramic Society 25 (12) (2005) 2687-2692
[11] M. Takano, J. Phys. Chem. Solids, 66 (2005) 697-700

[12]   M. Takano et al, Proc. Global 2003, Nov 16-20, 2003, New Orleans, 2285-2291

[13]   M. Takano et al, J. Alloys and Compounds, 439 (2007) 215-220

[14]   M. Pukari, J. Ejenstam, J. Wallenius, A Strategy for Fuelling Electra, presented at International Conference on Fast Reactors and Related Fuel Cycles (FR13), France, 4-7 March 2013

[15]   M. Takano et al, Journal of Alloys and Compounds, 327 (2001) 235-239

[16]   A.N. Christensen, S. Fregerslev, Acta Chem. Scand. Ser. A, 31 (1977), pp. 861–868.

[17]   N.J. Ashley, R.W. Grimes, K.J. McClella, J, Mater. Sci., 42 (2007), pp. 1884–1889

Performance assessment of MOX fuel with Alloy D9 cladding and wrapper irradiated in FBTR

Jojo Joseph, Divakar Ramachandran, C. N. Venkiteswaran, V. Karthik, T. Johny, B. P. C. Rao, T. Jayakumar

Metallurgy and Materials Group, Indira Gandhi Centre for Atomic Research, Kalpakkam, TN 603102, India

Presented by Divakar Ramachandran

Abstract A test fuel sub-assembly (FSA) with 37 fuel pins consisting of annular MOX fuel pellets encapsulated in Alloy D9 cladding and wrapper simulating the fuel design of the Prototype Fast Breeder Reactor (PFBR) was irradiated to a peak burn-up of 112 GWd/t in the FBTR and subjected to post-irradiation examination (PIE) at the Radiometallurgy Laboratory (RML) of IGCAR. The investigations consisted of non-destructive and destructive tests designed to evaluate the performance of the fuel and structural materials. Moderate fuel swelling and fission gas release of around 85% was observed. Non-destructive tests gave indications of changes in the central hole dimensions of the fuel pellet and Fuel-Clad Chemical Interaction (FCCI) and these were confirmed by metallographic sections. Initiation of FCMI was also revealed at the core top locations. The Alloy D9 cladding and wrapper have performed satisfactorily with respect to swelling resistance and residual mechanical properties up to the maximum displacement damage of about 60 dpa that has been attained in the FBTR. The results give confidence to operate PFBR with the designated fuel design.

INTRODUCTION

The Fast Breeder Test Reactor (FBTR) at Kalpakkam, India is being utilised as a test facility for irradiation of the fuel and structural materials envisaged for the future fast reactors. 500 MWe Prototype Fast Breeder Reactor (PFBR), the front runner of the commercial fast breeder reactors (CFBR) in India, is now in an advanced stage of construction at Kalpakkam. It is designed to operate with mixed-oxide (MOX) annular fuel pellets encased in cladding and wrapper made of Alloy D9 (Ti-modified austenitic stainless steel) at a linear heat rate (LHR) of 450 W/cm, with an initial target burn-up of 100 GWd/t. While considerable international irradiation experience is available with MOX fuels and Alloy D9 structural materials, it was required to demonstrate and evaluate the performance of the annular fuel design for a burn-up exceeding 100 GWd/t under conditions as close as feasible to the irradiation conditions in the PFBR. Accordingly, an experiment was performed to irradiate a few short length fuel pins containing MOX fuel with D9 cladding and wrapper in FBTR. Detailed PIE has been carried out on this test fuel sub-assembly (FSA). The results of the PIE campaign are reported in the present paper.

IRRADIATION EXPERIMENT AND POST-IRRADIATION EXAMINATION

The test fuel composition used in the present irradiation experiment was 29% PuO_2, 38% oxide of U^{233} and balance 33% oxide of natural Uranium. The composition was designed such that the test FSA operates at a peak LHR of 450 W/cm at the FBTR core centre when the Mark I driver fuel (U0.3 Pu0.7)C in the first ring is operated at a peak LHR of 320 W/cm. The test FSA had 37 fuel pins of 6.6 mm outer diameter and 5.7 mm inner diameter which is the same as that for PFBR. However the length of the fuel pin is 531.5 mm, same as that of FBTR fuel pin. The fuel pellet is 5.56 mm outer diameter with a nominal central hole diameter 1.75 mm. Active fuel column length is 240 mm as against 320 mm for FBTR fuel and the fuel column is arranged such that the top of the MOX fissile column is aligned with the top of the Mark I core. Salient FSA details are summarised in Table 1. The clad and wrapper are made of 20 % cold worked Ti-modified austenitic stainless steel of

composition (in wt %) Cr:13.5-14.5, Ni:14.5-15.5, Mo:2.0-2.50, Mn:1.65-2.35, Si:0.5-0.75, C: 0.035-0.050, Ti:5C-7.5C, P: 0.02 max.

Table 1. PFBR MOX Test fuel sub-assembly parameters

MOX fuel composition	29% PuO_2, 71% UO_2 (53.5% U^{233})
Fuel O/M ratio	2.00
No. of fuel pins & fuel stack length	37 pin, 240 mm
Fuel pellet linear mass (g/cm)	2.18
Fuel Density (%TD)	91 $\pm$ 1%
Annular pellet OD & ID (mm)	5.56 & 1.75
Fuel pin OD & ID (mm)	6.6 & 5.7
Clad & Wrapper material	Ti-modified SS 316 steel (20% CW)
Peak linear power & displacement damage	450 W/cm , 62 *dpa*

The test FSA loaded into the FBTR in June 2003 attained a burn-up of 112 GWd/t after nearly 90 months of irradiation with a peak LHR of 450 W/cm. The inlet sodium temperature range was 350 – 380 ℃ and the outlet sodium temperature range was 435 – 480 ℃. The FSA underwent an in-pile cooling period of four months and a further three months out of pile before it was received in the hot-cells of RML for PIE.

The hot-cells of RML are α/β/γ type, concrete shielded, with inert atmosphere and equipped with a range of PIE equipment, most of which are designed and fabricated in-house [1]. The test FSA was subjected to sodium removal using high purity ethanol in a recirculatory system followed by visual examination and remote metrological measurement to determine the irradiation induced dimensional variations of the FSA. It was subsequently dismantled and the fuel bundle was extracted using a laser based dismantling system. The fuel pins were subjected to non-destructive evaluations by profilometry, eddy current testing, X-radiography, neutron radiography and gamma scanning. Selected fuel pins were subjected to puncture test and sectioning for fission gas analysis and metallographic examinations respectively. Mechanical testing was carried out on clad tube specimens after removal of the fuel by dissolution, while wrapper mechanical tests were carried out on flat tensile specimen fabricated in the hot-cell using a CNC machine [2]. The specimens were subjected to swelling measurements by liquid immersion method within the hot-cell, prior to mechanical testing.

RESULTS AND DISCUSSIONS

1.1. Metrological measurements

Dimensional measurements were carried out on the FSA using a remotely controlled machine using an omni-directional induction type touch trigger sensor to determine the increase in the width-across-flats, increase in the corner-to-corner distances and the head-to-foot misalignment. The hexagonal wrapper indicated a head-to-foot misalignment of 1.8± 0.1 mm which is well within the permissible limit for safe fuel handling in FBTR. The increase in the width across flats for the FSA was found to be varying along its length with a maximum increase of 0.4 mm in the core centre region as compared to the dimensions at the ends of the FSA. The maximum increase in the corner-to-corner distance was found to be 0.31±0.02 mm at the axial location of FSA coinciding with the core centre as compared to the corresponding dimensions at the end of the FSA.

It is well known that the increase in the width across flats is influenced by swelling and creep strains whereas the increase in the corner-to-corner distance is influenced by the effect of swelling alone. Thus the swelling component of the total maximum strain for the wrapper, deduced from the corner-to-corner distances, is seen to be 0.54% compared to combined swelling and irradiation creep related strain of 0.8% deduced from the width across flats measurements. Irradiation induced swelling thus accounts for over 67% of the total strain for the wrapper, while irradiation creep accounts for the rest.

In the case of the fuel cladding material, the increase in diameter measured by profilometry ranged from 0.056 mm to 0.091 mm (Fig. 1) with the peak diametral strain ($\Delta D/D$) calculated to be about 1.38%. Irradiation induced swelling of the fuel cladding was determined from immersion density measurements. The cladding exhibited a maximal void swelling of 2% $\Delta V/V$. Comparing the two measurements, it is seen that the swelling component was only 45% (swelling strain ~ 0.6%) of the total diametral strain and the remaining could be attributed to irradiation creep strain possibly caused by the internal fission gas pressure.
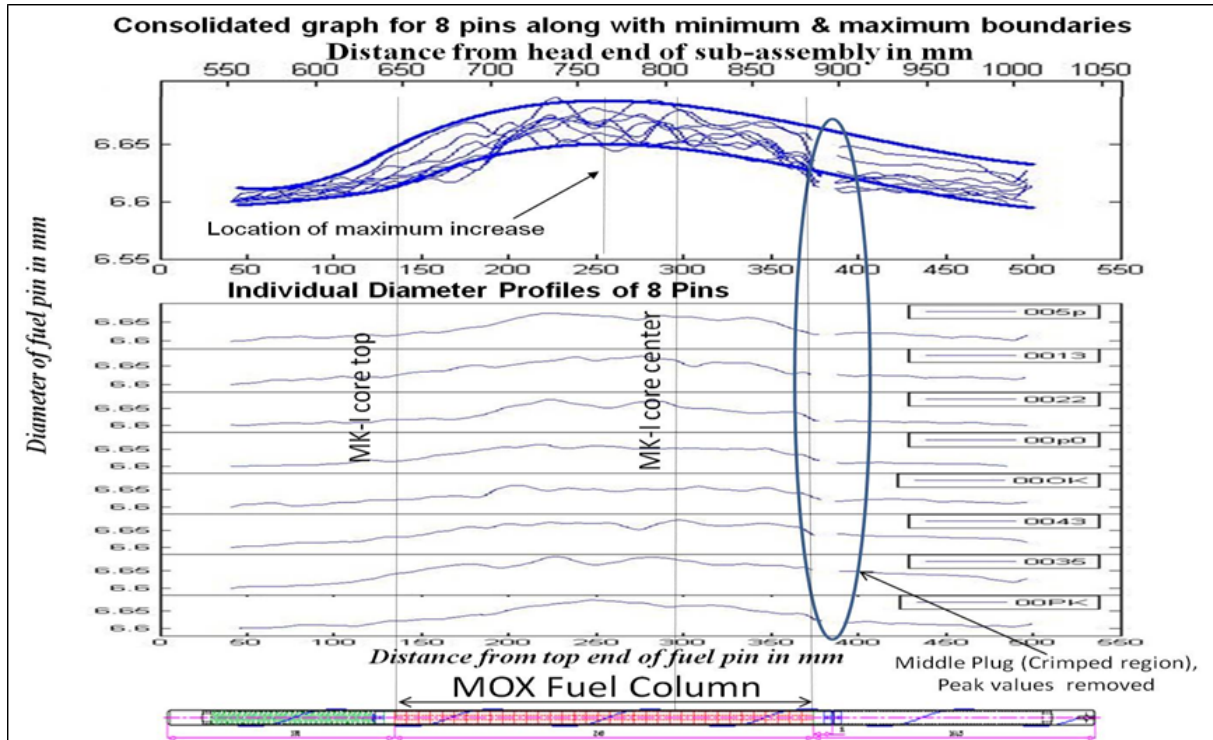

FIG. 1. Diameters of a few selected fuel pins as measured by profilometry

The swelling values of the Ti-modified austenitic stainless steel cladding and wrapper obtained by immersion density measurements confirm that this alloy swells much less compared to SS 316 used for the cladding and wrapper of the driver FSA of FBTR at similar displacement damages (Fig. 2). This is on expected lines due to the extension of the incubation dose for swelling of D9 as compared to 316 SS [3]. The swelling is seen to peak at locations corresponding to a mid wall temperature of about 500ºC. Alloy D9 cladding was seen to swell more as compared to the Alloy D9 wrapper specimens taken from the same axial locations along the fuel column. This is attributed to lower operating temperatures of the wrapper compared to the cladding and the differential swelling strains due to the temperature gradients across cladding wall.
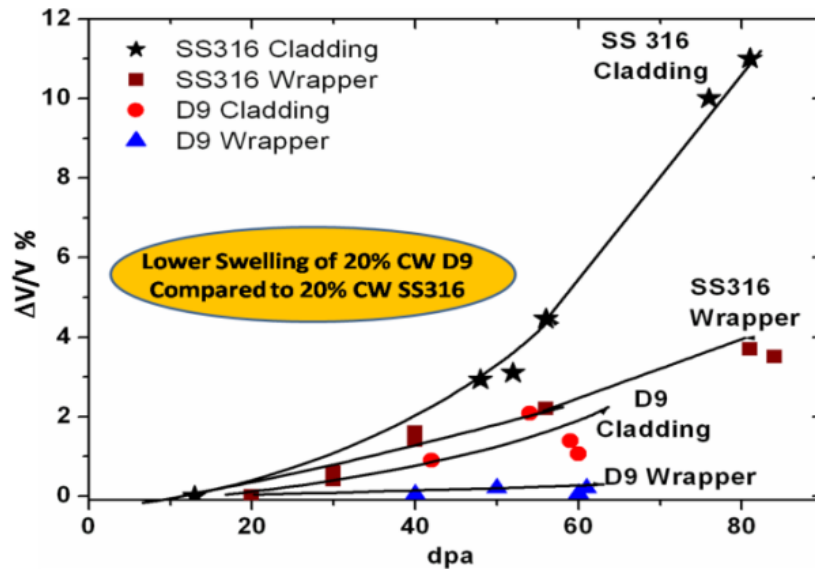
FIG. 2. Swelling of Ti-modified austenitic stainless steel clad and wrapper compared with SS316

1.2. Non-destructive Evaluation

The fuel pins were examined by X-radiograhy, eddy current testing (ECT), neutron radiography (NR) and gamma scanning techniques for nondestructive assessment. X-radiography was used to estimate the fuel stack length variation, pellet-to-pellet gap and pellet-to- clad gap to assess the integrity of the fuel pellets, while EC testing was carried out to assess the structural integrity of the cladding [4].

The X-radiography parameters such as applied voltage, current and exposure time were optimized to minimize the effect of gamma fogging on the film. A 6.6mm diameter dummy stainless steel fuel pin was used as a calibration pin for dimensional measurements. The radiography films were digitized and subjected to image processing operations such as contrast stretching and brightness adjustment followed by high-pass filtering. Detailed analysis on the radiographs revealed a maximum increase in the fuel stack length of 1.4% (~ 3.23mm) and minimum of 0.2% (~0.46mm). Radial cracks were observed in a few pellets as typically shown in Fig. 3. Pellet-to-pellet and pellet-to-clad gap were also seen at a few locations in some of the fuel pins.
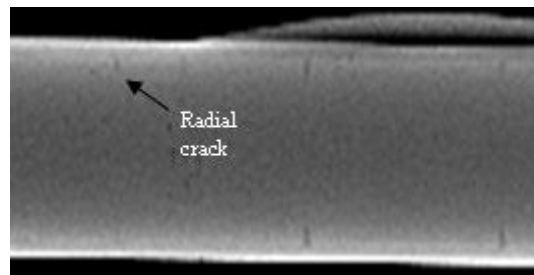
FIG. 3. Digitized radiography image of fuel column showing radial cracks.

For eddy current testing purpose, a differential encircling probe operating at 350 kHz was used. A 0.3 mm diameter hole was used as a reference defect to calibrate the EC instrument. A single stage vertical scanning system was used to move the EC probe over the fuel pin. EC data was continuously acquired during the scanning and later subjected to offline signal processing methods to remove drift and noise. Fig. 4 shows the typical horizontal, vertical and amplitude signals from a fuel pin. Detailed analysis of the processed EC signals revealed presence of defects on the inner surface of the clad tubes and this was later confirmed by sectional metallography.

FIG. 4. Typical eddy current signals from a fuel pin.

Gamma scanning was carried out for evaluating the distribution of gamma emitting fission products along the length of the MOX fuel pins (Fig. 5). The axial profile of Cs^{137} revealed its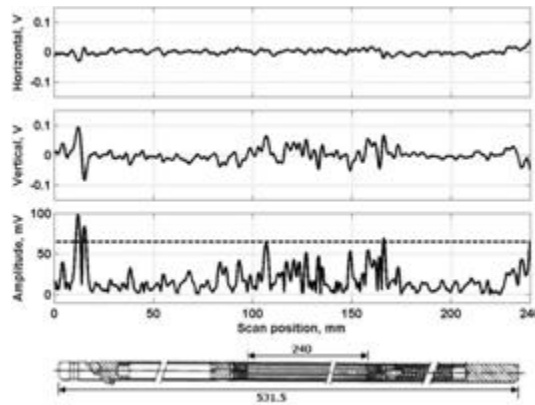 migration and deposition at the end of fuel column – insulation pellet interface, in addition to most of the inter-pellet gaps. The distribution of Ru^{106} indicates localized peaks in the bottom region of the fuel column; this is attributed to the migration and segregation of metallic fission product precipitates observed in irradiated mixed oxide fuels [5].
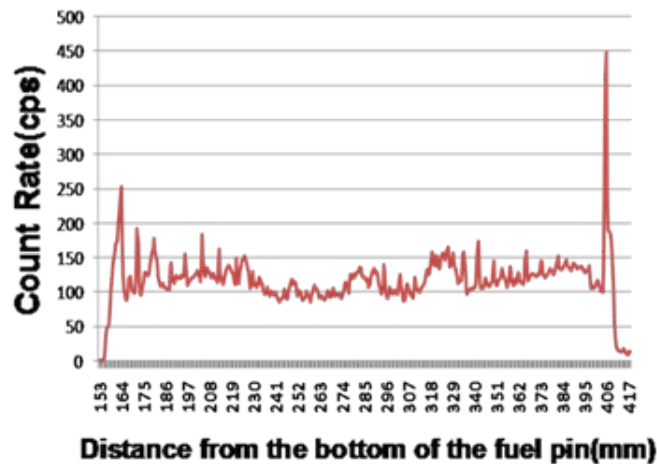

FIG. 5. Typical profile of Cs^{137} distribution along the fuel column.

Neutron radiographs of the fuel pins indicate large random variation in central hole diameter, within the adjacent pellets as well as across the pellet length. Pellet to Pellet gap also has been found to vary in different fuel pins. This was confirmed from the gamma scanning where the fuel pins with higher pellet-pellet gap show a number of cesium peaks which correspond to the pellet interfaces.

Fuel stack length measurements measured using different non-destructive techniques like X-radiography, N-Radiography and Gamma Scanning have indicated that the maximum axial fuel swelling is 1.4 %. Volumetric swelling estimated from the axial increase in the fuel column length indicates that the swelling rate is very low ($\approx$ 0.47 % per atom % burn-up). The low swelling rate is attributed to a combination of factors such as low fuel smear density, release of volatile fission products and high fission gas release.

1.3. *Fission gas analysis*

The fission gas release measurements on four fuel pins indicated internal pressure of 2.4 - 2.8 MPa at ambient temperature. The fission gas release is in the range of 82-85% typical of high burnup mixed oxide fuels [6]. The Xe/Kr ratio was found to be in the range of 5.1-5.5. This is indicative of

the higher contribution of U[233] fission relative to other fissioning isotopes for the present MOX fuel composition. High fission gas release of about 85% and a plenum pressure of 6 – 7 MPa at operating temperature support the earlier finding that about 60% of the pin diametral strain is attributed to irradiation creep.

1.4. Metallography

Metallographic examinations carried out on the transverse cut sections and longitudinal sections indicate widening of central hole in peak power location (Fig. 6) and significant shrinkage in core top location. Fuel-clad mechanical interaction is seen in core top location and fuel-clad gap is found in lower regions and near the peak power location. Metallic fission product inclusions were found in cracks and central hole. Indication of fuel-clad chemical interaction (FCCI) in the form of clad wall thickness reduction of the order of 80 µm has been observed. Eddy current examination of the fuel pins had revealed localized indications originating from the clad inner diameter. This could be attributed to corrosion attack by fission products.
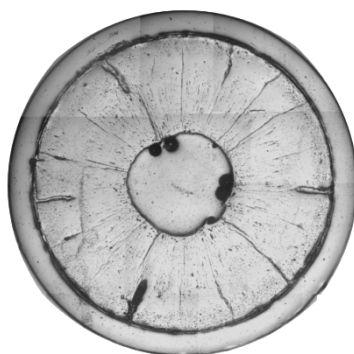

FIG. 6. Transverse cross-section of the fuel pin at peak power location

Microstructural evolution of the fuel has indicated the relative temperature profile at different axial locations. Metallographic cross-sections reveal that the temperature boundary of the columnar grain growth region is extending to higher fraction of the pellet diameter at the core bottom locations as compared to the core top indicating the strong influence of temperature gradient in restructuring. Indications of initiation of fuel-clad mechanical interaction (FCMI) are observed at the core top locations as seen by the depletion of the porosities and the reduction of the central hole diameter from the metallographic sections.

1.5. Tensile testing of cladding and wrapper

The mechanical tests on cladding and wrapper specimens are carried out as per ASTM E 8 and E 21 using a s crew driven Universal Test Machine installed in the hot cells. Both D9 cladding and wrapper irradiated to 60 dpa showed similar trends in the strength and ductility as a function of irradiation temperature. For low irradiation temperatures around 400ºC-450ºC (lower portion of fuel column), there is significant increase in YS and UTS with a decrease in uniform elongation. The hardening effects are more prominent in Alloy D9 wrapper compared to cladding due to its relatively lower operating temperatures compared to cladding at the same axial location. The hardening effect decreases in both cladding and wrapper as the irradiation temperature increases beyond 450ºC-480ºC. The recovery of ductility for irradiation temperatures beyond 480ºC (upper portions of fuel column) is seen in both clad and wrapper samples. The uniform elongation at operating temperatures is lower in the case of D9 cladding (~ 3%) as compared to D9 wrapper samples (~4.5%). The trends in tensile properties with dpa and irradiation temperature are similar to those reported in the literature for D9 alloy.

Overall, for the Alloy D9 cladding and wrapper irradiated to 60 dpa in FBTR, swelling is low (2% for clad and 0.2% for wrapper) and there is adequate retention of the mechanical properties of clad and

wrapper at irradiation temperature. Swelling does not seem to have influenced the degradation of mechanical properties.

CONCLUSIONS

The PIE results indicate that the MOX fuel and Alloy D9 clad/wrapper of the PFBR test FSA have performed well in FBTR upto a burn-up of 112 GWd/t. The low swelling of fuel, high fission gas release and variation of central hole diameter along the fuel column are the salient observations. The Alloy D9 clad/wrapper has performed satisfactorily with respect to swelling resistance and retention of mechanical properties at a displacement damage of 60 dpa achieved in FBTR. The PIE results validate the fuel and structural material design as well as the fabrication and quality control (QC) routes adopted for PFBR. They also indicate that FCCI could form the life limiting precursors for the fuel thereby providing inputs for evolving a strategy for achieving enhancement of burnup.

ACKNOWLEDGEMENTS

REFERENCES

[1] BALDEV RAJ et al., "Post Irradiation Examination of mixed (Pu,U)C fuels irradiated in the Fast Breeder Reactor", Influence of high dose irradiation on core structural and fuel materials in advanced reactor, IAEA-TECDOC-1039, Obninsk (1997) 57–68.

[2] KARTHIK, V., et al., Characterization of Mechanical Properties and Microstructure of Highly Irradiated SS 316, J. Nucl. Mater., (2012), in press.

[3] PITNER, A.L., et al., Irradiation performance of FFTF drivers using D9 alloy, WHC-SA-2261-FP, WestingHouse Hanford company, 1994.

[4] SASI, B. et al., Development of eddy current techniques for NDE of fuel cladding tubes, Proceedings of "Recent Advances in PIE" RAP-2008, Kalpakkam.

[5] BRAMMAN, J.I., et al., Metallic fission-product inclusions in irradiated oxide fuels, J. Nucl. Mater. 25 (1968) 201.

[6] MAEDA, KOJI, et al., Fission gas release in FBR MOX fuel irradiated to high burnup, J. Nucl. Mater. 346 (2005) 244.

Analysis of oxygen potentials in MOX and MA-bearing MOX fuels and application to nuclear fuel technologies

M.Kato, T. Abe

Advanced Nuclear System Research and Development Directorate, Japan Atomic Energy Agency, Muramatsu Tokai-mura Ibaraki, Japan

Presented by M.Kato

Abstract. Oxygen potentials of oxide nuclear fuels are important thermodynamic data in development of nuclear fuel technologies. Minor actinide bearing MOX fuels have been developed as fast reactor fuels. Content of Am which is one of the minor actinide elements causes oxygen potential to increase. Furthermore, the heating treatment in the pellet production process is expected to be affected by the oxygen potential change. In this paper, effects of the oxygen potential increase on the fuel pellet production process and the irradiation behavior were evaluated. Pellets of $(U_{0.7}Pu_{0.3})O_{2-x}$ and $(U_{0.66}Pu_{0.3}Am_{0.016}Np_{0.016})O_{2-x}$ were heated at 1873 K in an atmosphere of P_{H2}/P_{H2O}=133. The O/M ratio of $(U_{0.66}Pu_{0.3}Am_{0.016}Np_{0.016})O_{2-x}$ decreased to O/M=1.965 which was 0.005 lower than that of $(U_{0.7}Pu_{0.3})O_{2-x}$. Profiles of temperature and O/M ratio in the pellets were evaluated to better understand the irradiation behavior. From these data, local oxygen potential in the radial direction of the pellets was calculated, and was compared with free energy of compounds composed of fission products. Based on this comparison, it was concluded that Cs_2MoO_4 was likely formed at pellet periphery of $(U_{0.7}Pu_{0.3})O_{1.98}$ and $(U_{0.66}Pu_{0.3}Am_{0.016}Np_{0.016})O_{1.976}$. The extent of cladding tube inner surface oxidation was predicted by using the calculated oxygen potential. No significant difference between irradiation behaviors of $(U_{0.7}Pu_{0.3})O_{2-x}$ and $(U_{0.66}Pu_{0.3}Am_{0.016}Np_{0.016})O_{2-x}$ pellets was confirmed.

1. Introduction

Uranium and plutonium mixed oxide (MOX) fuels containing minor actinide (MA) elements such as Np and Am have been developed as fuels of sodium-cooled fast reactors [1]. In the development of such new type nuclear fuels, it is essential to know physical properties in order to establish a suitable pellet production process and to predict possible irradiation behavior. Some irradiation tests of MA-bearing MOX (MA-MOX) fuels have been carried out in the fast reactor *JOYO* [2][3][4][5]. The fuel pins were irradiated at a high heating rate of 430 W/cm for short times of 10 min or 24 h, as a function of oxygen-to-metal (O/M) ratio. Their post-irradiation examination was carried out, and re-structuring and MA re-distribution in radial direction on pellet section were evaluated. In the future these fuel pins will be irradiated to high burn-up of 100 GWd/t.

Physical properties of MA-MOX have been investigated so far, and the effects of Am and Np contents on melting temperature, thermal conductivity, lattice parameter, and oxygen potential were evaluated[5][6][7][8][9][10][11][12][13][14][15][16][17]. Kato et al.[5] reported that Am content caused the melting temperature to decrease. Morimoto et al. [8][9][10] investigated the effect of Am and Np contents on thermal conductivity of MOX and reported that Am and Np additions decreased thermal conductivity. Oxygen potentials of MOX containing Np and Am were reported by Nakamichi et al.[15]. They showed that Am led to a slight increase of the oxygen potential. It is a concern that the oxygen potential increase will affect the pellet production process and irradiation behavior; however, the effect of the oxygen potential change on the fuel technologies is not sufficiently understood. Therefore, it is important to evaluate the effect of the oxygen potential change caused by MA addition on the fuel technologies.

In the pellet production process, sintering and O/M-adjustment annealing are significantly affected by oxygen potentials. And it is essential to predict the extent of cladding tube inner surface oxidation dependence on burn-up in the irradiation behavior, which is related to the oxygen potential and is one of the important factors for determining fuel life. In this work, the oxygen potential of MA-MOX was compared with that of MOX, and the O/M change by heat treatment and cladding tube inner surface oxidation during the operating period were estimated.

2. ANALYSIS OF OXYGEN POTENTIALS

Many data on oxygen potentials of $(U,Pu)O_2$ have been measured. Fig. 1 shows measured data of $(U_{0.7}Pu_{0.3})O_{2-x}$ and $(U_{0.66}Pu_{0.3}Am_{0.02}Np_{0.02})O_{2-x}$ at 1623 K. The oxygen potential of $(U,Pu)O_{2\pm x}$ was systematically measured and a model to represent the oxygen potential was proposed [13][14][15][16][17][18]. The calculation results obtained by the model are plotted in Fig. 1. The data of $(U_{0.66}Pu_{0.3}Am_{0.02}Np_{0.02})O_{2-x}$ is higher than that of $(U_{0.7}Pu_{0.3})O_{2-x}$. Nakamichi et al.[15] reported influence of Am and Np additions on oxygen potential of MOX fuel. Addition of Np had little effect on the oxygen potential, but Am addition increased the potential. Therefore, the oxygen potential increase of $(U_{0.66}Pu_{0.3}Am_{0.02}Np_{0.02})O_{2-x}$ was attributed to the Am content. The calculated oxygen potentials are shown in Fig.2 as functions of temperature and O/M ratio.
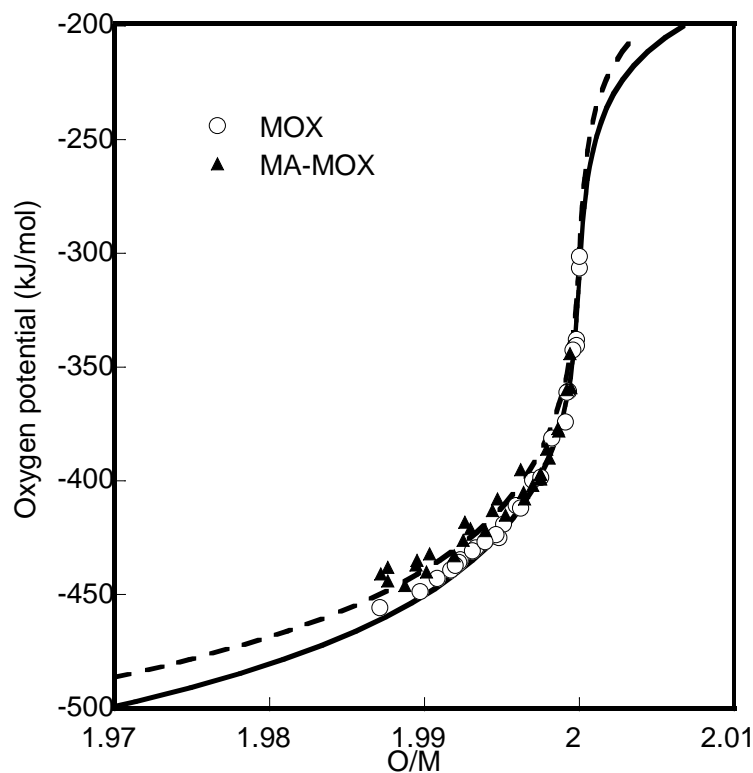

FIG. 1. Comparison of measured data at 1623 K between $(U_{0.7}Pu_{0.3})O_{2-x}$ and $(U_{0.66}Pu_{0.3}Am_{0.02}Np_{0.02})$ O_{2-x} is shown. The data of $(U_{0.66}Pu_{0.3}Am_{0.02}Np_{0.02})O_{2-x}$ are higher than that of $(U_{0.7}Pu_{0.3})O_{2-x}$. The dotted and solid lines are calculations by the oxygen potential model.

3.   EFFECT OF OXYGEN POTENTIAL ON PELLET PRODUCTION

Pellets of $(U_{0.7}Pu_{0.3})O_{2-x}$ and $(U_{0.66}Pu_{0.3}Am_{0.016}Np_{0.016})$ O_{2-x} were produced having O/M=1.98 and 1.96 and were irradiated in the fast reactor *JOYO* [2][3][4][5]. Fig. 3(b) shows O/M changes during heat treatment, which were measured by the thermo-gravimetric technique. In the heat treatment, pellets were held at 1873 K for 4 h in an atmosphere of P_{H2}/P_{H2O}=133 as shown in Fig.3 (a). The O/M ratios of $(U_{0.7}Pu_{0.3})O_{2-x}$ and $(U_{0.66}Pu_{0.3}Am_{0.016}Np_{0.016})$ O_{2-x} decreased to 1.976 and 1.975, respectively, after the heat treatment for 4h.

The calculated oxygen potentials are shown in Fig 2. The data of $(U_{0.66}Pu_{0.3}Am_{0.016}Np_{0.016})$ O_{2-x} were slightly higher compared with $(U_{0.7}Pu_{0.3})O_{2-x}$. The variation of oxygen potential controlled at P_{H2}/P_{H2O}=133 is also shown. The oxygen potential in that atmosphere was almost the same as that of O/M=2.00 at 800 K. Fig.2 shows that O/M ratio decreased with temperature and was almost 1.95 at 2000 K. The O/M ratio of $(U_{0.66}Pu_{0.3}Am_{0.016}Np_{0.016})$ O_{2-x} was expected to attain a lower value. The calculation result was consistent with the experimental data shown in Fig.3(b).
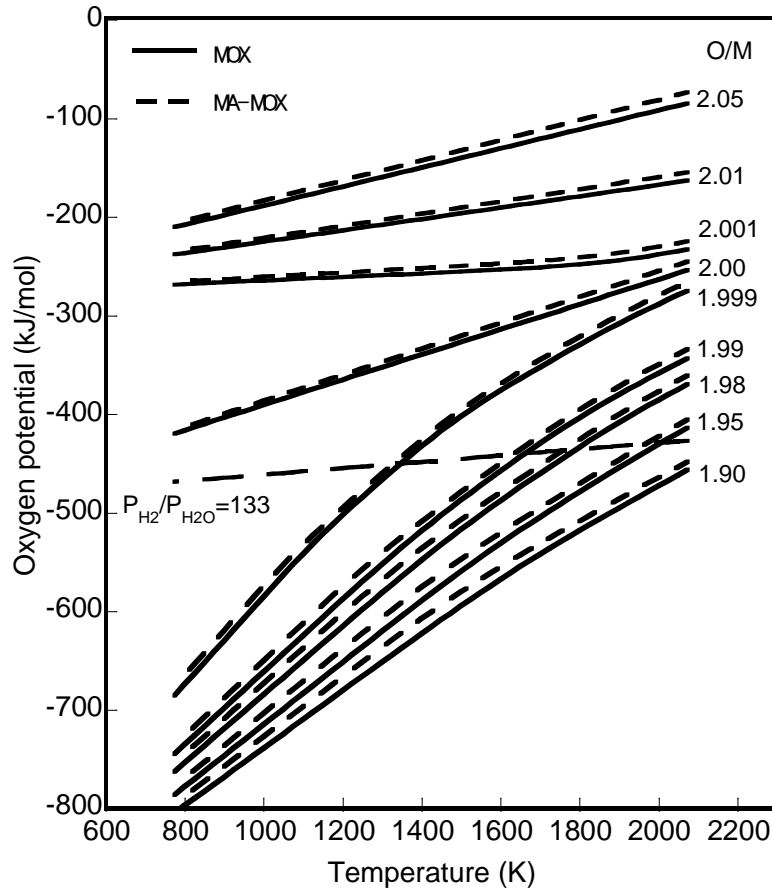
FIG. 2. Oxygen potentials of $(U_{0.7}Pu_{0.3})O_{2-x}$ and $(U_{0.66}Pu_{0.3}Am_{0.016}Np_{0.016})O_{2-x}$ were calculated as functions of O/M ratio and temperature.
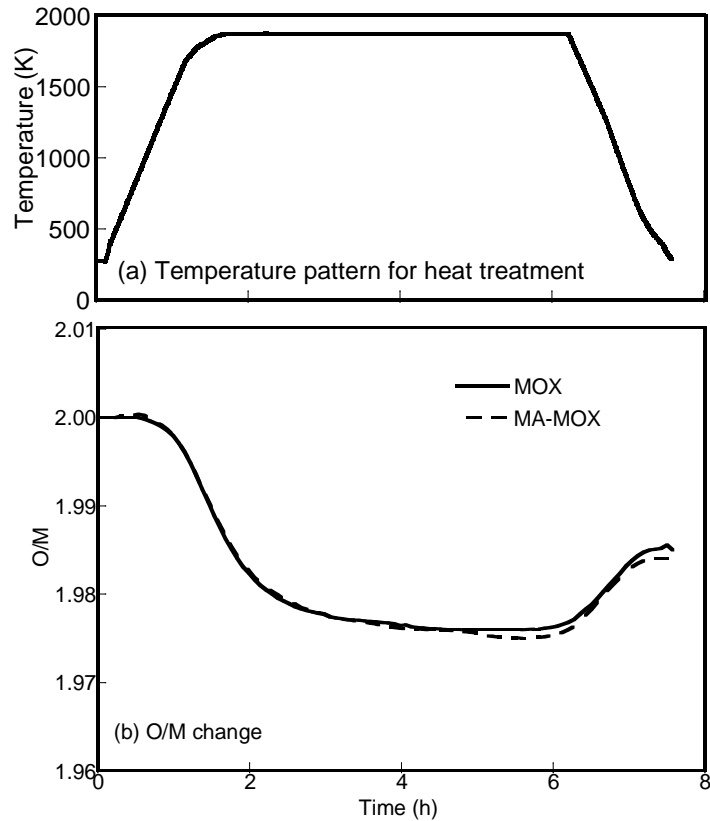
FIG. 3. O/M changes of $(U_{0.7}Pu_{0.3})O_{2-x}$ (MOX) and $(U_{0.66}Pu_{0.3}Am_{0.016}Np_{0.016})O_{2-x}$ (MA-MOX) were measured by thermo-gravimetry. The pellets were heated at 1873 K for 4 h in an atmosphere of $P_{H2}/P_{H2O}=133$.

4. EFFECT OF OXYGEN POTENTIAL ON IRRADIATION BEHAVIOR

4.1. Profile of local oxygen potential in radial direction of pellets

It is planned to irradiate fuel pins of $(U_{0.66}Pu_{0.3}Am_{0.016}Np_{0.016})O_{1.98}$ and $(U_{0.66}Pu_{0.3}Am_{0.016}Np_{0.016})O_{1.96}$ to 100 GWd/t. Then the change of local oxygen potentials in irradiated pellets was analysed. The parameters needed for the analysis are shown in Table 1. It was assumed that the effect of fission products on oxygen potential could be ignored.

Table 1. Parameters for calculation of oxygen potential

Item	Value
Pellet diameter	5.418 mm
Pellet density	93 %TD
Cladding tube inner diameter	5.56 mm
Linear heat rate	360 W/cm
Cladding temperature	873 K

In previous work [5], the temperature profile of MA-MOX was described taking into consideration oxygen redistribution in the radial direction of the pellet. The oxygen redistribution was calculated by eqs.(1)-(2).

$$\ln\left(\frac{x_1}{x_2}\right)=\frac{Q*}{R}\left(\frac{1}{T_2}-\frac{1}{T_1}\right) \tag{1}$$

$$Q*=7.0061\times10^6-6.1012\times10^6 V_{Pu}+1.7705\times10^6 V_{Pu}^2-1.7122\times10^5 V_{Pu}^3 \tag{2}$$

Here, x is deviation in $(U,Pu)O_{2-x}$, T is temperature, R is gas constant, $Q*$ is the molar effective heat of transport, and V_{Pu} is Pu valence. Profiles of the oxygen redistribution and temperature were calculated as a function of O/M ratio, and are shown in Figs.4(a) and (b), respectively. It was observed that the temperature increased with decreasing O/M ratio, and the O/M ratio decreased at the pellet centre. The temperature increase was caused by decreasing thermal conductivity due to lowered O/M [5].
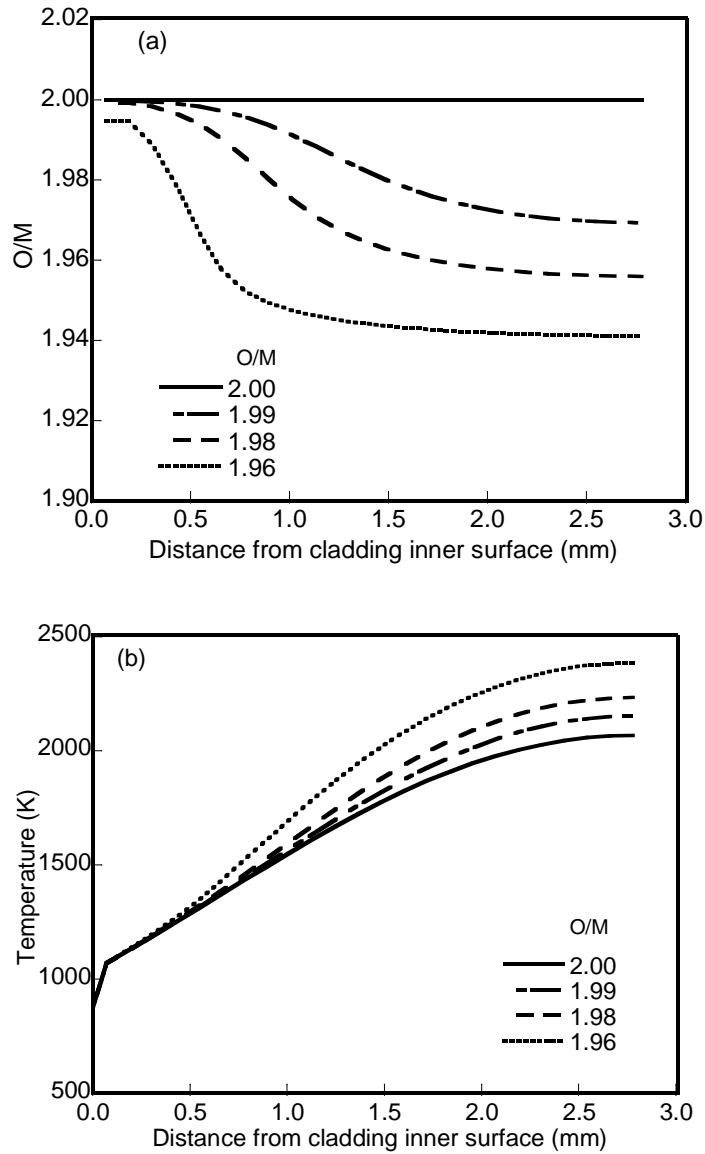

FIG. 4. (a) O/M redistribution and (b) temperature profiles in $(U_{0.66}Pu_{0.3}Am_{0.016}Np_{0.016})\,O_{2-x}$ pellets.

The calculated temperatures and O/M ratios in the radial direction shown in Figs.4 (a) and (b) can give local oxygen potential in a pellet. Fig.5 shows the change of the local oxygen potential. The free energies of Cs_2MoO_4 and MoO_2 are also shown [24]. The phase of Cs_2MoO_4 is known as the JOG and it is formed at the gap between the cladding and pellet [25]. It was expected that the phase would be observed for O/M of more than about 1.98. Molybdenum which is one of the major fission products would be transformed to MoO_2 when O/M=2.00. The oxide phase expanded from the periphery of the pellet. The analysis of local oxygen potential could give better understanding related to the chemical state of fission products inside the pellet.

The local oxygen potentials at the pellet surface are plotted in Fig.6 as a function of average O/M ratio of the pellet. The local oxygen potential at the pellet surface increased with increasing O/M ratio. The free energy of Cs_2MoO_4 and MoO_2 are also shown. MoO_2 would form at O/M=2.00 in both MOX and MA-MOX fuels, and formation of Cs_2MoO_4 occurred at 1.976 and 1.980, respectively, in MA-MOX and MOX pellets. The increase of O/M ratio during irradiation was estimated to be 0.005 with burn-up increase of 10GWd/t[26]. The difference of the O/M ratio for Cs_2MoO_4 formation corresponded to burn-up of about 8 GWd/t.

4.2. *Prediction of cladding tube inner surface oxidation during irradiation*

It has been observed that an oxide layer grows on the cladding tube inner surface during irradiation. The increase of the oxide layer causes a decrease of cladding strength. So, thickness of the oxide layer is one of important factors to evaluate the fuel life.

The relationship between the thickness of the oxide layer and the O/M ratio of the pellet was previously investigated. In the case of low O/M pellets (less than O/M=1.97), the oxide layer on the cladding tube inner surface was thin. It was considered that its thickness was significantly affected by the oxygen potential of the pellet surface. In this section, the oxide layer growth was predicted.

The following items were assumed for the prediction.

— The oxygen partial pressure at the cladding tube inner surface is determined by the O/M ratio of the pellet surface.
— The increase of average O/M ratio of the pellet is 0.05 for 10 GWd/t.
— The increase of the O/M ratio is stopped on reaching the free energy of the reaction Mo→ MoO_2.
— The effect of irradiation is ignored.

The local oxygen potential at the pellet surface was determined as shown in Fig.6. Sato at al. [27] evaluated the oxidation layer growth rate of stainless steel (PNC316) and derived the following equations

$$W^2=k_p \cdot t, \qquad\qquad (3)$$

and

$$k_p=2.7\times10^4 \cdot P_{O2}^{0.279} \cdot \exp(-109\times10^3 \cdot R^{-1} \cdot T^{-1}), \qquad (4)$$

where W is the oxygen uptake by cladding (kg/m^2), t is the time (s), K_p is the parabolic rate constant, P_{O2} is the oxygen partial pressure, R is gas constant (8.3145 J/mol), and T is absolute temperature(K).

M.Kato and T. Abe

Thickness of the oxide layer was calculated for $(U_{0.7}Pu_{0.3})O_{2-x}$ and $(U_{0.66}Pu_{0.3}Am_{0.016}Np_{0.016})$ O_{2-x} pellets having an initial O/M ratio of 1.96. The calculation results are shown in Fig.7. The thicknesses were 96 and 101 μm, respectively, for $(U_{0.7}Pu_{0.3})O_{2-x}$ and $(U_{0.66}Pu_{0.3}Am_{0.016}Np_{0.016})$ O_{2-x} when burn-up was 100 GWd/t. The difference was caused by the oxygen potential difference between the two fuels which was shown in Fig.6. The difference was small, so it was considered that the effect of the oxygen potential increase for the 1.6% Am addition on the cladding tube inner surface oxidation would be small.
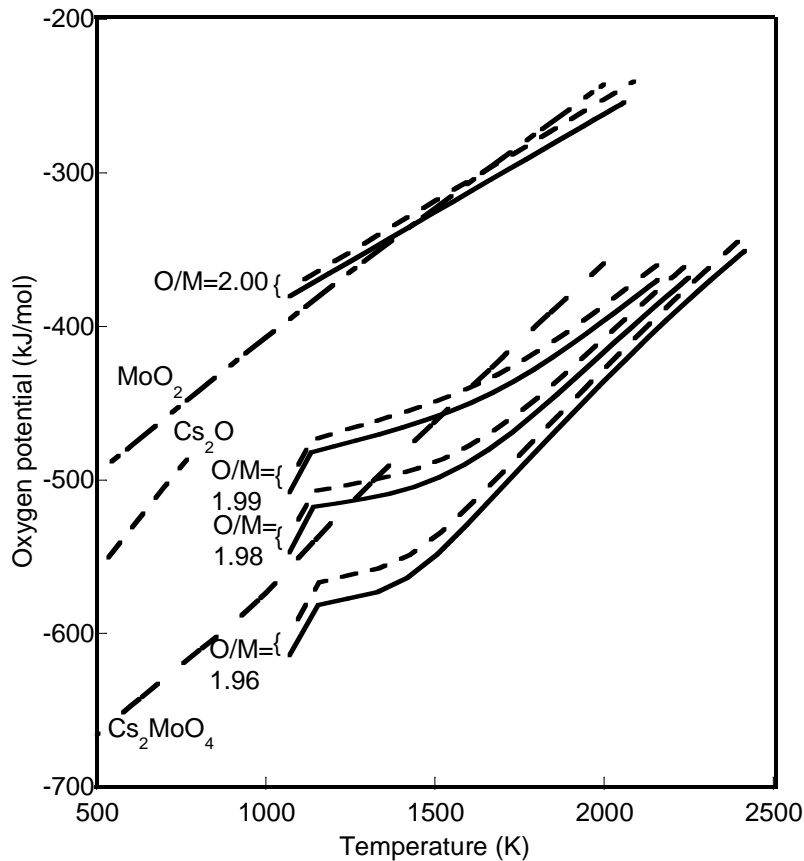
FIG. 5. The plot shows change of local oxygen potential in pellets of $(U_{0.7}Pu_{0.3})O_{2-x}$ and $(U_{0.66}Pu_{0.3}Am_{0.02}Np_{0.02})$ O_{2-x}. Free energies of MoO_2, Cs_2O and Cs_2MoO_4 are also shown.
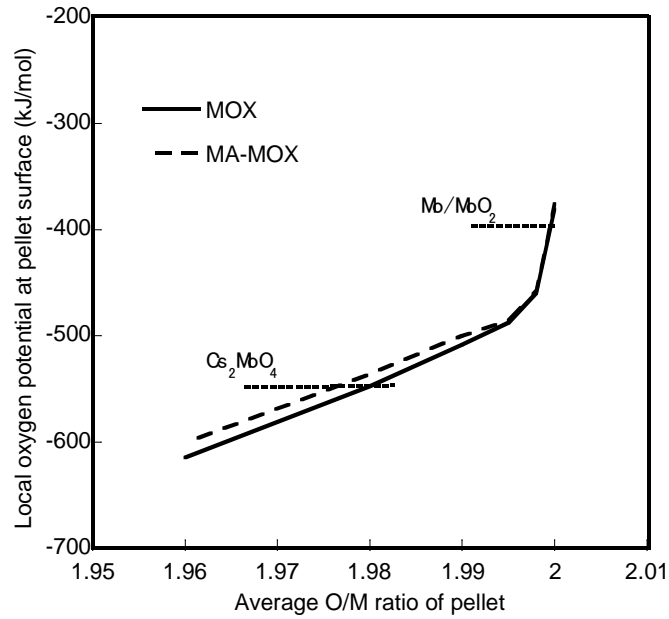
FIG. 6. The change of local oxygen potential at the pellet surface is shown as a function of average O/M ratio of pellet.
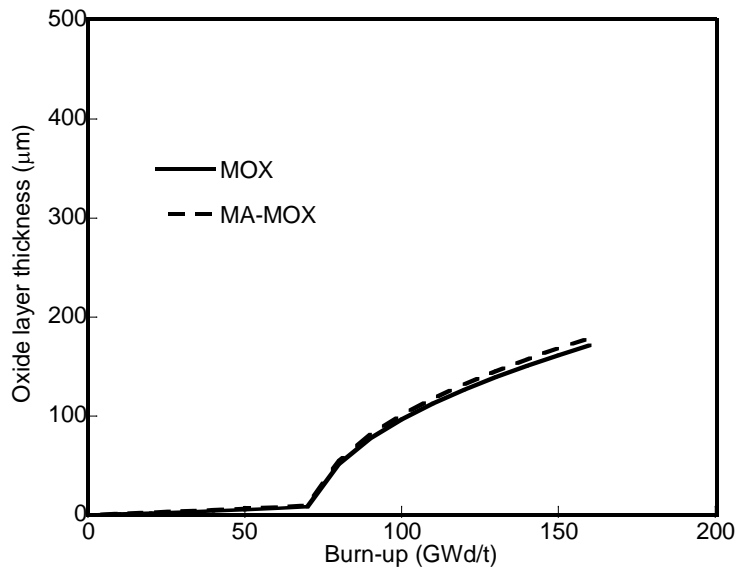
FIG. 7. Thickness of the oxide layer on the cladding tube inner surface was estimated for changing burn-up.

5. CONCLUSIONS

MA-bearing MOX fuels have been developed to reduce high-level waste by burning them in fast reactors. One of the MAs, Am, causes increased oxygen potential of the oxide fuel. Effects of the oxygen potential increase on the nuclear fuel technologies, pellet production process, and irradiation behavior were evaluated. The change of the O/M ratio in the heat treatment was investigated as the

effect on the pellet production process. In analysis of irradiation behavior, temperature and O/M re-distribution profiles in the pellets were evaluated, and local oxygen potential was calculated as a function of O/M ratio. The following results were obtained.

(1)   Pellets of $(U_{0.7}Pu_{0.3})O_{2-x}$ and $(U_{0.66}Pu_{0.3}Am_{0.016}Np_{0.016})O_{2-x}$ were heated at 1873 K for 4 h in an atmosphere of P_{H2}/P_{H2O}=133. The O/M ratio of $(U_{0.66}Pu_{0.3}Am_{0.016}Np_{0.016})$ O_{2-x} decreased to O/M=1.965 which was 0.005 lower than that of $(U_{0.7}Pu_{0.3})O_{2-x}$. This result was consistent with oxygen potential data measured in previous studies.

(2)   The change of local oxygen potential in the pellets was evaluated as a function of O/M ratio. The oxygen potential of $(U_{0.66}Pu_{0.3}Am_{0.016}Np_{0.016})O_{2-x}$ was 5 – 20 kJ/mol higher than that of $(U_{0.7}Pu_{0.3})O_{2-x}$.

(3)   It was expected that Cs_2MoO_4 was formed at the pellet periphery of $(U_{0.7}Pu_{0.3})O_{1.98}$ and $(U_{0.66}Pu_{0.3}Am_{0.016}Np_{0.016})O_{1.976}$. Transformation to Mo oxide would occur at the same value O/M=2.00 in both pellets.

(4)   The thickness of oxide layer on the cladding tube inner surface was predicted depending on burn-up in the fuel pellets with O/M=1.960. The thicknesses for MA-MOX and MOX were 101 μm and 96 μm, respectively. It was expected that the effect of MA addition on the cladding tube inner surface oxidation was small.

It is planned to irradiate fuel pins of MA-MOX and MOX to 100 GWd/t in the fast reactor *JOYO*. Effect of oxygen potential change on their irradiation behavior will be re-evaluated by using post-irradiation examination data.

ACKNOWLEDGEMENT

REFERENCES

[1]   T.Abe, T. Namekawa, K. Tanaka, Oxide fuel fabrication technology development of the FaCT Project(1) –Overall review of fuel Technology development of the project-, Proceedings of Global 2011, Makuhari, Japan, Dec.11-16, 2011, Paper No.387478

[2]   K. Maeda, S. Sasaki, M. Kato, Y. Kihara, Radial redistribution of actinides in irradiated FR-MOX fuels, J. Nucl. Mater. 389(2009) 78

[3]   K. Maeda, S. Sasaki, M. Kato, Y. Kihara, Behavior of impurity Si in Np/Am-MOX fuel irradiated in the experimental fast reactor Joyo, J. Nucl. Mater., 385(2009) 178

[4]   K. Maeda, S. Sasaki, M. Kato, Y. Kihara, Short-term irradiation behavior of minor actinide doped uranium plutonium mixed oxide fuels irradiated in an experimental fast reactor, J. Nucl. Mater. 385 (2009) 413

[5]   M. Kato, K. Maeda, T. Ozawa, M. Kashimura, Y. Kihara, Physical properties and irradiation behavior analysis of Np- and Am-bearing MOX fuels, J. Nucl. Sci. Tech., vol.48, No.4 (2011) 1

[6]   M. Kato, Melting temperatures of oxide fuel for fast reactors, Proceedings of ICAPP '09, Tokyo, Japan, May 10-14, (2009)Paper 9451(CD)

[7]   M. Kato, K. Morimoto, H. Sugata, K. Konashi, M. Kashimura, T. Abe, Solidus and liquidus temperatures in the UO_2–PuO_2 system, J. Nucl. Mater., 373(2008) 237

[8]   K. Morimoto, M. Kato, M. Ogasawara, M. Kashimura, Thermal conductivity of $(U,Pu,Np)O_2$ solid solutions, J. Nucl. Mater.389, 179-185(2009)

[9]   K. Morimoto, M. Kato, M. Ogasawara, M. Kashimura, Thermal conductivities of hypostoichiometric $(U, Pu, Am)O_{2-x}$ oxide, J. Nucl. Mater. 374(2008) 378

[10]   K. Morimoto, M. Kato, M. Kashimura, T. Abe, Thermal Conductivity of $(U, Pu, Am)O_2$ Solid Solution, J. Alloys and compounds, 452, 54-60(2008)

[11]   A. Komeno, H. Uno, T. Tamura, K. Morimoto, M. Kato, M, Kashimura, Phase separation behavior of $(U, Pu, Am, Np, Sm)O_{2-x}$, 2010 IOP Conf. Ser.: Mater. Sci. Eng. 9 (2010) 012016

[12] M. Kato, K. Konashi, Lattice parameters of $(U,Pu,Np,Am)O_{2-x}$, J. Nucl. Mater. 385 (2009) 117

[13] M. Kato, Oxygen potentials and defect chemistry in nonstoichiometric $(U,Pu)O_2$, Stoichiometry and Materials Science – When Numbers Matter, InTech (2012) 203

[14] M. Kato, K. Takeuchi, T. Uchida, T. Sunaoshi , K. Konashi, Oxygen potential of $(U_{0.88}Pu_{0.12})O_{2\pm x}$ and $(U_{0.7}Pu_{0.3})O_{2\pm x}$ at high temperatures of 1673-1873K, J. Nucl. Mater. 414 (2011) 120

[15] S. Nakamichi, M. Kato, T. Tamura, Influences of Am and Np on oxygen potentials of MOX fuels, CALPHAD 35 (2011) 648

[16] M. Kato, K. Konashi, N. Nakae, Analysis of oxygen potential of $(U_{0.7}Pu_{0.3})O_{2\pm x}$ and $(U_{0.8}Pu_{0.2})O_{2\pm x}$ based on point defect chemistry, J. Nucl. Mater. 389 (2009) 164

[17] M. Kato, T. Tamura, K. Konashi, Oxygen potentials of mixed oxide fuels for fast reactors, J. Nucl. Mater. 385 (2009) 419

[18] M. Kato, T. Tamura, K. Konashi, S. Aono, Oxygen potentials of plutonium and uranium mixed oxide, J. Nucl. Mater. 344, 235-23 (2005)

[19] K. Takeuchi, M. Kato, H. Sunaoshi, Influence of O/M ratio on sintering behavior of $(U_{0.8}Pu_{0.2})O_{2\pm x}$, J. Nucl. Mater. 414 (2011) ,156

[20] K. Takeuchi, M. Kato, H. Sunaoshi, Effects of H_2/H_2O ratio in the sintering atmosphere on the sintering behavior of MOX pellets, Proceedings of ICAPP '10, San Diego, CA, USA, June 13-17(2010) Paper 10044

[21] T. Murakami, M. Kato, H. Uno, Sintering behavior of MOX pellets containing carbon, Proceedings of ICAPP '10, San Diego, CA, USA, June 13-17 (2010) Paper 1004

[22] M. Kato, T. Segawa, K. Takeuchi, M. Kashimura, Y. Kihara, Development of an advanced fabrication process for fast reactor MOX fuel, Proceedings of Global 2009, Paper 9169, Sept. 6-11, 2009, Paris, France

[23] M. Kato, S. Nakamichi, T. Takano, Preparation of low oxygen-to-metal mixed oxide fuels for advanced fast reactors, Proceedings of Global 2007, Sept.9-13, 2007, Boise, Idaho, USA (2007)

[24] E.H.P. Cordfunke, R.J.M. Konings (Eds), Thermochemical Data for Reactor Materials and Fission Products, (North-Holland Elsevier Science Publishers B. V., Amsterdam, Netherlands, 1990)

[25] K. Maeda, K. Tanaka, T. Asaga, H. Furuya, Distributions of volatile fission products in or near the fuel-cladding gap of the FBR MOX fuel pins irradiated to high burn-up, J. Nucl. Mater. 344 (2005)274

[26] Hj. Matzke, Oxygen potential measurements in high burnup LWR UO_2 fuel, J. Nucl. Mater. 223 (1995)1

[27] I. Sato, M. Takaki, T. Arima, H. Furuya, K. Idemitsu, Y. Inagaki, M. Momoda, T. Namekawa, Oxidation of SUS-316 stainless steel for fast breeder reactor fuel cladding under oxygen pressure controlled by Ni/NiO oxygen buffer, J. Nucl. Mater. 304 (2002)21

Overview of CEA's R&D on GFR fuel element design: from challenges to solutions

M. Zabiégo[a†]**, C. Sauder**[b]**, P. David**[c]**, C. Guéneau**[b]**, L. Briottet**[d]**, J.J. Ingremeau**[a‡]**,
A. Ravenet**[a§]**, C. Lorrette**[b]**, L. Chaffron**[b]**, P. Guédeney**[a]**, M. Le Flem**[b]**, J.L. Séran**[b]

[a] CEA/DEN (DEC & DER) - Cadarache, 13108 Saint-Paul-lez-Durance, France

[b] CEA/DEN (DMN & DPC) - Saclay, 91191 Gif-sur-Yvette cedex, France

[c] CEA/DAM/DMAT - Le Ripault, BP 16 - 37260 Monts, France

[d] CEA/DRT/LITEN - Grenoble, 38054 Grenoble cedex, France

Presented by M. Zabiégo

Abstract. Over the period 2002-2012, CEA conducted some extensive R&D on the design of GFR fuel elements (together with related material and core/system studies). This paper reviews the challenges raised by this programme, the solutions proposed to address them, and the remaining issues. Studies were performed on the assembly duct, the pin bundle and the fuel pin. The main issues were related to the challenge of using silicon carbide composites (SiC/SiC) for the pin cladding and the assembly duct, as well as mixed uranium-plutonium carbide (UPuC) for the nuclear fuel. Emphasizing the pin design, key achievements are reviewed in this paper regarding such topics as fission product confinement and high burnup performance, for the sake of which original design options were recently patented.

1. Introduction

The Gas-cooled Fast Reactor (GFR) is one of the six reactor options considered by the Generation-IV International Forum (GIF) [1]. As such, it is assigned ambitious performance & safety objectives. Considering that the GFR imposes the difficulty of dealing with high temperature, high fast neutron flux and high power density, designing its fuel elements (pin & sub-assembly) represents quite a challenge. In a way, the GFR fuel element design combines some of the key difficulties of the Sodium-cooled Fast Reactor (SFR) and the High Temperature Reactor (HTR), as illustrated by the specifications indicated in table 1.

Table 1. Some GFR design specifications

GFR fuel operating conditions	
Structure temperature (cladding & duct)	400-1000°C (nominal regime) Up to 1600-2000°C (design basis accidents)
Fast neutron flux	A few 10^{19} n/m^2/s
Damage to structures (cladding & duct)	75-150 dpa
Power density	Core volume power density $\approx$ 100 MW/m^3 Fuel volume power density $\approx$ 50 W/g
Fuel burnup	5-10 at% (core average) 7.5-15 at% (maximum)

[†] Corresponding author: maxime.zabiego@cea.fr
[‡] Now working with DCNS - Issy les Moulineaux
[§] Now retired

In order to meet this challenge, the leading option is to rely on silicon-carbide based Continuous Fiber Ceramic Matrix Composites (CFCMC, such as SiC_f/SiC_m with pyrocarbon interphase) for the structures (cladding & SA-duct) and mixed uranium-plutonium carbide (UPuC) for the fissile phase (fuel pellets) [2].

During the decade 2002-2012, the French Commissariat à l'Energie Atomique et aux Energies Alternatives (CEA) conducted an important R&D programme on the GFR fuel element design (complementary to related studies on both reactor & systems, on the one hand, and materials, on the other hand), which led to proposing several important innovations, necessary to overcome critical technological bottlenecks. The aim of the present paper is to review some of these (other topics cannot be disclosed for now):

(1)   A mixed subassembly duct (hereafter SA-duct) with SiC/SiC shroud modules and a metallic skeleton [3], as illustrated in figure 1;

(2)   A fuel pin based upon

   (a)   stacked UPuC pellets, offering both high density and high thermal conductivity;

   (b)   the so-called "sandwich" cladding [4]: a thin refractory metal liner reinforced by SiC/SiC layers on its inner and outer sides, as illustrated in figure 2;

   (c)   the so-called "buffer" bond [5]: a porous layer made of braided carbon-based fibers, interposed in between the fissile column and the cladding, as illustrated in figure 3;

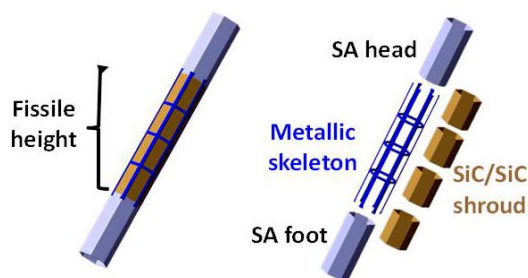   (d)   the possibility to manufacture the cladding with a blind end [6], as illustrated in figure 4.
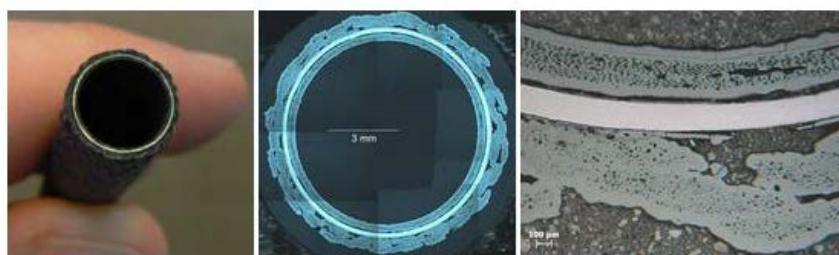

FIG. 1. Mixed CFCMC/metal SA-duct design[3]

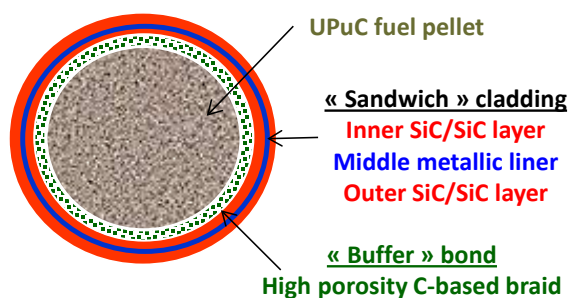

FIG. 2. CEA manufactured "Sandwich" cladding

FIG. 3. Pin cross-section and "Buffer" bond

FIG. 4. CEA manufactured blind-end SiC/SiC-based cladding

The paper aims at presenting the design issues raised through CEA studies, and the solutions proposed to solve the identified problems.

2. General comments on the use of SiC/SiC for nuclear fuel applications

The main challenge on the way to designing the GFR fuel elements certainly lies in the use of SiC/SiC for structural materials (pin cladding and SA duct). This choice is primarily imposed by the *high temperatures* that these materials must withstand during in-reactor operations. In addition, SiC-based structures offer the advantage of being *transparent to neutrons* (contrary to refractory metals, whose use for core structures is strictly limited). SiC-based structures also appear fairly *resistant to irradiation* [7][8]: although their thermal conductivity tends to degrade under irradiation, they can be subjected to high doses with no critical loss in neither *mechanical resistance* nor *dimensional stability*. The implementation of *thin-walled* and *elongated* SiC/SiC structures nevertheless appears challenging under conditions implying important heterogeneities (temperature, dose…) which can lead to *differential deformations* and *potentially high stresses*.

3. Mixed SiC/metal SA-duct

A SiC-based sub-assembly (SA) duct appears interesting in the context of the GFR because refractory materials are required. Metallic solutions are not acceptable, because refractory metals/alloys imply too high a neutronic penalty. However, considering that the design of the SA foot and head (*massive structures* below and above the fissile height) is expected to rely on metallic materials, a metal/SiC junction appears very challenging. For this reason, the proposed solution [3] is to combine a *light* metallic skeleton with SiC/SiC shroud modules, as illustrated in figure 1. The shroud modules ensure both the coolant channeling and the pin-bundle protection, while the skeleton ensures the mechanical continuity with the SA head and foot (notably for handling/shipping operations and the SAs' seismic response).

This innovative solution was preliminarily studied within the frame of GFR (and SFR) applications but complementary studies remain necessary as regards both thermal-mechanics and thermal-hydraulics. Shroud manufacturing studies are in progress, with particular emphasis on the winding/braiding of the fibrous preform and its densification.

4. "Sandwich" cladding

The GFR cladding design was a *technological bottleneck* for a long time. The use of SiC/SiC immediately raised several issues.

— The *fuel/cladding thermochemical compatibility* was identified as a potential problem. Indeed, UPuC and SiC tend to form some eutectic phase much below the ultimate temperature associated with the SiC peritectic decomposition (at about 2830°C): a CEA experiment, performed with $UC_{1.04}$ and SiC/SiC heated at 2000°C showed that half of the cladding thickness could be melted within 15 minutes (in agreement with thermodynamical computations, which predict that some liquid phase forms at about 1900°C).

⸺ *Leak-tightness*, and the associated fission product (FP) confinement issue, also appeared critical. Indeed, despite their favorable failure stress and strain (as illustrated in figure 5), SiC/SiC CFCMCs are known to undergo micro-cracking damage above the less favorable elastic limit. As a matter of fact, a tensile-permeation test performed at CEA, by subjecting a pressurized SiC/SiC (excess outer helium pressure: $\Delta P = 2$ bar) tube to some progressive uniaxial tensile stress, clearly established the link between the elastic limit and the leak-tightness loss, as evidenced by the sudden increase in a permeation coefficient measured in figure 6 (red curve).
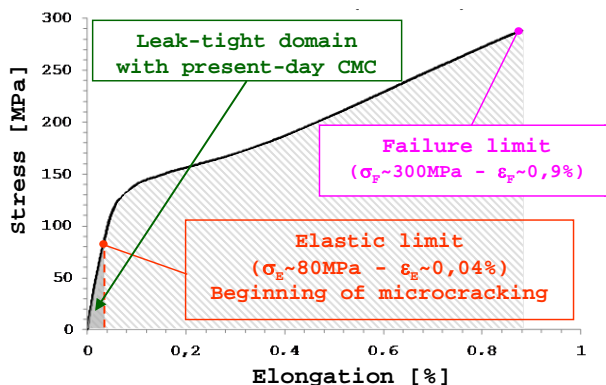
FIG. 5. Typical SiC/SiC tube mechanical behaviour
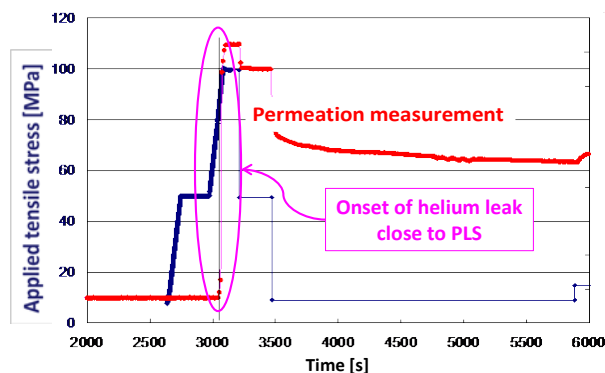
FIG. 6. SiC/SiC tube tensile-permeation test

Two different *multilayered cladding* solutions were initially proposed to address the leak-tightness issue.

⸺ The so-called "Triplex" cladding [9] was patented in the US (primarily for the sake of improving Light Water Reactor safety): in order to achieve leak-tightness, it relies on an inner layer made of monolithic SiC, which is presumably maintained in a compressed (hence leak-tight) state by an outer composite SiC/SiC layer. This fully-ceramic solution poses several difficulties (as partly discussed in [8], for instance), particularly as regards end-plug joining and the capability to ensure that the SiC layer remains leak-tight under all operating conditions. In the latter respect, thorough multilayered thermo-mechanical computations performed at CEA tend to call the SiC layer integrity into question under various conditions.

⸺ CEA's initial proposal [10], rather relied upon the addition of a thin metallic (refractory) liner on the inner (and possibly outer) side of the SiC/SiC cladding. Leak-tight end-plug joining appears more reliable with such a metal-based solution, and the presumably ductile behavior of the metallic liner (rather than the brittle behavior of the "Triplex" SiC layer) would make it more *tolerant to differential deformations*. However, following the exploration of many candidate materials (extensive thermo-chemical tests were particularly performed), identifying such a liner, complying with the essential requirements of *formability* and *compatibility with both SiC and UPuC* proved beyond reach.

In order to overcome these obstacles, CEA recently proposed (and patented [4]) the innovative "Sandwich" design, illustrated in figure 2. Placing the *thin* (typically 50-100 µm) metallic liner in between two SiC/SiC layers, although it may complicate manufacturing, offers several advantages.

— The metal choice depends on its *compatibility with SiC only*: UPuC is not anymore a concern (except for SiC/UPuC compatibility, of course, which is dealt with in section 5). This particularly alleviates the issues associated with both fission spikes, eutectic formation and corrosion by fission products. As regards thermochemical compatibility with SiC, several candidate metals/alloys are identified for the liner. Tantalum and niobium alloys, for instance, appear particularly favorable: they tend to form the most efficient barrier to the diffusion of Si and C atoms. Consistent with theoretical analyses, experimental tests performed at CEA (under neutral atmosphere) confirmed this excellent behavior for both SiC/Ta and SiC/Nb samples exposed to 850°C for 1000 hours, on the one hand, and Ta-lined "Sandwich" samples exposed to 2000°C for 15 minutes, on the other hand.

— The SiC/SiC layers protect the thin liner against aggressions. In particular, its (presumably fair) *ductility* ensures that the liner is capable of withstanding any strain imposed by the deformation of the protecting SiC/SiC layers, as far as to the point that leak-tightness could be guaranteed until SiC/SiC failure occurs, thus considerably extending the leak-tight domain highlighted in figure 5 (light, rather than dark, shaded domain). As illustrated in figure 7, this was recently confirmed by tensile-permeation tests performed at CEA upon pressurized "Sandwich" tubes subjected to progressive uniaxial tensile stress: no helium leak was detected prior to the ultimate tube failure (at about 365 MPa), far beyond SiC/SiC elastic limit (at about 80 MPa.)

— The "Sandwich" design appears particularly favorable as regards *resistance to flexural stress/strain* that could be fatal to the SiC layer integrity (hence, leak-tighness), in the case of the "Triplex" design. This is a serious concern for a *thin-walled elongated structure* such as a fuel cladding, which is exposed to bending under various circumstances: handling/shipping, pin bending induced by circumferential heterogeneities in both temperature and neutron flux…

— Beyond through-wall transport, leak-tightness also depends on the reliability of the *seal joining* at the cladding ends. This is identified as a major difficulty for the "Triplex" design: SiC-to-SiC joining (and its resistance to irradiation) remains a critical challenge [8]. For this reason, relying on the more conventional joining of metals/alloys appears favorable to the "Sandwich" design: tantalum and niobium alloys seem to allow dependable welding options.
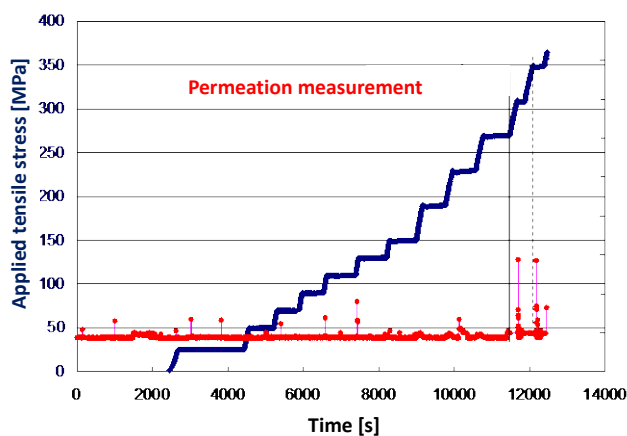
FIG. 7. "Sandwich" cladding tensile-permeation test

Multilayered claddings also raise the issue of *delamination*, the process by which initially joined layers tend to decouple under the effect of interfacial shear stress. For the "Triplex" design, delamination could damage the *brittle* SiC layer and call its leak-tightness into question. For the "Sandwich" design, since inter-layer binding is expected to be rather weak, delamination is less likely to affect the (presumably) ductile liner. Nevertheless, delamination could also affect through-

wall thermal conductivity by creating detrimental low-conductivity gaps (which could, in fact, pre-exist in the fabricated "Sandwich".)

5. "Buffer" bond

The complexity of the GFR pin design results from two additional difficulties associated with fuel/cladding compatibility.

(1) *Thermo-chemical compatibility* was already mentioned: UPuC and SiC form some eutectic phase for temperatures much lower (about 1900°C) than the UPuC melting point (about 2500°C) and the SiC peritectic decomposition (about 2830°C). Carbon atom depletion at the fuel pellet periphery, by way of diffusion into SiC, also promotes the formation of a low-melting-point U/Pu metallic phase.

(2) *Thermo-mechanical compatibility* is also known to be an issue for the pin geometry, as a result of the *Pellet/Clad Mechanical Interaction (PCMI)*, which is driven by the irradiation-induced fuel swelling. This is particularly critical for the UPuC-SiC/SiC combination considered for the GFR. Indeed,

(a) **PCMI occurs for moderate burnup**

The UPuC fuel is characterized by a *significant swelling rate* (of the order of 1.5-2 %/at%, primarily driven by gaseous swelling, at GFR operating temperatures), as illustrated in figure 8 (left graph). Unless some sufficient pellet/clad gap is provisioned in the fabricated state, UPuC swelling favors an early occurrence of PCMI. The possibility to increase the initial pellet/clad gap thickness is limited by two main constraints. First, owing to the poor thermal conductivity of the gap (a mixture of helium and gaseous FPs), increasing gap thickness results in a detrimental thermal penalty. Then, increasing gap thickness also increases the risk that some pellet fragment relocation within the gap prematurely leads to cladding puncturing by the fuel-swelling induced pressure exerted through the pellet fragment.

(b) **PCMI induces unbearable loads**

Because it is operated at "*cold*" temperatures (owing to its excellent thermal conductivity), the UPuC fuel offers limited possibilities of accommodating PCMI-induced loads (*fuel viscoplasticity*, which would operate with oxide fuels, for instance, is *relatively negligible* with carbide fuels: it reduces the fuel swelling rate –hence, the strain rate imposed to cladding– only slightly). Thus, hoop stress (most limiting for pin geometry) can only be accommodated through *cladding damage*. The latter ultimately leads to SiC/SiC failure, as soon as the strain imposed by fuel swelling exceeds about 1% (see figure 5). As illustrated in figure 8 (right graph), the hoop stress increase rate reaches about 400 MPa/at% shortly after PCMI is achieved at the pellet mid-plane (although it occurs earlier, PCMI at the inter-pellet plane only leads to some moderate increase rate).
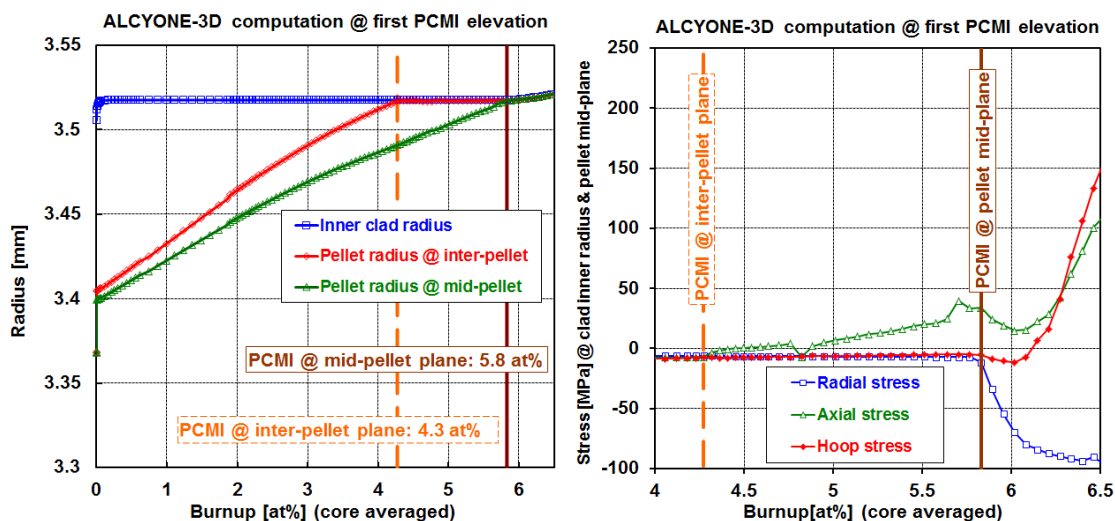
FIG. 8. Pellet/clad radius evolution and PCMI-induced cladding stress

For these reasons, fuel elements must be discharged from the core early enough to *prevent PCMI*. The target discharge burnup is evaluated by taking into account both the initial pellet/clad gap thickness and the fuel behavior. Complementary to the "nominal" (class 1 & 2) irradiation conditions illustrated in figure 9, accidental (class 3 & 4) scenarios must be taken into account too: PCMI must be prevented to occur during such scenarios as LOCA and RIA, for instance. Considering design margins sufficient to preclude PCMI-driven cladding failure, CEA studies established that helium-bonded GFR pins are doomed to achieve burnup performance limited to about 5 at% (core averaged) [11].

Although PCMI is key to designing the GFR fuel pin, it is not the only concern. Owing to its *poor thermal conductivity*, the SiC/SiC cladding is also susceptible to *thermal stresses*. Differential-strain induced loads, associated with the antagonistic *thermal expansion* and *irradiation-induced swelling* mechanisms, are shown to reach magnitudes potentially in excess of the elastic limit. As illustrated in figure 9, they are particularly reinforced (*stress concentration* factor potentially as high as 2) in the situation when the fissile column is *not centered* within the cladding, which is highly probable with helium-bonded pins.
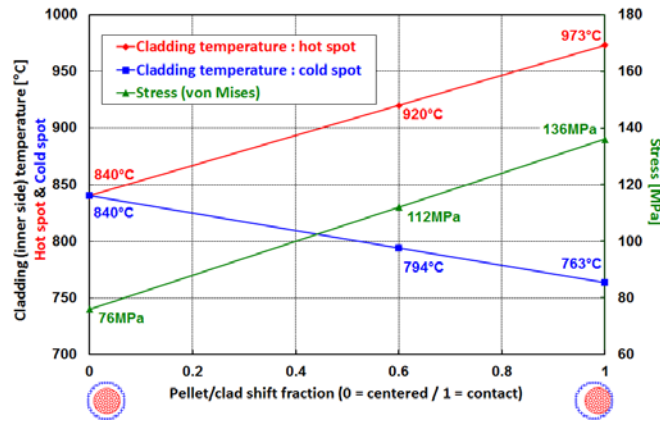
FIG. 9. Effect of pellet/clad off-centering

As illustrated in figure 10, for a fictitious irradiation history consisting of a power ramp followed by a power plateau interrupted by some shutdown phase (zero power but pressurized coolant).

— The early thermal-expansion induced stress is rapidly compensated by irradiation-swelling induced stress.

— Some low-and-stabilized stress level is reached after a few days of irradiation, once SiC swelling saturates.

— During shutdown phases, the cancelation of thermal-expansion induced differential strains restores potentially significant loads.
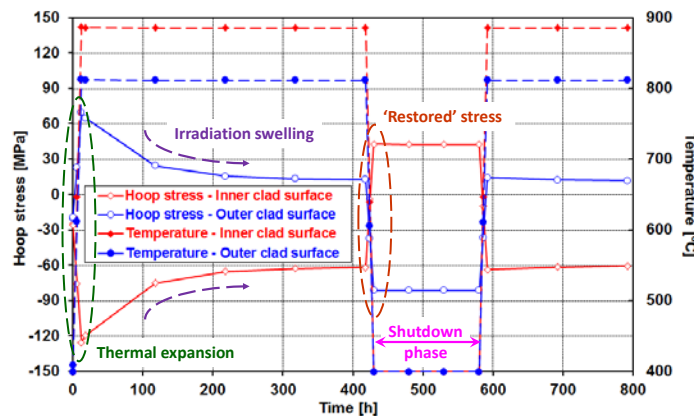
FIG. 10. Thermal stress in the SiC/SiC cladding

While thermal stress mechanisms unlikely lead to cladding failure by themselves (stress magnitude is concentrated at the cladding inner/outer surface and approaches failure level only for very high power densities), they could produce critical damage (micro-cracking) to the SiC/SiC layers. This particular issue unfortunately lacks proper experimental characterization, for the time being.

The innovative buffer-bond design (see figure 3) was proposed [5] in order to address these issues (both PCMI and thermal loads). This bond is implemented as a braided carbon-fiber web, with a fiber fraction of the order of 20-40%, which envelops the fissile column, as illustrated by the mockup in figure 11.
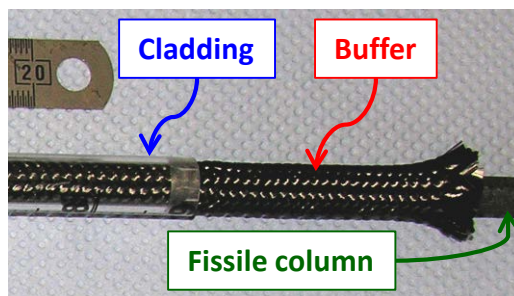
FIG. 11. "Buffer" bond mockup implementation

The advantages of the buffer are as follows.

— It allows increasing pellet/clad gap with limited thermal penalty, by favoring heat transfer through the solid structure of the buffer (a factor 3 increase in thermal conductivity is expected, relative to a helium bond with same thickness);

— It permits fuel (swelling) expansion with no cladding stress, by its capability to densify on its own porosity under moderate loads (experimental tests showed that a 10 MPa compressive stress is sufficient to achieve near-complete densification of the initial structure);

— It minimizes thermal flux heterogeneities and the associated thermal loads, by preventing pellet/clad off-centering (bond discontinuities must be precluded too: no tearing of the buffer should result from shear stresses induced by the pellet/clad differential axial expansion);

— It prevents relocation of tiny fuel fragments in the pellet/clad gap, thus allowing potentially large gaps without the risk of clad puncturing by such a fragment;

— It prevents detrimental fuel/cladding interactions by ensuring both fission-spike absorption and released FP retention (large exchange surface), on the one hand, and by providing a source of "free" carbon (fuel decarburizing is precluded, as evidenced by tests performed at 2000°C during 15 minutes, which showed no significant degradation of the fuel pellet, contrary to similar tests performed without a buffer, which led to large fuel melting), on the other hand.

The possibility to optimize the SiC/SiC-cladded pin-fueled GFR core by implementing the buffer-bond design was investigated with an innovative modeling approach, the so-called FARM tool [11]. FARM is based on integrating neutronics, thermal-hydraulics and thermal-mechanics, through meta-models; in such a way that core optimization, relative to both performance and safety, can be performed, for a simplified set of parameters and criteria, by exploring a very large design domain. FARM was used to compare optimum designs associated with helium-bonded and buffer-bonded SiC/SiC-cladded GFR pins. The obtained results suggest that buffer-bonded pins could allow significant improvements on performance and/or safety, relative to helium-bonded pins.

— Potentially important reductions in the in-cycle plutonium inventory are made possible by the buffer bond, which would facilitate the deployment of a GFR fleet: inventories only moderately higher than those of SFR-type reactors (about +30%) are found to be achievable with a buffer bond, while helium-bonded options generally lead to much larger inventories (+70%, at least).

⸺ While helium-bonded pins appear unlikely to significantly exceed the base-case 5 at% burnup objective, owing to PCMI limitations, buffer-bonded pins offer perspectives to approach (yet, not reach) the longer-term 10 at% objective prescribed by the GIF [1].

⸺ Safety indices, such as the fuel grace time and the supply pumping power, for instance, can also be improved with buffer-bonded pins, albeit less spectacularly than performance indices.

Performance benefits mostly result from the possibility to *increase power density with no detriment to such issues as PCMI* (which, on the contrary, would be a problem for helium-bonded pins). However, increasing power density (linear power in excess of $3 \ 10^4$ W/m) reinforces thermal stress, thus raising concerns about the above-mentioned potential cladding damage and resulting drop in resistance. In addition, FARM computations indicate that buffer-bond designs achieving optimum compromise between performance and safety tend to have a moderate thickness (≈ 300 µm), which does not facilitate their implementation, particularly for blind-end pins. For the most part, the buffer remains a theoretical concept: fabrications and characterizations are still necessary to prove the interest of this option, which nonetheless appears as a *compulsory step on the way to reducing pin design uncertainties and achieving high core performance*.

6. Blind-end cladding

The possibility to manufacture some blind-end SiC/SiC cladding is particularly interesting for the GFR because it might be requested that fuel elements be implemented as 2 independent half-pins joined end-to-end. Indeed, the resistance of elongated thin-walled SiC/SiC tubes to bending loads (during handling/shipping operations and seismic events) might be an issue that a half-pin design could attenuate. However, this would imply closing a half-pin end located at core mid-plane, where neutron flux is maximum, which poses the problem of end-plug joining resistance to high irradiation doses. Relying on the blind-end design patented by CEA [6] would help coping with this issue. Nevertheless, implementing such a design with the "Sandwich" cladding has not been attempted, yet. This would still necessitate welding the end-plug with the liner (both metallic), which does not seem to be an obstacle, particularly considering that this joining would only be required to warrant leak-tightness: mechanical resistance would be ensured by the outer SiC/SiC layer.

7. Conclusions and perspectives

This paper gives an overview of the progress made by CEA, in recent years, on the challenging task of designing GFR fuel elements. Although results are also presented for a mixed-CFCMC/metal duct design, the emphasis is mostly laid on the SiC/SiC-cladded (and UPuC-fueled) pin. The innovative "Sandwich" cladding and "Buffer" bond designs (CEA patents) are particularly introduced. *They are considered as credible solutions to technological bottlenecks identified as major obstacles in the early phase of the project*. They particularly aim at allowing high performance (such as high burnup and/or low plutonium inventory) and ensuring safety (integrity of the first confinement barrier, in particular) by overcoming the challenge of using SiC/SiC-based structures which is imposed to the GFR. Despite the fact that there exist preliminary achievements in terms of manufacturing and characterization of these innovations, significant studies and developments are still necessary before the viability of these fuel elements is actually established: GFR fuel R&D remains a long term perspective.

⸺ Several batches of "Sandwich" tubes (presently less than 20 cm in length) have been manufactured and subjected to various characterizations: geometrical measurements, tensile-permeation tests and high temperature thermochemical compatibility studies have been successfully performed, while high-dose irradiations are planned in BOR60. Nevertheless, *full-scale pins*, including the buffer bond and the end-plugs, are yet to be fabricated and confronted to the demanding GFR fuel requirements.

⸺ Pending the availability of *design rules applicable to SiC/SiC structures*, it is not possible to determine the acceptable operational domain of the "Sandwich" cladding. Present thermo-mechanical studies (which only assess stress levels but do not compare them to design criteria) indicate that the cladding of high performance GFR pins would have to withstand loads in excess of the SiC/SiC layers elastic limit. The recently performed tensile-permeation tests

firmly establish that the "Sandwich" design warrants cladding leak-tightness much beyond elastic limit (contrary to the "Triplex" design), potentially up to the SiC/SiC layers failure limit. However, operating the cladding beyond elastic limit would produce damages whose consequences on the cladding's ability to resist subsequent loads (notably associated with accidental transients) must be evaluated. This requires that integral tests be implemented, to model representative loading modes, such as thermal stresses and PCMI, which are not properly captured by the analytical tests presently implemented at CEA, which consist in either uniaxial tensile tests or internal-pressurization bursting tests.

ACKNOWLEDGEMENTS

REFERENCES

[1]   US Department of Energy, *A Technology Roadmap for Generation IV Nuclear Energy Systems*, Report USDOE-GIF-002-00 (2002)

[2]   R. Stainsby, J.C. Garnier, P. Guédeney, K. Mikityuk , T. Mizuno, C. Poette, M. Pouchon, M. Rini, J. Somers, E. Touron, *The Generation IV Gas-cooled Fast Reactor*, in Proceedings of ICAPP 2011 (Nice, France, May 2-5, 2011) Paper 11321

[3]   A. Ravenet, *Body for a Nuclear Fuel Assembly, and Nuclear Fuel Assembly Comprising such a Body*, Patent WO 2011/042406 A1, 14 April 2011, in French

[4]   M. Zabiégo, C. Sauder, C. Lorrette, P. Guédeney, *Tube multicouche amélioré en matériau composite à matrice céramique, gaine de combustible nucléaire en résultant et procédés de fabrication associés*, Patent submitted 1 August 2011, in French

[5]   M. Zabiégo, P. David, A. Ravenet, D. Rochais, *Solid Interface Joint with Open Porosity, for Nuclear Fuel Rod*, Patent WO 2011/157780 A1, 22 December 2011, in French

[6]   P. David, B. Bompard, J.L. Bonnand, *Closed Tubular Fibrous Architecture and Manufacturing Method*, Patent WO 2011/061249 A1, 26 May 2011, in French

[7]   Y. Katoh, T. Nozawa, L.L. Snead, K. Ozawa, H. Tanigawa, *Stability of SiC and its composites at high neutron fluence*, Journal of Nuclear Materials **417** (2011) 400-405

[8]   Y. Katoh, L.L. Snead, I. Szlufarska, W.J. Weber, *Radiation Effects in SiC for Nuclear Structural Applications*, Current Opinion in Solid State and Materials Science **16** (2012) 143-152

[9]   H. Feinroth, B. Hao, *Multilayered ceramic tube for fuel containment barrier and other applications in nuclear and fossil power plants*, Patent WO 2006/076039 A2, 26 July 2006

[10]   N. Chauvin, J.Y. Malo, J.C. Garnier, F. Bertrand, J.C. Bosq, A. Ravenet, D. Lorenzo, M. Pelletier, J.M. Escleine, I. Munoz, J.M. Bonnerot, *GFR Fuel and Core Pre-conceptual Design Studies*, in Proceedings of the (GLOBAL '07) International Conference on Advanced Nuclear Fuel Cycles and Systems (Boise, Idaho, USA, September 9-13, 2007) pp. 423-433

[11]   X. Ingremeau, G. Rimpault, P. Dumaz, S. David, D. Plancq, S. Dardour, M. Zabiégo, *FARM: A New Tool for Optimizing the Core Performance and Safety Characteristics of Gas Cooled Fast Reactor Cores*, in Proceedings of ICAPP 2011 (Nice, France, May 2-5, 2011) Paper 11053 (See also, for a detailed presentation: J.J.X. Ingremeau, *Méthodologie d'optimisation d'un cœur de réacteur à neutrons rapides, application à l'identification de solutions (combustible, cœur, système) permettant des performances accrues - Etude de trois concepts de cœurs refroidis à gaz, à l'aide de l'approche FARM*, Ph-D thesis, Université Paris-sud 11, December 2011, in French)

State of the art of the conceptual designs for ASTRID control and shutdown rods

I. Guénot-Delahaie, D. Lorenzo, B. Valentin, J.-M. Escleine, T. Helfer

French Alternative Energies and Atomic Energy Commission (CEA), Cadarache, France

Abstract. A critical look at the conceptual designs of control and shutdown rods and absorber elements, along with the lessons learnt from the operation of French fast reactors (Phénix and Super-Phénix especially) and the associated irradiation tests, has yielded improved and even innovative absorber assembly design concepts which are presented in this paper. To comply with the GEN IV objectives set for the 600 MWe Advanced Sodium Technological Reactor for Industrial Demonstration (ASTRID), these design concepts have been researched with a view to improved economy/sustainability and enhanced safety.

The two main measures undertaken to achieve economy, among many others, have been to reduce the absorber subassembly dimensions and boron carbide enrichment, as well as to extend the residence time. To achieve enhanced safety, measures could include improved components and/or structural materials and guidance surface coatings/hard-facings in active shutdown systems. As part of these measures, a new kind of absorber assembly has also been designed – called SEPIA[1] – pertaining to safety devices for the passive insertion of negative reactivity in the core.

Preliminary thermal-hydraulic and structural mechanical analyses have been carried out with the CADET and LICOS project codes to show their feasibility. Further detailed analyses need to be carried out to achieve optimum dimensions that comply with the RAMSES II design rules.

The paper discusses the basis of the conceptual designs, giving due consideration to emerging design concepts, analysis backups and further R&D required for design qualification.

1.   Preliminary discussions

In 2010, the CEA started the first phase of conceptual design for the 600 MWe Advanced Sodium Technological Reactor for Industrial Demonstration (ASTRID) prototype to define innovative technical options.

Designed with a defence-in-depth approach based on redundancy, diversity and independence, ASTRID has two distinct and independent fast-acting reactor shutdown systems. Each shutdown system consists of sensors, logic circuit, drive mechanisms and mobile neutron absorber rods in stationary wrappers. The rod and wrapper form the absorber subassemblies distributed in the core. The absorber subassembly of the first system dedicated to power regulation, compensation for the reactivity change during the lifetime and normal or emergency shutdown is called RBC subassembly, and that of the second system dedicated to emergency shutdown, RBS subassembly. The respective drive mechanisms, RBC-BK and RBS-BK, are housed in the control plug, which is a part of the reactor's top shield.

With a view to a more robust design and safety demonstration, additional core safety features/systems, called SEPIA, are designed as potential options based on passive insertion of negative reactivity equivalent to a 3rd shutdown system, allowing the return to a safe state in case of a loss of coolant accident without scram [1].

---

[1] This is an abbreviation for "SEntinal for Passive Insertion of Antireactivity".

2. Major design options

2.1. Itemising ASTRID specifications

The following main improvement objectives and related topics for subsequent investigation stemming from ASTRID specifications motivated the structure of RBC, RBS and SEPIA subassembly design activities:

(1) enhanced safety
   (a) lessons learned from previous fast-reactors operations
   (b) structural materials and guidance surface coatings/hard-facings
(2) projected cost savings
   (a) reducing absorber subassembly length
   (b) extending residence time: it is economically desirable to match the residence cycle and, if possible, life span of the absorber elements with those for the fuel cycles (4 runs of 360 or 400 effective full power days, or EFPD, each)
   (c) reducing the total number of absorber subassemblies
   (d) keeping the enriched absorber material requirement as low as possible

2.2. Value engineering

As regards RBC and RBS subassemblies within first phase of ASTRID conceptual design, it was decided to use the same design principles as for the French Phénix, Super-Phénix and EFR systems:

— alignment of all (fuel and absorber) subassembly heads in the core,

— retention of the mobile absorber rod inside the wrapper and maintaining its gravity actuation;

— for the RBS subassemblies, disconnection in case of scram, via an in-sodium electromagnet that does not extend beyond the absorber subassembly lifting head. This constitutes a diversification against common mode failure of insertion of control rods into the subassemblies that makes it possible to guarantee safe core shutdown in case of significant deformation of the reactor block that would be likely to block the RBC mobile rods in their wrappers (disconnection of the RBC rods takes place at the level of the slab).

With reducing the height of the subassemblies as an objective, the following options for the absorber subassemblies were chosen:

— RBC subassembly with lower guide bush and olive-shaped rod spike linked to an absorber drive mechanism with a bayonet-type gripper;

— RBS subassembly with a dashpot located in the lower part and an unsegmented absorber bundle linked to an electromagnetic gripper.

The current standard generic absorber element for the French RNR reactor type has been renewed as the reference option for the start-up core. This absorber element consists of a vented pin with a permanent sodium bond between the stainless steel cladding and the absorber column, which is equipped with a confining shroud (to prevent migration of the absorber fragments). The main absorber rods consist of bundles of such pins, which may or may not be enclosed within a cylindrical pin bundle wrapper depending on the cooling requirements. Boron carbide (B_4C), which may or may not be enriched in ^{10}B (the neutron-capturing isotope of the neutron-absorbing boron element) is currently the only neutron-absorbing material and is not currently being reassessed for the first cores. Most of the R&D and qualification requirements mentioned further on stem from the operating issues inherent to this type of design and/or absorber material. However, both the search for more durable standard absorber elements and the specific requirements for SEPIA system operational modes fully justify requirements that tend to break with current feedback on design/absorber type. Alternative absorber materials like HfB_2 and TiB_2, whether or not they are enriched in ^{10}B, and even Hf are all being considered for the longer term, along with a single- or double-donut shaped absorber column design.

As for the structural materials, the first ASTRID cores will be based on a choice of known and already tested materials, some of which have even been tested in Phénix cores, e.g. EM10 for the hexagonal tube material and

AIM1 for the cladding. All this helps to increase the reliability of rod insertion due to a better understanding and integration of irradiation swelling.

2.3. *Design features – Description*

2.3.1. *RBC subassembly*

The RBC subassembly consists of a mobile control rod in a stationary hexagonal wrapper tube identical to the fuel subassembly wrapper, as shown in Fig. 1. Its length is 4.5m and it is supported on grid plate. Nineteen absorber pins housed in the mobile RBC rod are held by guide rails and hang freely from the top. They are arranged in triangular pitch as a bundle, covered by a cylindrical wrapper. B$_4$C boron carbide pellets are stacked and shrouded in the absorber pin clad tubes. Sodium enters at the foot of the subassembly, passes through the absorber pin bundle and through the annular gap between the mobile RBC rod and stationary wrapper, and exits through the top of the cylindrical wrapper. RBC rod movement inside the stationary wrapper is guided at two levels: at the lower end of the rod spike (mobile guidance along a guide bush located over the spike) and along the entire length of the pin bundle wrapper (stationary guidance by means of pads located in the upper part of the subassembly). The parts of the wrapper in contact with the mobile rod (guide bush and pads) have a hard-faced surface to ensure the durability of guidance throughout the life of the subassembly.

FIG. 1. RBC subassembly
(red part representing the position of fissile core; orange arrow showing sodium flow entry)

A bayonet-type gripper at the bottom end of RBC-BK may be used to hold/release the head of the mobile RBC rod, as illustrated in Fig. 2.
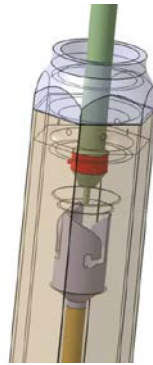
FIG. 2. How the RBC rod could be connected to a bayonet-type gripper
(courtesy of AREVA-NP)

2.3.2. *RBS subassembly*

The RBS subassembly consists of a mobile rod in a stationary hexagonal wrapper tube identical to the fuel subassembly wrapper, as shown in Fig. 3. The rod's mechanical structure is maintained by a central anchor shaft linking the connecting surface to the electromagnet (in the upper part of the rod) to the dashpot piston (in the lower part). A collar is attached to the anchor shaft, from which the pins are hung along with a centring grid at the lower end of the pins. Unlike for the RBC rods, the objective is not to optimize pin bundle cooling by channelling most of the sodium into a pin bundle wrapper, inasmuch as the absorber material here is not introduced into the core during operation. When the rod has dropped, shock absorption is activated by the piston, which enters a cylinder attached to the wrapper. A wide diametrical gap is engineered between the wrapper and

the rod along the entire length of the rod's stroke to ensure rod insertion even in conditions where the wrapper is significantly deformed (bending and/or crushing in the across-flat area).
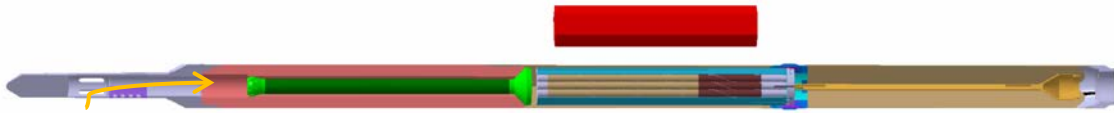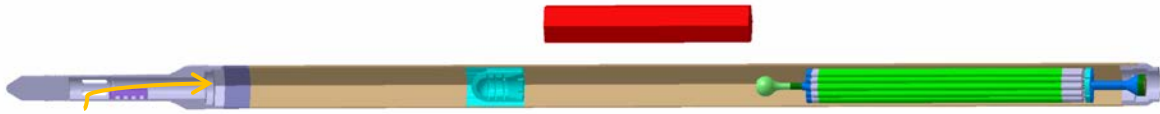

FIG. 3. RBS subassembly
(red part representing the position of fissile core; orange arrow showing sodium flow entry)

2.3.3. SEPIA subassembly

The safety directives for ASTRID are to develop a diversified negative reactivity insertion system that is independent from the two shutdown systems to ensure that if these fail, the hot zero power state in the core will occur at temperatures compatible with the thermal criteria for the fuel melting margin, the boiling point of sodium and the resistance of the structures. To the extent that the failure of the first two systems can be linked to the instrumentation and control system, a requirement is that the third system can be actuated directly in response to a physical phenomenon. A number of different concepts are under study, including a hydraulic actuation system (in response to a drop in flow rate) and a heat-actuated system (in response to an increase in temperature). The research on this last concept is more advanced; actuation is triggered by the differential expansion of two cylindrical shells under temperature transient caused by the loss of the primary flow and/or the secondary flow which is not protected due to the failure of the first two systems. This device, called SEPIA, is illustrated in Fig. 4.

SEPIA consists of a capsule inserted into the centre of a fuel subassembly pin bundle. The differential expansion of the two shells, which are located in the upper part of the capsule, causes several locking fingers on a column of spherical absorber pellets to rotate and thus the absorber elements to fall inside the capsule. This set of design options allows developing a system that is:

—— completely independent and distinct from the first two shutdown systems;

—— highly responsive to temperature transients, since the actuating system benefits directly from the fuel subassembly flow rate;

—— robust from the operational point of view, because the mechanical principle for the actuating system allows out-of-reactor qualification, a locking capability to avoid any risk of untimely triggering at handling temperatures, the development of sufficiently wide movement for the required actuating precision, and the possibility to use mechanical means to ensure reliable actuation. The system is also far enough away from the neutron flux that it is unaffected by irradiation swelling, and remains operational for conditions in which the subassemblies would be significantly deformed due to the mechanical decoupling of the capsule and the central wrapper, to the form of the absorber elements (column of spherical pellets) or to the wide diametral gap created between the absorber elements and the capsule;

—— not particularly significant in the core design because:
    a) it requires no absorber drive mechanism and therefore no slab penetration,
    b) it has a very low impact on the core's fuel volume fraction (less than one per cent),
    c) the design concept for the capsule-carrying fuel subassembly is qualified (DCC Phénix) and it is also required for irradiation experiments in ASTRID.

Studies have shown that the thermocouples placed over the subassemblies enable the detection and localisation of the absorber column insertion in a SEPIA subassembly. An ultrasonic detection system is also being investigated.

The main points that remain to investigate in terms of feasibility practically all have to do with qualification, in-pile tests for absorber elements and out-of-pile loop tests for the actuation technology.
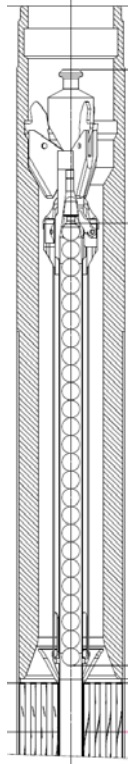
FIG. 4. Illustration of the SEPIA subassembly

3. Examples of studies carried out

3.1. Absorber element design methodology and topics/specific points to be investigated to match the required residence time

The generic design process aims to guarantee throughout the life of an absorber element both the integrity of the cladding in compliance with the RAMSES II design rules and with respect to the propagation of any internal cracks initiated by corrosion of the cladding material in connection with absorber cladding chemical interaction (ACCI), and the absence of: 1) melting of the absorber or of the shroud, 2) absorber cladding mechanical interaction (ACMI) or 3) interaction between absorber elements. Support calculations have been performed using the LICOS project code [4].

The issues relating to compliance with meltdown prevention criteria must be distinguished from life span issues. French feedback on these issues mostly concerns boron carbide (B_4C). Melting temperature and integral thermal conductivity under radiation are the parameters that, together with the geometry of the basic absorber entity (pellet, sphere, etc.), determine whether or not there is compliance with the meltdown prevention criterion. Currently, the most restrictive factor concerning B_4C is clearly the excessively conservative formalism describing the changes to its thermal conductivity under fast neutron flux.

The volumetric swelling of the absorber entity under irradiation and internal corrosion of the cladding material by the absorber material have been identified as the phenomena most likely to reduce the absorber element's life span. Independently, their kinetics determine the instant that ACMI occurs and the time it takes to reach the maximum acceptable corroded thickness relative to the cladding mechanical strength. Together, these phenomena determine the life span over and above which the loss of shroud ductility becomes incompatible with its containment function.

Due to the heavy production of helium when boron materials are subjected to neutron flux, the swelling kinetics are especially dependent on the changes in the capture density rate for [10]B. The absence of ACMI will then depend on not exceeding a certain capture density threshold. In the absence of a confining shroud, the appearance of ACMI is subject to the random behaviour of any fragments in the joint and to compression caused

by macro-/micro-fracturing of the absorber entity. By holding fragments in place and preventing compression, the shroud significantly slows down ACMI. Achieving long service lives such as those sought for ASTRID and the Generation IV sodium-cooled fast reactors is subject to the reliability and performance of this component.

Strict compliance with the B_4C and shroud meltdown prevention criteria as regards conventional absorber elements has never led to a technological impasse. With respect to the ASTRID project, compliance presents less of a design optimisation problem than it used to, now that ^{10}B enrichment has been scaled down. A life span of at least two runs out of the four required for ASTRID is an accessible objective to start with, by renewing the components and materials that have been validated in the Phénix and with the added reliability of the shroud and the use of "carbothermal"-generated B_4C instead of the "magnesiothermal"-generated B_4C [5] that is the sole basis for the knowledge gleaned from Phénix feedback. Even if in this respect the presence of a shroud is supposed to cancel out the B_4C fabrication differences, it still is necessary to update a behavioural comparison of the two types of product, including for the corrosive potential. Due to the neutron volume requirements for SEPIA absorber entities (solid spheres), the current conservatism of the thermal conductivity law for B_4C turns out to be incompatible with compliance with the meltdown prevention requirement for the absorber. This obstacle alone fully justifies experimental efforts to do away with or at least to better define this conservative approach and find alternative absorber materials that are significantly more conductive and/or heat-resistant than boron carbide. Another major research and development challenge, practically as important as the nature of the absorber material, is to perfect a suitable shroud for SEPIA absorber entities.

3.2. *Preliminary thermohydraulic analysis*

This analysis is done using CADET [3] and LICOS design tools, based on the thermal criteria that apply to the above-mentioned design process. Nominal operation scenarios and incidental scenarios involving the untimely dropping of a rod during nominal reactor operation are being considered.

The aims for the chosen criteria are to minimize carburisation of the cladding, to prevent meltdown of the absorber material and keep the sodium joint from reaching the boiling point.

3.2.1. *RBC and RBS subassemblies*

In the case of the RBC and RBS subassemblies, a flow rate of a few kg/s per subassembly enables compliance with all criteria in every scenario.

For both, the cavitation and fly-off risks still remain to be studied. Even so, the low flow rates required to cool these subassemblies makes it possible to significantly limit these two risks, so the feasibility studies reveal nothing that would disqualify the chosen designs. However, before launching a full thermohydraulic design for these two subassemblies, more thorough studies do need to be done.

3.2.2. *SEPIA subassembly*

A specific thermohydraulic feature of this subassembly is the column of spherical absorber pellets that are introduced into a device called the capsule, which is placed within a fuel pin bundle from which two rows of pins have been removed. The capsule has no internal flow rate for cooling the absorber spheres, so these are cooled by conduction and then by thermal coupling with the bundle coolant medium. The CADET code is used to do the design analysis to integrate the fuel pin bundle and the transverse thermocouples, while the LICOS code serves to assess the internal temperature of the designed absorber sphere. Two absorber materials are analysed: B_4C and hafnium diboride HfB_2. The limit value of thermal conductivity after irradiation is assumed for each one. The two above-mentioned scenarios are studied.

The design analysis shows that whatever the scenario, the fissile pin bundle is always correctly cooled with a flow rate of about 36 kg/s, even without flow inside the central wrapper. The most severe design scenario is the one featuring an untimely drop of the column of spherical absorber pellets with the reactor continuing nominal operation. Therefore, given the current knowledge on B_4C (especially on how its thermal conductivity changes under irradiation):

— for B_4C: it is not possible from the thermohydraulic viewpoint to ensure the meltdown prevention criterion, even with a flow inside the central wrapper or by increasing the flow rate in the fissile bundle;

—— only by replacing B_4C with HfB_2 can the meltdown be avoided.

So, the results do show, however, that the feasibility of the SEPIA subassembly is linked more to the chosen absorber material solution (B_4C *versus* HfB_2) than to its thermohydraulic feasibility, which remains to be refined and validated but so far does not give reason to abandon this design concept.

3.3. *Subassembly spikes with additional discriminatory feature*

The goal is to keep the core sub-critical under all plant conditions, including design basis conditions and design extension conditions. In order to meet this goal, the normal operating reactivity will be defined so that the sum of all credible reactivity insertions during normal operation is insufficient to cause criticality. During refuelling, absorber rods will be used to reduce the reactivity still further, to account for the additional reactivity associated with possible handling errors.

Additional protection against handling error during refuelling will be provided by including discriminatory features (currently under study) on the subassembly spikes to prevent substitution errors, e.g. the wrong type of subassembly from being completely lowered into the wrong position.

4. Outlook

4.1. *R&D and qualification requirements to support design options*

In 2012, the different requirements for R&D and qualification of the absorber subassemblies (including the materials) for the CFV core (low sodium void fraction) were analysed, which made it possible to identify the more structurally significant ones with respect to the ASTRID plan. The analysis was based on lessons learnt and on the identification of lacunae in the state of the knowledge and the experimental databases.

Given the current knowledge, as we progress with the ASTRID specifications with the perspective of at least matching the life span of the absorber elements and subassemblies to that of an ASTRID reactor fuel core, it emerges that the main qualification issues concern:

—— for absorber element R&D: shroud behaviour, structural corrosion (cladding and/or shroud), and absorber thermal behaviour, with the intent to use the most durable materials possible as a common thread,

—— for absorber subassembly R&D: the behaviour of hard-faced parts that are implicated in guidance problems.

The qualification issues relating to SEPIA were discussed above.

4.1.1. *Post-irradiation experiments on already irradiated objects*

Generally speaking, the qualification of absorber elements and subassemblies will broadly rely on the post-irradiation examinations of irradiation experiments carried out in the Phénix reactor. The objects of interest for the ASTRID core and the testing requirements were identified in connection with the "Phénix Treasures" project [2].

4.1.2. *R&D actions on shroud behaviour and cladding/shroud corrosion*

The shroud and corrosion behaviour studies must be linked. Before start-up, these studies will consist of sodium loop tests, specific mechanical tests of corroded specimens and analytical irradiation experiments. As for the conventional absorber elements, they must first consolidate or confirm (relative to the "carbothermal" B_4C) what can already be considered as acquired (half-life span) and then reach at least the intended life span of the conventional absorber elements by assessing other types of shroud and/or cladding materials (coatings included) and other design options. If no integral or even representative irradiation occurs prior to the start-up of ASTRID, the scenario will aim for two cycles for the initial loading of ASTRID, based on what we already know. These two cycles would be subject to an appropriate monitoring plan and efforts to introduce, as soon as possible, some precursor materials with the potential for longer life spans (cf. the Superphenix approach).

4.1.3. R&D actions on absorber materials

Three main areas for research and development on absorber materials were identified:

— Consolidating and advancing the knowledge on boron carbide (B_4C) to improve phenomenological modelling and formalisation of its irradiation behaviour. The first step is to make the best use of the most relevant irradiated absorber entities from the "Phénix Treasures" project, in particular those fabricated from "carbothermal" B_4C.

— Studying the changes in the properties and behaviour of HfB_2 and TiB_2 under irradiation. These diborides have been identified among other boron materials as potentially and globally the most capable of meeting the operating requirements for SEPIA systems. They also show the right potential to be appropriate long-term substitutes for the use of B_4C in general. A preliminary R&D step is needed to confirm whether or not they are capable of maintaining under neutron flux the initial properties they were chosen for, i.e. a high and distinctly metallic thermal conductivity and high refractoriness.

— Hafnium metal, which is a robust and durable alternative under rapid flux to boron materials as long as its low intrinsic absorbing power does not constitute an unacceptable handicap. It also has excellent mitigation potential, which is an advantage. The main question is whether it is capable of remaining under rapid flux for long periods (ageing) without unacceptable loss of its geometric integrity.

4.1.4. Irradiation

With respect to absorber qualification, investigations will be launched to carry out:

— irradiation of specific materials to qualify the coatings/hard-facings for guidance parts that are exposed to neutron flux,

— irradiation of absorber elements, using design and flux conditions that are as representative as possible of the start-up core in support of 1) validating the overall design-fabrication-service load process, 2) qualifying "carbothermic" B_4C and 3) demonstrating the shroud life span.

ABBREVIATIONS

ACCI Absorber–cladding chemical interaction

ACMI Absorber–cladding mechanical interaction

AIM1 Austenitic improved material 1

ASTRID Advanced sodium technological reactor for industrial demonstration

EFPD Effective full power days

EM10 Martensitic alloy

RAMSES II Design rules for the fast breeder core structures embrittled by irradiation

RBC-BK Drive mechanism associated with RBC subassembly

RBS-BK Drive mechanism associated with RBS subassembly

SEPIA Sentinal for passive insertion of antireactivity

ACKNOWLEDGEMENTS

REFERENCES

[1]   GAUCHÉ F., Generation IV reactors and the ASTRID prototype: lessons from the Fukushima accident, Comptes Rendus Physique 13 (2012) 365-371

[2]   MUNOZ I., Recovery of materials from PHENIX to support the qualification of ASTRID design options, this proceeding

[3]   VALENTIN B., The thermal-hydraulics of a pin bundle with an helical wire wrap spacer. Modelling and qualification for a new subassembly concept. *IAEA - IWGFG - TCM on thermal-hydraulics of LMFBRs sub-assemblies - Obninsk, Russia July 27-31, 1998*

[4]   MICHEL B., NONON C., SERCOMBE J., MICHEL F., MARELLE V., Simulation of the Pellet Cladding Interaction phenomenon with the PLEIADES fuel performance software environment. *Nuclear Technology, accepted 29-08-2012, to be published.*

[5]   KRYGER B., ESCLEINE J.-M., Absorber elements. *The nuclear fuel of pressurized water reactors and fast reactors – design and behaviour, chapter 7.* Edited by H. Bailly, D. Ménessier and C. Prunier, Intercept Ltd.

Review Paper

Alternative Fabrication Methods of Metal Fuel Slugs for SFR

Ki-Hwan Kim, Jong-Hwan Kim, Hoon Song, Seok-Jin Oh, Ho-Jin Ryu, and Chan-Bock Lee

Korea Atomic Energy Research Institute
Daedeok-daro 989-111, Yuseong-gu, Daejeon, Rep. of Korea

Abstract

Metal fuel slugs of U-Pu-Zr alloys for Sodium-cooled Fast Reactor (SFR) have conventionally been fabricated by a vacuum injection casting method. Recently, management of minor actinides (MA) became an important issue because direct disposal of the long-lived MA can be a long-term burden for a tentative repository up to several hundreds of thousand years. In order to prevent the evaporation of volatile elements such as Am, the alternative fabrication methods of metal fuel slugs have been studied applying gravity casting, improved injection casting, and centrifugal atomization method in KAERI, including melting under inert atmosphere. And then, metal fuel slugs and particulate metal fuel were examined with casting soundness, density, chemical analysis, particle size distribution and microstructurural characteristics.

1. INTRODUCTION

Korea Atomic Energy Research Institute (KAERI) seeks to develop and demonstrate the technologies needed to transmute the long-lived transuranic actinide isotopes in spent nuclear fuel into shorter-lived fission products, thereby dramatically decreasing the volume material requiring disposal and the long-term radio-toxicity and heat load of high level waste sent to a geological repository. Metal fuel for SFR has advantages such as simple fabrication procedures, good neutron economy, high thermal conductivity, excellent compatibility with a Na coolant and inherent passive safety [1]. U-Zr metal fuel for SFR is now being developed by KAERI as a national R & D program of Korea. In order to recycle transuranic elements (TRU) retained in spent nuclear fuel, remote fabrication capability in a shielded hot cell should be prepared. Moreover, generation of long-lived radioactive wastes and loss of volatile species should be minimized during the recycled fuel fabrication step. The fabrication technology of metal fuel for SFR is being developed in Korea as a national nuclear R&D program from 2007 [2-5]. The reference fuel for the Korean SFR is a metal alloy. Metal fuel has been studied and is also considered a leading candidate for advanced driver and transmutation fuels under the Fuel Cycle Research and Development (FCRD) program, formerly the Advanced Fuel Cycle Initiative (AFCI) program. The fabrication process for SFR fuel is composed of (1) fuel slug casting, (2) loading and fabrication of the fuel rods, and (3) fabrication of the final fuel assemblies. Fuel slug casting is the dominant source of fuel losses and recycled streams in this fabrication process.

Development of the vacuum injection casting method for fuel slugs was initiated late in 1956 with centrifugal casting considered as the backup process. Because the injection casting process is simple and compact, it is cost efficient and has the advantage of producing mass product while reducing the amount of radioactive waste. This process has developed into a remote operation which is capable of producing precision castings with a random grain orientation. U-Zr and U-Pu-Zr fuel slugs for test subassemblies irradiated in EBR-II and FFTF were fabricated by this injection casting method. More than 100,000 metal fuel slugs including both U-5wt%Fs and U-10wt.%Zr fuels were fabricated by

injection casting in the united states. U-Zr-Pu alloy fuels have been used related to the closed fuel cycle for managing MA actinides and reducing a high radioactivity levels since the 1980s.

However, casting alloys containing volatile radioactive constituents, such as Am, is problematic in the conventional injection casting method, because the furnace containing the fuel melt is evacuated. Not only is retention of Am important for successful transmutation of MA in a fast reactor, but any material lost must be efficiently recovered in a waste stream and subsequently dealt with, increasing the oveal facility cost and safety requirement. This is especially challenging in a remote fabrication environment, where all operation must either be automated or conducted with manipulators. Although an injection casting has been a well-established fabrication method for metal fuel for decades [6], Am addition to the metal fuel hampers conventional fuel fabrication processes because of the high vapor pressure of Am at melting temperature of uranium alloys [7]. An advanced fuel casting system to control transport of volatile elements during melting of a fuel alloy with MA has been developed. It is necessary to minimize the vaporization of Am and volume of radioactive wastes [8].

In this study, alternative fuel slug fabrication methods have been introduced to develop an innovative fabrication process of metal fuel of SFR for preventing the evaporation of volatile elements such as Am. Metal fuel slugs were fabricated by gravity casting, improved injection casting and centrifugal atomization method in KAERI. Volatile species can be retained through the use of cover gas over pressure, covered crucibles, and short cycle times under these fuel fabrication method [9-14]. Fuel slug and particulate fuel for SFR were fabricated and characterized to evaluate the feasibility of the alternative fabrication method.

2. EXPERIMENTAL PROCEDURE

The feasibility of imporved injection casting method including melting under inert atmosphere was evaluated in a small-size induction-melting furnace. As experimental equipment, its primary purpose was to explore and define various casting variables, e.g., casting temperature and pressure, pressurizing rate, mold coating method. Pure cupper was selected as a surrogate material, which has a melting temperature similar to uranium. The crucible is inductively heated up to 1400°C, which is sufficiently higher than the liquidus temperature of the surrogate material. All operations were done under argon atmosphere. At a predetermined superheat, the mold was lowered, immersing the open tip into the metal melt. When the metal has solidified, the mold was raised. After cooling, the surrogate fuel slug is taken out of the mold. Elemental lumps of depleted uranium, zirconium, manganese, rare-earth elements were used to fabricate U-10wt.%Zr, U-10wt.%Zr-5wt.%RE(RE: Nd 53wt.%, Ce 25wt.%, Pr 16wt.%, La 16wt.%), U-10wt.%Zr-5wt.%Mn and U-10wt.%Zr-5wt.%RE-5wt.%Mn fuel slugs by gravity casting method. Graphite crucibles coated with high-temperature ceramic plasma-spray coating method and quartz molds coated with high-temperature ceramic by slurry-coating method were used. Particulate metal fuels were fabricated with centrifugal atomization method, fabricating spherical U-10wt.%Zr powder.

After fabricating the fuel slugs in the casting furnace, the fuel losses in the crucible assembly and the mold assembly were quantitatively evaluated. The soundness and the chemical composition of as-cast fuel slugs were identified and analyzed. As-cast fuel slugs were inspected by gamma-ray radiography. The densities of the fuel slugs were also measured by Archimedean immersion method. Thw particle size distributions were examined by vibration-type sieve shaker. A scanning electron microscope (SEM) was used to study the microstructure of as-cast fuel slugs. Chemical compositions of as-cast fuel slugs were measured by energy-dispersive spectroscopy (EDS).

3. EXPERIMENTAL RESULT AND DISCUSSION

An alternative fabrication method is to fabricate the fuel slugs using a low pressure gravity casting system in which the melt in a crucible is cast into the mold under the crucible through a distributer by a gravity force under low pressure [3].

<div align="center">(a)   (b)</div>

FIG. 1. U-10wt%Zr fuel slugs (Φ5 mm x L300 mm) (a), and gamma-ray radiography (b), fabricated by low pressure gravity casting.

The melting and casting parameters of the fuel slug casting process such as melting batch size, coating method, pouring method, melting & casting temperature, mold pre-heating temperature and melt distributor pre-heating temperature have been investigated to get the sound fuel slugs. The metal fuel slugs with diameter of 5mm and length of 300mm were fabricated using the advanced fuel casting system, as shown in Fig. 1~3. Gamma-ray radiography was performed to detect internal defects such as cracks and pores inside the metal fuel slugs. The yield of fuel alloy melt to casting molds was about 90%. The alloy compositions and the densities of U-10wt.%Zr, U-10 wt.%Zr-5 wt.%RE, and U-10 wt.%Zr-5 wt.%RE-5 wt.%Mn fuel slugs were shown in Table 1 and Table 2. It was seen that the losses of these volatile elements such as Am can be effectively controlled to below detectable levels using modest argon overpressures. Based on these results there is a high level of confidence that Am losses will also be effectively controlled by application of a modest amount of overpressure.

<div align="center">(a)   (b)</div>

FIG. 2. U-10wt%Zr-5wt.%RE fuel slugs (Φ5 mm x L300 mm) (a), and gamma-ray radiography (b), fabricated by low pressure gravity casting.

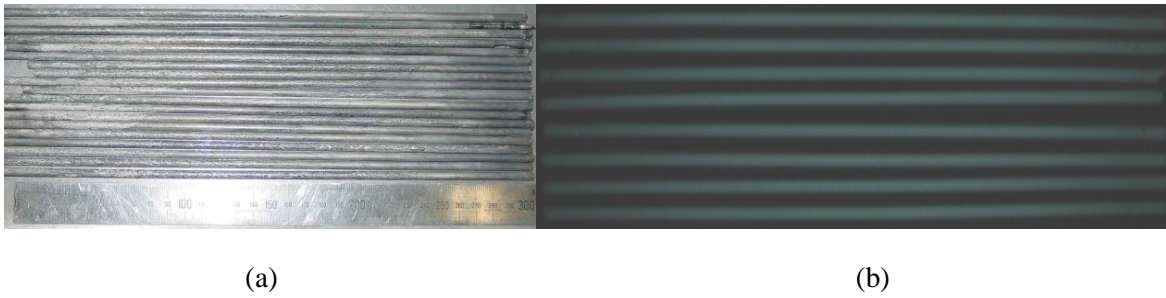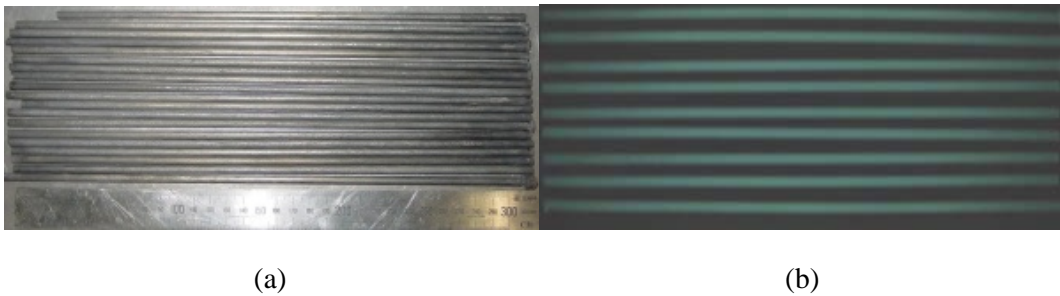<div align="center">(a)   (b)</div>

FIG. 3. U-10wt%Zr-5wt.%RE-5wt.Mn fuel slugs (Φ5 mm x L300 mm) (a), and gamma-ray radiography (b), fabricated by low pressure gravity casting.

TABLE 1. Alloy compositions of U-10Zr, U-10Zr-5RE, and U-10Zr-5RE-5Mn fuel slugs.

Ki-Hwan Kim, Jong-Hwan Kim, Hoon Song, Seok-Jin Oh, Ho-Jin RYu, and Chan-Bock Lee

Nominal Composition / Location	U-10Zr	U-10Zr-5RE	U-10Zr-5RE-5Mn
Top (g/cm^3)	15.9	14.7	12.5
Middle (g/cm^3)	16.1	14.7	14.0
Bottom (g/cm^3)	16.1	14.7	14.0

TABLE 2. Densities of U-10Zr, U-10Zr-5RE, and U-10Zr-5RE-5Mn fuel slugs.

Nominal Composition / Element	U-10Zr	U-10Zr-5RE	U-10Zr-5RE-5Mn
U (wt%)	90.4	84.1	79.1
Zr (wt%)	8.7	10.2	10.0
RE (wt.%)	-	2.9	4.4
Mn (wt.%)	-	-	4.6
C (ppm)	293	760	626
O (ppm)	546	560	1,150
N (ppm)	17	40	50

The scanning electron micrographs of the metal fuel slugs fabricated by gravity casting under loww pressure were shown in Fig. 4. The microstructure of U-10wt.%Zr fuel slugs showed UZr$_2$ or Zr particulate dispersions about 5μm in size and laminar structure below 0.5μm in thickness in matrix. The disperse precipitates of U-10wt.%Zr-5wt.%RE fuel slugs, over-etched with an etchant, were finely distributed below 5μm in size. The microstructure of U-10wt.%Zr-5wt.%RE-5wt.%Mn fuel slugs, over-etched with an etchant, showed some eutectic Mn-rich precipitate dispersions below 3μm in thickness. There was an increased amount of dendritic dispersion phases compared with U-10wt.%Zr fuel slugs, irrespective of atmospheric pressure. A considerable amount of Mn was contained in periphery of dendritic dispersions, and in the eutectic dispersions, approximately 1~2μm in size. There was a greater amount of eutectic matrix in the alloy melted under Ar atmosphere compared to the alloy melted under vacuum. This increased amount of eutectic phase in the U-10wt.%Zr-5wt.%Mn alloy melted under Ar atmosphere, resulted from a higher Mn content than the U-10wt.%Zr-5wt.%Mn alloy melted under vacuum.

The typical material balance in the crucible assembly and the mold assembly after fabrication of volatile surrogate U-10wt.%Zr-5wt.%Mn, and U-10wt.%Zr-5wt.%RE fuel slugs are shown in Table 3 and Table 4. A considerable amount of dross and melt residue remained in the crucible after melting and casting; however, most charge materials were recovered after fabrication of the fuel slugs. The mass fraction of fuel loss relative to the charge amount after fabrication of U-10wt.%Zr-5wt.%Mn, and U-10wt.%Zr-5wt.%RE fuel slugs was low, about 1.5%, and 0.1% respectively. It is thought that a lower fuel loss in case of casting of U-10wt.%Zr-5wt.%Mn and U-10wt.%Zr-5wt.%RE fuel slugs was related to melting of the U-Zr-Mn and U-Zr-RE alloy in a densely plasma-sprayed graphite crucible

with high-temperature ceramic materials, compared with casting of U-10wt.%Zr fuel alloy in a sparsely slurry-sprayed graphite crucible with high-temperature ceramic materials.
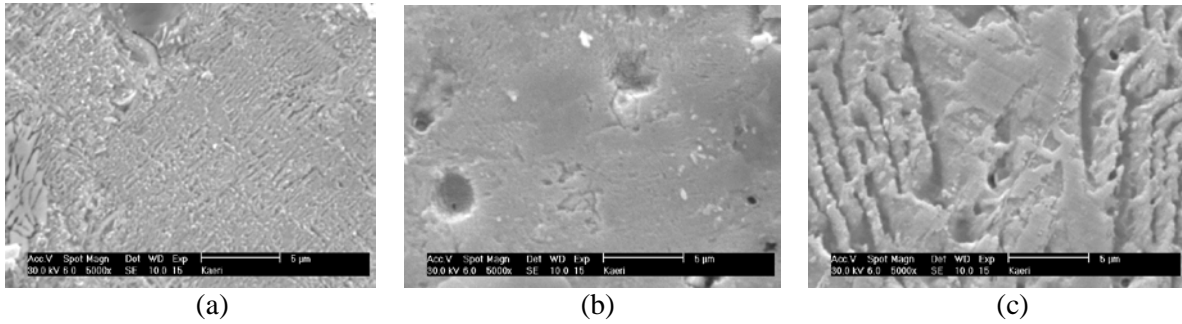

(a)   (b)   (c)

FIG. 4. Typical scanning electron micrographs of (a) U-10Zr, (b) U-10Zr-5RE, and (c) U-10Zr-5RE-5Mn fuel slugs; x5000.

As shown in Fig. 5-(a) the surrogate fuel slug was soundly cast by improved injection casting method, where the surrogate material is melted under inert atmosphere. The general appearance of the slug was smooth and the length was about 250mm. Some hot tears were observed in the upper part region, resulting from quick cooling. It was thought that this area of a casting was not allowed to shrink quickly, placing the area under tension from metal contraction due to solidification of the alloy. Contraction of the metal between the solidus and liquidus fronts tore away from the solidified casting causing these hot tears. The gamma-ray radiography of as-cast surrogate slug was performed to detect internal defects such as cracks and pores, as shown in Fig. 5-(b). Propagation of the solidification front occured toward the thermal center of the casting and grain growth simultaneously occurred in the partially liquid portion of the casting, which creates an increasing resistive path for molten metal to flow. The pores detected in the upper part region are expected to occur in areas of the casting where grain growth starved void areas casued by shrinkage of molten metal. This kind of defect becoms much more evident and challenging to overcome with increasing alloying element contents in fuel alloy, as the freezing range continues to widen. In order to control the void created by microshrinkage, it was judged to increase the pressure during casting and cooling, which effectively increases the feeding distance resulting in reducing the number and size of gas pores that are trapped at grain boundaries and, therefore, allowing an extended nucleation and growth process [11]. However, the internal integrity of as-cast metal fuel slugs in the lower part was generally satisfactory.

TABLE 3. Material balance after casting of U-10wt.% Zr-5wt.%Mn fuel slugs.

	Melting/ casting part	Mass (g)	Fraction (%)
Before casting	Crucible	1,122	100.0
After casting	Crucible assembly	67	6.1
After casting	Mold assembly	1,037	92.4
Fuel loss		18	1.5

TABLE 4. Material balance after casting of U-10wt.%Zr-5wt.%RE fuel slugs.

	Melting/ casting part	Mass (g)	Fraction (%)
Before casting	Crucible	1,464	100.0
After casting	Crucible assembly	167	11.3
After casting	Mold assembly	1,295	88.6
Fuel loss		2	0.1

(a)

(b)

FIG. 5. Typical surrogate fuel slug (a) and gamma-ray radiography (b), fabricated with the imporved injection casting process under inert atmospheric pressure.

Optical micrographs of the surrogate fuel slug cast according to solidifying position are shown in Fig. 6. The grain size was seen to increase from lower position to upper position. This is because the solidification rate at the upper position, where molten melt solidifies first, is very high compared to at lower position.

Ki-Hwan Kim, Jong-Hwan Kim, Hoon Song, Seok-Jin Oh, Ho-Jin RYu, and Chan-Bock Lee

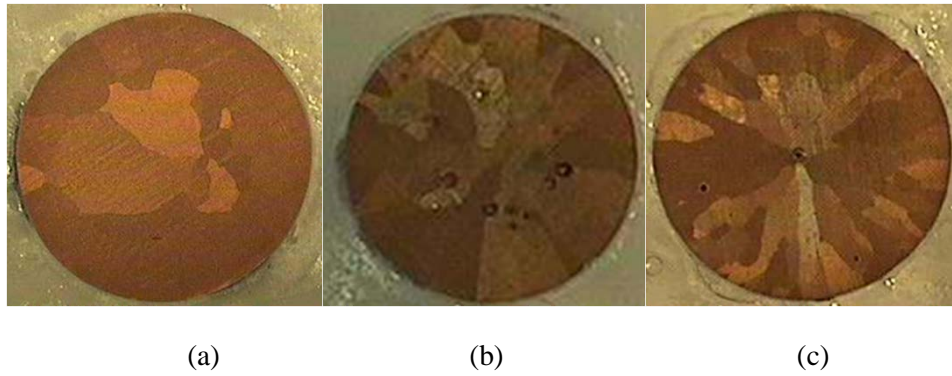(a)   (b)   (c)

FIG. 6. Optical micrographs of the surrogate fuel slug cast according to solidifying position; (a) lower position, (b) middle position, (c) upper position.

Spherical uranium alloy particles with various diameters can be easily produced by the centrifugal atomization technique developed by KAERI. Using the atomized uranium and U-Zr alloy particles, we fabricated various kinds of powder pack, powder compacts and sintered pellets. The microstructures and properties of the powder pack and pellets are presented. Spherical pure uranium particles and U-10wt%Zr alloy particles were fabricated by centrifugal atomization at 1400~1500°C. By adjusting the rotating speed of the spinning disk of the atomizer, U-10wt%Zr powder with bimodal size distribution was obtained. The size distribution of the atomized powder was measured by sieve classification. Green compacts of atomized uranium powder were fabricated by the addition of second element powder including Ti, Mo, Cr, and Zr. The compacts of mixed powder were sintered at 1000°C for 5 hours under vacuum. Cross-section microstructures of sintered pellets were observed using scanning electron microscopy.

(a)   (b)
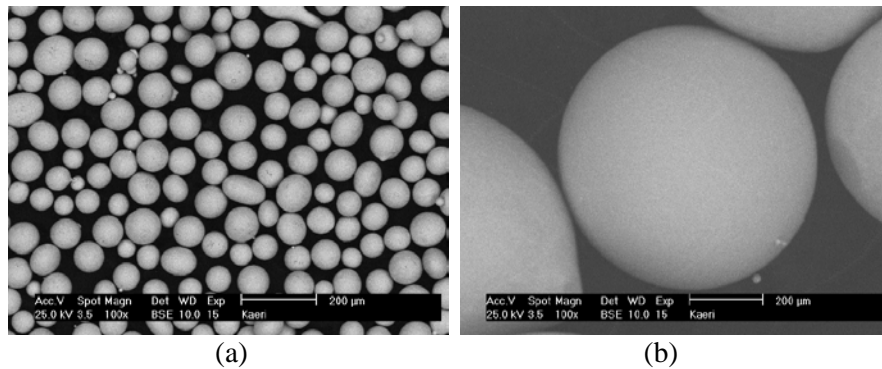
FIG. 7. Atomized U-10wt%Zr powder; (a) fine U-Zr powder, (b) coarse U-Zr powder.

In addition to the high fabrication efficiency, it is expected that particulate U-Zr fuel has lower fuel-cladding mechanical interaction owing to free restructuring during irradiation. The morphologies of atomized U-10wt%Zr particles were shown in Fig. 7. The average sizes of fine powder and coarse powder were about 70μm and 350μm, respectively, as shown in Fig. 7. The packing densities of the mixed powder were measured with the varying mixing ratio of the fine powder to the coarse powder. Having a pellet-type fuel has several advantages in fuel performance and fuel handling. In case of accident such as a cladding breach, consolidated fuel has more safety features than particulate fuel in terms of the release of fissile materials and fission products. Therefore, it is important to confirm the feasibility of pelletizing of particulate uranium alloy powder, because it is hard to get green pellets by using spherical particles without binders. There are several attempts to fabricate metal fuel using particulate uranium for SFR fuel.
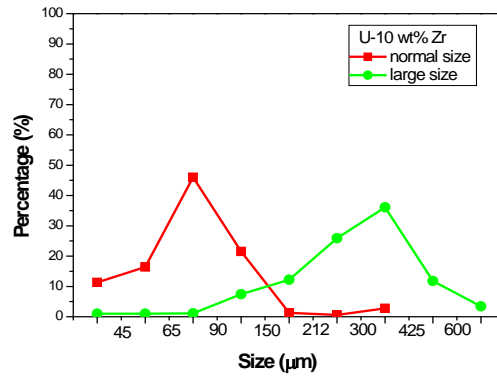
FIG. 8. Comparison of the size distribution of atomized U-10wt%Zr powder.

FIG. 9. Green compacts of metal uranium powder with the addition of 30 vol.% of chromium.

It was found that green compacts of uranium alloy powder could be obtained by the addition of secondary element powder to the uranium alloy powder at least 30 vol.%. The neutron absorption and activation of the secondary elements should be low and Cr, V, Mo, and Ti are candidate elements. Green compacts using secondary elements added to atomized uranium powder were fabricated as shown in Fig. 9 and some of them were sintered at 1000°C for the fabrication of loosely sintered pellets. Fig. 10 shows the cross-section microstructures of sintered samples with varying second elements. When interdiffusion of each element was active, a skeleton structure of powder was developed as in U-Mo. The microstructure of a U-Cr mixed powder pellet shows a hint of solidification because their eutectic melting temperature is below 1000°C. A surface morphology of uranium-chromium mixed powder pellet after sintering was shown in Fig. 11. Bonding of particles was not active in U-Ti and U-Zr mixed powder pellets, mainly because of their limited interdiffusion at the sintering temperature. When the secondary phase forms a continuous network, the thermal conductivity of particulate fuel will be enhanced. In addition, the use of sodium bond in the metal fuel cladding can be eliminated so that the handling of spent fuel containing radioactive sodium could be simplified.
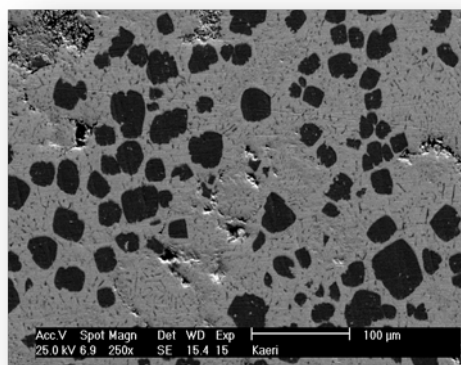
FIG. 10. Cross-section microstructures of sintered pellets with varying second elements after sintering at $1000^{o}C$ for 5 hrs.
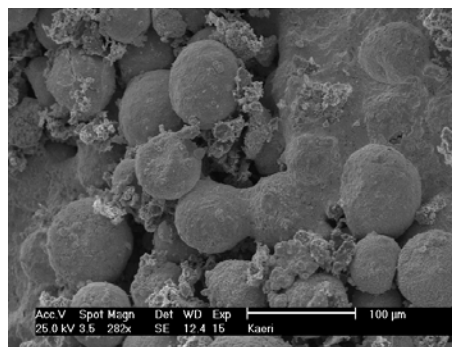
FIG. 11. A surface morphology of uranium-chromium mixed pellet after sintering at $1000\,^{o}C^{o}$ for 5 hours.

4. CONCLUSION

In order to prevent the evaporation of volatile elements such as Am, alternative fabrication methods of metal fuel slugs and particulate metal fuel have been applied and examined with gravity casting, improved injection casting and centrifugal atomization method in KAERI. U-10wt.%Zr, U-10wt.%Zr-5wt.%RE(RE: Nd 53wt.%, Ce 25wt.%, Pr 16wt.%, La 16wt.%), U-10wt.%Zr-5wt.%Mn, and U-10wt.%Zr-5wt.%RE-5wt.%Mn fuel slugs were soundly fabricated with gravity casting with retension of volatile surrogate element. Based on these results there is a high level of confidence that Am losses will also be effectively controlled by application of a modest amount of overpressure. A surrogate fuel slug was generally soundly cast by improved injection casting method where the fuel material is melted under inert atmosphere. Various routes for fabrication of particulate U-Zr fuels have also been investigated to characterize the properties of the particulate U-Zr fuels. Spherical U-Zr powder was fabricated by a centrifugal atomization technique using a spinning disk, and characterized with particle size distribution, power morphology, consolidation after compaction and sintering.

REFERENCES

[1]   G.L. HOFMAN, L.C. WALTERS, T.H. BAUER, "Metallic Fast Reactor Fuels", Progress in Nuclear Energy, 83(31), 1997.

[2]   C.B. LEE, B.O. LEE, S.J. OH, S.H. KIM, "Status of Metallic Fuel Development for Sodium-cooled Fast Reactor", Global-2009, Paris, France, Sep. 6-11, 2009.

[3]   C.T. LEE, S.J. OH, H.J. RYU, K.H. KIM, Y.S. LEE, S.K. KIM, S.J. JANG, Y.M. WOO, Y.M. KO, C.B. LEE, "Casting Technology Development for SFR Metallic Fuel", Global-2009, Paris, France, Sep. 6-11, 2009.

[4]   S.J. OH, K.H. KIM, C.B.LEE, C.T.LEE, S.J. JANG, "Effects of Ce Element Addition on the Characteristics of U-Zr Alloys", Nuclear Fuels and Structural Materials for the Next Generation Nuclear Reactors (NFSM-II), Anaheim, USA, June 8-12, 2008.

[5]   K.H. KIM, S.J. OH, J. T. LEE, Y. S. LEE, C.B. LEE, "Feasibility Study of Advanced U-Mo-X Metallic Fuel System for SFR", KNS Spring Meeting, Gyeongju, Korea, May 29-30, 2008.

[6]   H.F. Jelinek, G.M. Iverson, "Equipment for Remote Injection Casting of EBR-II Fuel", Nucl. Sci. Eng., 405(12), 1962.

[7]   C.L. Trybus, "Injection Casting of U-Zr-Mn, Suurogate Alloy for U-Pu-Zr-Am-Np", J. Nucl. Mater., 305(224), 1995.

[8]   P.S. Chen, W.C. Stevens, C.L. Trybus, "Reusable Molds for Casting U-Zr Alloys", Fall meeting of the Metallurgical Society and AIMPE, Chicago, USA, Nov. 1-5, 1992.

[9]   C. L. Trybus, J. E. Sanecki, and S. P. Henslee, "Casting of metallic fuel containing minor actinide additions", J. of Nuclear Materials, 50(204), 1993.

[10]   R.S. Fielding and D.L. Porter, "Volatile Species Retention During Metallic Fuel Casting", Proc. of Annual Meeting of American Nuclear Society, San diego, USA, Jun. 13-17, 2010.

[11]   J.J. Frawley, W.F. Moore, A.J. Kiesler, AFS Int. Cast Met. J., 31(5), 1980.

[12]   K.H. KIM, S.J. OH, Y. M. KO, C.T. LEE, C.B. LEE, R.S. FIELDING, "Casting Evaluation of U-Zr Alloy System Fuel Slugs for SFR Prepared by Gravity Casting Method", Global-2011, Nagoya, Japan, Sep. 4-9, 2011.

[13]   K.H. KIM, Y.M. WOO, S.J. OH, C.K KIM, C.B. LEE, "Characterization of Very-High-Temperature Ceramic Coatings Prepared by Plasma-spraying Method for Melting Crucibles of Metallic Fuels", Sintering 2011, Jeju, Korea, Aug. 28- Sep. 1, 2011.

[14]   K.H. KIM, S.J. OH, C.T. LEE, C.B. LEE, "Structural Characteristics of High Temperature Ceramic Coatings Prepared by Plasma-spraying Method", OUMRS-ICEM 2010, GyeongGi-Do, Korea, Aug. 22- 27, 2010.

Irradiation of SFR metal fuel in HANARO and the results of post irradiation examination

B.O. Lee, J.S.Cheon, J.H. Kim, S.B.Ahn, B.O.Yoo, H.M.Kim, W.S.Ryu, C.B.Lee

SFR Fuel Development,KAERI, Daejeon, Republic of Korea

Abstract. Irradiation of the SFR metal fuel was carried out in HANARO. The objectives of HANARO test are 1) to evaluate the irradiation performance of metal fuel for SFR, 2) to examine the effects of Rare Earth, 3) and to identify the characteristics of the Cr barrier. A total of twelve fuel rodlets were fabricated for irradiation and the composition of the fuel slug is U-10%Zr-(Ce). In order to simulate the fast reactor condition, the thermal neutron was shielded by Hf. Cladding temperature was raised by introducing the He-filled gap between the cladding and the sealed tube. HANARO irradiation test was done from 2010.11.15 to 2012.01.05. It was calculated that the burnup of metal fuel was about 3at%. The post irradiation examination started from 2012.04.15. The gamma scans were carried out for the twelve rodlets. The measurement of fission gas release and the microstructure analysis are being carried out.

1. Introduction

A sodium-cooled fast reactor(SFR) is being developed in combination with the pyro-processing of spent fuel [1]. U-Zr fuel will be used as a startup fuel, and then U-Zr fuel will be replaced by U-TRU-Zr fuel in combination with pyro-processing. The fuel rod of SFR consists of a metallic fuel slug and a liquid metal thermal bonding within FMS (ferritic martensitic staness steel), like the IFR (Integral Fast Reactor) fuel concept.

Fuel performance evaluation is being performed according to the following items: fuel irradiation test, fuel-cladding diffusion couple tests, fuel design, performance analysis model development, transient hot cell simulation test, out-of-pile test of fuel assembly and fuel performance evaluation in connection with pyro-processing [2].

An irradiation test is necessary to verify the in-reactor behavior of metal fuel. Irradiation tests of U-Zr-(Ce) fuel in HANARO under simulated fast reactor conditions are performed to investigate the fuel performance parameters such as fission gas release, swelling, elongation, radial distribution of fission products and heavy metal elements, and interaction between fuel and cladding, depending upon the different fuel compositions, dimension and manufacturing conditions.

The first HANARO Irradiation test was done from 2010.11.15 to 2012.01.05. The main objective of first HANARO irradiation test is to evaluate the irradiation performance of metal fuel under a temperature and a linear power similar to that of the SFR metal fuel. U-Zr-Ce along with U-Zr is put into the fuel rodlets to examine the level of impurities. Ce was selected as a representative of the rare earth elements.

PIE (Post irradiation examination) is being carried out from 2012.4.5. The gamma scans were carried out for the twelve rodlets. The measurement of fission gas release and the microstructure analysis are being carried out.

The current study presents the design of irradiation capsule, the irradiation conditions for the fuel test, the analysis of preliminary fuel performance, the irradiation history, and the progress results of PIE.

2. Irradiation test in HANARO and post irradiation examination

2.1. Irradiation of SFR metal fuel in HANARO

2.1.1. Irradiation Capsule Design and Irradiation Condition

Fuel irradiation test was carried out in the HANARO research reactor. The design of the irradiation capsule was completed in 2008, and the irradiation capsule was fabricated in 2009 [3]. An irradiation test started in November 2010.

The irradiation tests will be carried out in a fast neutron spectrum facility, but fuel in-pile behavior depends mainly on temperature as well as burnup [4-6]. So, it is possible to verify the metal fuel slug's in-reactor behavior in the HANARO research reactor by adjusting the temperature and burnup. The level of neutron flux in HANARO is too low, it takes long time to irradiate the cladding upto SFR's fluece condition. So, Irradiation test of metal fuel together with the cladding is still needed to be verified in fast reactor conditions.

The first Hanaro irradiation test with a maximum burnup of 3 at% was scheduled to identify the Ce-bearing fuel performance and the characteristics of barrier cladding. The linear power was ~300 W/cm, and the expected duration was ~180 EFPD (Effective Full Power Day).

Fig. 1 shows the irradiation capsule schematic diagram and coolant channel cross section [3]. There are two test sections and each section accommodates six rodlets. Six test fuel rodlets were U-10Zr including two Cr barrier claddings, and six test fuel rodlets were U-10Zr-6Ce including two Cr barrier claddings. The linear power of fuel rodlets in the lower section are expected to be 35% higher than that in the upper section. U-235 enrichment is 19.75% and a Ferritic Martensitic Steel is used for the fuel cladding. The fuel slug and cladding are sodium-bonded. The fuel rod is contained in the sealing tube for safety in case of sodium leakage from the cladding.
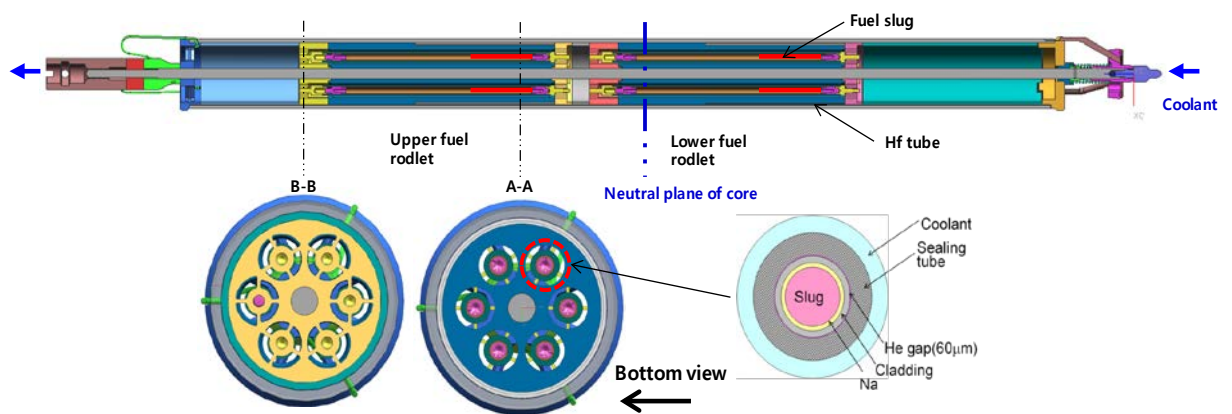

FIG. 1 Irradiation capsule schematic diagram

Thermal neutron is shielded by surrounding the capsule with neutron absorber such as Hf, which is expected to simulate the neutron energy spectrum similar to a sodium fast reactor. The temperature on the outer cladding surface is raised higher than 500℃ by introducing the He gap between the

cladding and the sealing tube. Linear power of the fuel rod is controlled by surrounding the capsule blocks by a thermal neutron absorber.

Table I shows the dimensions of fuel slug, cladding and sealing tube. The fuel slug has dimensions with a diameter of 3.7 mm and a height of 50 mm.

TABLE. I Dimensions of fuel slug, cladding and sealing tube

Fuel			Cladding			Sealing tube		
Outer dia. (mm)	Density (g/cm³)	Length (mm)	Outer dia. (mm)	Inner dia. (mm	Length (mm)	Outer dia. (mm)	Inner dia. (mm	Length (mm)
3.7	15.8	50	5.5	4.6	193	8.62	5.62	233

2.1.2. Performance Analysis of Fuel Rod

The design limits of the metallic fuel were established to ensure the integrity of fuel rod, so it is required to evaluate the design limits such as (1) cladding strain, (2) a CDF (cumulative damage fraction), (3) fuel melting, and (4) eutectic melting [7].

The preliminary design criteria during a steady-state operation related to the design limits for the SFR fuel rod design are as followings; (1) The cladding thermal strain is limited by 1%, (2) The cumulative damage fraction (CDF) of the cladding is limited by 0.2, (3) The centerline temperature of the fuel is less than its melting temperature, and (4)The temperature at the inner surface of the cladding is less than the eutectic melting temperature of the fuel.

Fuel performance in the first HANARO irradiation test was analyzed by using MACSIS fuel rod performance analysis code [8]. The temperature at the outer cladding surface is assumed to be 550 ℃ which is calculated by considering a heat transfer through the gap between the cladding and the sealing tube. The linear power of the fuel rod is taken conservatively in the analysis.

Figure 2 (a) is the temperature variation of the fuel rod with the fuel burnup. The centerline temperature of the fuel is less than 750 ℃. It increases due to the fuel thermal conductivity degraded by the porosities formed by the fission gas, then falls slightly by the infiltration of sodium into the fuel slug, and saturates at 730 ℃ after the thermal conductivity is recovered. The temperature at the inner cladding surface is not higher than 600 ℃.

Figure 2 (b) shows the behavior of fission gas release along with the burnup. It is estimated that the fission gas is released up to 90% around burnup of 1~2 at%. The internal pressure of the cladding also exhibits a relatively enhanced increase at the early stage, and it increases steadily up to 2.2 MPa at the end of the irradiation. The resultant hoop stress of the cladding is estimated to be 13 MPa which is far less than the yield strength. The cladding hoop strain and the CDF are negligible compared with the design criteria.

Therefore it was calculated that the integrity of the fuel rods is guaranteed during the 1st U-Zr Hanaro irradiation test.
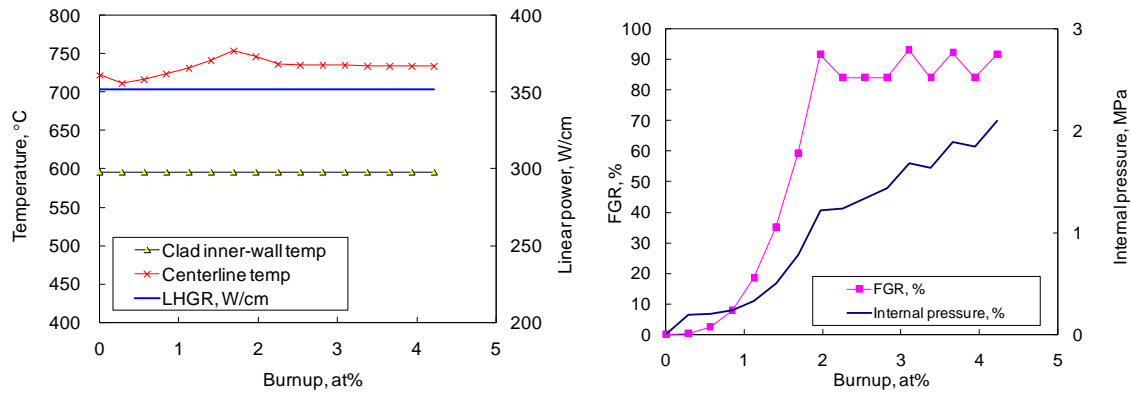
FIG. 2 Fuel rod behavior during the 1st U-Zr Hanaro irradiation test; (a) temperature, (b) fission gas release.

2.1.3. Irradiation History

1st HANARO irradiation test was done from 2010.11.15 to 2012.01.05. The projected periods of irradiation test were changed due to unexpected shutdown of the HANARO.

Fig. 3 shows the irradiation history of HANARO metal fuel [9]. Average burnup of metal fuel was about 3at.%. As-run linear heat rate was 240 W/cm at BOC, and decreased to 220 W/cm at EOC.
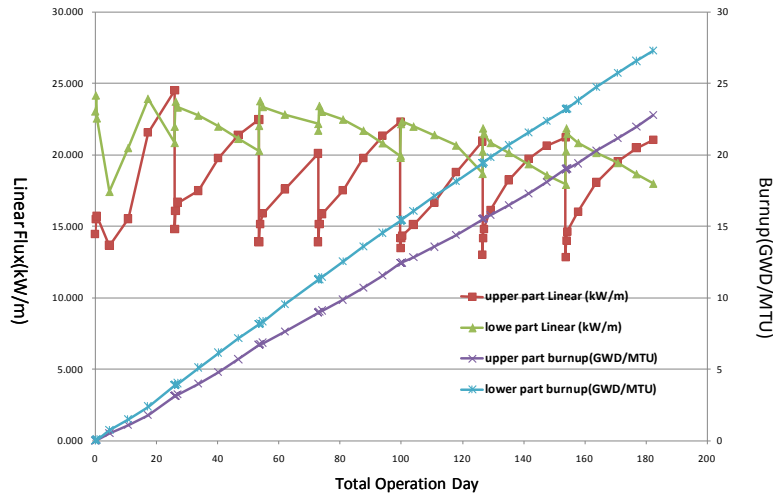
FIG. 3 Irradiation history including linear power and burnup

Overall weight of U235 was 16.1 g at fabrication. It was calculated that the weight of U235 decreased to 13.0g during irradiation, and 0.3 g of Pu was produced . Table II shows the calculated fuel mass at BOC and EOC.

TABLE. II Calculated fuel mass at BOC and EOC

Fuel Mass (g)	BOC	EOC
Total U	81.3	78.5
U 235	15.97	12.99
Pu		0.298

4

It was estimated that the projected Linear Heat Generation Rate (LHGR) limits for this HANARO irradiation test were met to satisfy the design limits. Programmatic burnup for HANARO irradiation test has been set at 3 at.%. As-run analysis show that the experiment reached average 2.73 at.% burnup at the completion of irradiation test. It was estimated that maximum burnup goal was satisfied.

2.2. *Results of post irradiation examination*

The post irradiation examination started from 2012.04.15. The fuel capsule was transferred to the IMEF (Irradiated Materials Examination Facility) through the channel connected with the pool by the use of bucket elevator. IMEF was constructed to provide PIE of the newly developed fuel or material irradiated at HANARO.

In IMEF, non-destructive tests such as a visual inspection, a dimension measurement, a gamma ray scanning, an eddy current, a X-ray radiography are performed in M1 cell. After non-destructive test a capsule or fuel rodlets is dismantled, and specimen are prepared for a metallography, a density measurement etc. Representative destructive tests for SFR metal fuel are to measure or observe fuel burnup, the microstructure, fission gas release, and the constituent redistribution. Transient behavior tests under simulated conditions will also be performed by using the irradiated fuel in the hot cell.

Gamma scan analyses were carried out for twelve rodlets. The fuel elements were scanned for distribution of total gamma radiation along the length of the fuel column. The activities were analyzed for a number of fission products (Cs-137, Nb-95, Rh-106m, Ru-103, Zr-95, Nb-95). Fig. 4 show the gamma scan results for U-Zr-Ce metallic fuel.

Gamma scans of Cs-137 shows the fission product behavior of irradiated metal fuel. Fig. 4 shows that the Cs-137 gamma ray intensity rises rapidly in the region of 55mm from the bottom of fuel slug. This profile indicates that a significant amount of Cs-137 is trapped and follows the Na relocation in the fuel pin, because Cs-137 is the alkali metal that dissolve to some extent in the bond sodium. This means the bonding sodium dissolving Cs has been extruded aboe the top of the fuel slug. Such Cs behavior was also observed in X501 and AFC tests [10, 11].
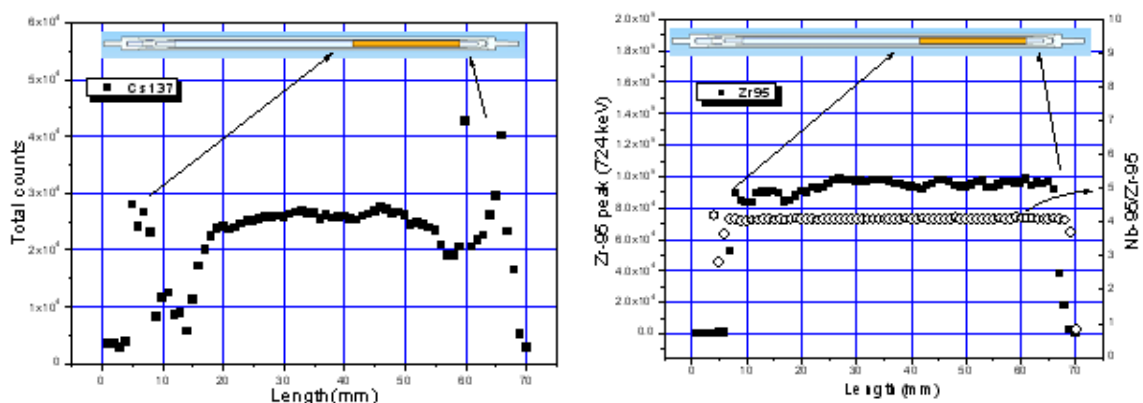
FIG. 4 Gamma scans off the irradiated metal fuel in HANARO

The shape of Zr-95 activity is nearly flat along the fuel rod, and then drop rapidly from the region of 55mm from the bottom of fuel slug. So it indicated that metal fuel elongation occurred because length of the unirradiated fuel slug was 50mm. The cutting of rodlet is being carried out to check the sodium level and fuel elongation.

Even though twelve rodlets were irradiated in HANARO, the destructive test was carried out on four rodlets (U-Zr/FMS, U-Zr-Ce/FMS, U-Zr/Cr barrier/FMS, and U-Zr-Ce/ Cr barrier/FMS) in 2012.

The conventional puncturing system for fission gas release measurement was too large, so a laser puncturing system for SFR metal fuel was used. Fuel rodlets were punctured in the plenum at room temperature to collect gases. The rodlet gas samples will be analyzed for elemental and isotopic composition at the Chemical Laboratory.

Fuel swelling is an important feature of metallic fuels. The metal fuel slug is designed with a 75% smeared density in order to accommodate fuel swelling [12]. In the metal fuel for HANARO, the smear density was designed to 65% to accommodate the signifcant swelling.

Figures 5 shows the cross-sectional metallography of the irradiated U-Zr specimen as-polished as well as that of unirradiated U-Zr specimen. The mounted specimens were stored in kerothene to retain the sodium in the fuel slug. The specimen exhibits significant radial swelling and are contact with the cladding.
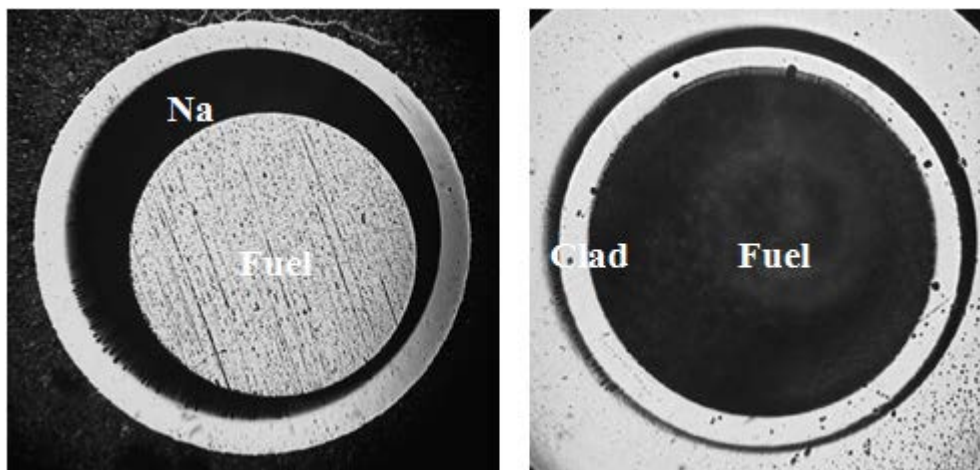
FIG. 5 Cross-sectional metallography of unirradiated U-Zr and irradiated U-Zr specimens

Figure 6 is micrographs of the U-Zr-Ce at the interior and edge regions. Interior and edge areas appear homogeneous, containing a high density of small pores.

The development of porosity in the fuel reduces the effective thermal conductivity, and, therefore, increases the temperature of the fuel. Even though the penetration of sodium into the pore would balance the overall thermal conductivity of the fuel and then decrease the temperature, an evaluation of the effect of sodium penetration into voids on the temperature profile will be carried out. Microsture analysis by SEM will also be carried out to evaluate the fuel composition along the cross sectional region.
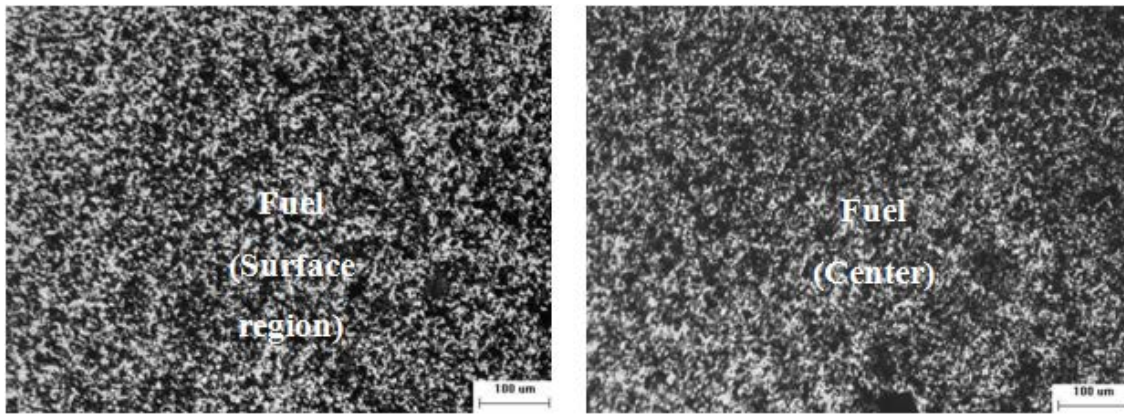
FIG. 6 Micrograph of U-Zr-Ce by OM

Figure 7 shows micrographs of the U-Zr-Ce with Cr barrier cladding at the interface regions. Some variations in thickness were observed along the electroplating Cr barrier. The circumferential difference of plating thickness was observed in all parts of the Cr layer [13], and the thickness of Cr barrier was 12-20 μm.

	Features	Center X	Leng
1	BL2	13.28440	19.80731
2	BL3	43.95930	19.85879
3	BL4	70.04504	19.13619
4	BL5	99.51226	20.05319
5	BL6	123.1827	20.77338
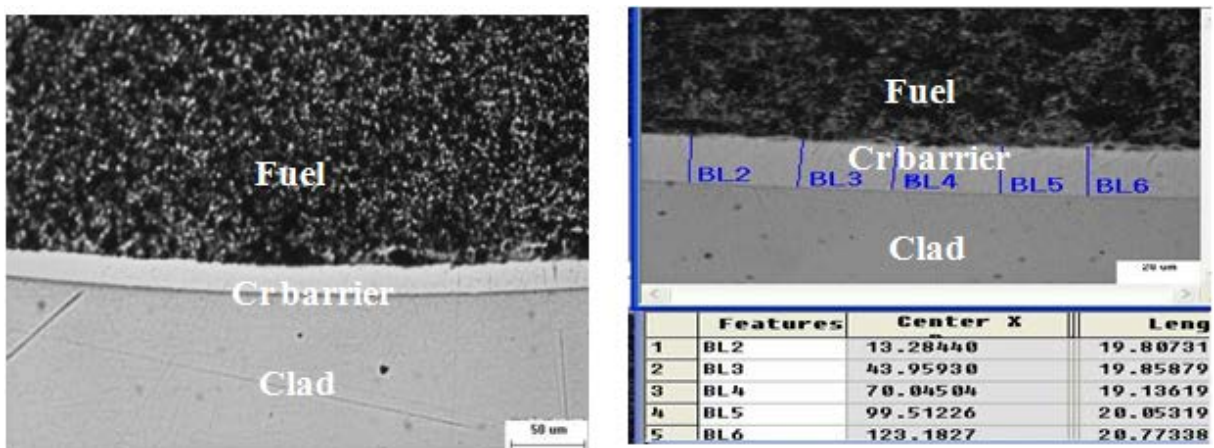
FIG. 7 Micrograph of the U-Zr-Ce with Cr barrier cladding at the interface regions

The diffusion couple test was carried out using unirradiated U-Zr metallic fuel, where it revealed as effective by preventing eutectic reaction as well as interdiffusion [14]. However, some cracks developed during the plating, which acted as a diffusion path for the fuel constituent to penetrate inside

Optical microscopy of a fuel cross section showed no evidence of fuel-cladding chemical interaction. Although no macroscopic reaction has occurred, some cracks have developed in the thin thickness regions. A further detailed study will be carried out by SEM and EPMA analysis.

3.   Conclusion

A sodium-cooled fast reactor (SFR) is being developed in combination with the pyro-processing of spent fuel. Development of a metal fuel should be verified by performance tests and evaluations. In this works, the design of irradiation capsule, the irradiation conditions for the fuel test, the analysis of preliminary fuel performance, the irradiation history, and the progress results of PIE were described.

First HANARO irradiation test for SFR metal fuel was carried out from 2010.11 to 2012.01. PIE has been carried out for the 1st HANARO irradiation test fuel since 2012.4. Gamma scans of twelve metallic fuel rodlets were completed: they show a significant amount of Cs-137 is disolved in sodium above the top of fuel slug.

The cross-sectional metallography of the irradiated U-Zr specimen shows significant radial swelling resulted in contact with the cladding. The micrography of the U-Zr-Ce with Cr barrier cladding at the interface regions shows there is no macroscopic reaction between fuel and cladding. However, some cracks are revealed, so further optimization study by reducing such a crack is needed.

Detailed examinations including fission gas puncture and analysis, metallography, and isotopics and burnup analyses will be carried out. This study will be used for the establishment of performance evaluation tools and design data bases.

ACKNOWLEDGEMENTS

REFERENCES

[1]   D. Hahn et al., Advanced Sfr Design Concepts and R&D Activities, Nuclear Engineering and Technology,Vol. 41, No. 4, (2009).

[2]   Lee, B.O., et al, SFR Metal Fuel Performance Evaluation Technology, KNS workshop on Gen IV Fuel Development Status and Prospects, Jeju, Korea, (2012)

[3]   J.S. Cheon., et al., Irradiation Test of U-Zr SFR Fuels in HANARO, Proceedings of KNS, May, (2009)

[4]   W.N. Beck, R.J. Fousek and J.H. Kittel, The Irradiation Behavior of High-burnup Uranium-Plutonium Alloy Prototype Fuel Elements, ANL-7388, May (1968)

[5]   S.L. Hayes, M.K. Meyer and D.C. Crawford, Irradiation Testing of Actinide Transmutation Fuels in the Advanced Test Reactor, Nuclear Applications in the New Millennium, Reno, NV, November (2001.)

[6]   J.L. McDuffee et al., Proposed fuel pin irradiation facilities for the high flux isotope reactor, ICAPP'08, Anaheim, CA USA, June 8-12, (2008)

[7]   LEE, B.O., et al., "Performance Limit Analysis of A Metallic Fuel for KALIMER", GLOBAL 2007-Advanced Fuel Cycles and Systems, September 9-13, (2007).

[8]   Hwang, W., et al., "MACSIS-A Metallic Fuel Performance Analysis Code for Simulating In-reactor Behavior under Steady-State Condition", Nuclear Technology. 123, 130 (1998).

[9]   B.O.Lee, et al., Irradiation Status and PIE Plan of Metallic Fuel for SFR, OECD/NEA workshop on characterization and PIE needs to support science-based development of innovative fuels, 16-17 June 2011 at NEA HQ, (2011)

[10] M.K. Meyer, S.L. Hayes, W.J. Carmack and H. Tsai, "The EBR-II X501 Minor Actinide Burning Experiment," J. Nucl. Mater., 392, 176, (2009).

[11] B.A. Hilton, D.L. Porter and S.L. Hayes, "AFC-1 Transmutation Fuels Post-Irradiation Hot Cell Examination 4 to 8 at.% Final Report - Irradiation Experiments AFC-1B, AFC-1F and AFC-1AE," INL/EXT-05-00785 Rev.1, Idaho National Laboratory (2006).

[12] G. L. Hofman, L. C. Walkers, Metallic fast fuels, in : R. W. Cahn, P. Haasen, E. J. Kramer (Eds.), Material Science and Technology - A Comprehensive Treatment, 10A Part I, VCH, Germany, pp. 28 (1994).

[13] S. W. Yang, H. J. Ryu, J. H. Kim, B. O. Lee and C. B. Lee, FCCI Barrier Performance of Electroplated Cr for Metallic Fuel, Journal of Nuclear Materials, Vol. 401, pp.98 (2010).

[14] J. H. Kim, K. S. Lee, S. W. Yang, B. O. Lee and C. B. Lee, Cr Electroplating Technology to prevent Interdiffusion between the Metallic Fuel and Clad Material, submitted for publication for Korean Journal of Metals and Materials (2011).

Progress in understanding of Fuel-Cladding Chemical Interaction in Metal Fuel

K. INAGAKI, K. NAKAMURA, T. OGATA

Central Research Institute of Electric Power Industry,
Tokyo, JAPAN

Abstract. In U-Pu-Zr metal fuels for fast breeder reactors, lanthanide fission products dominantly penetrate into the inner surface of the stainless steel cladding to form a brittle layer during normal reactor operation. When the cladding temperature exceeds a threshold temperature in case of off-normal transients, the fuel alloy dominantly reacts with the cladding and parts of the reaction zone are liquefied. These are called Fuel-Cladding Chemical Interaction (FCCI). In order to fully understand FCCI in metal fuels, diffusion couples consisting of Fe-base alloys and lanthanide alloys or U-Pu-Zr alloys were isothermally annealed at various temperatures. Examination of the reaction zones in these couples revealed the phase structures in the FCCI zones. The relation between threshold cladding temperature for the liquefaction onset and Pu content in the fuel alloy was clarified. These results can be the basis for FCCI modelling.

1.   Introduction

U-Pu-Zr metal fuel is a candidate for fast breeder reactor fuel. During irradiation, a metal fuel slug swells and comes into contact with the cladding. Then chemical interaction occurs between the fuel and the cladding, which is Fuel-Cladding Chemical Interaction (FCCI)[1]. FCCI results in the formation of a brittle layer on the inner surface of the cladding and it degrades the integrity of the cladding. Therefore, the evaluation of FCCI is significant in terms of the life time expectation of the metal fuel pins. The past examination of irradiated metal fuel pins has revealed that the diffusion of lanthanide fission products into the cladding is dominant during normal reactor operation[2]. On the other hand, in the transient event where the cladding temperature exceeds a threshold value, a liquid phase can be formed as a result of interdiffusion among the fuel and cladding consituents[3], and the cladding wastage rate is remarkably increased compared to that for normal reactor operation. In the present study, the reactions in two types of diffusion couples, a lanthanides alloy / cladding materials and U-Pu-Zr fuel aloy / Fe, were examined, and fundamental phase structures were revelaed for comprehensive understanding of FCCI.

2.   Experimental

2.1.   *Preparation of the alloy rods*

2.1.1.   *Fabrication of the lanthanide alloy rod*

The composition of the lanthanide alloy (13wt.%La-24wt.%Ce-12wt.%Pr-39wt.%Nd-12wt.%Sm) was determined based on the fission yield of lanthanide elements in irradiated fuels. This lanthanide alloy is designated as RE5 in this paper. RE5 alloy was prepared by arc-melting 99.9% purity metals of La, Ce, Pr, Nd and Sm and shaping them into a 5 mm in diameter $\times$ 80 mm in length rod with impurities of Fe<100ppm, Ca<200ppm and Mg<100ppm. The rod was annealed at 1173 K for 70 hours for homogenization.

2.1.2. Fabrication of the U-Pu-Zr rod

Two kinds of U-Pu-Zr alloys, U-9 wt.%Pu-10 wt.%Zr and U-16 wt.%Pu-10 wt.%Zr, were used in the present test. U-9Pu-10Zr alloy specimens were taken from the rod that had been fabricated in the previous study[4]. The U-16Pu-10Zr rod was manufactured from U-20Pu-10Zr alloy rod, pure uranium and pure zirconium by injection casting technique. The U-Pu-Zr alloy specimens were annealed at 1123 K for 30 hours for the homogenization. The compositions of the U-Pu-Zr specimens were measured with ICP-AES, as shown in Table 1.

Table 1. Composition of the fabricated U-Pu-Zr alloys [wt.%]

	U	Pu	Zr
U-16Pu-10Zr	73.0	16.4	10.7
U-9Pu-10Zr[4]	81.2	8.5	10.3

2.1.3. Cladding materials

Two kinds of ferritic/martensitic cladding materials, PNC-FMS[5] and HT9[1], oxide-dispersion-strengthened (ODS) steel[6], and Fe-12wt%Cr binary alloy were used to investigate the influence of the cladding alloying elements on the reaction with lanthanide alloy. Composition of these cladding materials is shown in Table 2. On the other hand, as Ogata, et al.[7] suggested that the additives in the HT9 steel, for exapmle, Cr and Mo, do not significantly affect the potential for liquefaction in the metal fuel peripheral region, the U-Pu-Zr alloys were coupled with pure Fe in this study.

Table 2. Composition of the cladding materials. [wt.%]

	C	Si	Mn	P	S	Ni	Cr	Mo	W	Ti	Nb	V	Y_2O_3
HT9(Nominal)[1]	0.2	0.2	0.2	-	-	0.6	12.0	1.0	0.5	-	-	0.3	-
PNC-FMS(Analytical)[5]	0.10	<0.1	0.5	<0.1	<0.1	<0.1	11.1	0.5	2.1	-	<0.1	0.19	-
ODS-steel (Nominal)[6]	0.13	<0.1	<0.1	<0.1	<0.1	<0.1	9.0	-	1.95	0.21	-	-	0.36
Fe-12wt%Cr	-	-	-	-	-	-	12.0	-	-	-	-	-	-

2.2. Diffusion couple

All metal rods were cut into 5 mm in diameter × 3 mm in thickness disks. Their surfaces were ground with #1500 emery paper, polished through 3μm diamond paste, and degreased with acetone. U-Pu-Zr alloy or the RE5 alloy disks were put together with a cladding alloy disk in the stainless steel holder so that the polished surfaces contact each other. The inside surface of the holder was lined with tantalum foils of 20μm thickness to prevent the couple from reacting with the holder as illustrated in FIG.1. The couples were isothermally annealed in an electric furnace. After annealing, the couples were taken out of the furnace

FIG. 1. Configuration of the diffusion couple.

and water-quenched. The test conditions are summarized in Table 3. The annealed couples were cut perpendicularly to the interface. The cross-section of the couple was ground and polished to investigate the reaction zone. The reaction zones in the RE5 diffusion couples were examined by scanning electron microscope (SEM) equipped with wave-length dispersive X-ray spectrometers. For the U-Pu-Zr diffusion couples, SEM equipped with an energy dispersive X-ray spectrometer was used, which is installed in a glove box.

Table 3. Summary of diffusion couple test conditions   .

Combination of the diffusion couple	Annealing temperature [K]	Annealing time [hours]
RE5/Fe-Cr	923	12
RE5/HT9	853	162
RE5/PNC-FMS	853, 923	12 -170
RE5/ODS-steel	853, 892, 923	12 -170
U-16Pu-10Zr/Fe	943, 963	25
U-9Pu-10Zr/Fe	963, 983	30

3.   Results and discussion

3.1.   *Reaction of the lanthanide elements*

3.1.1.   *Identification of the phases*

The reaction layers formed between RE5 and cladding materials are summarized in FIG.2. The phases formed in the reaction zones were identified as indicated in the Figure. The reaction layer formed in the cladding material side is called wastage layer in this report. In all of these diffusion couples, the wastage layer consisted of the matrix of $(Fe,Cr)_{17}RE_2$ and the precipitation of lanthanide-rich precipitate phase. On the RE5 side, the Fe_2RE-type phase was precipitated in all diffusion couples, and a liquid phase was formed only in the RE5/PNC-FMS diffusion couple annealed at 923 K, which was presumably due to the eutectic reaction between the Fe and lanthanide elements. However, the significant effect of this liquefaction on the growth rate of the reaction zone was not remarkable. Diffusion of the other alloying elements of cladding materials into the RE5 side was not obvious. These results imply that the reaction between various cladding materials and lanthanide elements are similar to each other. A more detailed description of each phase is given in a previous report[8].

(i)RE5/Fe-12Cr(923 K, 20hours)   (ii)RE5/HT9(853 K, 162hours)

(iii)RE5/ODS-steel(923 K, 50hours)   (iv) RE5/PNC-FMS (923 K, 12hours)

FIG. 2. Reaction layer formed in the diffusion couples of RE5/Fe-12Cr, RE5/HT9, RE5/ODS-steel and RE5/PNC-FMS.

3.1.2. *Reaction rate of the wastage layer*

The reaction rate constant was defined as δ^2/t where δ [m] is the thickness of the wastage layer and t [sec] is the time, based on the assumption that the reaction is diffusion controlled. To compare the temperature dependency of the growth rate of the wastage layer formed in the diffusion couples, the relation between the reaction rate consta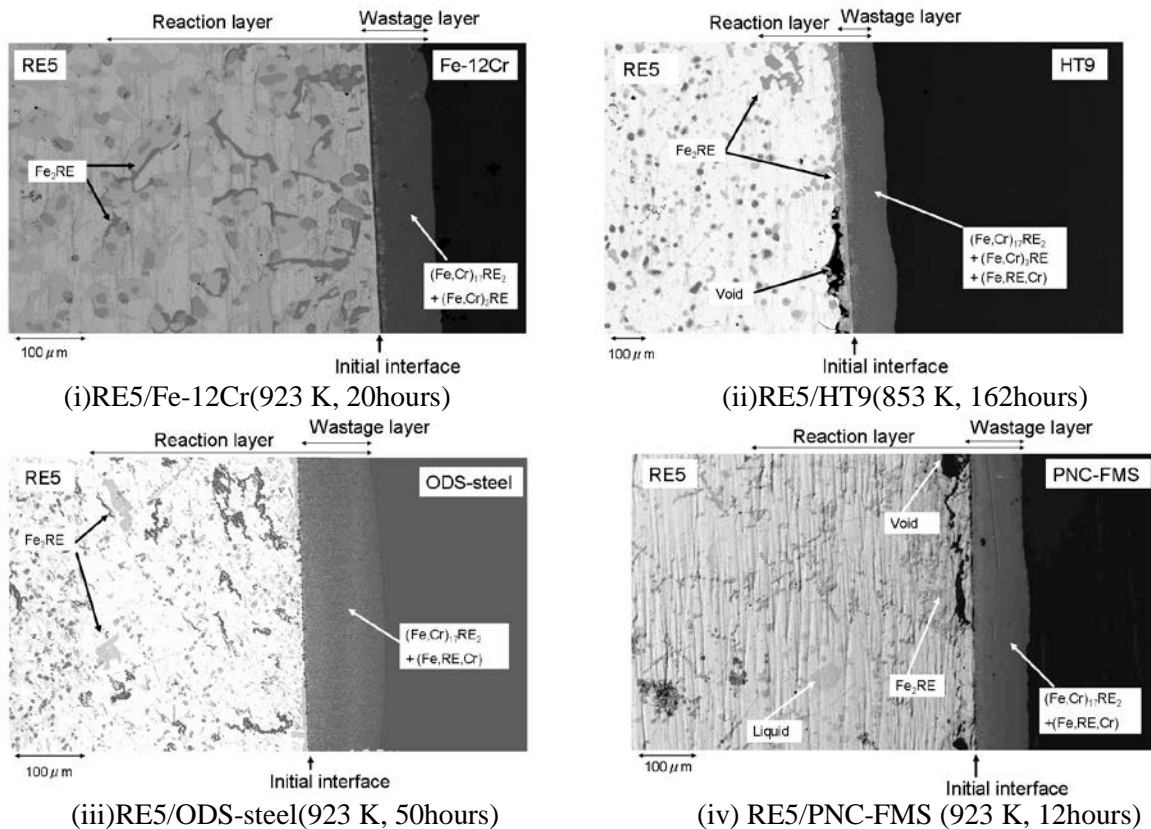nt and the inverse of temperature is shown in FIG.3. In the temperature range of 853-923K, the growth rate of the wastage layer in the RE5/PNC-FMS is larger than that in the RE5/ODS-steel and the difference is larger in the higher temperature region. This indicates that ODS-steel provides better resistance characteristics against the inner cladding wastage by lanthanide fission products. These results can be the basis of quantification of FCCI.
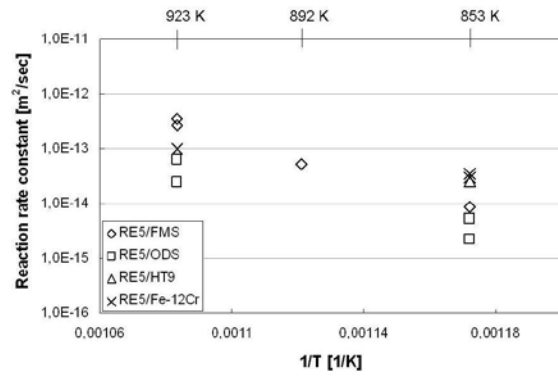
FIG.3. Relation between the reaction rate constant and inverse of the temperature[8].

3.2. **Reaction of the fuel elements**

The reaction layers formed in the U-16Pu-10Zr/Fe and U-9Pu-10Zr/Fe couples annealed at 943, 963 and 983 K are shown in FIG.4. In some of the couples, cracks were observed in the U-Pu-Zr alloy. They are considered to be formed by the compressive force during diffusion couple assembly. Large voids were observed in the U-16Pu-10Zr/Fe couple annealed at 963 K and the U-9Pu-10Zr/Fe couple at 983 K. On the other hand, in the lower temperature cases, no void was observed and the reaction zone width was markedly decreased.

The reaction zone structures are described in detail in the following sub-sections. The phases in the reaction zones were identified based on the U-Zr-Fe ternary phase diagram at 973 K, as shown in FIG.5[9], and the U-Pu-Zr-Fe quaternary phase diagram at 923 K[10][11].

3.2.1. *U-16Pu-10Zr/Fe at 963 K*

Back-scattered electron images of the cross-section of U-16Pu-10Zr/Fe couple annealed at 963 K are shown in FIG.6. The right hand side in FIG.6 corresponds to the Fe side. Zr-rich precipitates observed in the U-Pu-Zr alloy were presumably formed during the casting of the U-Pu-Zr alloy rod, and seem to have no effect on the reaction with iron. The results of phase identification are summarized in Table 4.

FIG. 4. Comparison of the reaction layers formed in the U-Pu-Zr/Fe couples.
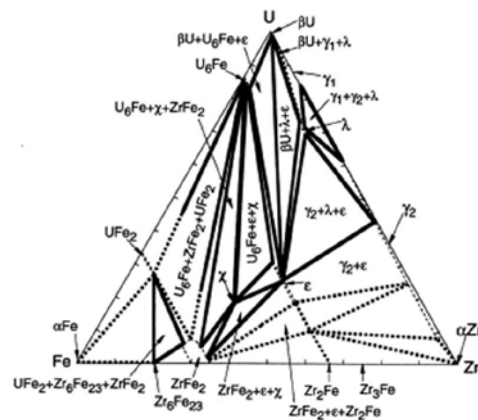
FIG. 5. U-Zr-Fe ternary phase diagram at 973 K[9].

The reaction layer was tentatively devided into several zones. Areas-a and -b correspond to the wastage layer, which was formed by the diffusion of fuel elements into Fe. It was suggested that area-

a was the single phase region of $(U,Zr,Pu)_2Fe$ because the composition ratio of $(U+Pu+Zr)$:Fe was 1:2. Although area-b was a multi-phase region, the phases were too small in size to evaluate independently. Hence, the average composition was measured. Since the measured average composition was on the tie-line between U_6Fe and UFe_2 in the U-Zr-Fe phase diagram, bright and dark phases in area-b were identified to be $(U,Zr,Pu)_6Fe$ and $(U,Zr,Pu)_2Fe$, respectively. In area-c, since the compositions of the dark phase were distributed on the tie-line between UFe_2 and $ZrFe_2$, the phase was estimated to be $(U,Zr,Pu)Fe_2+(Zr,U,Pu)Fe_2$. The bright phase was too small for the evaluation, but the result of the point analysis on the area including bright and dark phases suggested that the bright phase is $(U,Zr,Pu)_6Fe$. Since a large void was formed in this area, the bright phase was considered to consist of $(U,Zr,Pu)_6Fe$ and liquid phase.

In the bright phase in area-d, -e, and -f, the composition ratio of $(U+Pu+Zr)$:Fe was 1:6. Hence, these bright phases were considered to be $(U,Pu,Zr)_6Fe$. Since the composition ratio of $(U+Pu+Zr)$:Fe in the dark phase in area-d was 1:2, it was estimated to be $(Zr,U,Pu)Fe_2$ phase. Although the boundary is not clear, area-e was observed, where the precipitated phases were diluted between area-d and area-f. The dark phase in area-e was also proved to be $(Zr,U,Pu)Fe_2$ phase.

In areas-d and -e, the peritectic structure were observed around the $(Zr,U,Pu)Fe_2$ phase as shown in FIG.6-(iii). Since it is not likely to form the peritectic structure in an isothermal diffusion couple, they are considered to be formed during the quench. This implies that the bright phase in area-d and -e had been a two-phase region of $(U,Pu,Zr)_6Fe$ and the liquid phase. The Pu concentration varied from point to point (9.0-23.0 at.%) in the bright phase of area-d. The solubility limit of Pu in U_6Fe phase at 963 K is assessed to be about 10 at.%[10]. This can be additional evidence of the liquid phase formation in the reaction layer because the variability of the Pu concentration can be explained by a solidification path of the liquid phase based on the liquidus surface of the U-Pu-Fe system[12]. In area-f, two types of precipitation phases were observed. One phase (dark-1) was too small in size to independently evaluate that the resulting values were affected by the surrounding bright phase. Since the measured composition was on the tie-line between U_6Fe and χ phases, the dark-1 phase was estimated to be χ phase. On the other hand, the composition of another phase (dark-2) was similar to that of ε phase in the U-Zr-Fe ternary phase diagram. The bright phase in area-g had a similar composition to the initial composition of the U-Pu-Zr alloy and the composition of the dark phase was similar to that of the λ phase in the U-Zr-Fe ternary phase diagram.

Table 4. Average compositions of the phases in the reaction zones in the U-16Pu-10Zr/Fe couple at 963 K, and the results of the phase identification. (The name of the areas correspond to those in FIG.6)

Area	Colour of the phase	Composition ratio [at.%]				Identified phase
		Fe	Zr	U	Pu	
a	(single phase)	71.5	6.5	20.2	1.8	$(U,Zr,Pu)Fe_2$
b	(multi-phase)*	63.7	7.8	24.7	3.8	$(U,Zr,Pu)_6Fe+(U,Zr,Pu)Fe_2$
c	bright*	51.8	11.0	31.6	5.6	$(U,Zr,Pu)_6Fe+Liquid$
c	dark	67.9	13.6	16.4	2.1	$(Zr,U,Pu)Fe_2+(U,Zr,Pu)Fe_2$
d	bright	19.3	4.2	64.1	12.4	$(U,Pu,Zr)_6Fe+Liquid$
d	dark	65.9	19.1	13.0	2.0	$(Zr,U,Pu)Fe_2$
e	bright	19.8	3.5	69.1	7.6	$(U,Pu,Zr)_6Fe+Liquid$
e	dark	72.4	16.9	9.8	0.9	$(Zr,U,Pu)Fe_2$
f	bright	23.4	4.0	65.6	7.6	$(U,Pu,Zr)_6Fe$
f	dark-1*	29.9	15.7	46.6	7.9	χ
f	dark-2	34.9	35.9	25.4	3.8	ε
g	bright	0.9	14.9	71.9	12.2	bcc
g	dark	8.9	22.1	57.1	11.9	λ

The phase marked with * was small in size and the measurement was conducted over an area including other phases.

3.2.2. U-16Pu-10Zr/Fe at 943 K

Back-scattered electron images of the cross section of U-16Pu-10Zr/Fe couple annealed at 943 K are shown in FIG.7 and the composition and the stoichiometry of each phase is summrized in Table 5. In area-a and -b, which correspond to the wastage lalyer, the composition ratio of (U+Pu+Zr):Fe was 2:1. They were estimated to be the single phase regions of $(U,Zr,Pu)Fe_2$ and $(Zr,U,Pu)Fe_2$, respectively. In area-c, the size of the dark precipitate phase was too small for evaluation and that measurement was done over an area including both phases. Although the mesuared values had some dispersion, all the compositions were on the tie-line between $(U,Zr,Pu)_6Fe$ and $(Zr,U,Pu)Fe_2$. Also in area-d, the stoichiometric phases of this area were estimated from the averaged values of the composition ratio to be $(U,Zr,Pu)_6Fe$ and χ phases. Unlike the case at 963 K, ε-phase was not observed in area-d. In these areas, the peritectic structure (arrows in FIG.6-(iii)) or the variation of Pu concentration were not observed. Therefore, it was considered that no liquid phase was formed in these areas. Area-e consisted of the bcc and λ phases, as seen in the case at 963 K.

(i)Whole area.

(ii)Enlarged image of each areas.

(iii)Peritectic structure (arrows) in area-c and -d.
FIG. 6. Back-scattered electron images of the reaction zone formed in the U-16Pu-10Zr/Fe annealed at 963 K.

(i)Whole area.

(ii) Enlarged image of each areas.
FIG. 7. Back-scattered electron images of the reaction zone formed in the U-16Pu-10Zr/Fe annealed at 943 K.
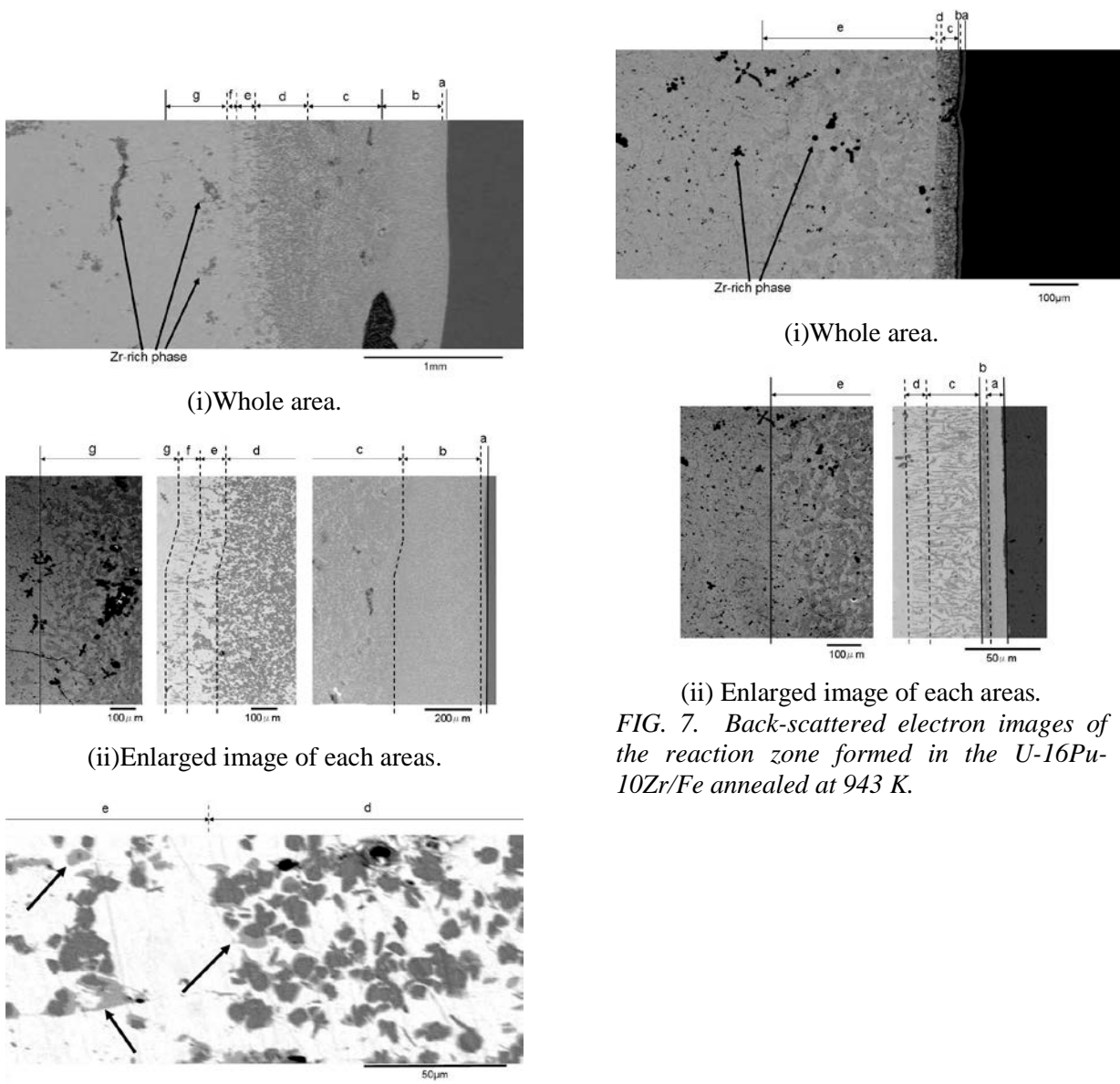
Table 5. Average compositions of the phases in the reaction zones in the U-16Pu-10Zr/Fe couple at 943 K, and the results of the phase identification. (The name of the areas correspond to those in FIG.7)

Area	Colour of the phase	Composition ratio [at.%]				Identified phase
		Fe	Zr	U	Pu	
a	(single phase)	73.1	3.5	21.9	1.5	$(U,Zr,Pu)Fe_2$
b	(single phase)	67.5	20.2	11.2	1.1	$(Zr,U,Pu)Fe_2$
c	(multi-phase)*	39.1	13.9	43.0	4.0	$(U,Zr,Pu)_6Fe+(Zr,U,Pu)Fe_2$
d	(multi-phase)*	25.6	11.6	57.6	5.3	$(U,Zr,Pu)_6Fe+\chi$
e	bright	0.6	12.5	74.0	12.9	bcc
e	dark	7.2	22.0	58.2	12.6	λ

The phase marked with * was small in size and the measurement was conducted over an area including other phases.
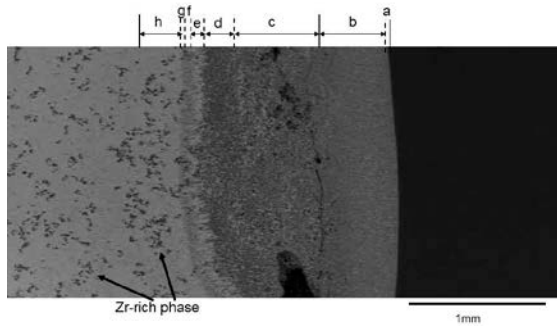
(i)Whole area.
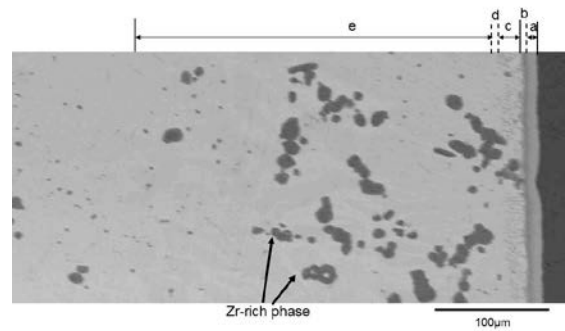
(i)Wole area.
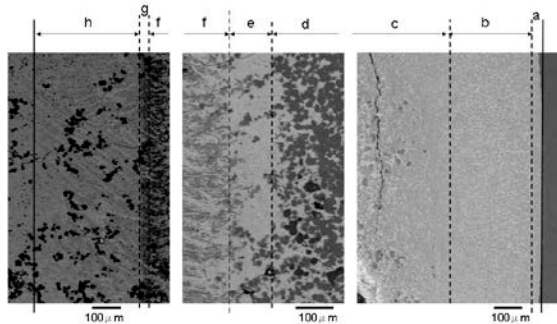
(ii) Enlarged image of each areas

(ii) Enlarged image of each areas

FIG. 9. Back-scattered electron images of the reaction zone formed in the U-9Pu-10Zr/Fe annealed at 963 K.

(iii)Peritectic structure (arrows) in area-d and -e.

FIG. 8. Back-scattered electron images of the reaction zone formed in the U-9Pu-10Zr/Fe annealed at 983 K.

Back-scattered electron images of the cross section of U-9Pu-10Zr/Fe couple annealed at 983 K are shown in FIG.8 and the composition and the stoichiometry of each phase is summrized in Table 6. The structure of the reaction layer was similar to that formed in U-16Pu-10Zr/Fe at 963 K. Although the local variation of Pu concentration was not clearly observed, the peritectic structrure was formed in area-d and -e as shown in FIG.8-(iii). And also, the large void was formed in area-c as seen in FIG.8-(i). These imply that the liquefaction occurred in these areas.

7

Table 6. Average compositions of the phases in the reaction zones in the U-9Pu-10Zr/Fe couple at 983 K, and the results of the phase identification. (The name of the areas correspond to those in FIG.8)

Area	Colour of the phase	Composition ratio [at.%]				Identified phase
		Fe	Zr	U	Pu	
a	(single phase)	71.5	6.4	21.1	1.0	$(U,Zr,Pu)Fe_2$
b	bright*	49.3	6.8	39.4	4.5	$(U,Zr,Pu)_6Fe$
b	dark	66.5	9.6	22.1	1.8	$(U,Zr,Pu)Fe_2$
c	bright*	46.4	8.5	40.1	5.0	$(U,Zr,Pu)_6Fe$+Liquid
c	dark-1	65.9	13.7	18.0	2.4	$(U,Zr,Pu)Fe_2$
c	dark-2(granular)	44.2	27.3	24.8	3.7	χ
d	bright	34.4	6.1	53.3	6.2	$(U,Zr,Pu)_6Fe$+Liquid
d	dark	68.3	20.6	10.1	1.0	$(Zr,U,Pu)Fe_2$
e	bright	21.3	4.3	70.0	4.4	$(U,Zr,Pu)_6Fe$+Liquid
f	(multi-phase)*	59.0	16.6	22.1	2.2	$(U,Zr,Pu)_6Fe$ $+ (Zr,U,Pu)Fe_2$
g	bright	-	-	-	-	$(U,Zr,Pu)_6Fe$
g	dark-1*	34.7	19.2	43.0	3.0	χ
g	dark-2*	26.7	21.0	48.0	4.3	ε
h	bright	0.7	15.1	74.2	10.0	bcc
h	dark	8.8	22.5	60.1	8.6	λ

The phase marked with * was small in size and the measurement was conducted over an area including other phases.

3.2.4. U-9Pu-10Zr/Fe at 963 K
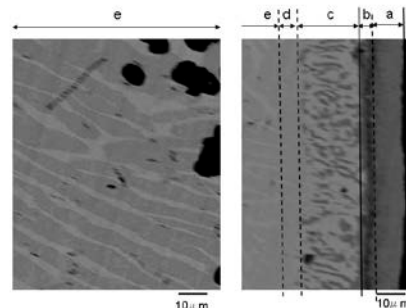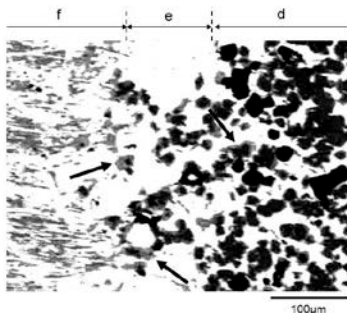
Back-scattered electron images of the cross section of U-9Pu-10Zr/Fe couple annealed at 963 K are shown in FIG.9 and the composition and the stoichiometry of each phase is summrized in Table 7. Compared to the U-16Pu-10Zr/Fe at 943 K, the structure of the reaction layer was similar except that the two phase layer of $(U,Zr,Pu)_6Fe$+$(Zr,U,Pu)Fe_2$ was not clearly observed.

Table 7. Average compositions of the phases in the reaction zones in the U-9Pu-10Zr/Fe couple at 963 K, and the results of the phase identification. (The name of the areas correspond to those in FIG.9)

Area	Colour of the phase	Composition ratio [at.%]				Identified phase
		Fe	Zr	U	Pu	
a	(single phase)	70.4	5.2	23.4	0.9	$(U,Zr,Pu)Fe_2$
b	(single phase)*	68.3	15.4	15.8	0.4	$(Zr,U,Pu)Fe_2$
c	(multi-phase)*	31.2	13.9	52.6	2.3	$(U,Zr,Pu)_6Fe$+χ
d	(single phase)*	10.9	19.7	64.2	5.1	λ
e	bright	0.7	16.2	76.9	6.2	bcc
e	dark	4.6	18.2	70.6	6.6	λ

The phase marked with * was small in size and the measurement was conducted over an area including other phases.

3.2.5. Liquid phase formation criteria

NAKAMURA et al.[7] confirmed that liquefaction does not occur below 923 K when the atomic ratio of Pu/(U+Pu) is less than 0.25. And also, they predicted that the threshold temperature for liquefaction is dependent on the atomic ratio of Pu/(U+Pu) in the U-Pu-Zr alloy while independent of the Zr content. The present study verified the threshold temperature for liquefaction in the lower Pu content region as shown in FIG.10. The threshold temperature for liquefaction is between 963 and 983 K when the Pu/(U+Pu) is 0.09. In the case where Pu/(U+Pu) is 0.18, the threshold temperature is between 943 and 963 K. It was confirmed that the threshold temperature increases as the Pu/(U+Pu) ratio decreases as suggested by Nakamura et al. This result enabled the prediction of the threshold temperature for the liquefaction as a function of Pu content.
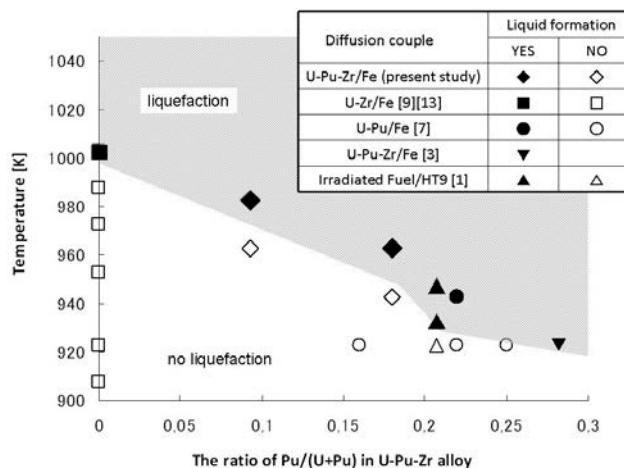
FIG. 10. Liquefaction map on the metallic fuel-cladding system.

4. Conclusion

In order to fully understand FCCI in metal fuels, diffusion couples consisting of Fe-base alloys and lanthanide alloys or U-Pu-Zr alloys were isothermally annealed. The reaction layers formed in the couples were examined and all the phases were identified. These results give basic information about the FCCI layer structure for examining irradiated fuel pins. It was confirmed that the liquefaction threshold temperature is between 963 and 983 K when the Pu/(U+Pu) is 0.09 in U-Pu-Zr metal fuel. In the case where Pu/(U+Pu) is 0.18, the liquefaction threshold temperature is between 943 and 963 K. Hence, the threshold cladding temperature for the liquefaction onset was determined as a function of Pu content in the fuel alloy, which can be the basis in designing metal fuel pins.

REFERENCES

[1] COHEN, A.B., et al., "Fuel/cladding compatibility in U-19Pu-10Zr/HT9-clad fuel at elevated temperatures", J. Nucl. Mater., **204**, (1993) 244-251.
[2] MURPHY, W.F., et al., "Postirradiation examination of U-Pu-Zr fuel elements irradiated in EBR-II to 4.5 atomic percent burnup", ANL-7602, Argonne National Laboratory (1969).
[3] OGATA, T., et al., "Reactions between U-Pu-Zr alloys and Fe at 923K", J. Nucl. Sci. Technol., **37** 3, (2000) 244-252.
[4] NAKAMURA, K., et al., "U-Pu-Zr metallic fuel fabrication for irradiation test at Joyo", in: Proc. FR09, Kyoto, Japan, Dec. 7-11, (2009).
[5] NOMURA, S., et al., "Development of long life FBR core materials", proc. of Inter. Conf. on Fast Reactors and Related Fuel Cycles, **1**, (1991) 7.4-1.
[6] KAITO, T., et al., "High temperature oxidation behaviors of ODS steels", J. Nucl. Mater.,

329-333, (2004) 1388-1392.

[7] NAKAMURA, K., et al., "Reactions of U-Pu alloys with Fe", J. Nucl. Sci. Technol. **38** 2, (2001) 112-119.

[8] INAGAKI, K, et al., "Reaction of Rare-Earth Elements with Cladding Material for Metallic Fuel FBR", Proceedings of the International Conference on Advanced Nuclear Fuel Cycles and Systems, Makuhari, Japan, 11-15 Dec. (2011).

[9] NAKAMURA, K., et al., "Equilibrium phase relations in the U-Zr-Fe ternary system", J. Nucl. Mater., **275** 2, (1999) 151-157.

[10] KURATA, M., et al., "Thermodynamic Evaluation of the Quaternary U-Pu-Zr-Fe System - Assessment of Cladding Temperature Limits of Metallic Fuel in a Fast Reactor", J. Nucl. Mater., **294** 1-2, (2001) 123-129.

[11] NAKAMURA, K., et al., "Phase relations in the quaternary Fe-Pu-U-Zr system", J. Nucl. Mater., **304** 1, (2002) 63-72.

[12] NAKAMURA, K., et al., "Phase relations in the Fe-Pu-U ternary system", J. Phase Equilibria, **22** 3, (2001) 259-264.

[13] OGATA, T, et al., "Reactions between U-Zr alloys and Fe at 1003 K", J.Nucl. Mater., avaliable on line 11 October (2012).

New Fuel Alloys Seeking Optimal Solidus and Phase Behavior for High Burnup and TRU Burning

R.D. Mariani[a], **D.L. Porter**[a], **V.S. Blackwood**[b], **Z.S. Jones**[b], **D.L. Olson**[b], **B. Mishra**[b], **J.R. Kennedy**[a], **S.L. Hayes**[a]

[a] Nuclear Fuels and Materials Division, Idaho National Laboratory, Idaho Falls, Idaho, USA

[b] Department of Metallurgical and Materials Engineering, Colorado School of Mines, Golden, CO, USA

Presented by Robert Mariani

Abstract. Recent modifications to fast reactor metallic fuels have been directed toward improving the melting and phase behaviors of the fuel alloy, for the purpose of ultra-high burnup and transuranic (TRU) burning. Improved melting temperatures increase the safety margin for uranium-based fast reactor fuel alloys, which is especially important for transuranic burning because the introduction of plutonium and neptunium acts to lower the alloy melting temperature. Improved phase behavior—single-phase, body-centered cubic—is desired because the phase is isotropic and the alloy properties are more predictable. An optimal alloy with both improvements was therefore sought through a comprehensive literature survey and theoretical analyses, and the creation and testing of some alloys selected by the analyses. Summarized here are those analyses, the impact of alloy modifications, and recent experimental results for selected pseudo-binary alloy systems that are hoped to accomplish the goals in a short timeframe.

INTRODUCTION

Ultra-high burnup fuels hold significant potential not only for potential economic gains, but also for reduced footprint of long-term wastes. Their attractiveness is increased if they can also accommodate transuranic burning, to reduce the presence of long-lived actinides in long-term waste. Metallic fast reactor fuels have demonstrated significant promise in both regards, as demonstrated with U-10Zr fuel qualified to 10 atom percent heavy metal burnup in the EBR-II reactor, which was eventually to include high loadings of plutonium in some alloys. The U-Pu-Zr alloys were tested extensively.[1]

Recent research efforts have been directed at fuel features that must be improved to reach ultra-high burnups, i.e., 30 to 40 atom percent heavy metal burnup.[2] The targeted research innovations include decreased fuel smear density, annular fuel compared to solid rod fuels, coatings or liners on inner cladding walls, vented fuel pin, advanced fabrication methods, targeted fuel alloy additions, U-Mo based fuel alloy, and compatibility with an electrochemical fuel recycle. The research is a collaborative effort between Argonne National Laboratory and Idaho National Laboratory (INL). Irradiation testing has already begun in the Advanced Test Reactor (ATR) at INL, and more irradiations are planned to begin this next year.[3]

A portion of the research focuses on U-Mo based alloy development.[4] For the U-Mo based alloy development, a collaborative effort was established with researchers of the Colorado School of Mines Department of Metallurgy. The objective is to find alloys with higher melting temperatures and lower onset temperatures for the cubic phase. Higher melting alloy temperatures are useful for burning transuranics, because plutonium and neptunium additions act to lower the melting temperatures of fuel alloys. Lower onset temperatures for the cubic phase are valuable because fuel properties are improved—single phase cubic will give isotropic expansion and more uniform properties such as thermal conductivity, which also will simplify fuel modeling. The cubic phase has much greater

solubility for alloying components, minimizing fuel constituent migration during operation. This report summarizes recent findings and sheds light on some of the developments.

BACKGROUND

Alloys are used in metallic nuclear fuels to modify the fuel properties such as melting temperature and expansion characteristics, as compared to pure uranium.[5] The U-10Zr alloy was qualified by the U.S. DOE to 10 atom percent heavy metal burnup in EBR-II. Its melting temperature is on the order of 1250 °C [6], but the alloy exhibits fuel constituent migration driven by the thermal gradients in the fuel and the multiple phases possible for the temperature range.[7][8][9] The fuel temperature ranges from approximately 450 °C at the bottom surface up to 700 °C near the top center line. Other alloys have been investigated, and U-10Mo is particularly interesting because of its single-phase cubic symmetry above 550 °C [10] and higher thermal conductivity compared to U-10Zr. However, the melting point of U-10Mo is virtually the same as uranium metal, and some evidence suggests that substitution of some plutonium for uranium in U-10Mo alloy destabilizes the fuel phase more than the same substitution in pure uranium. These observations prompted research into more slightly more complex U-Mo alloys, that is, U-Mo based alloys.

Ternary alloy investigations include U-Mo-Ti as well as quaternary alloys of U-Mo-Zr-Ti. To date, the ternary U-Mo-Ti system has undergone relatively little investigation. The goal of selecting these alloys is to take advantage of the cubic phase stabilization offered by Mo while not compromising the melting temperature.

A sense of the stabilization effect offered by additions of Zr and/or Ti may be estimated from examining the Mo-Ti-Zr system, which exhibits the body-centered cubic (bcc) phase over a considerable range of compositions below 600 °C [11], despite the existence of the low-temperature hexagonal phases for Ti and Zr, and the complete solid solubility of Ti and Zr. The stability of the bcc phase over more than 25% of the Mo-Ti-Zr ternary phase diagram at 600 °C, even with high Zr and Ti concentrations, may help to stabilize the bcc phase for the uranium alloys phase while these same additions should raise melting temperature compared to only Mo additions. To manage the extent of activities to a reasonable time frame, certain compositions were selected based on review of the relevant phase diagrams. The compositions were chosen because they 1) were believed a good prospect for success (high Mo), and 2) would bound the amount of alloying thought to be required (high Ti and high Zr). The composition range for the non-fuel alloying components would total less than 15 weight percent (i.e., 85-95 weight percent uranium or heavy metal), in keeping with traditional fuel alloy compositions such as U-10Zr and U-10Mo.

Traditional alloy theory models have been applied relative to the three solid phases of uranium: alpha (orthorhombic), beta (tetragonal), and mainly gamma (body centered cubic).[12] The Darken-Gurry and Miedema models, with modications based on concepts of Waber, Gschneidner, and Brewer have been used to predict the behavior of four types of solutes: 1) those associated with alloying the uranium (eg. Zr, Mo and Ti) to increase phase stability and reduce the potential for reaction of the uranium fuel with cladding materials 2) Transuranic elements in the uranium 3) Rare earth fission products (lanthanides) and 4) other transition, alkali and noble metal fission or activation products. Using these solute map criteria, elemental behaviors have been predicted as highly soluble, marginally soluble, or immiscible (intermetallic phase formers) and have been used to compare solute effects during uranium phase transformations. The overlapping of these solute maps are convenient first approximation tools for predicting alloy behavior.

A key goal for these alloys is compatibility with existing processes and systems, from fabrication through fuel cycle and waste form production. For example, a possible concern is the presence of technetium as an activation product arising from molybdenum. However, the presence of technetium as a fission product has already been addressed in the Zr-alloyed fuels, and the use of molybdenum does not introduce a new waste issue. The electrorefining of these alloys in molten LiCl-KCl has been discussed with regard to their potential effect on their retention in cladding hulls and their effect on metal waste forms, e.g., retention of heavy metal with the cladding. In addition to fuel processing, the

effect on neutronics should be assessed, since the cross-sections for Mo, Ti, and Zr are different. The impact of these fuel alloy modifications, and others besides, has been examined, and the use of these new alloys is compatible with the highly developed U-10Zr alloy system.[13]

A variety of cast alloy samples were examined with differential scanning calorimetry, optical microscopy, scanning electron microscopy (SEM), and x-ray diffraction. Here described are some of those experimental details and results, mainly the onset temperatures for the cubic phase and the solidus temperatures for two pseudo-binary systems, U-x(50Mo-43Ti-7Zr), and U-x(73Mo-27Ti), where x varies up to 15 wt% and all values indicate weight percent.

EXPERIMENTAL

To produce a casting, a 40 by 40 by 0.025 mm piece of molybdenum foil was weighed and folded into a container for powders. The powders of molybdenum, titanium, and zirconium were weighed and transferred to the folded piece of molybdenum foil. Titanium foil was used to reduce the amount of titanium powder encapsulated in the molybdenum foil. The molybdenum encapsulated powder, titanium foil (0.127 mm thickness) and uranium bar stock were set into a copper hearth and arc melted using a gas tungsten arc (GTA) powered by a GTA welding power supply. The alloys were flipped and re-melted seven to ten times to ensure that the alloy was macro-homogenized. In a second hearth a final casting was done to produce a small diameter rod (see Figure 1). This rod was used to obtain samples for alloy characterization.

FIG. 1. A casting of a uranium alloy (a U.S. quarter, ~23 mm diameter, is placed in the figure for scale).

Two separate castings of the same composition were analyzed using differential scanning calorimetry (DSC). Both castings showed reproducible onset and end transition temperatures for both heating and cooling cycles. In addition, the macro-homogenization of the casting process was tested by cutting a DSC sample from the end of the cast rod closest to the sprue and cutting another sample closest to the end of the mold. The DSC analyses showed similar patterns and little variation between onset and end temperatures for the heating and cooling cycles of these two specimens. The lack of significant differences in DSC analysis between specimens indicated acceptable macro-homogenization.

The DSC results from testing the homogenous pseudo-binary alloys were then used to investigate the effects of the alloying on the melting temperature (solidus) and the transformation temperature to the gamma phase. Details of the other characterization testing will be published in future manuscripts.

RESULTS AND DISCUSSION

One unique perspective taken here is that the chemical stability of the alloy is directly related to the melting temperature. This argument can be made for two reasons. First, the melting point of a pure, extended solid indicates its bond strength, and therefore its thermodynamic stability. For example, diamond and tungsten have very high melting points, and melting point is correlated with cohesive energy. When bonding types are the same, as in elements with the same crystal structure, the relative order of melting points can be used to estimate the order of bond strength. This is difficult, however, when bond types and crystal structures are not alike.

Secondly, in the case of conventional uranium fuel alloys, melting proceeds from the γ-U phase to the liquid phase. In alloy systems with this characteristic, a direct comparison among alloys can be made, because the melting transition occurs from the bcc lattice for each alloy. On this basis, the solidus for U-19Pu-10Mo (~ 990 °C [14]) should not be expected to increase much compared to U-19Pu (~ 980 °C), because the solidus for U-10Mo increases very little compared to the melting of pure uranium (approx. 15 C degrees increase). On the other hand, the solidus U-19Pu-10Zr (~ 1100 °C [15]) is increased compared to U-19Pu, just as the U-10Zr solidus shows a large increase relative to the uranium melting point (approx. 100 C degrees increase). Analogous arguments can be made for the chemical compatibility of the fuel alloy with the cladding, because both U-10Zr and U-10Mo melt from the γ-U phase. For example, iron (from the cladding) diffusing into the fuel lowers the melting point of uranium; the addition of an element like Zr can increase this melting temperature.These same concepts may also be applied toternary or more complex U-10Mo systems wherein one or more alloying agents are introduced to raise the solidus temperature. Figure 2 illustrates the desired behavior for a new alloy (red lines) in comparison to U-Zr and U-Mo alloys.
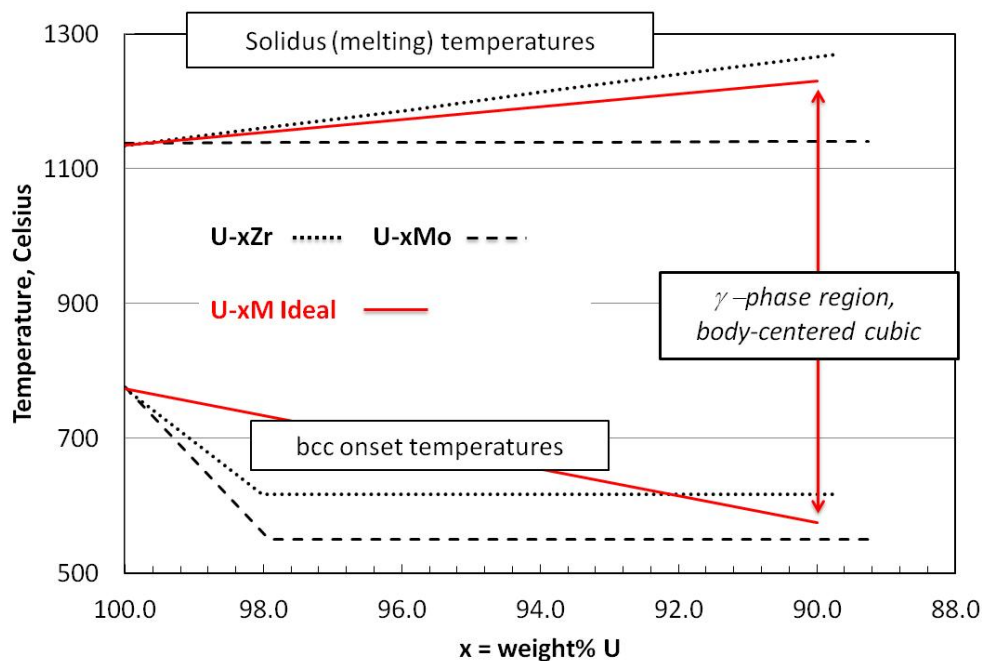

FIG. 2.*Onset temperatures for the body-centered cubic (bcc) phase and for melting in the U-Zr and U-Mo systems. The ideal (i.e., desired) behavior is illustrated with the solid lines, such that the bcc region is increased with decreasing uranium content.*

The onset temperature for the fuel alloy to transform, on heating, to the bcc γ phase may be similarly influenced. In adding Mo to U, the bcc onset temperature is lowered to 550 °C, and stays at 550 °C for Mo additions ≥10 wt%. However, the melting behavior is far from ideal, giving no substantial increase in solidus temperature up to approximately 12 weight percent molybdenum [10], which will not support additions of plutonium and neptunium for transuranic burning. The U-Zr system shows improved solidus temperature, but also shows multi-phase behavior at fast reactor fuel temperatures (approximately 450 to 750 °C), which complicates fuel performance and modeling.

Figure 3 summarizes the results for the two pseudo-binary systems: U-xM_A and U-xM_B, where x varies up to 15 weight percent. M_A designates the constant weight ratio (50Mo-43Ti-7Zr), and M_B designates the constant weight ratio (73Mo-27Ti). It may be noted that both systems offer the desired improvement in melting temperature, and they behave similarly to the U-Zr binary system. However, the U-xM_A does not appear to offer the desired benefit for lowering the bcc onset temperature substantially in comparison to U-Zr. Characterization of the U-xM_A system includes optical microscopy, SEM, and x-ray diffraction.[16] The U-xM_B system appears more promising, because the minimum onset temperature has not been observed yet, and the curve has not leveled off. Higher concentrations of M_B need to be explored to find the minimum onset temperature.
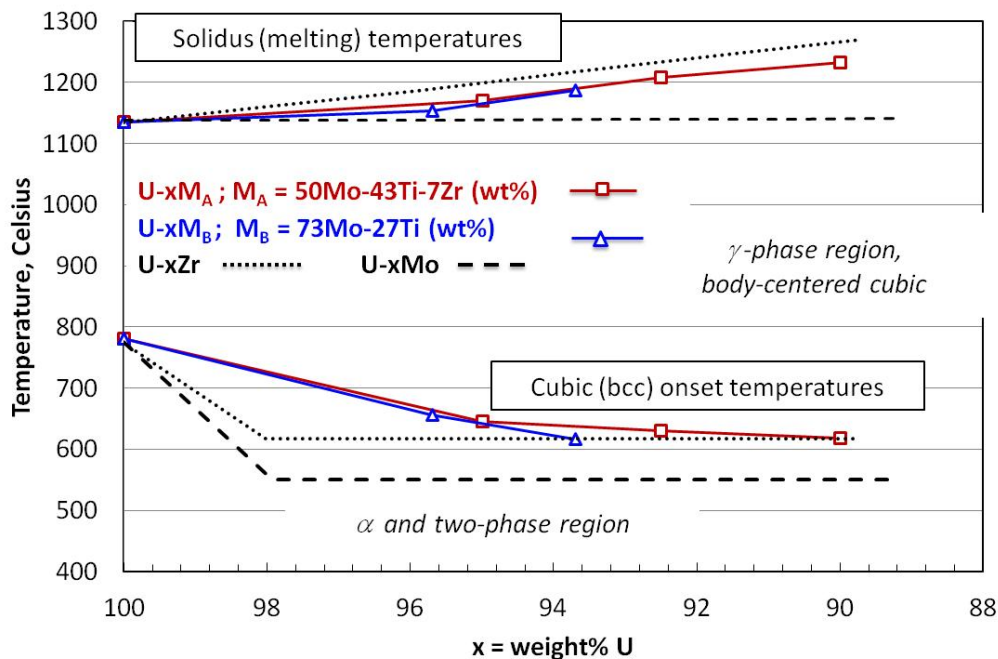
FIG. 3. Variation of onset temperatures and solidus temperatures for uranium alloy systems. Two systems (see inset legend) are compared to U-Zr and U-Mo systems. Simplified view; existence and transition temperatures for β-phase are not indicated. See text.

In Figure 3, the U-M_B system does not exhibit onset temperatures for the solvus and eutectoid because all alloys except U-5M_B are metastable. The temperatures representing the onset temperatures for the lower boundary of the bcc-phase field may arise from a transition of beta titanium and zirconium to alpha, or beta (two phase field) to alpha titanium and zirconium. Heterogeneous segregation of titanium and zirconium possibly result from nucleation of carbides (impurity content) during cooling of the casting (molybdenum remains relatively unaffected). With higher purity uranium and

adjustments to the casting process, the solidus onset temperatures for the U-M$_B$ system could be higher as a result of higher concentrations of zirconium and titanium being retained in the gamma phase field of the U-Mo component of the alloys. These uncertainties are being explored will be reported in a full paper in preparation.

CONCLUSION

Some recent research efforts on new uranium fuel alloys are directed toward improving the chemical stability of the fission products to mitigate FCCI and toward improving the thermodynamic stability of the fuel phases. In comparison to the base alloy of U-10Zr, titanium and molybdenum would be used with zirconium as alloy constituents (fuel matrix) to improve fuel properties, particularly increased melting temperature with a decreased onset temperature for the cubic phase. The increased melting temperature is particularly important for transuranic burning. Plutonium and neptunium always lower the alloy melting temperature and this lowering must be compensated for to have a reasonable safety margin.

 The electromotive series for these elements in molten LiCl-KCl eutectic indicates that their presence should not unduly complicate the electrorefining process and that they should behave comparably to zirconium. Analysis of the extensive research literature, recent experimental results, and the assessed impacts of the alloy modifications indicate that an improved alloy can be successfully developed with modest effort in a reasonable time. These alloys can be reasonably expected to bring performance improvements, such as high burnup, and permit transuranic burning with an improved safety margin toward fuel melting.U-xM alloys (M = some combination of Mo-Ti-Zr) are expected to be beneficial overall with little impact.

ACKNOWLEDGEMENTS

REFERENCES

[1] CRAWFORD, D.C, PORTER D.L., HAYES, S.L., Fuels for sodium-cooled fast reactors: US perspective, J. Nucl. Materials 371 (2007) 202.

[2] WRIGHT, A.E., HAYES, S.L., BAUER, T.H., CHICHESTER, H.J., HOFMAN, G.L., KENNEDY, J.R., et al. "Development of Advanced Ultra-High Burnup SFR Metallic Fuel Concept—Project Overview", Embedded Topical on Nuclear Fuel and Structural Materials (Trans. Conf. Chicago, 2012), American Nuclear Society (2012) 1102-1105.

[3] CHICHESTER, H.J., MARIANI, R.D., HAYES, S.L., KENNEDY, J.R., WRIGHT, A.E., KIM, Y.S., et al. "Advanced metallic fuel for ultra-high burnup: irradiation tests in ATR", Embedded Topical on Nuclear Fuel and Structural Materials (Trans. Conf. Chicago, 2012), American Nuclear Society (2012) 1349-1351.

[4] MARIANI, R.D., PORTER, D.L., HAYES, S.L., KENNEDY, J.R., "Chemical stabilization of metallic nuclear fuels", Embedded Topical on Nuclear Fuel and Structural Materials

(Trans. Conf. Chicago, 2012), American Nuclear Society (2012) 1098-1101.

[5]   HOFMAN, G.L., WALTERS, L.C., "Metallic fast reactor fuels", **MATERIALS SCIENCE AND TECHNOLOGY, VOL. 10, NUCLEAR MATERIALS, PART I** (CAHN, R.W., HAASEN, P., KRAMER, E.J., Eds.) VCH, New York (1994) 1–44.

[6]   LEIBOWITZ, L., BLOMQUIST, R.A., PELTON, A.D., Thermodynamics of the uranium zirconium system, J. Nucl. Mater. 167 (1989) 76.

[7]   PORTER, D.L., LAHM, C.E., PAHL, R.G., Fuel constituent redistribution during the early stages of U-Pu-Zr irradiation, Metall. Trans. A 21A (1990) 1871.

[8]   KIM, Y.S., HOFMAN, G.L., HAYES, S.L., SOHN, Y.H., Constituent redistribution in U-Pu-Zr fuel during irradiation, J. Nucl. Materials 327 (2009) 139-150.

[9]   KIM, Y.S., HAYES, S.L., HOFMAN, G.L., YACOUT, A.M., Modeling of constituent redistribution in U–Pu–Zr metallic fuel, J. Nucl. Materials 359 (2006) 17.

[10] OKAMOTO, H., "Mo-U (molybdenum-uranium)", **BINARY ALLOY PHASE DIAGRAMS**, 2nd ed., (MASSALSKI, E.B. Ed.) Vol. 3 Materials Park, Ohio (1990) 2682-2683.

[11] PROKOSHKIN, D.A., ZAKHAROVA, M.I., Isothermal cross sections at 600 and 750 °C of the phase diagram of the system molybdenum-titanium-zirconium, Inorg. Mater. 3 (1967) 70.

[12] BLACKWOOD, V.S., KOENIG, T.W., PORTER, J.M., OLSON, D.L., MISHRA, B., MARIANI, R.D., PORTER, D.L., "Elemental solubility tendency for the phases of uranium by classical models used to predict alloy behavior", Energy Technology 2012: Carbon Dioxide Management and Other Technologies, (Proc. Conf. Orlando, 2012) The Minerals, Metals, & Materials Society (2012) 357–370.

[13] MARIANI, R.D., PORTER, D.L., HAYES, S.L., KENNEDY, J.R., Metallic Fuels: The EBR-II Legacy and Recent Advances, ATALANTE 2012, Nuclear Chemistry for Sustainable Fuel Cycles (Proc. Int. Conf. Montpellier 2012, POINSSOT, C., Ed.) Procedia Chem. 7 (2012) 513–520.

[14] MARDON, P.G., et al., The constitution and fabrication of uranium-molybdenum-plutonium fuels (7)", **PLUTONIUM 1960** (Proc. 2nd Int. Conf. Grenoble 1960) Cleaver-Hume, London (1961) 329-352.

[15] LEIBOWITZ, L., VELECKIS, E., BLOMQUIST, R.A., PELTON, A.D., Solidus and liquidus temperatures in the uranium-plutonium-zirconiumsystem, J. Nucl. Mater. 154 (1988) 145.

[16] BLACKWOOD, V.S., JONES, Z.S., MARIANI, R.D., PORTER, D.L., PORTER, J.M., OLSON, D.L, MISHRA, B., Pseudo-binary alloy, thermal and metallographic property investigations of as-cast uranium-M alloys where M is 50 wt. pct. molybdenum, 43 wt. pct. titanium, and 7 wt. pct. zirconium (in preparation).

Advanced Sphere-pac Fuel Design
Improving the Particle Fuel Performance with an Internally Cooled Pin

Manuel A. Pouchon, Cedric Cozzo

Nuclear Energy and Safety, Paul Scherrer Institut, 5232 Villigen PSI, Switzerland

Presented by Manuel Alexandre Pouchon

Abstract. Sphere-pac is a particle fuel type facilitating the remote production and being therefore designed for high minor actinide contents. The production of conventional pellet fuel contains many fabrication steps involving powder handling and mechanical processing. If a fuel is part of a combined light water and fast reactor cycle, it will most probably contain minor actinides and fission products, increasing the radiation dose of its reactants to a level, where a processing in hot-cells is necessary. In this case the conventional production route becomes difficult, as powder handling with the connected contamination risk in hot cells represents a major concern. Furthermore the maintenance of mechanical devices in hot cells is difficult and expensive. The suggested wet route by internal gelation is almost powder-less and requires only a solution mixing, drop generation plus heating and washing procedures. After those thermal treatment procedures follows which completes the production of the fuel particles. The paper describes some advances in the production method, plus new Sphere-pac designs for performance increase.

1. Introduction

Sphere-pac fuel is a particle fuel concept which has been researched in many countries since several decades [1, 2, 3]. The other particle fuel type which is also looked at is the Vibropack, which follows similar targets of simplifying the production route for minor actinide containing fuels for recycling or transmutation purpose. The here suggested Sphere-pac fuel is produced in a wet route using the internal gelation process, producing fuel beats in the range from 40 μm to about 1 mm. The internal gelation procedure was developed to a very high level, where continuous productions, including washing operation, were implemented. The conventional method however contains a hot silicon bath, where the solidification, the gelation, takes place. Besides the silicon oil, this also implies special organic solvents in order to clean the product. Both of these processing fluids have to be recycled, which implies a large amount of equipment. At PSI a research project suggests an improvement of the silicon oil based internal gelation method, by replacing the silicon oil heat carrier by a contactless heating mode using microwaves. Here the falling droplets are heated in a microwave cavity, resulting in solidification before they are received in an ammonia washing solution. After a thermal treatment the final product are fuel spheres which are directly filled in the cladding tube. The Sphere-pac is then the final product of the cladding contained arrangement of fuel beads. This concept has also been elaborated in many production and irradiation tests. An overview of tests is contained in [1]. Besides the experiment also calculation/simulation tools have been developed in order to better understand the behavior of this new nuclear fuel concept [4]. With regards to reactor performance the experiments showed a good behavior and even some advantageous properties compared to pellet fuel. One of these is the swelling behavior, which has been documented in [5] for carbide fuel in a fast reactor. A major drawback is higher fuel temperatures, coming from the reduced conduction through the Sphere-pac (small touching points between spheres). This paper therefore suggests a new pin type, which provides a major improvement in heat transfer with an internal cooling channel.

2. Actual development of Sphere-pac fuel

2.1. Production of Spheres

The spheres for both size fractions, the smaller typically being 50-100 μm and the large being around 500 to 1000 μm, are produced by the internal gelation method. Details on this method can be found in [1]. It has been developed to a very high technical level with continuous washing procedures and recycling equipment of the necessary liquids for a unit where the internal gelation is triggered by a temperature step in a hot silicon oil bath. All the cleaning and recycling equipment takes more than half of the total installation in place and cost. Additionally some liquid waste arises from the silicon oil based process. Therefore an alternative heating technique to activate the gelation reaction is researched. This process is based on microwaves heating. The idea is not new and was already elaborated in the 1980s, especially also at the Paul Scherrer Institute, as can be seen in [6]. Because of the decreasing interest in the fast reactor cycle in the later 1980s, this approach was not further developed, but all programs relied on the silicon oil bath based installation. Many irradiation programs were conducted and in the early 2000s it was decided that the production plus fuel concept were developed to a stage where further research was not necessary anymore. With this perspective and with the GenIV initiative it was decided to research the microwave route again and to apply for a Swiss funded program, which resulted in the PINE project [7].

The microwave internal gelation requires advanced knowledge in the application of microwave techniques, as the heating procedure is conducted during the free fall of droplets trough a microwave cavity and is therefore very limited in time. In the earlier studies, such as [6], it was found to be advantageous or even crucial to use a frequency in the X-Band, because the energy is efficiently coupled into water based objects, like the droplets of the feed solution which have to undergo gelation. In order to fully understand the heat transfer and also the heat loss processes during the fall, different models have been developed, see [8, 9, 10]. The basic idea is hereby to model on one hand the energy coupling as a function of the cavity type, the resulting field distribution and the droplet position within the cavity. On the other hand the droplet will loose some energy according to its temperature (radiation heat) and its velocity (convectional heat losses). All these factors are integrated into a model in order to well characterize the temperature evolution. The PINE project [7] is conducted in collaboration with partners not being able to handle nuclear materials, therefore the active ingredients such as uranium and plutonium are being replaced by the surrogate element cerium. This seems obvious, but bears the difficulty, that almost all past gelation experience is with uranium based materials and the internal gelation for cerium materials has to be newly developed. This also includes an optimisation for the gelation procedure for speed, since the gelation process is performed in free fall, as mentioned before, see also [11].

All these aspects are developed and the gelation of cerium based droplets reliably works. In the next step the newly developed gelation unit has to be integrated into a sealed environment, in order to allow the production of actinide containing materials. The integration also contains a concept where the unit is divided into parts being kept outside the contaminated area, the glovebox, and the part of equipment which inevitably has to enter the box [12]. The most important and difficult aspect in this separation is the realisation of the interface, which are mainly the transfer of the microwaves and a heat exchanger for the cooling circuit, necessary to hinder a premature gelation of the feed solution, and in order to cool the microwave cavity. In order to realize the implementation, another program was initiated, called MeAWaT for "Methods of Advanced Waste Treatment" [13].

2.2. New Pin Type

The Sphere-pac concept has proven its high potential in many international irradiation programs (see [1]) and for a better understanding of its performance in reactor two codes have been developed at PSI, allowing the simulation of its initial thermal behavior (code SPACON) and the general performance during reactor operation, like the fission gas release and sintering behavior (code SPHERE). The principle of these codes is described in [4]. Fast reactor fuel is largely realized with an oxide matrix, but carbide and nitride matrices are also strongly discussed, as they bear two major advantages over

the oxides: an importantly increased thermal conductivity and a higher metal content in the matrix. Both of these aspects are eminently important for fast reactors since the linear heat rate can be very high and since fast reactor cores require a high density of fissile material. One of the major disadvantages of these non oxide ceramics is however the comparatively high volume increase due to irradiation, commonly called swelling. The Sphere-pac arrangement bears here the advantage that a volume increase can be accommodated by the space between the spheres. Furthermore the touching points between the spheres are initially small and offer a high potential of deformation, which helps to soften the fuel arrangement to and to transmit less stress to the cladding. This feature remains as longs as the fuel has not restructured (sintered), which mainly happens in the hot fuel center and almost does not in the cladding near region. The soft behavior therefore remains in the location where it seems important. This behavior has been experimented in a sophisticated irradiation program conducted in a fast reactor [5].

The small touching points have however also a major disadvantage. As the thermal conduction is mainly taking place in the material, the touching points between the spheres are bottle necks for the heat transfer, and the gas conduction becomes important. This effect is mitigated by the initial necking between the spheres and the later restructuring. The many irradiation programs have shown, that the lower conductivity can be handled in regular operation, in a power ramp scenario however a partially restructured Sphere-pac bears a slight disadvantageous behavior compared to a pellet fuel. As the outer fuel region keeps its Sphere-pac character, the thermal conductivity is lower. In a power ramp the temperature increase of the inner restructured ring is higher, leading to a large thermal expansion. Because of the high speed of this process, the deformation of the outer spheres will not exploit its deformation potential, and the outer region is pushed towards the cladding. It was therefore found that the Sphere-pac induces more fuel-cladding mechanical interaction.

The solution to this issue is an enhancement of the heat transfer: besides choosing a more conducting matrix such as carbide or nitride ceramics, following a geometrical approach is also possible. Examples are a reduction of the pin diameter, a plate design as originally suggested for the gas cooled fast reactor [14], a cross like pin shape and the here suggested annular pin design, where a ring shaped cross section between two concentric tubes accommodates the fuel. The inner space of the smaller tube provides an additional duct for an inner cooling. This idea is not new and has already been suggested for light water reactors combined with Vibropac fuel and a silicon carbide cladding [15] or filled with annular pellets and a normal Zircaloy cladding [16]. Both of these ideas are motivated by the wish of increasing the heat transfer and the potential to increase the specific power of the reactor.

Here this annular pin design is primarily suggested for a sodium cooled fast reactor with steel cladding and a Sphere-pac fuel. The suggestion of this combination is obvious, as on one hand the introduction of the fuel into the cladding is easier for a particle fuel (similar to [15]) as no annular pellets have to be produced with small inner and outer dimensional tolerances, and on the other hand the Sphere-pac fuel production is designed to contain minor actinides, which goes together with the fast reactor cycle. In order to study the feasibility of such a pin concept the standard pin design of the European sodium cooled fast reactor (ESFR) is taken as reference. The dimensions and the arrangement in the assembly can be seen on the left side of Fig. 1. For the new pin design the geometry was varied in a way to meet the same ratios of fuel to cladding and to coolant fractions. Figure 1 on the right side shows such an annular pin design, plus the arrangement in the wrapper. Three aspects are hereby studied, the neutronics, the thermal-hydraulics and the heat transfer within the fuel section [17]. As the materials ratios are equivalent to the reference design, no large change is expected from the neutronics point of view. This is also shown in [17]. The most important change here is when the fuel matrix is changed, e.g. from oxide to carbide. The thermal hydraulic aspect is found to be more challenging, as two different coolant ducts exist throughout the assembly, pin external and pin internal channels. The cross-section is hereby slightly and the geometry totally different. The pin outer surface is additionally equipped with a wrapper wire, acting as a distance holder to the next pin. The first calculations resulted in a slightly higher resistance of the inner channel. This issue can be addressed by applying an additional flow resistance to the outer channel [17]. The main motivation of the concept is the enhanced heat transfer from the fuel. Already in Fig. 1 it is obvious, that the maximal fuel to cladding distance is much decreased for the annular pin design (about 2.28 compared to 3.865 mm). In order to

calculate the temperature profile, the SPACON code [4, 18] is used, which simulates the fuel at startup condition, when it did still not undergo restructuring. From a thermal conductivity point of view this is the worst case for the Sphere-pac fuel, as later partially a pellet like structure is formed.
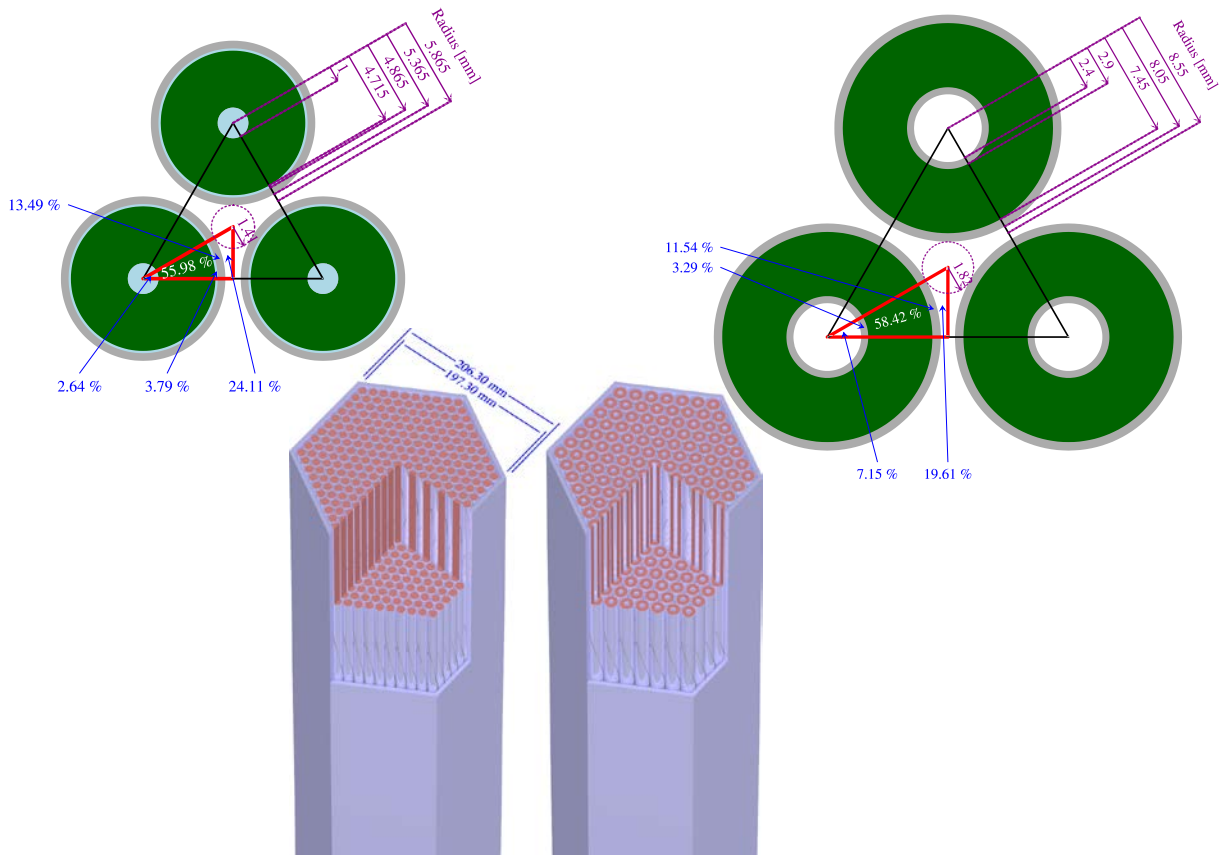
FIG. 1. Pin designs for ESFR [17]. On the left the conventional pellet with the according fuel element, on the right the annular design, being suggested for improved heat transfer.

Figure 2 shows the resulting temperature profiles [17]. The x-axis represents the axial position in the pin, and the y-axis the temperature. On the left is the ESFR reference pin design with the central hole. In the centre is the temperature profile of the same pin design filled with Sphere-pac fuel and on the right that of the suggested annular pin filled with Sphere-pac. For each of these arrangements two calculations are performed: for MOX with 20% Pu (red dotted line) and for mixed carbide with the same Pu content (green solid line). For each temperature profile the corresponding average temperature is denoted with a box. For the calculation the coolant temperature is set to 470 °C and the linear heating rate is set to 293 and 626 W·cm^{-1} for the conventional pin and the annular design respectively. The reason for the difference is the larger fuel cross-section of the annular design. For more details about the calculations see [17].

In the conventional pin design the Sphere-pac fuel shows a much lower heat transfer, resulting in a much increased fuel centre temperature for both the oxide and the carbide matrices. It is important to mention here, that the annular pellet design helps to importantly reduce its centre temperature. Compared to this the annular pin design shows a much enhanced heat transfer. In case of the oxide fuel the maximal temperature becomes even much lower than the corresponding pellet fuel, and for the carbide fuel the maximal temperature is only slightly higher. Especially for the oxide fuel the disadvantageous heat transfer of Sphere-pac fuel becomes even advantageous, when used in the annular pin design. This feature is very important since with lower temperatures the restructuring is less important and therefore the power ramp scenario which is mentioned earlier does not represent a drawback for this fuel design anymore.
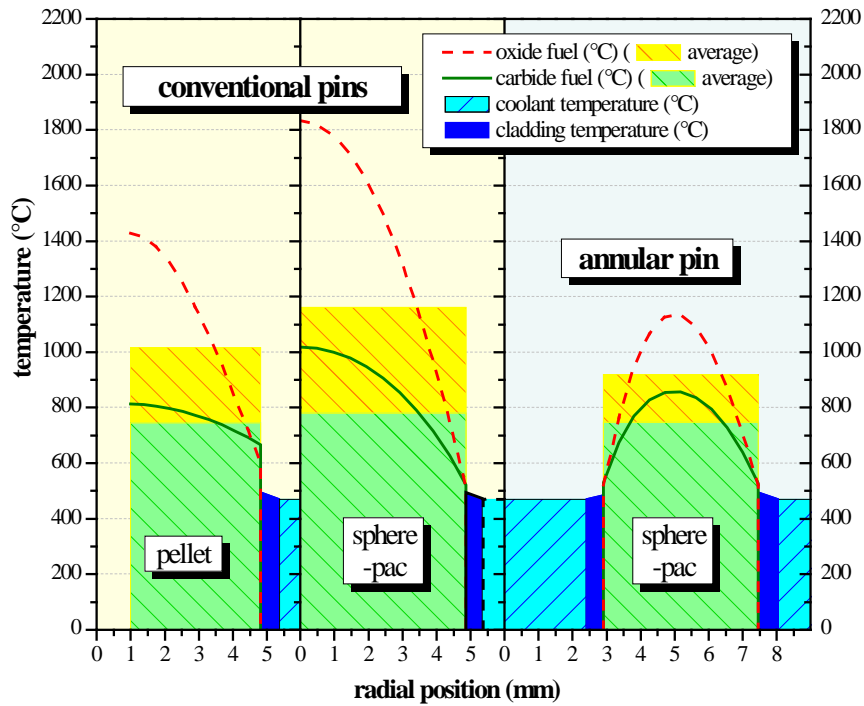
FIG. 2. Temperature profiles of different pin concepts [17]. On the left the pellet with a centre hole, in the middle the same conventional pin geometry, but filled with a Sphere-pac, on the right the new annular pin design with two concentric cladding tubes.

Besides the thermal conductivity aspect, the suggested design also presents some mechanical advantages. With the increased diameter and the double structure, the pin has a much increased component stiffness and under a given bending load the stresses in the structure are highly decreased. This becomes especially important when new materials are considered in future like for example silicon carbide based composites as presently suggested for light water reactor cladding material. In this design the cladding surface to fuel volume ratio is also increased, which again provides a better heat transfer.

3.   Summary, Conclusions and Outlook

Sphere-pac fuel is designed to accommodate minor actinides because of its simple production method, and therefore the eligibility to be produced remotely. The production method of the fuel particles has been further developed, allowing an even simpler and cost saving fabrication. In order to also improve the performance of the Sphere-pac concept, a new pin design is suggested here. This offers an internal cooling channel and importantly increases the heat transfer. This feature is demonstrated with a simulation code being especially developed for Sphere-pac fuel. For oxide fuel a much decreased maximal temperature is calculated, which even outbalances the one of the conventional pellet fuel. Besides these thermal features, the suggested pins also offer a much enhanced mechanical behavior compared to the conventional ones. These first considerations are very promising, and the annular pin design is therefore further elaborated with more detailed fuel performance calculations for the swelling, restructuring and the gas release behavior.

Manuel A. Pouchon and Cedric Cozzo

REFERENCES

[1] Pouchon M.A., Ledergerber G., Ingold F., and Bakker K. (2012) Sphere-Pac and VIPAC Fuel. In: Konings R.J.M., (ed.) Comprehensive Nuclear Materials, Volume 3, pp. 275-312, Amsterdam: Elsevier. (DOI: 10.1016/B978-0-08-056033-5.00059-8)

[2] "Simposio Nucleare Internazionale di Torino" in I processi sol-gel per la produzione di combustibili ceramici, Torino, Italy, 1967.

[3] "Symposium on sol-gel processes and reactor fuel cycles", CONF-700502, Gatlinburg, 1970.

[4] Pouchon M.A., Nordström L.-Å., and Hellwig Ch. (2012) Modeling of Sphere-Pac Fuel. In: Konings R.J.M., (ed.) Comprehensive Nuclear Materials, Volume 3, pp. 789-817, Amsterdam: Elsevier. (DOI: 10.1016/B978-0-08-056033-5.00129-4)

[5] G. Bart, F.B. Botta, C.W. Hoth, G. Ledergerber, R.E. Mason, R.W. Stratton, "AC-3-irradiation test of sphere-pac and pellet (U,Pu)C fuel in the US Fast Flux Test Facility", Journal of Nuclear Materials, Volume 376, Issue 1, 15 May 2008, Pages 47-59, ISSN 0022-3115, 10.1016/j.jnucmat.2008.01.022.

[6] G. Ledergerber, "Internal gelation using microwaves", Technical Report, IAEA-TECDOC, Advanced Fuel Technology and Performance (Proc. of An Advisory Group Meeting, Würenlingen, Switzerland, 4-6 Dec. 1984), 352, 165-174, 1985.

[7] CCEM.ch project Platform for Innovative Nuclear FuEls (PINE), www.ccem.ch/pine

[8] M. Cabanes-Sempere, C. Cozzo, S. Vaucher, J.M. Catalá-Civera, M.A. Pouchon, "Innovative production of nuclear fuel by microwave internal gelation: Heat transfer model of falling droplets", Progress in Nuclear Energy, Volume 57, May 2012, Pages 111-116, ISSN 0149-1970 (DOI: 10.1016/j.pnucene.2011.12.011)

[9] M. Cabanes Sempere, C. Cozzo, J.M. Catalá-Civera, F.L. Peñaranda-Foix, K. Ishizaki, S.Vaucher, M.A. Pouchon, "Characterization of Free Falling Drops inside a Microwave Cavity", Proceedings of the International Microwave Symposium IMS 2012, June 17-22, 2012, Montreal (Canada), pp. 1738-1740. ISBN: 978.1.4673.10868.4. (DOI: 10.1109/MWSYM.2012.6259757)

[10] M. Cabanes-Sempere, J.M. Catalá-Civera, C. Cozzo, S. Vaucher, M.A. Pouchon, "Innovative production of nuclear fuel by Microwave Internal Gelation: Theoretical microwaves-microspheres interaction", Proceedings of the 13th International Conference on Microwave and RF Heating, AMPERE 2011, September 5-9, 2011, Toulouse (FRANCE), pp. 231-234. ISBN: 978.2.85428.978.7

[11] C. Cozzo, S. Vaucher, K. Ishizaki, D. Megias-Alguacil, M.A. Pouchon, "Chemistry of uranium surrogate during microwave assisted internal gelation for fuel fabrication", Proc. of GLOBAL 2011, December 11-16, 2011, Makuhari (JAPAN), paper No. 392501

[12] C. Cozzo, M. Cabanes-Sempere, and Pouchon, M. A., "Methods of advanced waste conditioning by microwave internal gelation: set up development and modeling", in 12th Information Exchange Meeting on Actinide and Fission Product Partitioning and Transmutation, Prague, Czech Republic, 2012.

[13] CCEM.ch project Methods of Adv. Waste Treatment (MeAWaT), www.ccem.ch/meawat

[14] L. Brunel, N. Chauvin, T. Mizuno, M.A. Pouchon, J. Somers, The Generation IV Project "GFR Fuel and other Core Materials", Proceedings of the GIF Symposium - Paris (France) - 9-10 September 2009, 135-141 (www.gen-4.org ISBN: 978-92-64-99115-6)

[15] Kazimi M.S.; Hejzlar P., MIT technical report (2005) MIT-NFC-PR-082, DOI: 10.2172/876439

[16] Yong Sik YANG, KAERI, Journal of NUCLEAR SCIENCE and TECHNOLOGY, Vol. 46, No. 8, p. 836–845 (2009)

[17] Manuel A. Pouchon, Bojan Niceno, and Jiří Křepel, "Innovate Pin Design for Sphere-Pac Fuel in Sodium Cooled Fast Reactors", Paper No. 358351 in Proceedings of Global 2011, Dec.11-16,2011 at Makuhari Messe, Chiba, Japan

[18] F. Botta and C. Hellwig, "SPACON - A Theoretical Model for Calculating the Heat Transport Properties in Sphere-Pac Fuel Pins", Nuclear Science and Engineering, vol. 135, no. 2, pp. 165–176.

6

Manuel A. Pouchon and Cedric Cozzo

Minor Actinide Transmutation Performance in Fast Reactor Metal Fuel
Isotope Ratio Change in Actinide Elements upon Low-Burnup Irradiation

H. Ohta[a], T. Ogata[a], S. Van Winckel[b], D. Papaioannou[b], V. V. Rondinella[b]

[a] Central Research Institute of Electric Power Industry,
Tokyo, Japan

[b] European Commission, Joint Research Centre, Institute for Transuranium Elements,
Karlsruhe, Germany

Abstract. Metal fuel alloys containing 5 wt% or less minor actinide (MA) and rare earth (RE) were irradiated in the fast reactor Phénix. After nondestructive postirradiation tests, a chemical analysis of the alloys irradiated for 120 effective full power days was carried out by the inductively coupled plasma - mass spectrometry (ICP-MS) technique. From the analysis results, it was determined that the discharged burnups of U-19Pu-10Zr, U-19Pu-10Zr-2MA-2RE, and U-19Pu-10Zr-5MA were 2.17, 2.48, and 2.36 at.%, respectively. Actinide isotope ratio analyses before and after the irradiation experiment revealed that Pu, Am, and Cm nuclides added to U-Pu-Zr alloy and irradiated up to 2.0 - 2.5 at.% burnups in a fast reactor are transmuted properly as predicted by ORIGEN2 calculations.

1. Introduction

Much attention has been paid to the technologies for recovering the minor actinides (MA) neptunium (Np), americium (Am), and curium (Cm) as well as uranium (U) and plutonium (Pu) from spent nuclear fuel and burning them in fast reactors to reduce the radioactive toxicity of and heat generation from high-level waste. In recent years, various irradiation experiments for MA-burnup, such as FUTURIX-FTA and AFC-2, have been carried out throughout the world [1][2]. The Central Research Institute of Electric Power Industry (CRIEPI) has been developing uranium-plutonium-zirconium (U-Pu-Zr) alloy fuels containing MA in cooperation with the Joint Research Centre, Institute for Transuranium Elements (JRC-ITU), considering that this type of fuel is advantageous for efficiently transmuting MA in fast reactors [3]. The characterization experiments on U-Pu-Zr-MA alloys were previously carried out, where the contamination effect by rare earth elements (RE) was also taken into account. Those experiments indicated that U-Pu-Zr fuels containing 5 wt% or less MA and RE can be fabricated homogeneously with no significant change in the mechanical or thermal properties compared with those of the conventional U-Pu-Zr ternary alloy fuels [4]. On the basis of these results, metal fuel pins including MA-containing alloy segments in the fuel stacks were fabricated for an irradiation experiment. The irradiation was conducted in the fast reactor Phénix with the support of Commissariat à l'Energie Atomique (CEA), France, and the target peak burnups of approximately ~2.5 at.%, ~7 at.%, and ~10 at.% were attained by 2008. Nondestructive postirradiation tests, i.e., axial profilometry and axial gamma-ray spectrometry, showed that no significant damage due to the irradiation experiment was found on the cladding [5][6][7].

In this work, the actual burnups for low-burnup irradiation fuel alloys will be quantified on the basis of composition analysis results. Then, the MA transmutation performance of low-burnup metal fuels will be discussed.

2. Irradiation Experiment [7]

Fast reactor metal fuel pins, in which four kinds of fuel alloys containing 5wt% or less MA and RE were loaded into part of the U-Pu-Zr fuel stacks, were irradiated in the fast reactor Phénix. The schematic views of axial profiles of the metal fuel pins compared with that of the oxide driver fuel pin and of the fuel pin arrangement in an irradiation capsule are shown in Fig. 1. Three irradiation capsules of identical configuration were prepared to achieve three different peak burnups with the following irradiation periods: 120 equivalent full-power days (EFPD[1]) (~2.5 at.%, METAPHIX-1), 360 EFPD (~7 at.%, METAPHIX-2), and 600 EFPD (~10 at.%, METAPHIX-3).

Table I shows analysis results of the initial composition of irradiated fuel alloys. These fuel rods, which were fabricated by casting arc-molten alloys with yttria molds, contain large uncertainties of the elemental composition by the sample positions due to the heterogeneity of the molten alloys as well as the analysis errors. For instance, more than 5 - 6 % uncertainties are found in each actinide concentration in some analyzed samples.
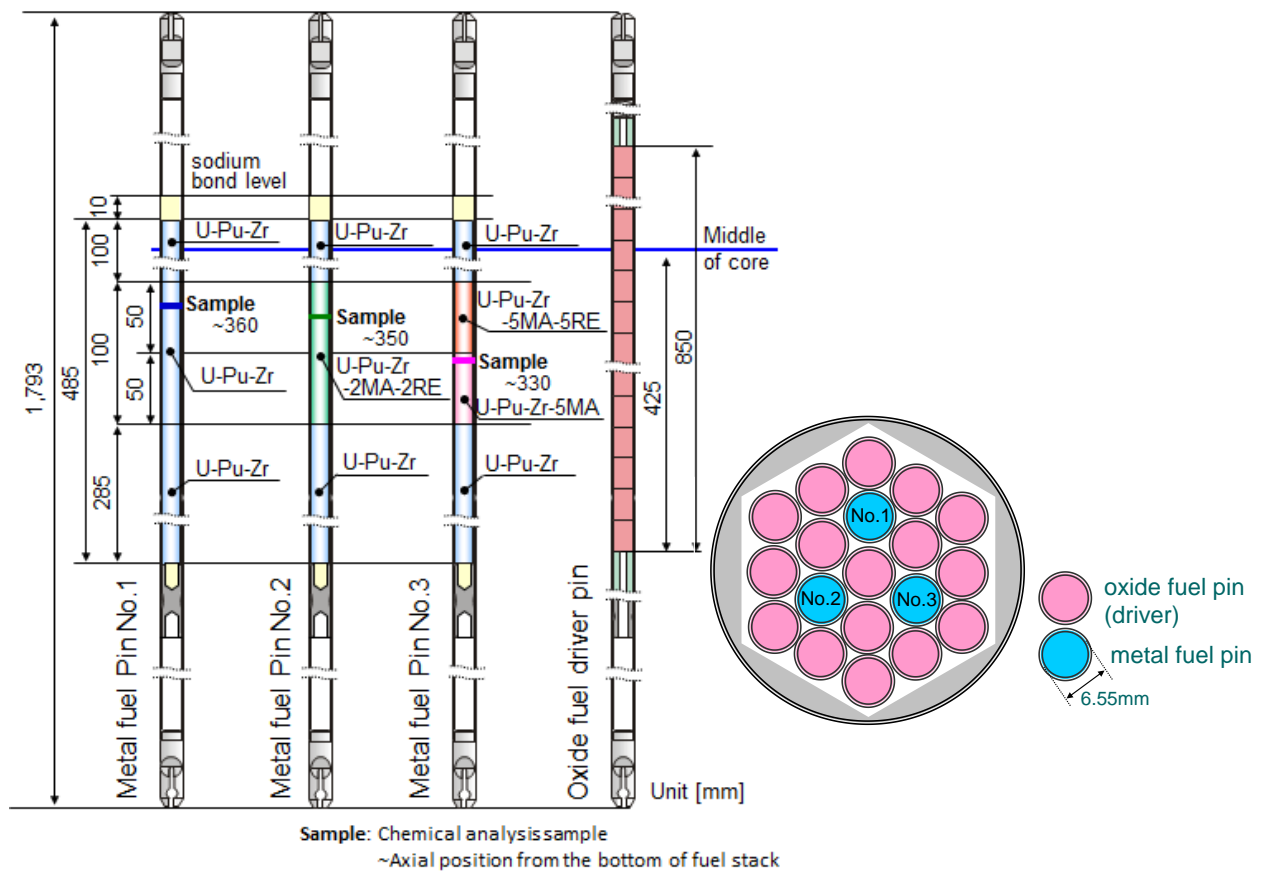
Fig. 1 Schematic views of metal fuel pins fabricated for irradiation experiment and pin arrangement in irradiation capsule.

---

[1]Since Phénix was operated at 62% of its rated full power, actual irradiation days were 1.6 times longer than effective full-power days. That is 120, 360, and 600 EFPDs correspond to 193, 580, and 965 days, respectively.

Table I Analysis Results of Initial Fuel Composition* [wt.%]

Element	U-19Pu-10Zr		U-19Pu-10Zr-2MA-2RE	
	Target	Average of 14 samples	Target	Average of 2 samples
U	71	$70.43^{+2.60}_{-5.46}$	67	66.85±1.55
Pu	19	$18.85^{+1.02}_{-0.74}$	19	19.80±0.20
Np	-	-	1.2	1.29±0.09
Am	-	$0.03^{+0.11}_{-0.02}$	0.6	0.67±0.02
Cm	-	-	0.2	0.18±0.02
Zr	10	$10.73^{+5.07}_{-4.30}$	10	9.46±1.16
Y	-	-	0.2	0.12±0.07
Ce	-	-	0.2	0.20±0.00
Nd	-	-	1.4	1.25±0.12
Gd	-	-	0.2	0.16±0.03

Element	U-19Pu-10Zr-5MA		U-19Pu-10Zr-5MA-5RE	
	Target	Average of 2 samples	Target	Average of 2 samples
U	66	66.30±1.30	61	63.50±2.50
Pu	19	19.35±0.05	19	19.75±0.55
Np	3.0	2.97±0.02	3.0	3.04±0.16
Am	1.6	1.45±0.05	1.6	1.52±0.20
Cm	0.4	0.32±0.02	0.4	0.31±0.14
Zr	10	8.97±1.17	10	8.19±1.69
Y	-	-	0.5	0.31±0.05
Ce	-	-	0.5	0.45±0.11
Nd	-	-	3.5	2.30±1.11
Gd	-	-	0.5	0.32±0.15

*: Impurities < 0.3wt%

3. Chemical Analysis

Three kinds of alloy samples, U-19Pu-10Zr, U-19Pu-10Zr-2MA-2RE, and U-19Pu-10Zr-5MA, were sliced from METAPHIX-1 fuel pins and individually dissolved with the cladding material in HNO_3-HF mixture at ~100°C. The irradiation position of each alloy sample is shown in Fig. 1. The solution was collected through the filter of 1μm mesh. Although a slight amount of the cladding hulls remained after dissolution in some cases, any other residues were not found on the filter. That is the fuel alloys, including fission products (FP), were completely dissolved by the acid. Then, the compositions of these samples were analyzed by inductively coupled plasma - mass spectrometry (ICP-MS).

4. Burnup Evaluation

A conventional burnup evaluation method using neodymium-148 (^{148}Nd) [8] is not applicable in this study because the rare earth elements including Nd were added in some of the fresh fuel alloys. Furthermore, ^{148}Nd is not sufficiently appropriate as a burnup indicator for fast reactor fuel as its fast fission yield is relatively low. In the present study, burnups of irradiated fuels were evaluated using lanthanum-139 (^{139}La), ruthenium-102 (^{102}Ru), or ruthenium-104 (^{104}Ru) as the burnup indicator [9]. In addition, ^{148}Nd was also used in the case of fuel alloys without RE addition, i.e., U-19Pu-10Zr and U-19Pu-10Zr-5MA. The fission yield data were obtained from the ENDF/BVII library provided by the NEA data bank [10]. The evaluated burnups are summarized in Table II. The results evaluated using those indicator nuclides correspond well to each other and are within the range of predictions based on the irradiation condition. This means that ^{102}Ru and ^{104}Ru can be applied as alternative burnup indicator nuclides for recycled low-decontamination fuel with significant amounts of RE.

In this study, burnups of METAPHIX-1 fuel alloys were determined by taking the average of results evaluated using ^{139}La, ^{102}Ru, and ^{104}Ru.

Table II Evaluated Burnups of Three Kinds of METAPHIX-1 Fuel Alloys [at.%]

Sample		U-Pu-Zr	U-Pu-Zr-2MA-2RE	U-Pu-Zr-5MA
Irradiation position [†1]		~360mm	~350mm	~330mm
Burnup indicator	^{148}Nd	2.11	-	2.30
	^{139}La	2.18	2.52	2.50
	^{102}Ru	2.19	2.40	2.32
	^{104}Ru	2.14	2.51	2.27
Average		2.17	2.48	2.36
Prediction [†2]		2.10-2.52	2.15-2.58	2.12-2.55

[†1]: Axial position from the bottom of the fuel stack.

[†2]: Based on the irradiation condition. Uncertainty in the prediction comes from the variation in initial fuel composition and uncertainty of irradiated fuel density owing to axial swelling.

5. Isotope Ratio Change in Actinide Element

In the case of low-burnup irradiation experiment such as METAPHIX-1, it is difficult to evaluate MA transmutation performance through elemental composition change during an irradiation experiment. Moreover, the large uncertainty of the initial fuel composition, as shown in Table I, also complicates the evaluation of MA transmutation performance. On the other hand, the isotope ratio in each actinide element is expected not to vary with the position on the initial fuel rods. Thus, the change in the isotope ratio in actinide elements was investigated in this study.

The actinide isotope ratio analyzed by ICP-MS is shown in Table III along with the results of ORIGEN2 [11] calculations using data from the ORLIBJ40 library [12]. In the ORIGEN2 calculation, the one-group cross section library for a prototype MOX fuel fast reactor was employed because only three metal fuel pins are loaded into an irradiation capsule with sixteen oxide fuel pins, as shown in Fig. 1. As shown in Table III, most analysis results agree well with ORIGEN2 calculations, though C/E spreads to 0.25 - 2.00 in the case of trace isotopes such as ^{234}U, ^{236}U, ^{242}Pu, and ^{242}Cm.

4

Table III Analyzed and Calculated Isotope Ratios in Each Actinide Element

	U-19Pu-10Zr Burnup = 2.17at.%				U-19Pu-10Zr-2MA-2RE Burnup = 2.48at.%			
	As fabrication	Analysis* (E)	Calculation (C)	C/E	As fabrication	Analysis* (E)	Calculation (C)	C/E
U								
^{234}U	0.001	0.004	0.001	0.25	0.001	0.00	0.01	-
^{235}U	0.40	0.38	0.37	0.97	0.40	0.44	0.36	0.82
^{236}U	0.002	0.03	0.02	0.67	0.002	0.03	0.02	0.67
^{238}U	99.60	99.59	99.62	1.00	99.60	99.52	99.61	1.00
Pu								
^{238}Pu	0.007	0.01	0.02	2.00	0.007	0.58	0.66	1.14
^{239}Pu	95.28	92.49	92.62	1.00	95.28	91.93	91.42	0.99
^{240}Pu	4.62	7.20	7.17	1.00	4.62	7.24	7.70	1.06
^{241}Pu	0.08	0.28	0.17	0.61	0.08	0.22	0.19	0.86
^{242}Pu	0.007	0.02	0.01	0.50	0.007	0.03	0.03	1.00
Np								
^{237}Np	-	-	100	1.00	100	100	100	1.00
Am								
^{241}Am	100	100	98.56	0.99	40.92	42.22	41.26	0.98
^{242m}Am	-	-	1.31	-	0.29	0.97	0.96	0.99
^{243}Am	-	-	0.12	-	58.79	56.81	57.78	1.02
Cm								
^{242}Cm	-	-	-		0.00	0.014	0.015	1.07
^{243}Cm	-	-	-		0.00	0.14	0.14	1.00
^{244}Cm	-	-	-		85.66	79.30	79.58	1.00
^{245}Cm	-	-	-		7.78	11.74	11.67	1.00
^{246}Cm	-	-	-		6.27	8.26	8.09	0.98
^{247}Cm	-	-	-		0.29	0.54	0.49	0.91

|	U-19Pu-10Zr-5MA Burnup = 2.36			
	As fabrication	Analysis* (E)	Calculation (C)	C/E
U				
^{234}U	0.001	0.016	0.02	1.25
^{235}U	0.40	0.40	0.37	0.93
^{236}U	0.002	0.02	0.02	1.00
^{238}U	99.60	99.57	99.60	1.00
Pu				
^{238}Pu	0.007	1.50	1.46	0.97
^{239}Pu	95.28	90.08	90.54	1.01
^{240}Pu	4.62	8.20	7.76	0.95
^{241}Pu	0.08	0.17	0.19	1.12
^{242}Pu	0.007	0.04	0.05	1.25
Np				
^{237}Np	100	100	100	1.00
Am				
^{241}Am	40.92	39.04	40.42	1.04
^{242m}Am	0.29	0.83	0.94	1.13
^{243}Am	58.79	60.13	58.64	0.98
Cm				
^{242}Cm	0.00	0.01	0.02	2.00
^{243}Cm	0.00	0.14	0.15	1.07
^{244}Cm	85.66	79.92	80.56	1.01
^{245}Cm	7.78	11.54	11.11	0.96
^{246}Cm	6.27	7.89	7.69	0.97
^{247}Cm	0.29	0.49	0.46	0.94

* : Results of ICP-MS analysis.

The isotope ratio change in major nuclides of Pu, Am, or Cm from the initial analysis data at the time of fuel fabrication was evaluated as follows:

$$\text{Isotope ratio change} = \frac{(\text{Isotope ratio at the time of fuel fabrication}) - (\text{Isotope ratio after fuel fabrication})}{(\text{Isotope ratio at the time of fuel fabrication})}.$$

Figures 2, 3, and 4 show the calculated history of isotope ratio changes in METAPHIX-1 fuels of U-19Pu-10Zr, U-19Pu-10Zr-2MA-2RE, and U-19Pu-10Zr-5MA, respectively. In these Figs., the chemical analysis results of irradiated fuel samples are also indicated by dots. In the ORIGEN2 calculation, the experimental history, such as ~9 years waiting, ~0.53 years irradiation, and ~4.0 to ~5.5 years cooling, is properly reflected. These figures reveal that the isotope ratio changes markedly during neutron irradiation and changes also in the waiting period and cooling time due to radioactive decay reactions. Considering that the composition analysis using ICP-MS might contain uncertainties of more than several percent including the handling errors during sample preparation, it is judged, from the results of comparing analyses and calculation data on the actinide isotope ratio, that the actinide isotope composition was analyzed with high accuracy. In particular, in Cm isotopes where the nuclear data accuracy is anticipated to be somewhat low, the calculations are in reasonable agreement with the analytical results. This is because Cm isotopes are negligibly affected by isobar overlaps and adjacent broad large peak interference in ICP-MS analysis. On the other hand, the analysis accuracy of ^{241}Pu is expected to be low because of the presence of a dominant isobar, ^{241}Am. These results suggest that minor actinide burnups and radioactive decay reactions after fuel fabrication can be simulated using the ORIGEN2 code.

As for the Np isotope, the transmutation performance could not be estimated through the isotope ratio change because ^{237}Np is the only nuclide before and after this experiment. However, it is expected that a concentration of ^{237}Np that has practically no isobar could be analyzed by ICP-MS with sufficiently high accuracy.
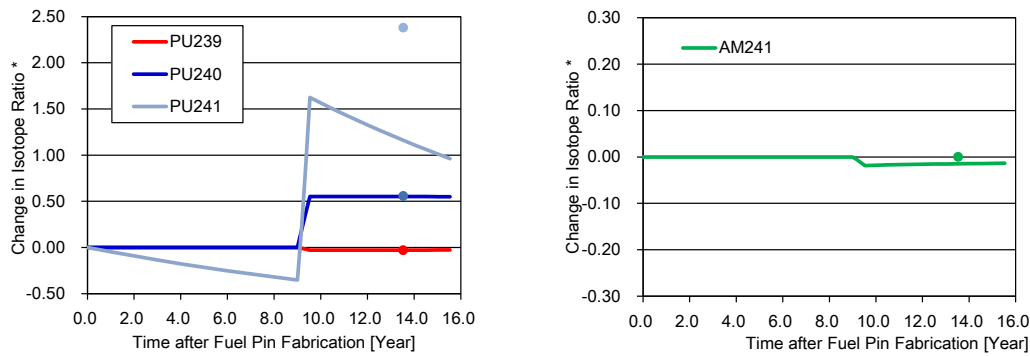
$$*: \text{change in Isotope Ratio} = \frac{(\text{Isotope ratio at the time of fuel fabrication}) - (\text{Isotope ratio after fuel fabrication})}{(\text{Isotope ratio at the time of fuel fabrication})}$$

Fig. 2   History of isotope ratio change in Pu and Am in U-Pu-Zr alloy fuel on the basis of the initial isotope ratio at the time of fuel fabrication. Irradiation was carried out from 9 to 9.53 years after fuel fabrication. Discharged burnup =2.17at.%.

$*$: change in Isotope Ratio $= \dfrac{\text{(Isotope ratio at the time of fuel fabrication)} - \text{(Isotope ratio after fuel fabrication)}}{\text{(Isotope ratio at the time of fuel fabrication)}}$
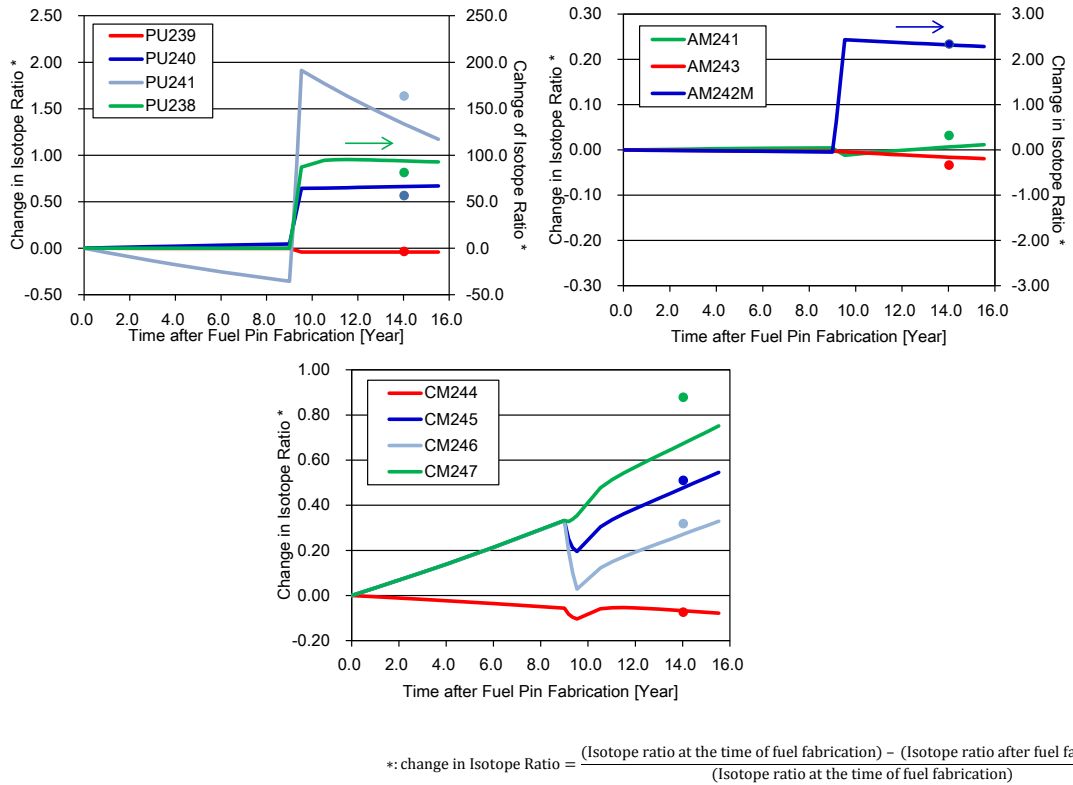
Fig. 3   History of isotope ratio change in Pu, Am, and Cm in U-Pu-Zr-2MA-2RE alloy fuel on the basis of the initial isotope ratio at the time of fuel fabrication. Irradiation was carried out from 9 to 9.53 years after fuel fabrication. Discharged burnup = 2.48at.%.

$*$: change in Isotope Ratio $= \dfrac{\text{(Isotope ratio at the time of fuel fabrication)} - \text{(Isotope ratio after fuel fabrication)}}{\text{(Isotope ratio at the time of fuel fabrication)}}$
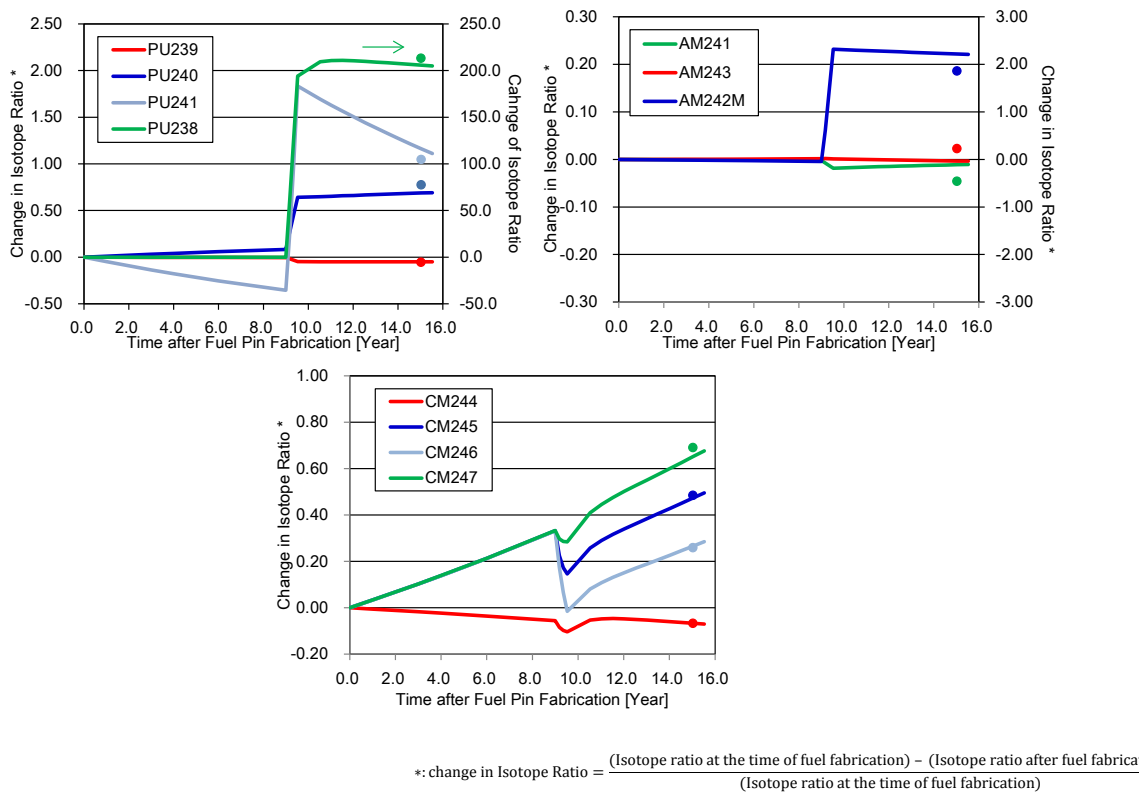
Fig. 4   History of isotope ratio change in Pu, Am, and Cm in U-Pu-Zr-5MA alloy fuel based on the basis of the initial isotope ratio at the time of fuel fabrication. Irradiation was carried out from 9 to 9.53 years after fuel fabrication. Discharged burnup = 2.36at.%.

6. Discussion – Estimate of Initial Fuel Composition

To evaluate MA transmutation performance, the as-fabricated fuel composition as well as the postirradiation composition has to be properly determined. However, as mentioned in chapter 2, the initial composition of fuel alloys fabricated for this irradiation experiment contained fairly large uncertainties by the axial position of the fuel stack. On the other hand, it was found from the investigation of isotope ratio changes during the irradiation experiment including the waiting period and cooling time that actinide burnups and radioactive decay reactions can be calculated reasonably using the ORIGEN2 code. Therefore, the initial fuel compositions were estimated from the results of ORIGEN2 calculations and postirradiation composition analysis. Table IV summarizes the estimated initial composition for each sample. These estimated compositions are approximately within the uncertainties of initial analysis data of 5 - 6 %. Accordingly, the actual initial composition of respective samples could have been close to those estimated results.

Table IV Initial Composition of Fuel Alloy Samples Estimated using ORIGEN2 Code with Postirradiation Analysis Results [wt% in actinides]

	U-19Pu-10Zr	U-19Pu-10Zr-2MA-2RE	U-19Pu-10Zr-5MA
U	78.73 (78.86)	73.62 (75.30)	72.77 (73.35)
Pu	21.24 (21.11)	23.78 (22.30)	22.03 (21.41)
Np	0.00 (0.00)	1.48 (1.45)	3.13 (3.29)
Am	0.01 (0.03)	0.81 (0.75)	1.68 (1.60)
Cm	0.00 (0.00)	0.21 (0.20)	0.39 (0.35)

Within parentheses are average values in initial analysis results.

7. Summary

Burnups of three kinds of METAPHIX-1 fuel alloys, U-19Pu-10Zr, U-19Pu-10Zr-2MA-2RE and U-19Pu-10Zr-5MA, which were irradiated for 120EFPD were determined quantitatively on the basis of the composition analyses by ICP-MS. The evaluated burnups were within the range of predictions under the adopted irradiation conditions.

The analysis results of the actinide isotope ratio before and after the METAPHIX-1 irradiation experiment were compared with the results of ORIGEN2 calculations. It was confirmed that Pu, Am, and Cm nuclides added into U-Pu-Zr alloy and irradiated up to 2.0 - 2.5 at.% burnups in a fast reactor are transmuted properly as expected. For Np, the transmutation performance of which could not be evaluated through the isotope ratio change, it was expected that the analyzed concentration had sufficiently high accuracy because ^{237}Np has practically no isobar interfering with the ICP-MS analysis.

REFERENCES

[1]   P. Jaechi, et al., "Update on the FUTURIX-FTA Experiment in Phénix", *Proc. Int. Conf. GLOBAL2005 Nuclear Energy Systems for Future Generation and Global Sustainability*, Tsukuba, Japan, Oct. 9-13, 2005

[2]   H. J. MacLean, et al., "Irradiation of Metallic and Oxide Fuels for Acyinide Transmutation in the ATR", *Proc. Int. Conf. GLOBAL2007 Advanced Nuclear Fuel Cycles and Systems,* Boise, Idaho, Sept. 9-13, 2007.

[3]   H. Ohta et al., "Development of Minor Actinide Transmutation by CRIEPI", *Actinide and Fission Product Partitioning and Transmutation, Eleventh Information Exchange Meeting,* San Francisco, California, USA, 1-4 Nov. 2010.

[4]   H. Ohta et al., "Development of Fast Reactor Metal Fuels Containing Minor Actinides", *J. Nucl. Sci. and Technol.,* Vol. 48, No. 4, pp. 654-661, 2011.

[5]   L. Breton, et al., "METAPHIX-1 Non Destructive Post Irradiation Examinations in the Irradiated Elements Cell at Phenix", *Proc. Int. Conf. GLOBAL2007 Advanced Nuclear Fuel Cycles and Systems,* Boise, Idaho, Sept. 9-13, 2007.

[6]   H. Ohta, et al., "Irradiation Experiments on Fast Reactor Metal Fuels Containing Minor Actinides - Non-Destructive Postirradiation Examinations and Irradiation behavior Analyses for 2.5at.% or 7.0at.% Burnup Fuels –", *CRIEPI Nuclear Technology Research Laboratory Rep.* No. L08005, Feb. 2009 (in Japanese

[7]   H. Ohta, et al., " Irradiation Experiment on Minor Actinide-Containing Metal Fuels to ~10at.% Burnup" *Proc. Int. Conf. GLOBAL2011 Innovative Nuclear Energy Systems toward 2030 and beyond,* Makuhari, Japan, Dec. 11-16, 2011.

[8]   *Standard Test Method for Atom Percent Fission in Uranium and Plutonium Fuel (Neodimium-148 Method)*, Annual Book of ASTM Standards 12.02 (E321-79), 91 (1995).

[9]   H. Ohta, et al., "Burnup Evaluation Method for Low Decontamination Fuel" *Proc. 2011 Fall Meeting of the Atomic Energy Society of Japan,* F02, Kitakyusyu, Japan, Sep. 19-22, 2011 (in Japanese).

[10] http://www.oecd-nea.org/dbforms/data/eva/evatapes/endfb_7/nfy-ENDF-VII0.endf/

[11] A. G. Croff, "A User's Manual for the ORIGEN2 Computer Code," *ORNL/TM-7175* (1980).

[12] K. Kojima, K. Okumura, S. Asai, et.al., "New ORIGEN2 Libraries Based on JENDL-4.0 and Their Validation for Long-Lived Fission Products by Post Irradiation Examination Analyses of LWR Spent Fuels," *Proc. Int. Conf. GLOBAL2011 Innovative Nuclear Energy Systems toward 2030 and beyond*, Dec. 11-15, Makuhari, Japan (2011).

Irradiation and Postirradiation Examination of AFC-1 Transmutation Metallic Fuels for Fast Reactors

H.J.M. Chichester, S.L. Hayes, D.L. Porter

Idaho National Laboratory, Idaho Falls, Idaho, USA

Abstract. The Fuel Cycle Research & Development program is examining advanced metallic fuels for transmutation in fast reactors. These fuels contain varying amounts of uranium, plutonium, americium, and neptunium, e.g., U-29Pu-4Am-2Np-30Zr. Such fuel alloys are being studied in order to understand how fuel incorporating transuranic elements from recycled light water reactor fuel would perform in fast reactors, with particular focus on transmuting actinides. Irradiation experiments conducted in the Advanced Test Reactor (ATR) at Idaho National Laboratory are designed to mimic prototypic fast reactor neutron spectra and high burnups, up to 30 at.% HM achieved to date. Irradiation experiment hardware incorporates a cadmium-shrouded basket to simulate a fast reactor neutron spectrum in the light water moderated ATR. Non-destructive and destructive postirradiation examinations of these alloys have been completed, primarily within the hot cell at the Hot Fuel Examination Facility. Baseline postirradiation examinations included neutron radiography, gamma scanning, fission gas release, optical microscopy, and microhardness testing. Select results will be presented and compared to results from lower burnup companion experiments and the historical metallic fuel performance database.

1. Introduction

The U. S. Fuel Cycle Research and Development (FCRD) Program seeks to develop and understand the technologies needed to transmute the long-lived transuranic actinide isotopes contained in used nuclear fuel into shorter-lived fission products, thereby dramatically decreasing the volume of material requiring disposition and the long-term radiotoxicity and heat load of high-level waste sent to a geologic repository. The Advanced Fuel Cycle (AFC)-1 irradiation experiments are designed to evaluate the feasibility and provide fuel specimens for scientific investigations of the use of actinide-bearing fuel forms in advanced sodium-cooled fast reactors for the transmutation of transuranic elements from nuclear fuel [1].

The AFC-1D and AFC-1H experiments contain fuel compositions designed for accelerator- and reactors-based transmutation, respectively. Each experiment is a high-burnup companion to a previous low-burnup experiment. The experiments were irradiated in Idaho National Laboratory's (INL) Advanced Test Reactor (ATR) to a final burnup of 15-30 at.% HM (heavy metal). The primary purpose of the experiments is to characterize the relative performance of metallic fuel forms for actinide transmutation advanced fuel cycles, to provide scientific characterization data to support modeling and simulation development, and to allow an initial estimate of the feasibility of various fuel designs being tested.

2. Experiment Description

The U.S. does not have an operating fast reactor, so the AFC experimental hardware is designed to simulate typical fast reactor fuel conditions (temperature and power profiles) in ATR, a thermal test reactor. This is accomplished through the use of a cadmium-shrouded basket to absorb the thermal

neutrons before they reach the experiment. The fuel experiments are designed as miniature fuel pins, known as rodlets.

The rodlet assembly is designed as a miniature fast reactor fuel rod with a standard diameter and reduced length. The rodlet assembly consists of the metallic fuel column, sodium bond, stainless steel Type 421 (HT-9) cladding, and an inert gas plenum. A Type 316L stainless steel capsule assembly contains a vertical stack of six rodlet assemblies. The capsule and rodlet radial dimensions of the metallic fuel specimens are described in a previous publication [2]. The annular gap between the fuel column and rodlet inner diameter is initially filled by the sodium bond and is designed to accommodate fuel swelling during irradiation. The annular helium-filled gap between the rodlet outer diameter and capsule inner diameter is designed to provide the thermal resistance necessary to achieve the design irradiation temperature of the fuel specimen.

The fuel rodlet assembly axial dimensions for the metallic fuels are also provided in a previous publication [2]. The design length of the metallic fuel column is 38.1 mm (1.5-in.) with the exception of the Pu-60Zr fuel composition which is 25.4 mm (1.0-in.); the metallic fuel column may consist of a maximum of two pin segments, and the design diameter is 4.01 mm (0.158-in.) The sodium bond is designed to exceed the fuel column length by 12.7 mm (0.50-in.) in length. The cladding for all rodlets is 152.4 mm (6.0-in.) in length (including welded endplugs), with 5.84 mm (0.230-in.) outer diameter and 4.93 mm (0.194-in.) inner diameter. The capsule, containing a vertical stack of 6 rodlets, is 132 cm (52 in.) long, with an inner diameter of 5.94 mm (0.234 in.), and an outer diameter of 8.99 mm (0.354 in.).

The irradiation test assembly consists of the experiment basket and one capsule assembly, which contains six rodlet assemblies. The experiment basket of the test assembly is designed to interface the capsule assembly with the ATR and to act as a thermal neutron flux filter with the use of cadmium. The capsule assemblies and the rodlet assemblies are designated by unique serial numbers.
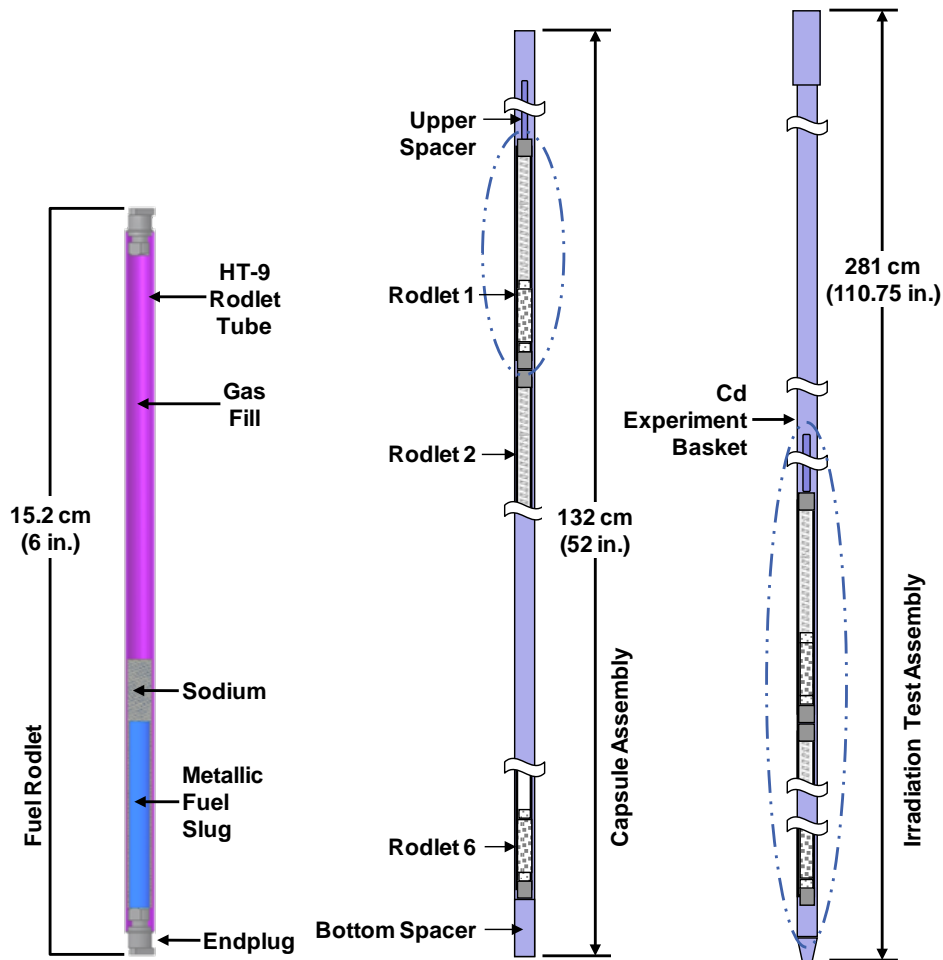
FIG. 1. AFC-1 Irradiation Test Assembly for ATR East Flux Trap Positions

The AFC-1D and AFC-1H experiments were designed to mimic fast reactor fuel operating conditions with a target linear heat generation rate of 330 W/cm. Based on results from neutronic analysis, the ^{235}U enrichment was varied in order to achieve the desired power in each rodlet. Select experiment design conditions are shown in Table 1.

Table 1. AFC-1D and AFC-1H Experiment Design Conditions

Performance Parameter	AFC-1D, AFC-1H
Fissile Burnup Goal	25-40 at.%
Peak Rodlet Linear Power	
- Normal Operation	330 W/cm
- Off-Normal Limit	400 W/cm
Peak Cladding Temperature	
- Normal Operation	550°C
- Off-Normal Limit	650°C
Peak Fuel Temperature	
- Normal Operation	900°C
- Off-Normal Limit	1100°C

3. Experiment Irradiation

The AFC-1D and AFC-1H experiments were irradiated in the ATR East Flux Trap irradiation position and were designed as high burnup experiments. AFC-1D was inserted in ATR cycle 131A and

discharged after cycle 139A, for a total of 582 effective full power days (EFPD) and a peak heavy metal burnup of 26.7 at.%. AFC-1H was inserted in ATR cycle 135B and discharged after cycle 142B for a total of 653 EFPD and a peak heavy metal burnup of 30 at.%. As-run neutronics analyses were performed after each ATR irradiation cycle. Calculated time-averaged rodlet powers and peak burnup are given in Table 2 and Table 3 [3].

Table 2. AFC-1D Irradiation Experiment Neutronics As-Run Data

Rodlet	AFC-1D Nominal Composition †	AFC-1D 582 EFPD			
		Average LHGR (W/cm)	Fission Density (f/cm^3)	Burnup (at.%)	
				^{239}Pu	HM
1	Pu-12Am-40Zr	134	1.96 E21	24.13	15.68
2	Pu-10Am-10Np-40Zr	153	2.24 E21	30.79	17.70
3	Pu-40Zr	228	3.30 E21	33.34	22.57
4	Pu-12Am-40Zr	193	2.84 E21	34.08	22.59
5	Pu-60Zr	151	2.25 E21	39.55	26.71
6	empty rodlet				

AFC-1D inserted cycle 131A, discharged cycle 139A, 582.4 EFPD
† Fuel composition expressed in weight percent

Table 3. AFC-1H Irradiation Experiment Neutronics As-run Data

Rodlet	AFC-1H Nominal Composition †	AFC-1H 653 EFPD					
		Average LHGR (W/cm)	Fission Density (f/cm^3)	Burnup (at.%)			
				^{235}U	^{239}Pu	^{235}U + ^{239}Pu	HM
1	U-29Pu-4Am-2Np-30Zr	176	2.79 E21	25.04	24.74	24.91	18.01
2	U-34Pu-4Am-2Np-20Zr	223	3.48 E21	32.23	26.37	28.32	17.16
3	U-25Pu-3Am-2Np-40Zr	225	3.54 E21	36.86	39.18	37.83	30.15
4	U-29Pu-4Am-2Np-30Zr	248	3.91 E21	34.92	36.91	36.00	26.68
5	U-28Pu-7Am-30Zr	250	3.96 E21	31.04	36.37	33.24	26.10
6	U-25Pu-3Am-2Np-40Zr	176	2.77 E21	27.60	31.88	29.40	22.49

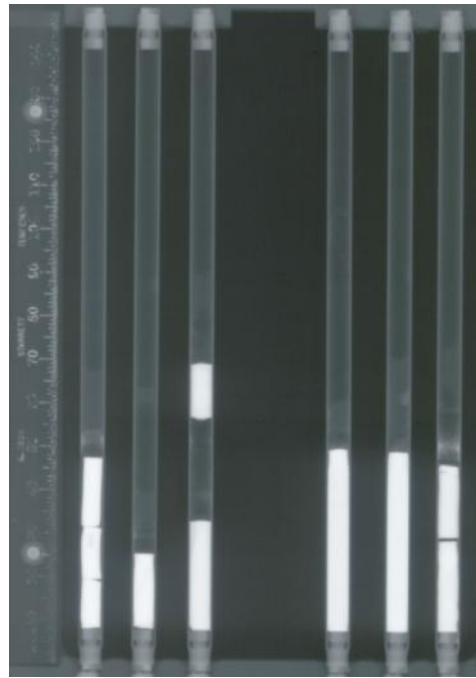AFC-1H inserted cycle 135B, discharged cycle 142B, 653.2 EFPD
† Alloy composition expressed in weight percent

4. Postirradiation Examination (PIE)

Baseline PIE has been conducted on the AFC-1D and AFC-1H rodlets. Baseline PIE includes visual inspection, dimensional inspection, neutron radiography (see Figure 2a and 2b), axial-scanned gamma-ray spectroscopy, fission gas release analysis, metallography (see Figure 3 for examples), microhardness testing, and analytical chemistry for burnup determination. Analysis and evaluation of the data is on-going, but current results appear to follow the trends for fast reactor metallic fuel behavior (e.g., fuel swelling and fission gas release). Fission gas release analysis indicated that two rodlets from the AFC-1D experiment, rodlets 3 and 4, had been breached. Additional PIE and analysis is required to identify specific failure phenomena.

a) AFC-1D   b) AFC-1H

FIG. 2. Neutron radiography images of the (a) AFC-1D and (b) AFC-1H rodlets.

a) 1DR2 (MNT 13T) meaning?

b) 1DR3 (MNT 27T) meaning?

c) 1HR2 (MNT 33T) meaning?
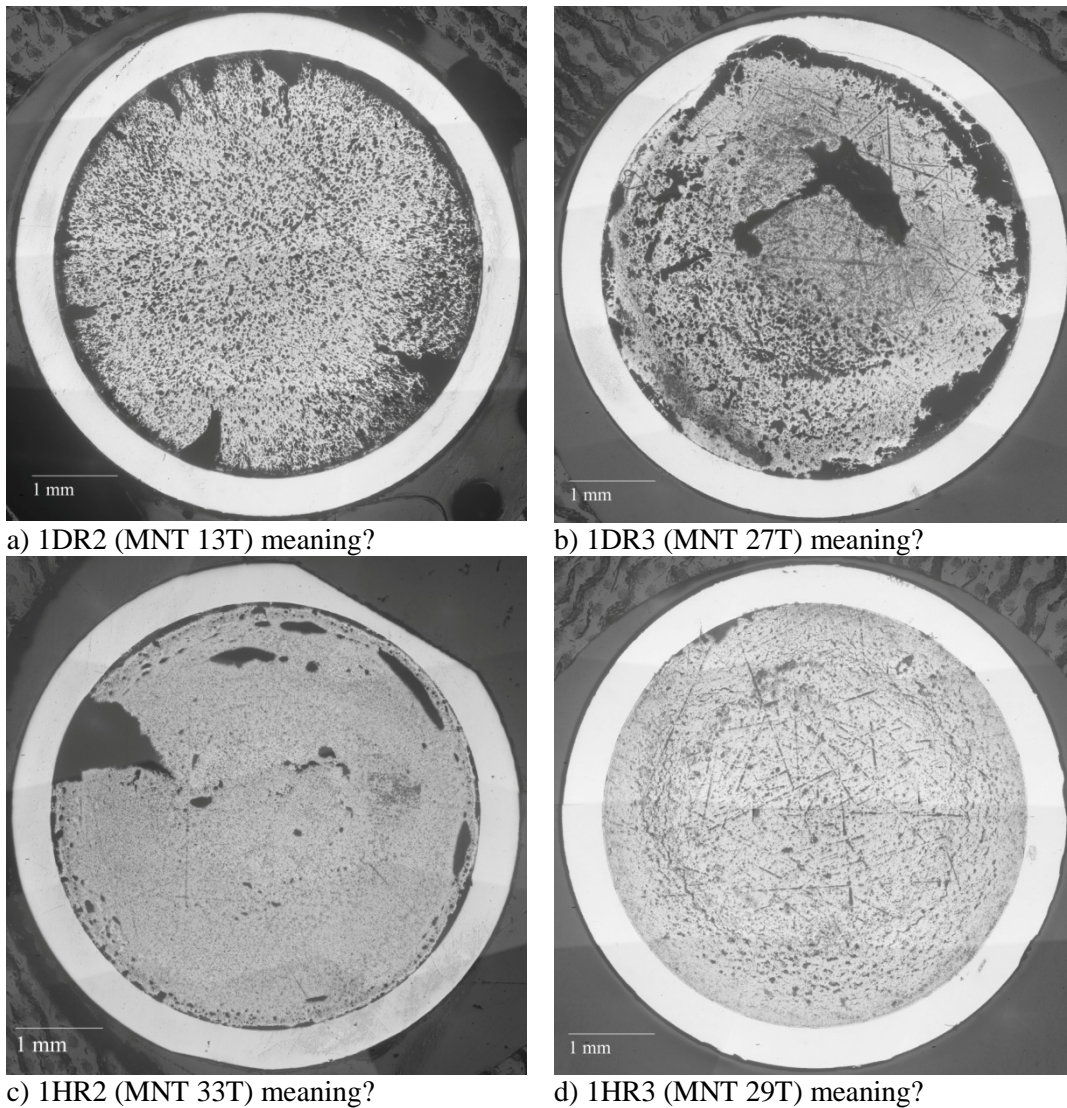
d) 1HR3 (MNT 29T) meaning?

FIG. 3. Optical microscopy of selected AFC-1D and AFC-1H rodlets. Note fuel/cladding interaction in 3b. Cladding thinning in 3c resulted from milling operation during capsule disassembly.

Additional PIE will be conducted when shielded electron microscopy techniques are available at INL in order to investigate constituent redistribution, actinide phase formation, and detailed microstructural behavior.

5. Conclusions

The AFC-1D and AFC-1H irradiation experiments contained non-fertile and fertile fuels, to examine the behavior of transmutation fuels for accelerator and reactor applications, respectively. The experimental hardware is designed to simulate fast reactor fuel power and temperature conditions in the Advanced Test Reactor. Initial PIE results suggest that the fuel behavior of the minor actinide-bearing fuels follows similar trends to standard fast reactor fuels. Results will be compared to results from identical fuels irradiated in the Phénix fast reactor along with the historical database of fast reactor fuel performance. Additional PIE will be conducted to further understand constituent distribution and microstructural evolution of these fuels due to irradiation.

REFERENCES

[1]   S.L. Hayes, B.A. Hilton, M.K. Meyer, G.S. Chang, F.W. Ingram, S. Pillon, N. Schmidt, L. Leconte, and D. Haas, "U. S. Test Plans for Actinide Transmutation Fuel Development," Trans. American Nuclear Society. Nucl. Soc., 87: 353, *American Nuclear Society Winter Meeting*, Washington, DC, 17-21 November 2002.

[2]   B.A. Hilton, S.L. Hayes, M.K. Meyer, D.C. Crawford, G.S. Chang, and R.G. Ambrosek, "The AFC-1Æ and AFC-1F Irradiation Tests of Metallic and Nitride Fuels for Actinide Transmutation," *Embedded Topical Meeting on Advanced Nuclear Energy Systems (GLOBAL 2003)*, New Orleans, Louisiana, 16-20 November 2003.

[3]   H.J.M. Chichester, D.L. Porter, B.A. Hilton, "Postirradiation Examination of AFC-1D, 1G, 1H, and 2A Experiments," Idaho National Laboratory Report INL/LTD-11-23242, September 2011.

Summary of the Minor Actinide-bearing MOX AFC-2C and -2D Irradiations

K.J. McClellan[a], H.J.M. Chichester[b], S.L. Hayes[b], S.L. Voit[c]

[a] Los Alamos National Laboratory, Los Alamos, New Mexico, USA

[b] Idaho National Laboratory, Idaho Falls, Idaho, USA

[c] Oak Ridge National Laboratory, Oak Ridge, Tennessee, USA

Abstract. The AFC-2C and AFC-2D irradiations were conducted by the US-DOE under the Advanced Fuel Cycle program with primary objectives of: 1) evaluating the use of a Cd-shrouded capsule to mimic fast neutron spectrum conditions for testing transmutation fuels in the Advanced Test Reactor (ATR), and 2) obtaining a preliminary assessment of the performance characteristics of minor actinide bearing mixed oxide (MA-MOX) fuel under conditions for service in a fast reactor. The AFC-2C and AFC-2D tests targeted intermediate and high burn-ups, respectively, where each test included nominal MA-MOX compositions of $(U_{0.75}Pu_{0.20}Np_{0.02}Am_{0.03})O_{2-x}$ with x=0.02 and 0.05 along with reference $(U_{0.80}Pu_{0.20})O_{1.98}$ MOX. This paper describes the design of the ATR irradiation configuration and fabrication of the MA-MOX fuel and associated test hardware. In addition, the specifics of the AFC-2C and AFC-2D irradiation tests are presented along with the baseline nondestructive and destructive postirradiation examination (PIE) that has been completed to date.

1. Introduction

The U.S. Fuel Cycle Research and Development (FCRD) program seeks to develop and understand the technologies needed to transmute the long-lived transuranic actinide isotopes contained in spent nuclear fuel into shorter-lived fission products, thereby dramatically decreasing the volume of material requiring disposition and the long-term radiotoxicity and heat load of high-level waste sent to a geologic repository. The AFC-2 series of irradiation tests are designed to evaluate the feasibility and provide fuel specimens for scientific investigations of the use of actinide-bearing fuel forms in advanced sodium-cooled fast reactors for the transmutation of transuranic elements from nuclear waste [1]. The design, fuel fabrication and irradiation testing was initiated under the Advanced Fuel Cycle Intiative and the PIE and associated analysis are being continued under the FCRD program.

The U.S. currently does not have an operating fast test reactor and in order to enable transmutation fuel development has employed testing in the Advanced Test Reactor at the Idaho National Laboratory (INL) with spectrum-filtered drop-in capsules. The objective of the test configuration is, to a sufficient degree, to mimic fast reactor testing relative to fuel temperature distribution. The configuration used for the minor actinide-bearing mixed oxide tests consisted of a stack of up to six miniature fuel rodlets within an un-instrumented (drop-in) capsule which was situated within a cadmium-lined basket. The tests were irradiated in the ATR's east flux trap (EFT).

The AFC-2C and AFC-2D fuel tests presented in this paper consisted of MOX and MA-MOX fuel rodlets for a preliminary assessment of the performance characteristics of minor actinide bearing mixed oxide transmutation fuel under conditions for service in a fast reactor. The AFC-2C and AFC-2D tests targeted intermediate and high burn-ups, respectively, where each test included nominal MA-MOX compositions of $(U_{0.75}Pu_{0.20}Np_{0.02}Am_{0.03})O_{2-x}$ with x=0.02 and 0.05 along with reference

$(U_{0.80}Pu_{0.20})O_{1.98}$ MOX. The tests were designed to enable initial assessment of irradiation behavior, such as minor actinide redistribution and pellet-cladding interaction (PCI), as a function of oxygen-to-metal ratio (O/M) and burnup relative to conventional MOX.

2.   Shrouded drop-in capsule testing

In the absence of a U.S. fast test reactor, the irradiation basket assembly was designed to enable testing of transmutation fuels in the ATR under conditions that are reasonably prototypic for a subset of key fuel performance phenomena such as irradiation growth and swelling, helium and fission gas release fractions, fission product and fuel constituent migration, fuel phase equilibria, and fuel-cladding chemical interaction [2]. The test configuration for the AFC-2 tests consisted of a double encapsulated stack of six minuture rodlets contained within a Cd-lined experiment basket in the EFT (Fig. 1).
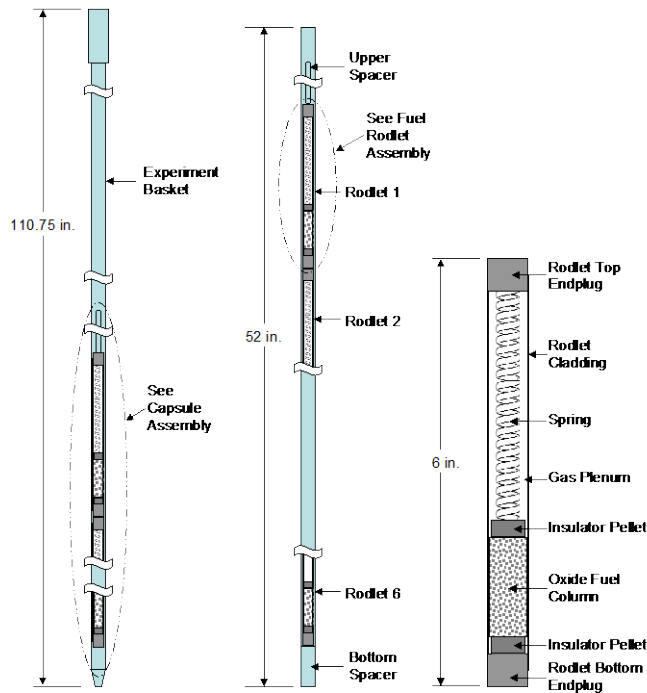

FIG. 1. AFC-2 Series Irradiation Test Assembly for ATR East Flux Trap Positions.

The capsule assembly function is to: 1) provide a gas gap between the fuel rodlet and secondary capsule to elevate the rodlet cladding temperature to a value prototypic of a fast reactor environment (approximately 550°C), 2) provide a second, robust barrier between the water coolant and the fuel and fission products, and 3) provide additional free volume for expansion of helium and fission gases should the cladding of any number of rodlets be breached during irradiation (the free volume is sufficient to reduce the gas pressure on the capsule to below 500 psi assuming all six rodlets are breached). The capsule assembly containing the rodlet is the safety envelope for the Experiment Safety Assurance Package (ESAP) and is fabricated to meet the intent of the American Society of Mechanical Engineers Section III, Class I pressure vessel when loaded with fuel rodlets. Experiment temperature is controlled by fissile density and static helium-filled gas gaps within the rodlets and in the capsule assembly. The ESAP limits for the AFC-2C and AFC-2D tests are given in Table 1 along with nominal target test parameters.

An unaltered ATR spectrum would result in significant self-shielding in the MA-MOX transmutation fuels, so the cadmium shroud is employed which filters neutrons with energies below the Cd cut-off. The resulting spectrum is not fully prototypic in terms of the fast neutron component of a fast reactor spectrum; however, the largely epi-thermal flux seen by the fuel rodlets inside the cadmium shroud is responsible for most fissions during the test, and substantially alleviates the self-shielding issue (Fig. 2). Analysis of the AFC-2C and AFC-2D tests included radial power profiles calculated by MCNP,

fuel and Cd shroud depletion calculated using the MCWO (MCNP coupled with ORIGEN2) analysis methodology, and 1-D thermal analysis using the radial power results.

Table 1. AFC-2C and AFC-2D Experiment Design Conditions.

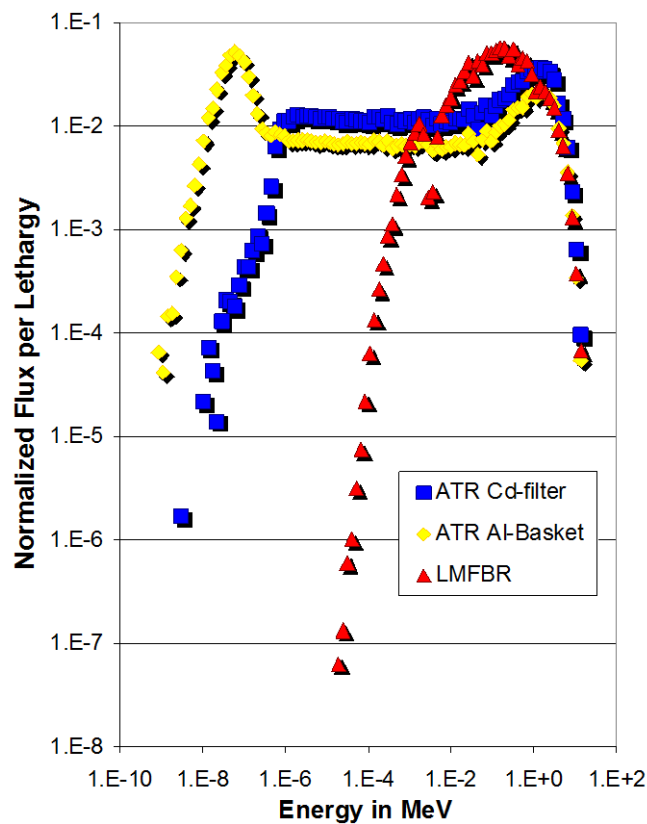| Performance Parameter	AFC-2C & -2D
Maximum Burnup	40 at.%
Peak Rodlet Linear Power	
– Normal Operation	371 W/cm
– Off-Normal Limit	440 W/cm
Peak Cladding Temperature	
– Normal Operation	550°C
– Off-Normal Limit	650°C
Peak Fuel Temperature [3]	2600°C

FIG. 2. Unfiltered and Cd-filtered ATR spectra relative to that for a fast reactor.

Based upon the thermal analysis, the linear heat generation rates (LHGR) for the rodlets were designed to target fuel temperature profiles similar to that for a sodium fast reactor (Fig. 3). Based upon prior fast reactor irradiation of mixed oxide fuel, it was determined that the centerline fuel temperature needed to exceed about 1700°C in order to mimic thermally-driven phenomena of interest such as central void formation, restructuring, and species thermomigration. Enrichment with [235]U was varied for the different rodlets to compensate for the reactor axial flux profile in order to achieve the targeted linear heat generation rates per the irradiation test goals.
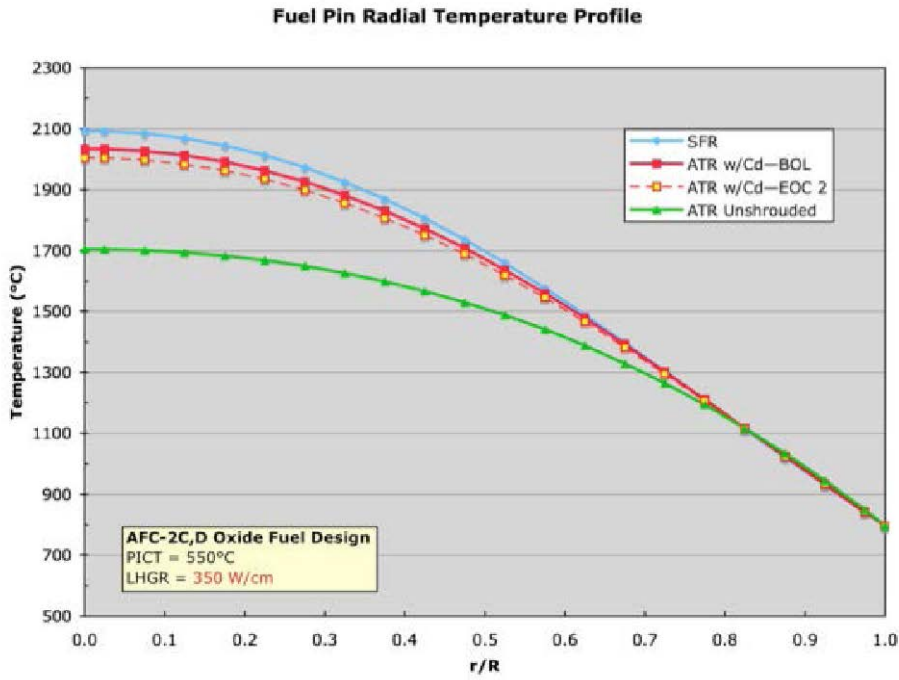
Fuel Pin Radial Temperature Profile

FIG. 3. Calculated radial temperature distributions for unfiltered and Cd-filtered fuel relative to that for a nominal sodium fast reactor.

3. AFC-2C fuel fabrication

A traditional cold press and sinter method was used for the fabrication of the "baseline" fast reactor MOX and MA-MOX pellets with target compositions of $U_{80}Pu_{20}O_{1.98}$ and $(U_{0.75}Pu_{0.20}Np_{0.02}Am_{0.03})O_{2-x}$ with x=0.02 and 0.05. Actinide oxide feedstock powders were blended then milled with the addition of 1 wt.% polyethylene glycol and 5 wt.% pre-sintered recycle MOX and MA-MOX. Milled powder was pressed into cylindrical pellets, no dish or chamfer features were used, and the pressing pressure was optimized at 200 MPa for the MOX pellets and 125 MPa for the MA-MOX pellets. A low temperature binder burnout step was used to remove the organic additives prior to sintering. Green pellets were sintered at 1750ºC in a high temperature refractory metal furnace to achieve a target density of 85-90% of theoretical. Sintered pellets were ground to meet the specified diameter and subsequently thermally treated for adjustment of the oxygen stoichiometry. The affect O/M on fuel performance for MOX with minor actinides is not known therefore two O/M variants were chosen, MAMOX-1 with an O/M=1.98 and MAMOX-2 with an O/M=1.95. Pellets within tolerance for physical and chemical characteristics were selected and packaged for shipment to the INL where the rodlets and capsules where assembled, sealed and tested. The actual composition for the AFC-2C and AFC-2D oxide fuel pellets is given in Table 2.

Table 2. Composition of AFC-2C & AFC-2D test pellets.

Pellet Type:	Density (g/cm3)	Total U* (wt.%)	Total Pu (wt.%)	Am-241 (wt.%)	Np-237 (wt.%)	O/M
MOX	9.87	70.6	17.0	0.0	0.0	1.98
MAMOX-1	9.64	66.6	17.0	2.4	1.3	1.99
MAMOX-2	9.62	66.6	17.0	2.4	1.3	1.96

* U-235/U-238 ratio was tailored to meet experiment goals for LHGR.

4. AFC-2C and AFC-2D irradiation tests

The AFC-2C and AFC-2D experiments were nominally low and high burn-up tests, respectively, containing U, Pu, Am, and Np and were irradiated in two of the ATR East Flux Trap positions using the hardware initially designed for the AFC-1 test series [4] and described above. Both tests were inserted in ATR cycle 143A in September 2008. AFC-2C was discharged at the end of cycle 145B in January 2010 after 260 effective full power days (EFPD), and AFC-2D was discharged at the end of cycle 150B in December of 2011 after 685 EFPD. Analysis of the irradiation power and burn-up characteristics are given in Table 3.

Table 3. Calculated average linear heat generation rate over the test duration and burn-up at discharge.[*]

Rodlet	Composition*	AFC-2C 262 EFPD				AFC-2D 633 EFPD			
		Avg. LHGR (W/cm)	Fission Density (10^{21} f/cm^3)	Burnup (at.%)		Avg. LHGR (W/cm)	Fission Density (10^{21} f/cm^3)	Burnup (at.%)	
				^{235}U + ^{239}Pu	HM			^{235}U + ^{239}Pu	HM
1	$(U_{0.75},Pu_{0.20},Am_{0.03},Np_{0.02})O_{1.95}$	219	0.92	10.4	5.8	217	2.22	24.5	13.3
2	$(U_{0.80},Pu_{0.20})O_{1.98}$	296	1.25	13.8	7.1	291	2.99	32.1	16.9
3	$(U_{0.75},Pu_{0.20},Am_{0.03},Np_{0.02})O_{1.98}$	321	1.35	15.0	8.4	315	3.22	34.9	19.1
4	$(U_{0.80},Pu_{0.20})O_{1.98}$	335	1.41	15.4	7.9	Empty Rodlet			
5	$(U_{0.75},Pu_{0.20},Am_{0.03},Np_{0.02})O_{1.95}$	299	1.25	14.1	7.9	295	3.01	32.8	17.9
6	$(U_{0.75},Pu_{0.20},Am_{0.03},Np_{0.02})O_{1.98}$	241	1.02	11.5	6.4	240	1.85	27.2	14.8

[*] Fuel compositions expressed in mole percent.

5. Postirradiation examination

Baseline PIE has been conducted on four of the six AFC-2C rodlets with two rodlets undergoing nondestructive examination only; these rodlets are being reserved for future advanced nondestructive examination using proton and neutron beam-based techniques. The AFC-2D test remains in the ATR canal for postirradiation cooling and is scheduled for PIE starting in 2013. Completed PIE include visual inspection, dimensional inspection, gamma scan, neutron radiography, fission gas analysis, ceramography, microhardness testing, and analytical chemistry of the fuel rodlets. Analysis and evaluation of the data is on-going, but results appear to be within predicted behavior for the AFC-2C MOX fuel rodlets. Of particular note is that the results to date show higher LHGR rodlets exhibiting restructuring, central void formation (Fig. 4), and high fission gas release values validating the thermal analysis and Cd-shrouded test configuration. Additional PIE will be performed to further define and understand the microstructural and compositional evolution that occurred during irradiation with particular emphasis on minor actinide distribution.
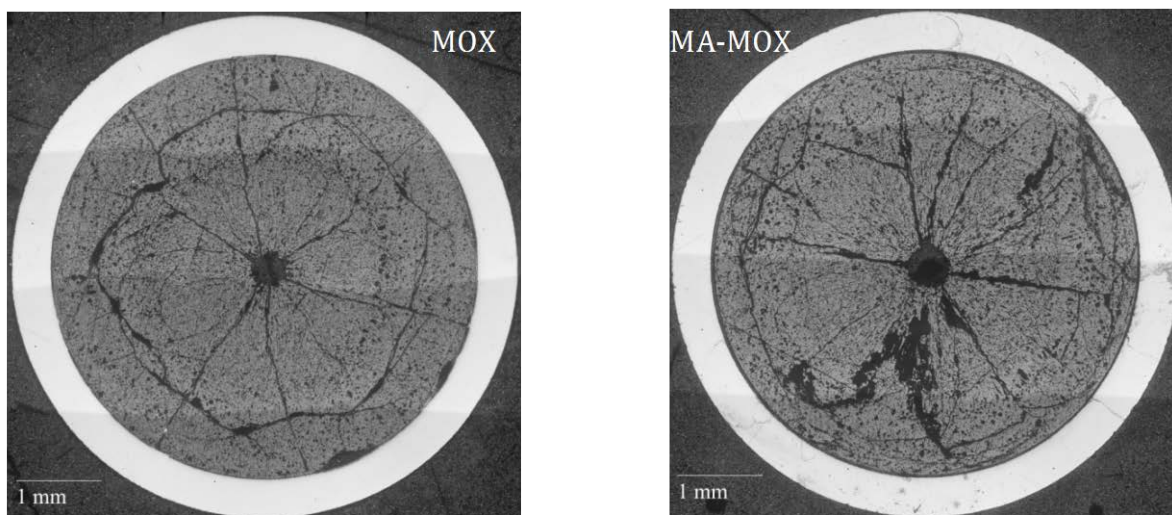
FIG. 4. Ceramography of AFC-2C MOX and MA-MOX showing central void, radial and circumferential cracking.

6. Conclusions

The AFC-2C and AFC-2D irradiation tests consisted of MOX and MA-MOX compositions targeted at: 1) evaluating the use of a Cd-shrouded capsule to mimic fast neutron spectrum conditions for testing transmutation fuels in the Advanced Test Reactor, and 2) obtaining a preliminary assessment of the performance characteristics of minor actinide bearing mixed oxide fuel under conditions for service in a fast reactor. Preliminary PIE results show higher LHGR rodlets with central void formation and high fission gas release values validating the thermal analysis and Cd-shrouded test configuration. No anomolous performance difference have been observed to date between the MA-MOX and reference MOX fuel compositions. Additional PIE will be performed to further define and understand the microstructural and compositional evolution that occurred during irradiation with particular emphasis on minor actinide distribution.

REFERENCES

[1] S.L. Hayes, B.A. Hilton, M.K. Meyer, G.S. Chang, F.W. Ingram, S. Pillon, N. Schmidt, L. Leconte, and D. Haas, "U. S. Test Plans for Actinide Transmutation Fuel Development," Trans. American Nuclear Society. Nucl. Soc., 87: 353, *American Nuclear Society Winter Meeting*, Washington, DC, 17-21 November 2002.

[2] H.J. MacLean, "Irradiation of AFC-2C and -2D Oxide Fuels for Actinide Transmutation in the ATR," Idaho National Laboratory, PLN-2764, August 2008.

[3] K. Morimoto, et al., "Preparation and characterization of (Pu, U, Np, Am, simulated FP)O$_{2-x}$, *J. Phys. Chem. Solids*, **66**, 2005, 634-638.

[4] S.L. Hayes, "Irradiation of Nitride and Metallic Fuels for Actinide Transmutation in the Advanced Test Reactor: Final Experiment Description and Design & Data Package for AFC-1A, AFC-1B, AFC-1C & AFC-1D," Argonne National Laboratory (West) Document No. W7520-0481-ES-02, February 2003

New Concept of Designing Composite Fuel for Fast Reactors with Closing Fuel Cycle

A.M. Savchenko, A.V. Vatulin, V.I. Sorokin, G.V. Kulakov, S.V. Maranchak K.V. Lipkina[†]

Open Joint Stock Company
"A.A. Bochvar All-Russia Research Institute of Inorganic Materials" (VNIINM),
Moscow, Russia Federation

Abstract. A possibility is considered for use in fast reactors in place of the base pelletized type MOX or metallic U-Pu-Zr fuel, the dispersion type fuel elements (composite of metallic high uranium content fuel, U-Mo or U-Zr with PuO_2 powder distributed in Zr alloy matrix). Basic approach to fuel element development - separated operations of fabricating uranium meat fuel element and introducing into it Pu or MA dioxides powder, that results in minimizing dust forming operations in fuel element fabrication. According to new fuel element design a frame fuel element having a porous uranium alloy meat is filled with standard PuO_2 powder of less than 50 micron fractions prepared by pyrochemical or other methods. Proposed composite fuel features higher characteristics in comparison to metallic or MOX fuel.

Novel approach to reprocessing of composite fuel is demonstrated, which allows to separate uranium from plutonium as well as the newly generated fissile plutonium from burnt one without chemical processes with repeated use in fast, PWR or CANDU reactors, which simplifies the closing of the nuclear fuel cycle.

1. Introduction

Currently as promising fuel for fast reactors two basic types of fuel are under consideration. The first one is metallic U-Pu-Zr fuel. The second one is MOX fuel $(U,Pu)O_2$ [1, 2]. High-density U-Pu-Zr fuel features high thermal conductivity and a higher uranium content which provides for the high conversion ratio, negative reactivity factor and increases the passive safety of fast reactors. The metal fuel disadvantages comprise lower processability, fuel-cladding interaction, large swelling at high burnup and the needed availability of sodium in a fuel-cladding gap. MOX fuel is highly irradiation resistant and in terms of technology it has been more mastered. However, its low thermal conductivity restricts the heat flow in a fuel element and its insufficiently high density lowers down the major parameter of fast reactor cost effectiveness, i.e., the conversion ratio. Hence, MOX fuel is unable to provide the conversion of plutonium without a blanket. Besides, at high burn-up of MOX fuel the interaction is observed between fuel and cladding.

Therefore, the optimal solution might be to design novel composite $U-PuO_2$ fuel that would combine the favourable features of both fuel types as well as application of novel design and fabrication process [3-6].

[†] Present address: Open Joint Stock Company
"A.A. Bochvar All-Russia Research Institute of Inorganic Materials" (VNIINM)
Moscow, Russia Federation sav-alex111@mail.ru

2. Major approaches to designing composite U-PuO$_2$ (Metal-Dioxide) fuel

The suggestion is to change over from the pelletized fuels of the container type to dispersion or composite type fuel elements (Fig. 1) [6, 7].
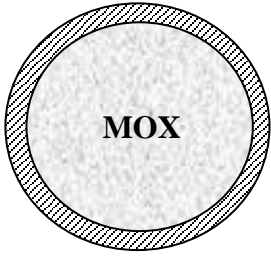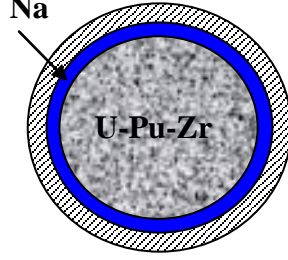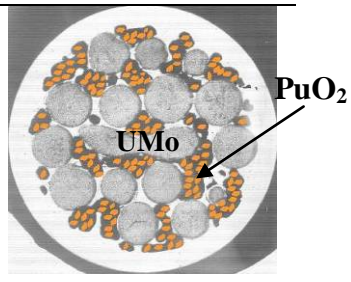
Parameters	MOX (U, Pu)O$_2$	U-20Pu-10Zr alloy	Composite U-PuO$_2$ fuel
	Pelletized type	Pelletized type	Dispersion
Fuel element design			
Smeared density, ρ^{eff}, g/cm^3	8.3-8.5	11.0	10.8-11.0
Maximum fuel temperature, ^{o}C	2000-2250 (IFR, EFR)	<800 (IFR)	790 (BN-K)
Fuel - cladding interaction	Mean	High	No interaction

FIG 1. Design of container type fuels (MOX and U-20Pu-10Zr metal fuel) and novel composite U-PuO$_2$ dispersion fuels for fast reactors [4-7]

In the suggested design metal fuel of U-Mo, U-Zr and U-Zr-Nb alloys forms a porous frame bonded by a zirconium matrix alloy; the pores of the frame contain PuO$_2$ powder manufactured by pyrochemical or other methods [4-7]. The fuel meat metallurgically bonded to a cladding promotes the high thermal conductivity to mixed U-PuO$_2$ fuel, while the Zr-base matrix alloy improves the compatibility between fuel components. This approach can be also implemented with the use of Th granules instead of dump uranium.

The dispersion fuel is known to have a high irradiation resistance and thermal conductivity as well as a metallurgical bond between cladding and fuel which not only protects a cladding against interaction with fuel and fission products but also lowers down the operating temperatures of fuel.[2] The major drawback of dispersion fuel, viz., its low uranium content in this design is compensated for the applied high density uranium metal fuel and compatible with it zirconium alloy matrices [4-7].

The process of the fuel element fabrication comprises 2 stages. At the first major stage of production under conventional conditions of a plant a fuel element frame is fabricated from uranium alloy particles bonded with a zirconium matrix. At the second final stage of the fuel rod fabrication under protective conditions through the fuel skeleton the standard PuO$_2$ powder is filled and after that a fuel element is sealed. In this way the dust forming operation with Pu are minimized while the processability and ecology of the production are enhanced.

The composite fuel retains the advantages inherent in metallic and ceramic types of fuel. Since the contribution into the total burnup is made not only by the metallic fuel at the final irradiation stage as

plutonium is generated, but also by plutonium dioxide at the initial irradiation stage, the total swelling of the metallic fuel is reduced due to a lesser build-up of fission fragments in it.

3. Characteristics of fuel meat and fabrication process

The initial components of the composite fuel are granules of depleted uranium alloys, PuO_2 powder [8] and granules of zirconium matrix alloys. The characteristics of novel fuel and fuel composition are tabulated in Tables 1 and 2; the appearance the original components is illustrated in Fig. 2.

Table 1. Characteristics of Composite U-PuO_2 Fuel Components [3-4]

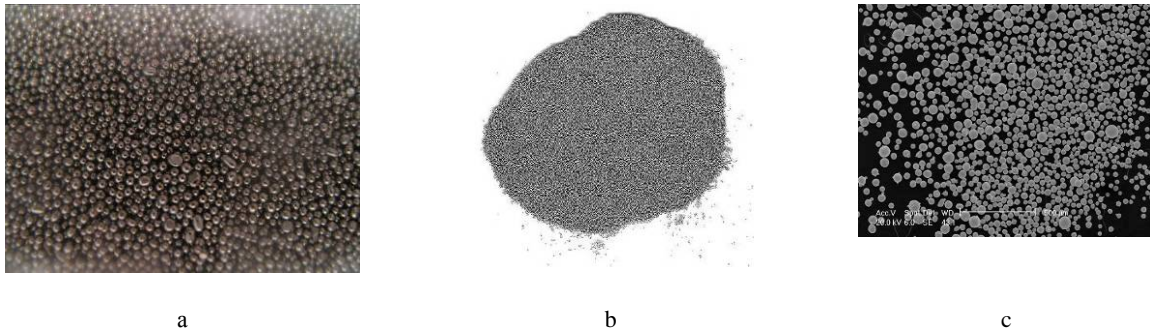|	Components	Granules size, μm	Temperature of melting, ^0C
Metal fuel	U-(1-9)Mo, U-(5-10)Zr, U-(2-5)Zr,Nb U-(1-9)Mo-(0.1-0.6)C	500-1200	1200-1300
Zr-matrix alloy	Zr-(1.5-2.5)Be-(4-7)Fe Zr-(6-12)Fe-(6-12)Cu Additional –Ti, Nb, Gd, etc	100-300	800 860-900
PuO_2		20-70	2200

FIG. 2. Appearance of initial components of composite U-PuO_2 fuel, (a) U-Mo alloy granules, (b) Zr-Fe-Cu alloy matrix granules, (c) PuO_2 powder manufactured by pyrochemical method [3, 6, 7]

Table 2. Characteristics of Composite U-PuO_2 Fuel [3, 6-8]

Components of fuel composition	Volume fraction, %	U(Pu) content under cladding, g/cm^3	Temperature of melting after manufacture, ^0C
Metal fuel	55-60	9-10	1300-1400
Zr-matrix alloy	7-15		1150-1250
PuO_2	10-20	0.9-1.8	2200
Pores	10-15 (30-40 without PuO_2)		

It is suggested to use as fuel the high density U alloys of U-Mo (from 1.5 to 9% Mo), U-Zr (from 5 to 10% Zr), U-Zr-Nb (from 5 to 10% Zr and Nb in total) systems as well as alloys of U-Mo with carbon

A.M. Savchenko, A.V. Vatulin, V.I. Sorokin, G.V. Kulakov, S.V. Maranchak

in which carbon as an impurity forms carbide phases in the structure, enhances the irradiation resistance and compatibility between fuel and cladding. The sizes of the fuel granules range from 0.5 to 1.2 mm [4-7]. Zirconium eutectic alloys are used as matrices [9-11]. The sizes of the matrix granules are 0.1 – 0.3 mm.

At the first stage frame fuel having porous meat is fabricated by the capillary impregnation method. Granules of fuel (U-Mo, U-Zr or U-Zr-Nb alloys) of depleted uranium and of a matrix are loaded into a fuel element cladding and the fuel element is heated to a temperature 50^0C higher than the melting temperature of a matrix (Fig. 3a, b) [9, 10].
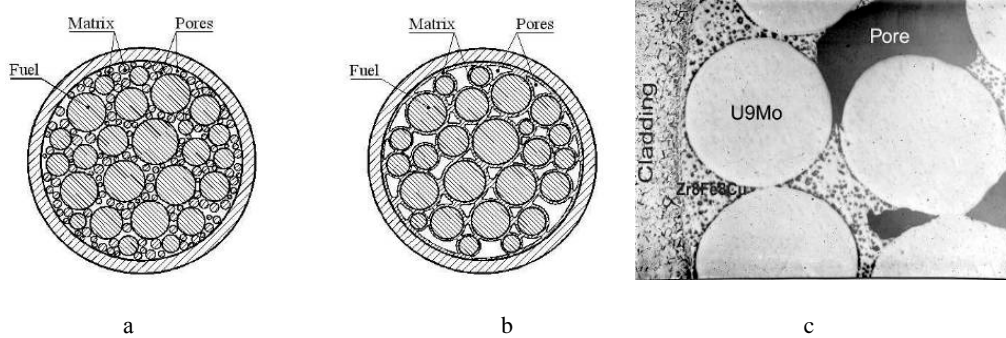

FIG. 3. Schematic presentation of fuel element cross-section, (a) as vibropacked, (b) as capillary impregnated, (c) structure of fuel meat, [9, 10]

The matrix alloy melts down and under capillary forces moves into gaps between fuel components to form metallurgical bonds. This technology provides the formation of controllable open porosity from 30% to 40% within the resultant frame fuel element, to further accommodate oxides of plutonium and MA. A layer of a Zr matrix alloy that is available at the inner surface of a fuel cladding protects it against cesium induced corrosion.

Since zirconium forms the base of the matrix alloys the alloys are compatible with high uranium content fuel both upon fabricating fuel elements and after long-term isothermal anneals of fuel compositions at 750 ^{0}C for 6000 hours [4, 9, 12, 13].

After fuel element fabrication the melting temperature of the Zr matrix alloys increases over 200-300 degrees as its composition alters due to the ingress of components from cladding and fuel. Since the Zr matrix alloys are deep ternary and quaternary eutectics any change in the alloy composition leads to a drastic rise of its melting temperature. As a result the alloy melting temperature increases, the alloy solidifies and the further interaction stops. This was confirmed by annealing a fuel element at 1000^0C for 30 minutes without any changes in the fuel dimensions and structure, as well as by in-pile irradiation of the matrix material in contact with the stainless steel cladding at 750^0C. This special design fuel element for Pu incineration reached the burn-up of 1.5 g.fiss/cm^3 under the fuel element cladding with the temperature of steam up to 600^0C.

At the second stage of the fuel element fabrication the powder of PuO_2 is filled into the frame (Fig. 4) [4, 7]. The PuO_2 powder is manufactured by the already mastered methods, viz., the pyrochemical one [8] or using the. The sizes of the powder particles are 0.02–0.07 mm. Then the second plug is welded up, and the finished fuel elements are subjected to the instrumental control. In this method of fabrication the dust forming technological operations minimized and all benefits of dispersion type fuel – (high uranium density, low fuel temperature, workability in transients, high burn-up) – will remain. It is one of the options of closing fuel cycle.

At 500–800^{0}C the thermal conductivity of the porous fuel meat makes up 20-25 W/m·K and increases with the temperature. Depending on the alloy used and its volume fraction the content of uranium per a unit fraction under the fuel cladding makes up 9-10 g/cm^3 that together with PuO_2 in the fuel element gives the smeared density up to 11 g/cm^3.
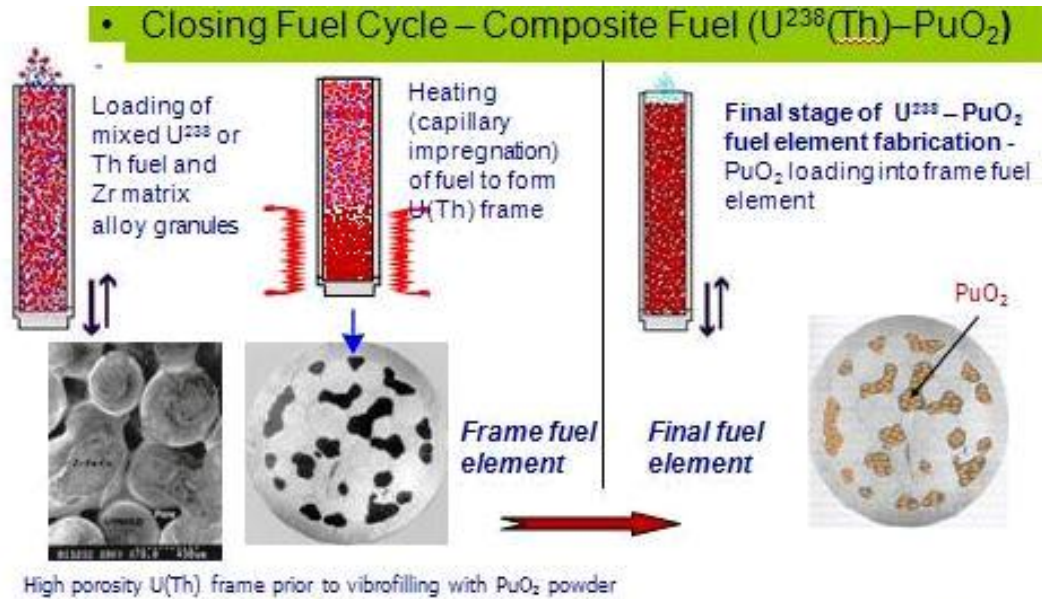
FIG. 4. U-PuO$_2$ dispersion composite fuel in place of MOX and fabrication stages [4, 7]

In this method of fabrication the dust forming technological operations minimized and all benefits of dispersion type fuel – (high uranium density, low fuel temperature, workability in transients, high burn-up) – will remain. It is one of the options of closing fuel cycle. Microstructure of composite fuel, where UO$_2$ is used in place of PuO$_2$ is illustrated in Fig. 5. In this option granules of Zr matrix and UO$_2$ were loaded simultaneously into fuel element cladding before annealing.
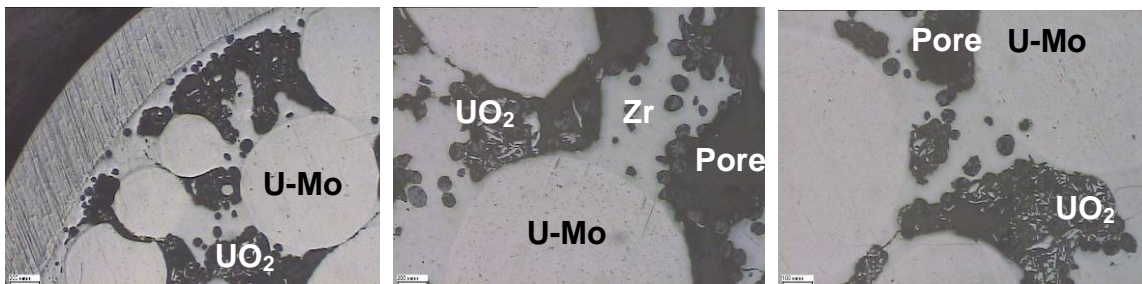

FIG. 5. Microstructure of composite fuel (UO$_2$ is used in place of PuO$_2$)

Mechanism of composite U(Th)-PuO$_2$ fuel operation. As example, mechanism of composite fuel operation for thermal reactors is represented in the Table 3 in comparison with MOX fuel. The similar mechanism and advantages will be for fast reactors. First PuO$_2$ burns up in METMET fuel frame while Pu generates in the METMET fuel that first serves as a breeding blanket and then begins to burn up. That is why the components of the composite fuel have different Pu isotope compositions at the cycle end. The plutonium dioxide powder will basically accumulate non-fissionable isotopes while the METMET fuel – fissionable ones. Hence, at the average MOX fuel burn-up of 45 MW*d/kgU, the METMET fuel shall contain 75 % fissionable isotopes while in PuO$_2$ there will be only 42 % (Table 4). By the mechanical separation METMET frame from PuO$_2$ powder the other without chemical reprocessing the composite fuel may be used many times at a high efficiency in this way saving natural uranium. In MOX fuel at the above burn-up the concentration of fissionable isotopes makes up only 55 %, hence, its re-use is economically not beneficial.

It has also to be noted that in the combined fuel the burn-up is distributed about equally between the PuO$_2$ powder and the granules of uranium alloys therefore the mechanically extracted granules will contain about two times less fission fragments having a high parasitic neutrons capture.

Table 3. Assessed Quantities of Fissionable Isotopes in Composite and MOX Fuel of VVER-1000 Operated on Three Year Cycle as Applied to Fuel Cycle Closing

Initial fuel MOX or PuO$_2$ powder	MOX pellets	Spent composite U-PuO$_2$ fuel		
	Spent MOX fuel	In METMET fuel granules	In PuO$_2$ powder	Average
66%	55%	75%	42%	58%

4.   Reprocessing of composite fuel

Novel fuel dissolves in hot nitric acid (typical reprocessing) as content of Zr matrix alloy in fuel meat is low, only 10-15% of fuel meat volume. In addition due to large volume fraction of intermetallic phases, available in the structure of Zr matrix alloy it is also dissolved in acid (but not as rapidly as uranium fuel itself).

Fuel elements from central (active) core of fast reactors. The basic difference of novel fuel is the separated arrangement of a depleted uranium alloy and PuO$_2$. Due to this fact the degree of their burn-up and their isotope composition will differ. While PuO$_2$ will almost fully burn and its composition will not practically contain fissile isotopes the metal fuel will build up Pu with fissile isotopes prevailing and having a high power value. Hence, as distinct from the standard design of a fuel element with homogeneously distributed heavy atoms (MOX or U-Pu-Zr) where the separation of fissile isotopes in Pu is a complicated task, in the novel fuel they are separated initially.

Hence, as applied to the novel fuel one may use a reprocessing flow sheet that is similar to DUPIC, but more simple one [6, 12, 13]. First, like in DUPIC via heating gas fission products are removed from fuel. Then a fuel element is subjected to a light deformation. Zr alloy matrix bridges between fuel granules are destroyed and a fuel element content is emptied on to a sieve where finer fractions of the burnt PuO$_2$ powder and the zirconium matrix alloy are separated from coarser granules of metallic fuel that also contains generated Pu (Fig. 6).
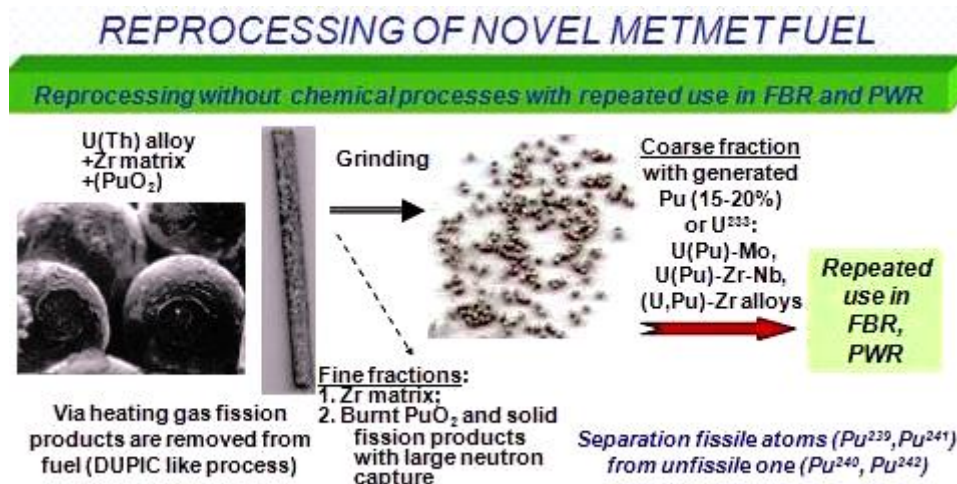

FIG. 6. Bridges between particles of a frame fuel element; its appearance without cladding and individual granules of frame fuel (U-2Mo-1Si) after crushing and sieving. Out-of-pile investigations.

Thus, the process of separating fissile components proceeds without fuel dissolving and chemical reprocessing. Drawn out isolated granules of U-Pu-Mo or U-Pu-Zr composition depending on their content of generated Pu might be re-used in fast or thermal reactors (PWR, CANDU) fuel. Using the

method of capillary impregnation a frame type fuel element can be fabricated (filling cladding with mixed fuel and matrix granules followed by anneal). In this case the components are selected in such a way as to achieve the minimal porosity (15-20%) that is needed to accommodate swelling. The resultant dispersion type (METMET) fuel element for thermal reactors (BWR, HPWR, CANDU) in comparison to the standard UO_2 pelletized fuel element has a higher uranium content, low temperatures of fuel (cold fuel) high burn-up and is serviceable under transients conditions.

Fuel elements from blanket. In the fast reactor blankets it is advisable to use fuel elements of the vibrofilled type with depleted uranium alloy granules. After they are removed from fuel element claddings they might be used for fuel elements of thermal reactors (BWR, HPWR, CANDU) using the above schema.

Thus, as distinct from the DUPIC the novel composite fuel does not require pulverization (pounding) of burnt pellets, an intricate process of manufacturing new fuel pellets from high activity powder. Moreover, in the new process the valuable in terms of the power plutonium isotopes (Pu239 and Pu241) are for the most part separated from Pu 242 and Pu 240. This makes fuel reprocessing more workable and environmentally friendly, which simplifies the closing of the nuclear fuel cycle.

5. Comparative characteristics and advantages of novel composite fuel

Comparative characteristics of fuel are shown in Table 4, taken from INL and DOE review on promising fuel for fast reactors - MOX and metallic U-Pu-Zr fuel. We have introduced into the table the version of new alternative composite $U-PuO_2$ fuel. MOX fuel has a high irradiation resistance but low thermal conductivity which limits the heat flux in a fuel element, and a relatively low uranium content which decreases the main parameter of fast reactor – conversion ratio. The U-Pu-Zr metal fuel having a high uranium content interacts with a fuel cladding and is more intricate in terms of the fabrication technology. The suggested $U-PuO_2$ composite fuel having a high conversion factor and thermal conductivity like metallic fuel does not interact with a fuel cladding since Zr matrix coats the cladding and protects against fuel-cladding interaction. Fabrication technology is simple and environment-friendly.

Table 4. Comparative Characteristics of Various Fuel Versions for Fast Reactors [1, 3]

Parameters	MOX $(U,Pu)O_2$	U-20Pu-10Zr	$UMo – PuO_2$
Content of fuel in fuel element (% of theoretical)	80-85%	75%	75% (55%+20%)
Fuel - cladding gap	0.1 mm He	0.7 mm Na	0.0 mm Metallurgical bond
U+Pu content under fuel cladding	8.3 g/cm³	11.0 g/cm³	11.0 g/cm³
Thermal conductivity of fuel, W/m.K	2-4	15-20	20-30
Adaptability of fuel element fabrication	mean	mean	high
Environmentally clean production	low	low	high

Major advantages of novel composite $U-PuO_2$ fuel:

- High contents of U and Pu compared to MOX fuel and, hence, high conversion ratio which makes it feasible to close nuclear fuel cycle.

- Lower damage of fuel by fission products and, hence, lower swelling compared to that of U-Pu-Zr fuel.

- Novel fuel is dispersion type fuel, therefore the existence of metallurgical bond between fuel and cladding not only decrease fuel temperature, but also protects fuel cladding from interaction with fuel and fission products.

- High fabrication adaptability and ecology of production – actually the main part of fuel element fabrication is carried on under conventional conditions and only the final operation of fuel element fabrication needs remote implementation. In this case PuO_2 is used as a powder not as pellets. All this minimizes process operations with Pu and makes the fuel element fabrication environmentally clean.

6. Fuel density increase and protection against fuel-cladding interaction via coating of cladding

One more interesting use of novel fabrication technology for composite fuel is its application for traditional rod type fuel – MOX and metallic U-Pu-Zr fuel (Fig. 1). As it has been mentioned above, while fabricating novel combined fuel a steel cladding is coated automatically with a low melting point Zr alloy matrix, that protects from fuel-cladding interaction.

But we can also produce such coatings on a hollow cladding from 5 to 50 microns thick (regulated sizes) to be further loaded with fuel meat. The technology is very simple and based on the contact between an inner surface of cladding and a molten matrix material. The layer of Zr alloy is metallurgically bonded with a steel cladding (Figs 7c, 7b) and protects it against interaction. Therefore, a cladding becomes compatible with pure uranium up to 800-900^{0}C.
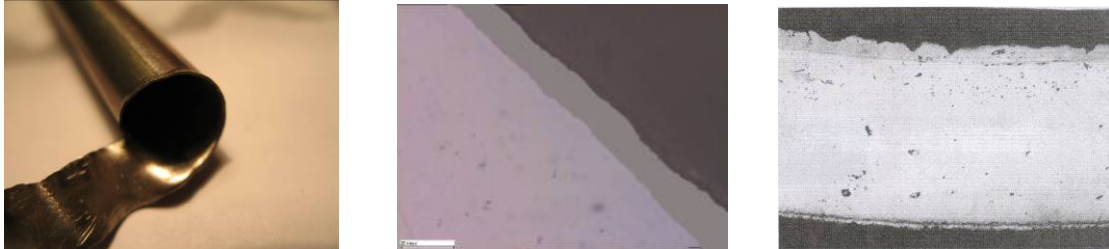

FIG. 7. Coated stainless steel cladding, (a, b) – as fabricated, c – after Cs_2O induced corrosion 700^{0}C – 1000 h.

Advantages for metallic U-Pu-Zr fuel. It is known that fuel-cladding interaction is one of the life-controlling factors in metal fuel. Preliminary results show that there was no fuel-cladding interaction with coated cladding up to 900^{0}C, while an uncoated cladding interacts with fuel at 700-750^{0}C.

Therefore, one can lower down Zr content in metallic fuel, which to increase U-Pu density. Moreover, *one* can also exclude Na in a gap, which simplifies the fabrication technology as well as diminishes fuel-cladding gap, since increasing U-Pu density.

Advantages for MOX fuel. The other problem for FBR MOX fuels, especially at high burn-ups, is fuel-cladding chemical interaction with fission products. That is the reason why MOX pellets of a low O/M ratio is required for a high burn-up FBR fuel. The other solution is to use an oxidized getter of zirconium alloys. The problem that a getter material is located only on the ends of the cladding, where an oxygen absorption takes place, while a larger part of a cladding is out of protection. In novel design a layer of a Zr matrix alloy that is available at the inner surface of a fuel cladding fully protects it against cesium induced corrosion, which was confirmed by testing steel claddings in a Cs oxide

environment at 700^0C for 1000 h (Fig. 7c) [3]. In this case no interaction was observable. Moreover, an alloy coat also serves as a getter.

7. Design of fuel element to burn MA

To burn up MA or Pu in IMF of thermal or fast reactors instead of pelletized fuel element with YSZ $(Er,Y,Pu,Zr)O_2$ a novel fuel design is suggested where oxides of MA is isolated in the fuel minielements (thin **steel** or Zr claddings) that are placed inside a fuel element. Inner space is filled with Zr matrix alloy (Fig. 8) [10, 14]. This design fully comply the requirements for 'Rock Fuel' and shall extend the burn-up, lower down the fuel temperature, accommodate swelling and make a fuel element serviceable under transient conditions.
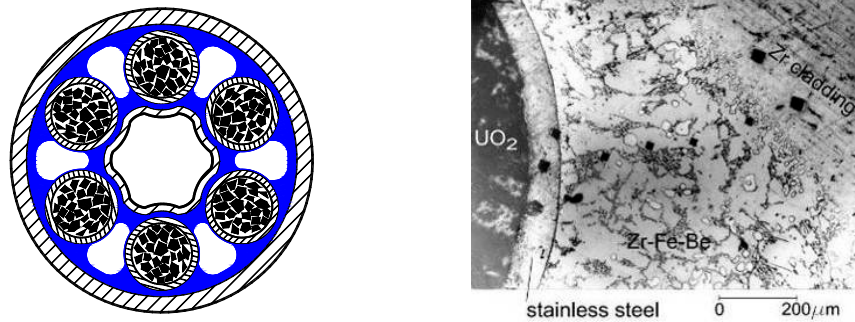

FIG. 8. Fuel element design with fuel minielements for MA incineration [10, 14]

8. Collaboration on composite fuel

This Dispersion-type Metallic Matrix Fuel is designed to solve the key challenges of ultra-high burn-up
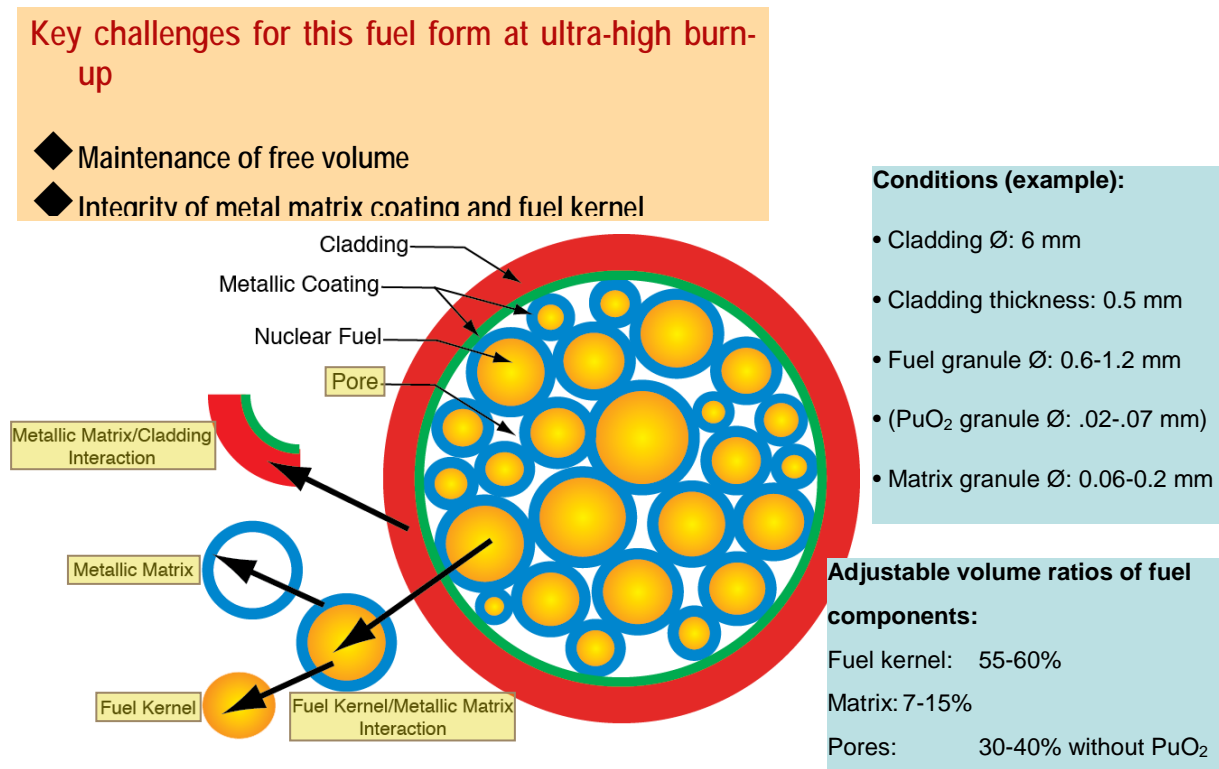

Key challenges for this fuel form at ultra-high burn-up

◆ Maintenance of free volume
◆ Integrity of metal matrix coating and fuel kernel

Cladding
Metallic Coating
Nuclear Fuel
Pore
Metallic Matrix/Cladding Interaction
Metallic Matrix
Fuel Kernel
Fuel Kernel/Metallic Matrix Interaction

Conditions (example):
• Cladding Ø: 6 mm
• Cladding thickness: 0.5 mm
• Fuel granule Ø: 0.6-1.2 mm
• (PuO$_2$ granule Ø: .02-.07 mm)
• Matrix granule Ø: 0.06-0.2 mm

Adjustable volume ratios of fuel components:
Fuel kernel: 55-60%
Matrix: 7-15%
Pores: 30-40% without PuO$_2$

FIG. 9. Key challengers to reach ultra-high burn-up (from LLNL Project "Ultra-High Burn-up Metallic Inert Matrix Nuclear Fuel"[15]

9

A.M. Savchenko, A.V. Vatulin, V.I. Sorokin, G.V. Kulakov, S.V. Maranchak

The idea of using composite fuel instead of pelletized one is becoming very popular in many countries. Patrice Turchi and Mike Fluss from LLNL USA prepared the Project "Ultra-High Burn-up Metallic Inert Matrix Nuclear Fuel" that was delivered to DOE for approval.[16]

Fig. 9 represents some main approaches of the Project. The main idea: "The proposed fuel form consists of actinide nuclear fuel particles, metallic or oxide, coated with a thin layer of Zr-based alloy metallurgically bonded with cladding (zircaloy or ferritic steel), and with porosity acting as built-in plenum for fission gas management and swelling mitigation" [15].

9. Conclusion

A possibility is considered for use in fast reactors in place of the base container type MOX or metallic U-Pu-Zr fuel, the dispersion type fuel elements (composite of metallic high uranium content fuel, U-Mo or U-Zr with PuO_2 powder distributed in Zr alloy matrix).Basic approach to fuel element development - separated operations of fabricating uranium meat fuel element and introducing into it Pu or MA dioxides powder, that results in minimizing dust forming operations in fuel element fabrication. According to new fuel element design a framework fuel element having a porous uranium alloy meat is filled with standard PuO_2 powder of less than 50 micron fractions prepared by pyrochemical or other methods. In this way a high uranium content fuel meat metallurgically bonded to cladding forms a heat conducting framework, pores of which contain PuO_2 powder. Framework fuel element having porous meat is fabricated by capillary impregnation method with the use of Zr eutectic matrix alloys, which provides metallurgical bond between fuel and cladding and protects it from interaction.

Proposed composite fuel features higher characteristics in comparison to metallic or MOX fuel.

A possibility is discussed of fabricating coated steel claddings to protect from interaction with fuel and fission products when use standard rod type MOX or metallic U-Pu-Zr fuel.

Novel approach to reprocessing of composite fuel is discussedwhich allows to separate uranium from plutonium as well as the newly generated fissile plutonium from burnt one without chemical processes with repeated use in fast, PWR or CANDU reactors, which simplifies the closing of the nuclear fuel cycle.

Basing on proposed design a novel concept "Ultra-High Burn-up Metallic Inert Matrix Nuclear Fuel" has been developing now at LLNL (USA) in cooperation with A.A. Bochvar Institute. The proposed fuel form consists of actinide nuclear fuel particles, metallic or oxide, coated by a thin layer of Zr-based alloy metallurgically bonded with cladding (zircaloy or ferritic steel) with retained porosity to accommodate fuel swelling.

REFERENCES

[1] CRAWFORD D. et al., Fuels for sodium-cooled fast reactors: US perspective, J. Nucl. Mater., 371 (2007) 202-231.
[2] IAEA-TECDOC-1374, Vienna (2003), 37-54.
[3] SAVCHENKO A.M. et al., New Concept of Designing Fuel for Fast Reactors, Proceedings of the International Conference Global-2009, Paris, France, 6-11 September, 2009, (available on CD)
[4] SAVCHENKO A.M. et al., Fuel of Novel Generation for PWR and as Alternative to MOX Fuel, Journal of Energy Conversion & Management, 51 (2010) 1826-1833.
[5] SAVCHENKO A.M., KONOVALOV I.I. "METMET Fuel with Zirconium Matrix Alloys",

Proceedings of the 7th International Conference on WWER Fuel Performance, Modelling and Experimental Support (WWER-2007), 17-21 September 2007, Albena (Bulgaria), 247-258

[6]   SAVCHENKO A.M. et al., New Concept of Designing combined Fuel for Fast Reactors with closing fuel cycle, Proceedings of the 10th US-Russian Workshop on Fundamental Properties of Plutonium, RAS, Moscow, Russia, 12-16 July, 2010, 271-278.

[7]   SAVCHENKO A.M. et al., New Concept of Designing Pu and MA Containing Fuel for Fast Reactors, J. Nucl. Mater., 385 (2009) 148-152.

[8]   BYCHKOV A.V. et al., Experience in closing nuclear fuel cycle developments, Proceedings of All-Russia Conference MAYAT-2007, Zvenigorod, 19-22 October 2007, 34-39.

[9]   SAVCHENKO A.M. et al., Dispersion type zirconium matrix fuels fabricated by capillary impregnation method, J. Nucl. Mater., 362 (2007) 356-363..

[10] SAVCHENKO A.M. et al., IMF with low melting point zirconium brazing alloys, J. Nucl. Mater., 352 (2006) 334-340.

[11] SAVCHENKO A.M. et al., Possibilities of closing nuclear fuel cycle with innovative METMET fuel, Proceedings of the 10th US-Russian Workshop on Fundamental Properties of Plutonium, RAS, Moscow, Russia, 12-16 July, 2010, 296-303.

[12] A.M. Savchenko, A.V. Vatulin, E.M. Glagovsky, et al., Possibilities of closing nuclear fuel cycle with innovative METMET fuel, Proceedings of the 10th US-Russian Workshop on Fundamental Properties of Plutonium, RAS, Moscow, Russia, 12-16 July, 2010, 296-303.

[13] SAVCHENKO A.M. et al., Fuel of Novel Generation for VVER and PWR, Proceedings of the International Conference TopFuel-2009, Paris, France, 6-10 September, 2009, (available on CD).

[14] SAVCHENKO A.M. et al., Main Results of the Development of Dispersion Type IMF at A.A. Bochvar Institute, J. Nucl. Mater., 396 (2010) 26-31.

[15] SAVCHENKO A.M., TURCHI P. E. A. et al., Evaluation of protective layer values in dispersion type IMF, Proceedings of the International Conference EMRS-2011 Spring Meeting, Nice, France, 9-13 May, 2011.

[16] P.Turchi Ultra-High Burn-up Metallic Inert Matrix Nuclear Fuel Concept, conract DE-AC52-07NA2734, LLNL, USA

Design of Neptunium-bearing Fuel Assembly for Transmutation Research in CEFR

Baoyu Xu, Chen Huang

China Institute of Atomic Energy,Beijing, Poeple's Republic of China

Abstract. In order to have a better understanding of irradiation performance of the fuel containing neptunium, an experimental assembly is designed for future irradiation in CEFR. There is only one fuel pin in the assembly with neptunium content of 5%. Temperature monitors and neutron fluence detectors are attached. The report presents the basic structure of the fuel pin and the assembly.

1.   INTRODUCTION

China Experimental Fast Reactor (CEFR) completed a series of start-up tests in 2010 and was connected to the grid on 40% nominal power in 2011. Now it is just before the stage of power elevation test, not far from taking on its role as a multifunctional experimental platform. To study the irradiation performance of the fuel containing minor actinides and to explore the transmutation technology, an experimental assembly containing neptunium is designed on the basis of the standard fuel assembly of CEFR. It is to be irradiated in the first row of the stainless steel reflector assemblies for about 240 effective full power days, i.e. 3 cycles of CEFR.

2.   DESIGN PRINCIPLES

The design of the experimental assembly observes the following principles. Firstly, the test assembly should have the same outline with the adjacent assemblies. Secondly, it can be loaded into or unloaded from the core through the refueling system of CEFR. Thirdly, coolant and detergent can be discharged thoroughly when the assembly is being removed out of the core and cleansed. Fourthly, the maximum pressure drop of the coolant through the assembly is 0.27MPa, the same with the stainless steel reflector assemblies. Fifthly, under all operational scenarios, the experimental assembly can retain its position and will not float from the small diagrid.

3.   DESIGN DETAILS

The experimental assembly is composed of head, upper adapter, hexagonal thimble, fuel pin subassembly, stainless steel pins, grid, lower adapter and foot, as shown in **FIG. 1**.

The head matches the claw of fuel-handling machine, and has coolant outlet holes on it.

The upper adapter connects the head and the hexagonal thimble, and it has protruding pads at six corners for radial location with the neibouring assemblies. It is connected to the head by screw thread and pins.

The hexagonal thimble is welded to the upper and lower adapters at the ends.
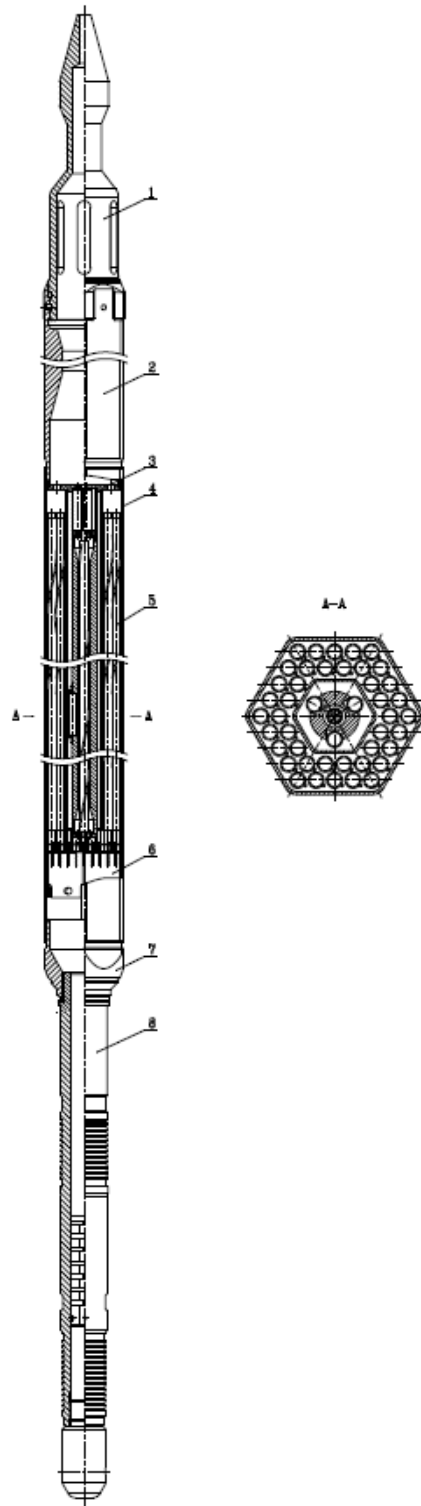
1- head 2-upper adapter 3-fuel pin subassembly 4-outer thimble 5-stainless steel pins 6-grid

7-lower adapter 8-foot

FIG. 1. Experimental assembly.

The lower adapter connects the hexagonal thimble and the foot. It has a spherical surface which forms sealing with the conical surface of the small diagrid.

The foot, as a round tube, matches the small diagrid which it is supposed to sit on. There are coolant inlet holes on its side surface and a flux-regulator inside. It is welded to the lower adapter.

One single fuel pin is hung from above in the center of the assembly, with 3 neutron fluence detectors circumferentially set in even pattern on the midplane and 3 temperature monitors settled at the outlet. The neutron fluence detectors are embedded in the grooves of the thick-walled lower tube outside the fuel pin and fixed by retainers which are welded to the lower tube. The upper plate, the middle plate and the lower plate are used for axial location of the fuel pin and the temperature monitors. The upper tube connects the upper plate and the lower tube. The combination of the above parts is called "the fuel pin subassembly", as shown in **FIG. 2**. It is welded to the upper adapter.

The fuel pin basically consists of one cladding and two end- plugs and is about 1.3m in length. The cladding tube is 6.0mm in diameter and 0.4mm in wall thickness. The pellet is 5.0mm in diameter and 6.5~9.0mm in length with Np content of 5% and barren uranium for the rest. The fuel smear density is about 9.6g/cm3. The pellet column is 96mm in length. A spiral spring over the pellet column and the two end plugs altogether fix the pellet column axially. The cladding tube is filled with helium and the initial pressure is 0.11MPa. There is a wire winding along the outer surface of the cladding. Its diameter is 0.95mm and the pitch is 100mm.

The peripheral of the fuel pin is occupied by 42 stainless steel pins, which has similar structure with the fuel pin. In the middle of each stainless steel pin there is a gas plenum which gives way to neutrons. The plenum is 450mm long in accordance with the active zone of the core. The stainless steel pins ride on the grid comprised of several onion-shaped plates and there are no welds involved. The grid is welded to the hexagonal thimble.

To equalize the coolant sub-channels, a smaller hexagonal tube is used to separate the central fuel pin from the surrounding stainless steel pins. Accordingly, the coolant splits into two branches. One goes through the central fuel pin, and the other cools down the stainless steel pins.

Physical and thermal-hydraulic computations were made to estimate the temperature distribution inside the assembly, which helped wih the decision of key structure parameters of the assembly.

The main characteristics of the experimental assembly are summarized in **Table 1**.

Table 1. Characteristics of experimental assembly

Parameter	Value
Length of the assembly, mm	2592
Length of the fuel pin, mm	1325
Length of the pellet column, mm	96
Length of the stainless steel pin, mm	1350
Weight of the assembly, kg	28
Irradiation period, effective full power days	240
Maximum linear power, W/cm	22
Maximum burnup of the fuel pin, MWd/kg	2.3
Maximum temperature of the pellet, ℃	568
Maximum temperature of the cladding, ℃	500
Inlet temperature of the coolant, ℃	360
Outlet temperature of the coolant, ℃	500
maximum pressure drop of the coolant, MPa	0.27

Up to now, the design has been completed and the assembly is under manufacturing.

To obtain the accurate dimension of the flux-regulator in the foot and to validate the design, a dummy assembly is to be manufactured at first. A Series of out-pile tests are to be conducted on the dummy one. They include the flux-allocating test, the eroding test and the flow-induced vibration test.
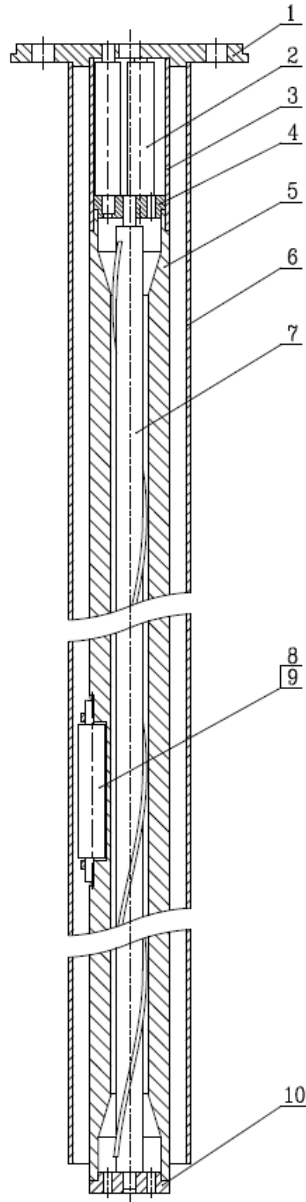
1-upper plate 2-temperature monitor 3-upper tube 4-middle plate 5-lower tube

6-small hexagonal tube 7-fuel pin 8-neutron fluence detector 9-retainer 10-lower plate

FIG. 2. fuel pin subassembly.